Werkstofftechnik

UNIVERSITÄT SIEGEN

Chunqiang Zhuang

Theoretical Investigation and Experimental Confirmation of Crystalline and Amorphous Si, B, C, N-based Hard Materials

Schriftenreihe der Arbeitsgruppe des Lehrstuhls für Oberflächen- und Werkstofftechnologie im Institut für Werkstofftechnik

Herausgeber: Prof. Dr. rer. nat. habil. Xin Jiang

Band 2

Chunqiang Zhuang

Theoretical investigation and experimental confirmation of crystalline and amorphous Si, B, C, N–based hard materials

Schriftenreihe der Arbeitsgruppe des Lehrstuhls für Oberflächen-und Werkstofftechnologie im Institut für Werkstofftechnik

Impressum
Prof. Dr. rer. nat. habil. Xin Jiang
Lehrstuhl für Oberflächen- und Werkstofftechnologie
Institut für Werkstofftechnik
Universität Siegen
57076 Siegen
ISSN: 2194-0096
Zugl.: Siegen, Univ., Diss., 2013

THEORETICAL INVESTIGATION AND EXPERIMENTAL CONFIRMATION OF CRYSTALLINE AND AMORPHOUS SI, B, C, N–BASED HARD MATERIALS

Vom Department Maschinenbau

der Universität Siegen

zur Erlangung des akademischen Grades

Doktor-Ingenieur

genehmigte

Dissertation

von:	M. Sc., Chunqiang Zhuang
aus:	Henan, China
eingereicht am:	08. May 2013
Mündliche Prüfung am:	17. July 2013
Referent:	Prof. Dr. rer. nat. habil. X. Jiang
Korreferent:	Prof. Dr. W. H. E. Schwarz

Zusammenfassung

In den vergangenen zwei Jahren zog die neu entdeckte kubische BC_2N Phase großes Interesse auf sich. Gründe hierfür liegen in einem Härtewert der neuartigen superharten Phase von ~ 76 GPa, der nur knapp unterhalb von Diamant (~ 100 GPa) liegt. Es gilt als das zweit härteste jemals bekannte Material und ist noch härter als kubische BN (~ 50 GPa). Nach den Untersuchungsergebnissen gewann die unvorstellbare superharte Eigenschaft sofort eine breite Aufmerksamkeit. Allerdings wurde die Kristallstruktur dieser neuartigen Phase bisher noch nicht bestimmt. Experimentelle Ergebnisse des Kristalls sind ebenfalls widersprüchlich. Theoretische Berechnungen wurden verwendet, um die Kristallstruktur der Phase durch das Erstellen verschiedener Strukturmodelle zu enthüllen. Aufgrund von Unterschieden in den Strukturmodellen sind diese berechneten Ergebnisse ebenso widersprüchlich.

Wir schlagen hier ein Mischkristall–Modell vor, um mögliche Strukturen der kristallinen Phase zu finden, das durch den Parameter des Mischungsgrades klassifiziert ist. Die beeindruckende Eigenschaft unseres Modells liegt im folgenden Aspekt: es erläutert nicht nur die Diskrepanz experimenteller Beobachtungen, sondern vereinigt auch die in theoretischen Berechnungen gezeigte Inkonsistenz. Mittlerweile erweiterten wir unser Model auf B–C–N Zusammensetzungen entlang der C–BN isoelektronischen Linie und weitere Bereiche in dem ternären B–C–N Phasendiagramm neben BC_2N, mit der Annahme potentielle superharte Phasen zu entdecken, die vergleichbar und sogar härter als das kubische BC_2N sind. Tatsächlich existieren solche Bereiche in dem ternären B–C–N Phasendiagramm, in denen sie härter als BC_2N sind. Unsere Vorhersage von der superharten Phasenbildung stellt eine allgemeine Orientierungshilfe für experimentelle Arbeiten dar, um bewusst solche superharten Phasen mit entsprechend einstellbaren experimentellen Parametern herzustellen. Zusätzlich erweiterten wir unser Modell auf kubische B–C Kristalle. Die hervorragende Übereinstimmung zwischen experimentellen und unseren theoretischen Ergebnissen zeigen deutlich die Übertragbarkeit unseres Modells auf andere ähnlich kovalent Kristallmaterialien.

Nach bestem Wissen führten wir zum ersten Mal die theoretischen Berechnungen von amorphen B–C–N Materialien im atomaren Maßstab durch. Basierend auf grundsätzlichen Berechnungen wurde der Zusammenhang zwischen chemischer Zusammensetzung, Gefüge

und mechanischen Eigenschaften hergestellt. Dies ist auch das erste Mal, dass dieser Zusammenhang in Abhängigkeit von so vielen chemischen Anordnungen von amorphen B–C–N Schichten hergestellt wurde. Das Verhältnis kann die allgemeine Darstellung der Verteilung von mechanischen Eigenschaften im ternären B–C–N Phasendiagramm angeben. Dadurch kann es die experimentellen Arbeiten anleiten, um diese Zusammensetzungen mit besseren mechanischen Eigenschaften herzustellen. Wir synthetisierten auch amorphe B–C–N Schichten, indem verschiedene experimentelle Parameter geändert wurden, um unsere theoretischen Ergebnisse zu verifizieren. Die erhaltenen experimentellen Zusammensetzungen liegen meist, nachgewiesen durch theoretische Berechnungen, in dem Bereich geringer Bildungsenergie, entsprechend der am einfachsten herzustellenden Zusammensetzung. Mit anderen Worten, unsere experimentellen Arbeiten können die theoretischen Arbeiten mit hinreichender Genauigkeit reproduzieren.

Neben B–C–N Materialien wurden Si–C–N Materialien hergestellt in der Erwartung die Beziehungen zwischen mechanischen Parametern, wie das Verhältnis von Härte zu Elastizitätsmodul, für das kovalente amorphe Material zu extrahieren, da es bisher noch kein geeignetes Modell zur Berechnung der Härte von amorphen Materialen gibt. Wenn einige andere mechanische Größen ermittelt werden, die in einem guten Zusammenhang mit der Härte stehen, dann kann die Härte indirekt durch theoretische Berechnungen ermittelt werden. Außerdem wurden Substrateffekte für solche kovalent amorphen Materialen diskutiert.

Acknowledgements

At this moment, I really appreciate all people who supported me during the last four years. Without their help, the quality of my thesis could not be guaranteed.

I am very grateful to my supervisor Professor X. Jiang for giving me an opportunity to study in his group. During the last four years for my Ph.D work, he helped me a lot with all kinds of problems, both in my life and in my work. I received numerously valuable suggestions from him. He made great efforts in critically correcting my presentation and thesis. I have also received many novel ideas from him concerning how to do good scientific research work. I really appreciate his great help for me during the last four years in Germany.

Special thanks with my greatest respect are given to Professor W. H. E. Schwarz for his kindness to be the co-referee of my thesis. I also would like to than Professor R. Trettin and Professor H. Foysi for their contributions to the examination of my thesis.

I would like to thank another Professor J. J. Zhao, the supervisor of my master degree. It is he that guides me to do scientific research from the very beginning that I knew nothing about scientific research till now that I am deeply in love with scientific research. He played the crucial role. I really appreciate him for his kindness and great patience with me.

I want to thank all my colleagues, especially my German colleagues Thomas Degen, Michael Vogel, Regina Fuchs, Christoph Schlemper, and Staedler Thorsten. I learned so many things from them and had a very pleasant time in Germany. I also would like to thank my master students, Yuan Wen, Xue Jiang, Fuchao Jia, and Changyu Guan, for their participation in my Ph.D work.

Last but not least, I would like to give my unique thanks to my family for their tolerance and support of my scientific research.

Siegen, in July 2013 Chunqiang Zhuang

List of Publications

In this thesis, the following publications have been included:

[1] **Structural Stability, Mechanical and Electrical Properties of Cubic BC_xN Crystals within a Random Solid Solution Model**

C. Zhuang, J. Zhao, X. Jiang, and X. Jiang, J. Phys.: Condens. Matter 21 (2009) 405401.

[2] **Structural and Elastic Properties of Crystalline and Amorphous BC_2N Solids**

C. Zhuang, X. Jiang, J. Zhao, and X. Jiang, J. At. Mol. Sci. 1 (2010) 126.

[3] **Stability and Mechanical Properties of BC_x Crystals: the Role of B–B Bonds and Boron Concentration**

C. Zhuang, X. Li, J. Zhao, L. Liu, and X. Jiang, J. Phys.: Condens. Matter 22 (2010) 215401.

[4] **Fluctuations of Tensile Strength and Hardness of c–BC_2N Crystals Induced by Difference in Atomic Configuration**

C. Zhuang, X. Li, J. Zhao, H. Samra, and X. Jiang, J. Phys.: Condens. Matter 23 (2011) 465401.

[5] **Structure and Mechanical Properties of Cubic BC_2N Crystals within a Random Solid Solution Model**

J. Zhao, C. Zhuang, and X. Jiang, Diamond Relat. Mater. 19 (2010) 1419.

[6] **Mechanical Behavior of Completely Amorphous Si–C–N Films Characterized by Nanoindentation**

C. Zhuang, C. Schlemper, R. Fuchs, M. Vogel, T. Staedler and X. Jiang. (under review)

[7] **Mapping Distributions of Mechanical Properties and Formation Ability on the Ternary B–C–N Phase Diagram**

X. Jiang, C. Zhuang, X. Li, L. Sai, J. Zhao, and X. Jiang, Diamond Relat. Mater. 20 (2011) 891.

[8] **Searching Superhard Cubic Phase in the Ternary B–C–N Phase Diagram Using First–Principles Calculations**

Y. Wen, C. Zhuang, X. Jiang, J. Zhao, and X. Jiang, Diamond Relat. Mater. 27-28 (2012) 14.

[9] **Preparation of B–C–N Films by Magnetron Sputtering with Different N_2/Ar Flow Ratios**

F. Jia, C. Zhuang, C. Guan, J. Zhao, Y. Bai, and X. Jiang, Vacuum 85 (2011) 887.

[10]**Relationship between Chemical Compositions of Magnetron Sputtered B–C–N Films and Various Experimental Parameters**

C. Guan, J. Zhao, F. Jia, C. Zhuang, Y. Bai, and X. Jiang, Vacuum 86 (2012) 1499.

Table of Contents

List of Abbreviations

AFM	Atomic Force Microscopy
c–BN	Cubic Boron Nitride
CVD	Chemical Vapor Deposition
DFT	Density Functional Theory
ECR–CVD	Electron Cyclotron Resonance Chemical Vapor Deposition
FCC	Face–Centered Cubic
FESEM	Field–Emission Scanning Electron Microscope
FTIR	Fourier Transform Infrared Spectroscopy
FWHM	Full Width at Half Maximum
GGA	Generalized Gradient Approximation
h–BN	Hexagonal Boron Nitride
HF	Hartree–Fock
HF–CVD	Hot Filament Chemical Vapor Deposition
HPHT	High Pressure High Temperature
IBAD	Ion Beam Assisted Deposition
IR	Infrared Spectroscopy
LDA	Local Density Approximation
NCPP	Norm–Conserving Pseudopotional
NMR	Nuclear Magnetic Resonance
NVT	Canonical Ensemble
PA–CVD	Plasma Assisted Chemical Vapor Deposition
PAW	Projector Augmented Wave
PLD	Pulsed Laser Deposition
PMB	Pyrrolidino Diethylamine
PVD	Physical Vapor Deposition
RDF	Radial Distribution Function
RF	Radio Frequency

RMM–BISS	Residual Minimization Scheme, Direct Inversion in the Iterative Subspace
RMS	Root Mean Square
RPA–CVD	Remote Plasma Assisted Chemical Vapor Deposition
SAED	Selected Area Electron Diffraction
SCCM	Standard Cubic Centimeter Per Minute
T–CVD	Thermal Chemical Vapor Deposition
TEM	Transmission Electron Microscopy
TMB	Trimethylborazine
USPP	Ultrasoft Pseudopotential
VASP	Vienna Ab Initio Simulation Package
XANES	X–Ray Absorption near Edge Structure
XPS	X–Ray Photoelectron Spectroscopy
XRD	X–Ray Diffraction

Abstract

The newly discovered phase, cubic BC_2N, has attracted great interest during the past two decades. This is because the hardness of the novel superhard phase can even reach up to ~ 76 GPa, only behind diamond (~ 100 GPa). It is ranked as the second hardest material ever known, even harder than cubic BN (~ 50 GPa). The fantastic property of superhardness immediately gained wide attention after the findings. However, the crystal structure and atomic configuration of the novel phase have still not been determined so far due to the similar atomic size of B, C, and N. Experimental results of the crystal are also inconsistent. Theoretical calculations are employed to attempt to unveil the crystal structure of the phase by constructing diverse structural models. Due to the difference of the structural models, these calculated results are contradictory as well.

Here we propose a solid solution model to search possible structures of the crystalline phase, which are classified by the parameter of the degree of mixture. The powerful feature of our model lies in the aspect that it not only successfully illustrates the discrepancy observed in experiments, but also unifies the inconsistency shown in theoretical calculations. Meanwhile, we extended our model to B–C–N compositions along the C–BN isoelectronic line and broader areas in the ternary B–C–N phase diagram besides BC_2N, with the expectation of discovering potential superhard phases that can be comparable to or even harder than cubic BC_2N. Indeed, there exist such areas in the ternary B–C–N phase diagram in which they are harder than BC_2N. Our prediction of superhard phases can provide general guidance for experimental works to intentionally prepare such superhard phases by regulating correspondingly experimental parameters. In addition, we also extended our model to cubic B–C crystals. The excellent agreement between experimental results and our theoretical ones clearly demonstrates the transferability of our model to other similar covalent crystalline materials.

To the best of our knowledge, we performed, for the first time, theoretical calculations of amorphous B–C–N materials at the atomic scale. Based on first–principles calculations, the

relation among chemical composition, microstructure, and mechanical properties was established. This is also the first time to build the relation depending on so many chemical compositions of amorphous B–C–N films. The relation can give the general description of the distribution of mechanical properties in the ternary B–C–N phase diagram. Thus it can also guide the experimental works to prepare those compositions with better mechanical properties. We also synthesized amorphous B–C–N films by changing diverse experimental parameters to verify our theoretical results. The obtained compositions in experiments are mostly located in the area that has lower formation energy according to our theoretical calculations, corresponding to those compositions that are easier to obtain. In other words, our experimental works can reproduce the theoretical works well with reasonable accuracy.

Besides B–C–N materials, Si–C–N materials were also prepared with the expectation of extracting the relations between mechanical parameters for covalent amorphous materials, such as the relation of hardness and Young's modulus. If some other mechanical quantities can be found to have good relations with hardness, then the hardness can be indirectly evaluated by theoretical calculations. In addition, the substrate effects were also discussed for such covalent amorphous materials.

1 Introduction

1.1 Research Background

Nowadays, hard wear protective coatings have gradually become more dominant in broad industrial applications [1]. The importance of such protective coatings has been demonstrated by their extensive use in cutting tools, which are commonly covered by wear resistant materials [2]. In general, wear resistant materials coated on cutting tools need to possess one important attribute, that is, high hardness [2, 3]. Therefore, superhard coatings, defined as the Vickers hardness not less than 40 GPa, have developed into a hot topic both for basic scientific research and for potential industrial applications. Among numerous candidates, diamond and cubic boron nitride (c–BN) are two kinds of traditional superhard materials.

The diamond structure is composed of two interpenetrating face centered cubic lattices (FCC). They are distributed along the body diagonal direction of diamond. As shown in Figure 1.1, each carbon atom is bonded to four other neighbor ones in terms of a tetrahedral bonding mode. It is such a unique bonding style that allocates various excellent properties to diamond. For example, diamond is the hardest material ever known, with hardness values of 80 ~ 100 GPa [4]. It can scratch any other materials at room temperature. This makes it the first choice assembled on grinding/drilling tools, cutting devices, and polishing equipments. It has high thermal conductivity, which is nearly four times higher than that of copper or silver at low temperature. In addition, it displays the highest refraction index for the applications to optical devices. However, diamond also has some fatal deficiencies. It has low oxidation resistance, it can be oxidized around 600 ^{o}C and burned into carbon dioxide at 800 ~ 900 ^{o}C in air [5]. It can also react with elemental iron. Thus it cannot be used to cut iron–based materials. All these together limit its application to the field of cutting machining steels.

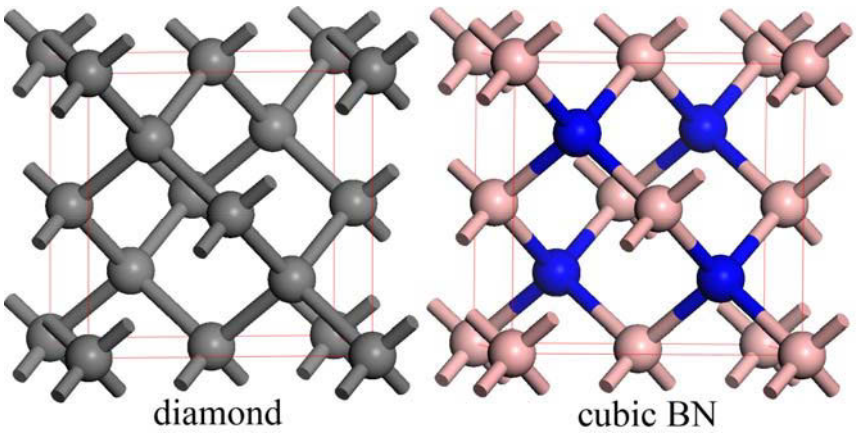

Figure 1.1: *Structures of diamond and cubic BN (c–BN). Boron: pink; carbon: grey; nitrogen: blue.*

c–BN, the second hardest material, has a similar crystal structure as diamond. Its structure can be considered as the case: carbon atoms in diamond lattice are replaced by boron and nitrogen atoms in terms of alternate arrangements. Compared with diamond, c–BN does not react with iron. In addition, it does not dissolve in most of common metals. It has high–temperature oxidation resistance in air [6]. However, its hardness is only about half of that of diamond. Therefore, it is expected that B–C–N materials would have both the high hardness inherited from diamond and the super oxidation inertness from c–BN. It is also anticipated that they would be good electronic materials with super electrical properties.

In principle, it is possible to form such kinds of ternary B–C–N solid solution materials based on the following considerations. Boron, carbon, and nitrogen are near neighbor elements. They have similar atomic sizes. Furthermore, diamond and c–BN have similar crystal structures, closely matched lattice parameters (diamond: 3.567 Å; c–BN: 3.615 Å) [7], high melting points (diamond: 3850 K; c–BN: 3300 K) [8], large bulk moduli (diamond: 442 GPa; c–BN: 368 GPa) [9], and low thermal expansion coefficients. The potential properties of such B–C–N materials, inherited from the combination of diamond and c–BN, make them highly desirable for numerously industrial applications. Consequently, they have been extensively investigated as novel superhard materials during the last two decades. In the following sections, a comprehensive review of crystalline and amorphous B–C–N materials will be given firstly from the perspective of both experiments and theoretical calculations.

1.2 Crystalline B–C–N Materials

1.2.1 Experimental Findings

Novel $B_xC_yN_z$ materials were firstly pioneered by Wedlake and Penny in 1980 (US Patent: 4187083). They prepared cubic B–C–N materials with the preferred composition of BCN by static high pressure and high temperature (HPHT) techniques. The pressure and the temperature, i.e. the experimental conditions they used, were 5 ~ 10 GPa and 1300 ~ 2000 ^oC, respectively. The Knoop hardness of BCN was 4050 ~ 9000 kg/mm^2, which can be viewed as comparable to that of diamond and c–BN (1GPa ≈ 102 kg/mm^2). Afterward, Badzian prepared a dedicated work to Niemyski for his pioneering work in the field of high pressure high temperature research (HPHT) [10]. Cubic BN–C crystals were obtained by the direct phase transformation of graphite and hexagonal boron nitride (h–BN) under a pressure of 14 GPa and a temperature of ~ 3600 ^oC. The obtained materials were speculated to have a diamond–like structure according to XRD analysis.

The medium–term research works of B–C–N materials are mainly performed by Japanese scientists in the years 1990 ~ 2000. For example, Sasaki et al. attempted to transform the graphite–like B–C–N materials to cubic phases with the addition of a cobalt catalyst under HPHT conditions (5.5 GPa, 1400 ~ 1600 ^oC) [11]. Their powder X–ray diffraction patterns show the information of the starting material: the graphite–like BC_2N crystal, giving broad lines to (001), (002), (10), and (11) reflections. Under compression of 5.5 GPa, the diffraction pattern is significantly changed. Two new cubic phases were detected. The lattice parameters of the two new phases are 3.6162 Å at 1400 ^oC; 3.6169 Å at 1500 ^oC; 3.6162 Å at 1500 ^oC for one cubic phase, and 3.5656 Å at 1400 ^oC; 3.5660 Å at 1500 ^oC; 3.5662 Å at 1500 ^oC for the other one. They can be assigned to diamond (3.5567 Å) and c–BN (3.6158 Å). This indicates that the products obtained are mainly a mixture of diamond and c–BN.

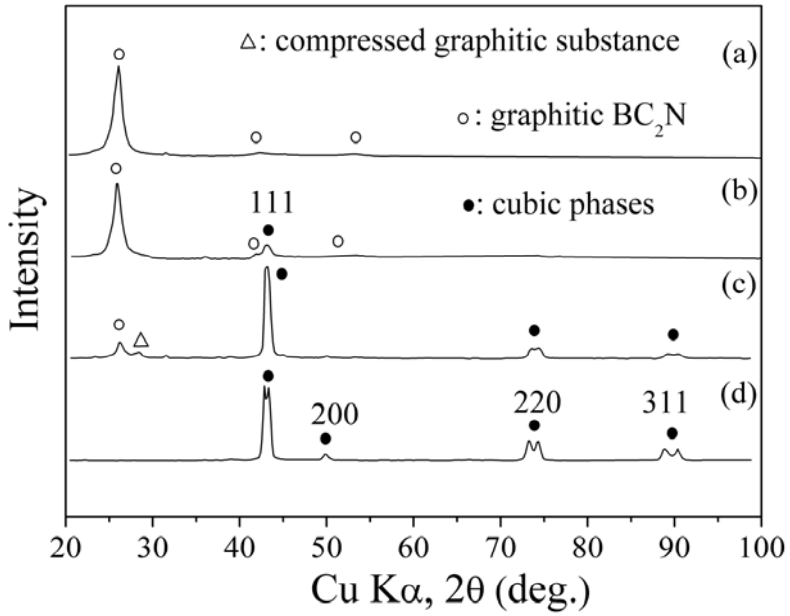

Figure 1.2: *Powder XRD patterns of the product prepared at 7.7 GPa and (a) 2000 °C, (b) 215 °C, (c) 2300 °C, and (d) 2400 °C. (from Ref.[12])*

Without the addition of a catalyst, Nakano et al. examined the graphite–like BC_2N under HPHT conditions (7.7 GPa, 2000 ~ 2400 °C) [12]. They found that their products were very sensitive to the temperature. As indicated by the XRD patterns in Figure 1.2, the product obtained at 2000 °C is nearly the same as the starting material: graphite–like BC_2N. When the temperature increased up to 2150 °C, new diffraction peaks located at (111), (200), (220), (311), (400) and (331) are presented. As shown in Figure 1.2c, further increment of the temperature up to 2300 °C results in higher yield of cubic products. While at a temperature of 2400 °C, the splitting peaks indicates the segregation of cubic products into c–BN and diamond.

Komatsu et al. thought that static HPHT conditions provide products such a long time for structural relaxation that they were decomposed again into other phases that are more thermodynamically stable [13-17]. Therefore, they predicted that rapid quenching can probably be suitable to obtain such kinds of non–equilibrium materials. They attempted to use the shock compression technique to transform the hexagonal $BC_{2.5}N$ compound into a cubic one in a very short time [13]. Their XRD patterns show that the starting material has a hexagonal structure. However, after transformation the (100), (222) and (420) diffraction peaks disappear. Combining *d* values, intensities and lattice parameters from XRD results,

they gave the conclusion that their products have a diamond–like structure. The deposition mechanism was also demonstrated under shock compression from the transformation of liquid phase to solid phase [16]. They thought that a diamond–like structure can be formed by rapid crystallization from the liquid phase, and then rearranged by slow crystallization with cooling of the liquid phase. In subsequent works, they also successfully prepared B–C–N heterodiamond compounds with other compositions, such as BCN, BC_2N, BC_3N, and BC_5N as identified by XRD. However, the yield was very low [14].

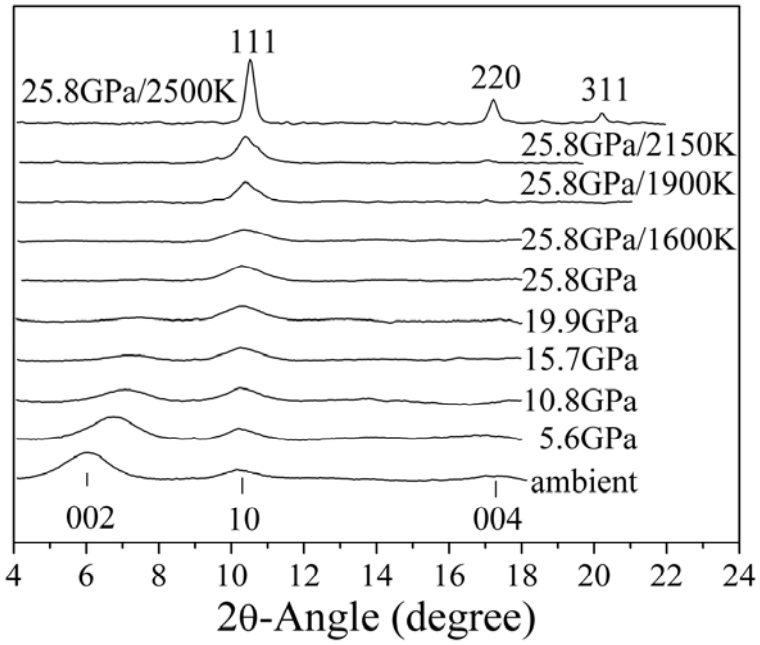

Figure 1.3: *XRD pattern under different pressures and temperatures. Bottom and top patterns correspond to g–BC_2N and c–BC_2N, respectively. (from Ref.[18])*

Since the beginning of the 21st century, B–C–N materials have again received intensive investigations due to the report of Solozhenko [18]. He declared that the superhard cubic BC_2N crystal was successfully synthesized by the HPHT technique. The hardness of the crystal reached up to ~ 76 GPa, ranked only next to diamond, even larger than that of c–BN. They confirmed the cubic phase by detailed XRD results as shown in Figure 1.3. At ambient pressure, the XRD pattern shows the diffraction information of the starting material: graphite–like BC_2N. With pressure increasing up to 19.9 GPa, the intensity of the (002) Bragg line decreases dramatically, and even disappears when the pressure reaches up to 25.8 GPa, leaving only the (10) asymmetric lines observed. Then they fixed the pressure at 25.8 GPa and

attempted to increase the temperature. With temperature lower than 1600 K, the XRD pattern shows no much difference from that at room temperature. However, as the temperature gets higher than 2200 K, especially at 2500 K, unambiguous diffraction peaks located at (111), (220), and (311) can be observed, clearly revealing that a new phase is formed. They demonstrated that the new phase is not the mixture of c–BN and diamond by further XRD analysis. Besides, the new cubic phase was also detected by Raman characterization [19].

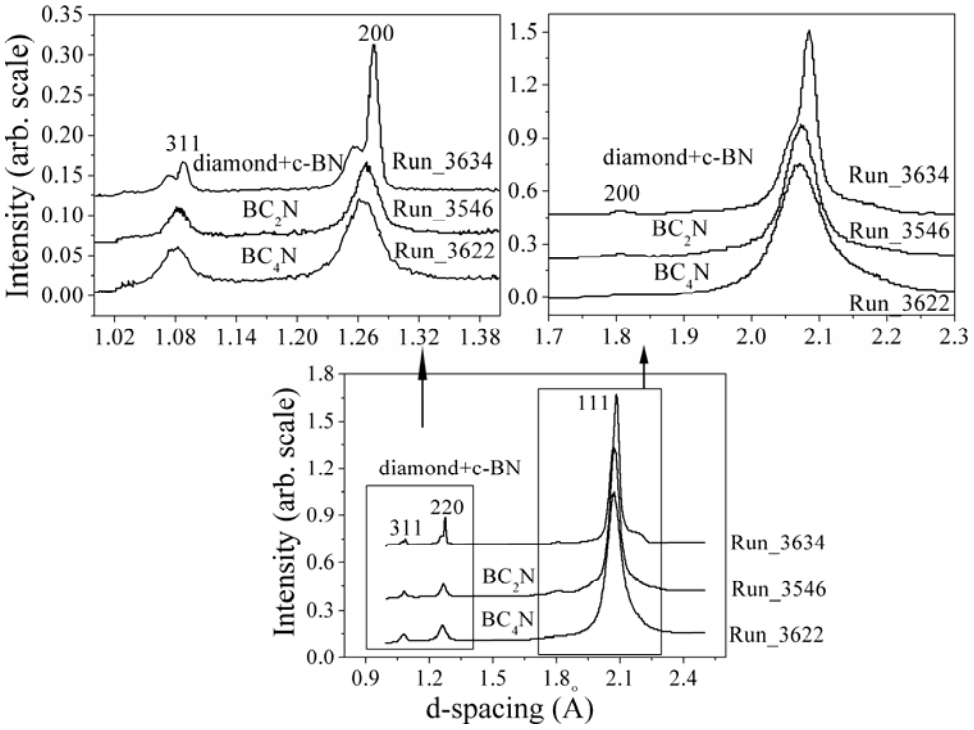

Figure 1.4: *Synchrotron XRD patterns of BC_2N, BC_4N, and diamond–BN samples. The top two panels show detail comparison. All these samples were synthesized at 20 GPa and 2200 ~ 2250 K. (from Ref.[20])*

Another classical work is conducted by Zhao et al. [20]. They prepared cubic B–C–N samples from the mixture of graphite and h–BN. Firstly, the mixture of graphite and h–BN with specific stoichiometry was milled to get extreme homogeneous materials, which were used as precursors. The ball–milling process was expected to break some of the sp^2 bonding styles and to introduce some amount of hybrid sp^3 bonding seeds. Then HPHT technique (20 GPa, 2200 K) was used to compress and heat the fine–milled B–C–N powder. Finally well–sintered products were obtained.

To confirm that their products are not the phase separation of diamond and c–BN, they also prepared segregated products (diamond and c–BN) from the raw mixture of h–BN and graphite but without the ball–milling process. The products were treated with the same HPHT condition as that of BC_2N and BC_4N samples. Synchrotron XRD patterns of all these samples were shown in Figure 1.4 for comparison. The peak splitting in the XRD pattern of diamond–BN was not observed in BC_2N and BC_4N samples, clearly verifying that single B–C–N ternary phases were obtained.

Besides cubic B–C–N crystals, hexagonal and orthorhombic B–C–N crystals are also reported to be successfully synthesized [21-23]. For example, Kawaguchi et al. prepared graphite–like B–C–N compounds with the compositions of BCN and BC_3N by chemical methods. That is, BCN and BC_3N compounds were respectively obtained by the reaction of acetonitrile with boron trichloride in an atmosphere of hydrogen and nitrogen, and the reaction of acrylonitrile with boron trichloride in a N_2 atmosphere within the reactor of a quartz tube. He et al. [21] prepared B–C–N precursors by chemical reaction between boric acid and melamine. These precursors were treated by a pressure of ~ 5.5 GPa and a temperature of 1600 ^{o}C. Afterwards, orthorhombic B_2CN crystals were successfully obtained.

In general, hexagonal B–C–N crystals are mainly prepared by chemical methods. Boron, carbon, and nitrogen sources are provided by commercially available organic or inorganic compounds, such as acrylonitrile, malononitrile, polyacrylonitrile and BCl_3. After adduct–formation, carbonization and graphitization, the obtained products are then heated and dried in furnaces by post heat treatments. For diamond–like and orthorhombic B–C–N crystals, hexagonal B–C–N samples are usually taken as starting materials. Then these hexagonal materials experience phase transformation to form cubic or orthorhombic B–C–N crystals with the treatment of HPHT or shock compression techniques.

At present, experimental results are controversial on crystalline B–C–N materials. For example, most of the measured lattice parameters of cubic BC_2N obey Vegard's law as a linear interpolation of diamond and c–BN [13, 15, 20, 24]. However, the lattice parameter measured by Solozhenko et al., which is higher than that of c–BN [18], violates the rule. The bulk modulus of c–$BC_{2.5}N$ samples, synthesized from shock compression, is 401 GPa [15]. This

value lies between that of diamond (443 GPa) and c–BN (368 GPa). In contrast, bulk and shear moduli of c–BC_2N crystals obtained in Solozhenko's experiments are much lower than that of c–BN [18, 25]. The essential reason derives from the fact that the structures of crystalline B–C–N are not clear.

Now, the open issues for the preparation of cubic B–C–N crystalline materials are as follows: (I) Crystalline B–C–N materials synthesized under HPHT conditions are very sensitive to the parameters of pressure and temperature. They are easily decomposed into other crystalline materials like diamond and c–BN. (II) The yield of crystalline B–C–N is very low. Usually, obtained B–C–N products contain many impurities. (III) Chemical compositions of cubic B–C–N crystals ever synthesized are limited. They are mainly BC_2N, BCN, BC_4N, and BC_6N, located along the C–BN isoelectronic line in the ternary B–C–N phase diagram. (IV) Although the cubic BC_2N crystal is declared to be the second hardest material, its structure is still not clear.

1.2.2 Theoretical Investigations

As stated in the last section, the structure of crystalline B–C–N crystals is still not clear. This is because the atomic sizes of boron, carbon, and nitrogen are so similar and small that they cannot be distinguished by the resolution of present analytical X–ray devices. In addition, pure B–C–N crystalline phases are hard to obtain in experiments. In most cases, B–C–N crystals are obtained along with amorphous materials or nanocrystalline particles. Thus, their mechanical properties cannot accurately reflect the feature of pure phases. In contrast, theoretical calculations can provide the detailed bonding states among boron, carbon and nitrogen atoms at the atomic level. Furthermore, theoretical calculations can also focus on single B–C–N crystals and estimate its mechanical properties without the influence of impurities. Therefore, ever since the successful synthesis of crystalline B–C–N materials, numerous theoretical works have been carried out to unveil the atomic structure of crystalline B–C–N materials and evaluate their physical properties.

Among various crystalline B–C–N materials, cubic BC_2N crystals have attracted more attention. They have a similar crystal structure as diamond. They also have a unique chemical

composition, BC_2N, an isoelectronic compound. That is, two carbon atoms contribute eight covalent electrons, boron and nitrogen atom together also supply eight covalent electrons. Thus the crystal can be written in a more clear way as $BN–C_2$. In addition, the chemical composition is located at the special position, the center of the ternary B–C–N phase diagram. Therefore, the crystal is expected to have unique physical properties.

There are two fundamental works in the earlier stage. One was performed by Tateyama et al. They proposed synthesis paths for diamond–like BC_2N considering pressure effects [26]. This is based on the fact that crystalline B–C–N materials are normally prepared under extreme conditions (such as HPHT), as described in the last section. Several kinds of possible structures were constructed. They are graphite–like BC_2N, $\alpha–BC_2N$, $\beta–BC_2N$, $\gamma–BC_2N$, $\delta–BC_2N$ and superlattice–BC_2N. Several possible paths of phase transformation were designed based on these structures (Figure 1.5).

The feasibility of these proposed paths was evaluated by relative enthalpy as a function of pressure. Seen from Figure 1.6, at ambient pressure $\beta–BC_2N$ and $sl–BN/C_2$ are two more stable structures comparing with $gr–BC_2N$ and $\gamma–BC_2N$. When the pressure is higher than 11 GPa, $\gamma–BC_2N$ phase becomes more stable than $gr–BC_2N$. With regard to $sl–BN/C_2$, it is already more stable than $\beta–BC_2N$ at zero pressure. It will transform into $\beta–BC_2N$ when the pressure is higher than 16 GPa. Thus two potential paths are possible for the synthesis of $\beta–BC_2N$. That is, it can be obtained from layered $gr–BC_2N$ even at ambient pressure or $sl–BN/C_2$ under high pressure (~ 16 GPa).

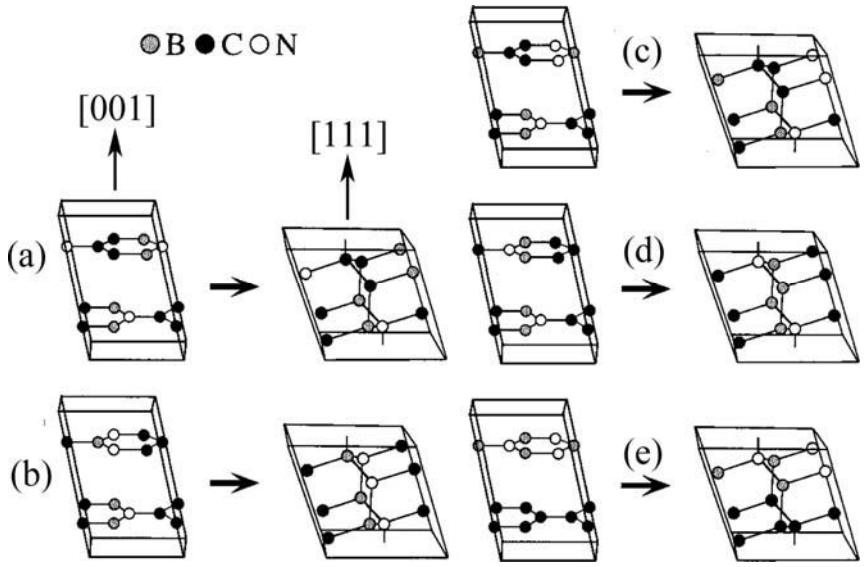

Figure 1.5: *Schematic representation of the transformation paths for various potential BC_2N structures: (a) g–BC_2N(I)→α–BC_2N; (b) g–BC_2N(I)→β–BC_2N; (c) g–BC_2N(II)→γ–BC_2N; (d) g–BC_2N(II)→δ–BC_2N; (e) sl–BN/C_2→β–BC_2N. (from Ref.[26])*

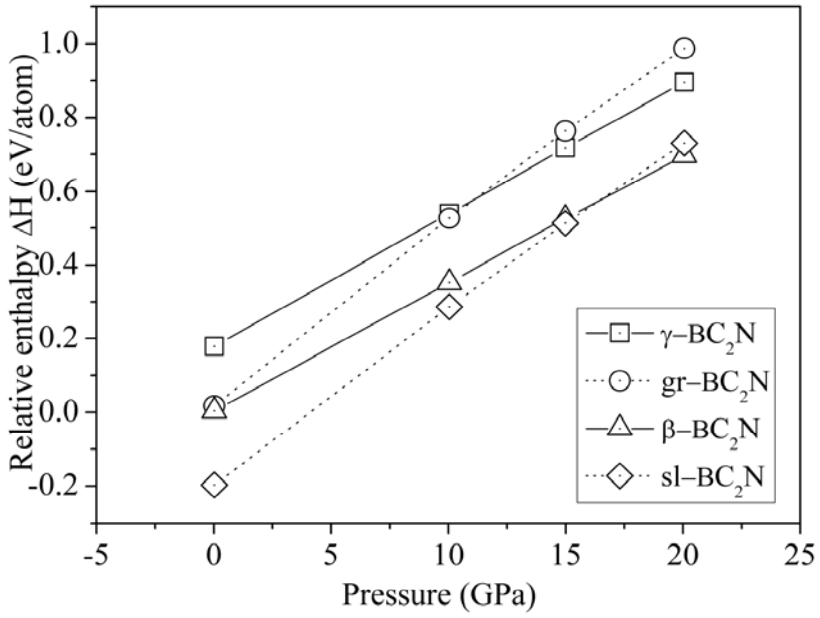

Figure 1.6: *Relationship between relative enthalpy and pressure for graphite–like BC_2N (open circle), β–BC_2N (triangle), γ–BC_2N (square), and sl–BN/C_2 (rhombus). (from Ref.[26])*

The other work was carried out by Zhang et al. [27]. The structural model was constructed along the [001] direction as shown in Figure 1.7. The formation energy was presented as a function of the number of layers. Clearly, the formation ability of β–BC_2N can

be weakened by increasing the crystal thickness. This reveals that superlattices, with alternative arrangements of diamond and c–BN, are more stable than β–BC_2N. In other words, β–BC_2N tends to phase separation into diamond and c–BN as the crystal thickness increases.

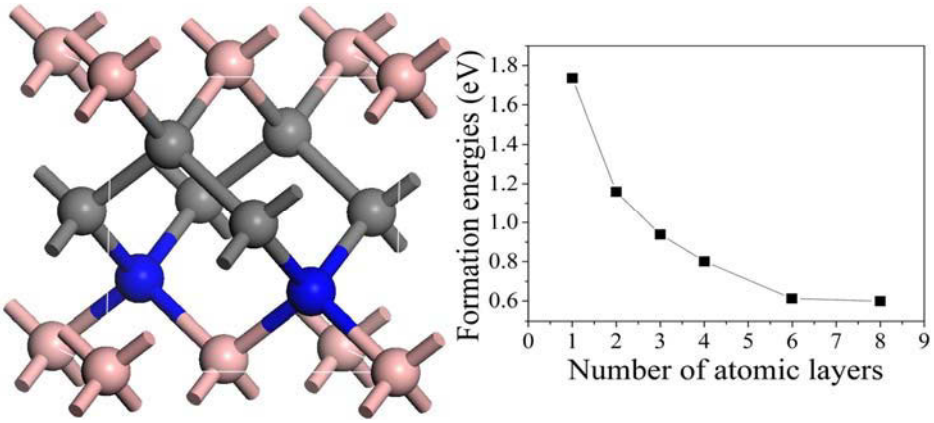

Figure 1.7: *(Left) representative atomic structure of β–C_2BN. B: pink, C: grey, and N: blue. (Right) Formation energy as a function of the number of atomic layers. (from Ref.[27])*

With respect to these two fundamental works, Sun et al. [28] directly searched all possible topological configurations of BC_2N based on an eight–atom unit cell of diamond from the mathematical point of view. Possible structures are shown in Figure 1.8. Among them, structures (1) and (2) have higher bulk/shear moduli than that of c–BN. But they thought that bulk and shear moduli of materials cannot give an accurate estimation of their hardness. Another mechanical parameter, ideal strength, was taken by them as the criterion to evaluate the hardness of the materials [29].

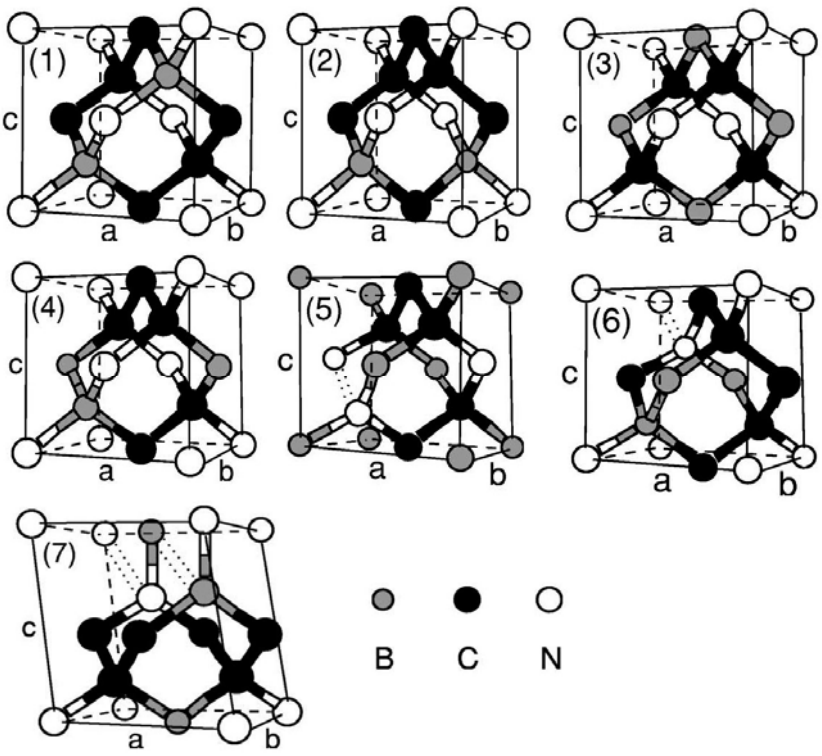

Figure 1.8: *Possible topologically structures of cubic BC_2N based on an eight–atom unit cell of diamond. (from Ref.[28])*

By calculating the ideal strength along body diagonal direction, they found that the ideal strength was limited by the global alignment of weak bonds in cubic BC_2N. When the applied strain increased, the weakest bonds were broken firstly. Further increment of strain resulted in the collapse of the structural models. The maximum ideal strength of all these possible structures is ~ 56 GPa along <111> directions, still lower than that of c–BN (~ 65 GPa). Their results are not consistent with the experimental ones. They interpreted that the high hardness measured in experiments was probably due to the nanocrystalline size effects inside of their obtained products. Nevertheless, this value is only below diamond and c–BN. Therefore, they took it as the third hardest material.

Besides, they also investigated the phase transformation of their structures under high pressure [30]. g–BC_2N-1, g–BC_2N-2, graphite and h–BN were used as starting materials. As shown in Figure 1.9, structural stability shows diverse features as a function of pressure. The curves of the formation enthalpy cross each other at different pressures for different structural models and starting materials. This indicates that cubic BC_2N crystals can probably be

obtained by various synthesis paths according to different starting materials.

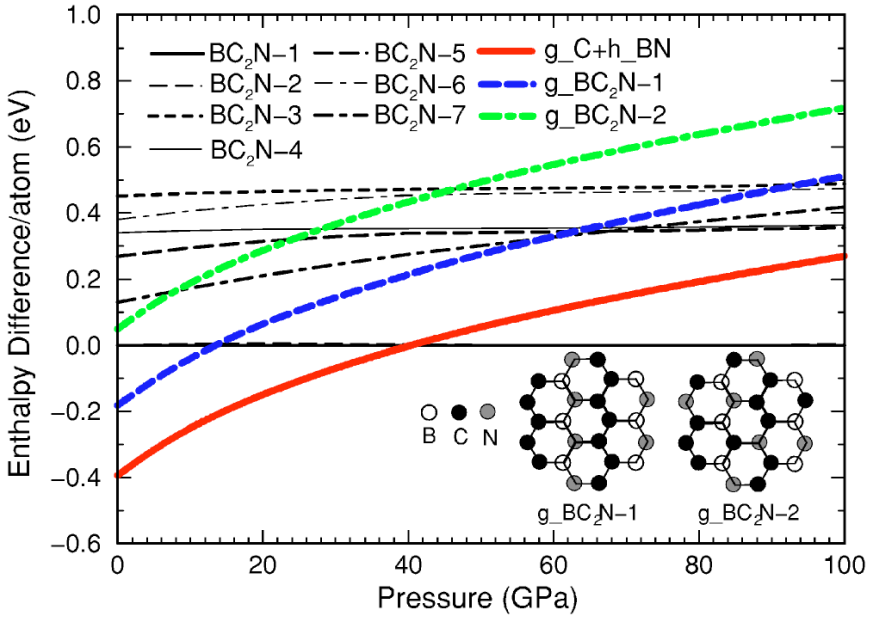

Figure 1.9: *Enthalpy as a function of pressure for seven cubic BC_2N structures together with three different starting materials: the mixture of graphite and hexagonal BN (g_c+h_BN); two kind of graphite–like BC_2N (g_BC_2N_1 and g_BC_2N_1). (from Ref.[30])*

During this period of exploring the crystal structure of B–C–N materials, Tian and Wang's groups also performed plenty of theoretical calculations [31-37]. They declared that the most likely phase of cubic BC_2N was obtained. The structural models were constructed from the sixteen–atom supercell of diamond, which is shown in Figure 1.10. They prove their structural models through structural stability as described by the formation energies, by the structural information obtained by XRD, and by the mechanical parameter presented by their empirical model.

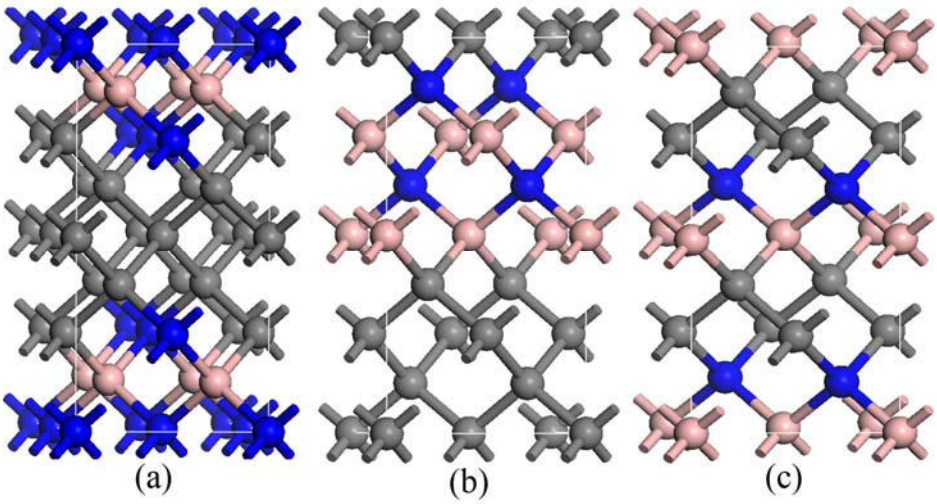

Figure 1.10: *Proposed structural models. (a) z–BC_2N, (b) β^*–BC_2N, (c) β–BC_2N. B: pink, C: grey, and N: blue. The first two models were proposed by authors. The last model is from previous works for comparison. (from Ref.[32])*

Structural stability was firstly evaluated by the calculation of formation energy. Comparing with all previously predicted c–BC_2N structures, their structural model was declared to be the most stable one according to their computational results. Meanwhile, the structural information was further confirmed by simulated XRD spectra. Figure 1.11 shows the simulated XRD spectra of the proposed structural models. Experimental results were also shown for comparison. Excellent agreement can be seen between simulated and experimental data. The mechanical parameter, hardness, was also evaluated by their empirical method. The hardness is 75.9 GPa, very close to experimental one (76 GPa).

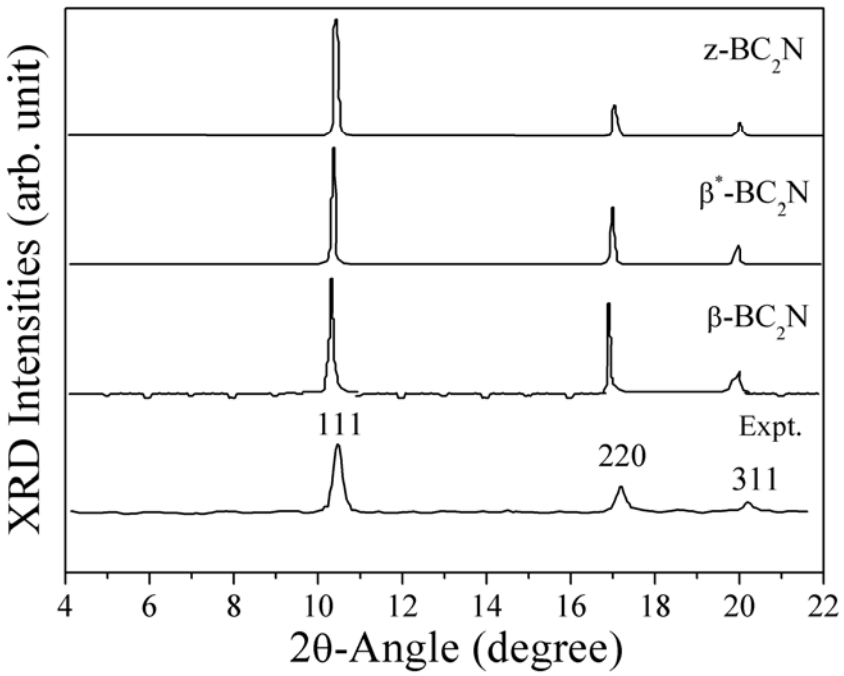

Figure 1.11: *Simulation of XRD spectra for z–BC_2N, β*–BC_2N, β–BC_2N. Experimental result is also shown for comparison. (from Ref.[32])*

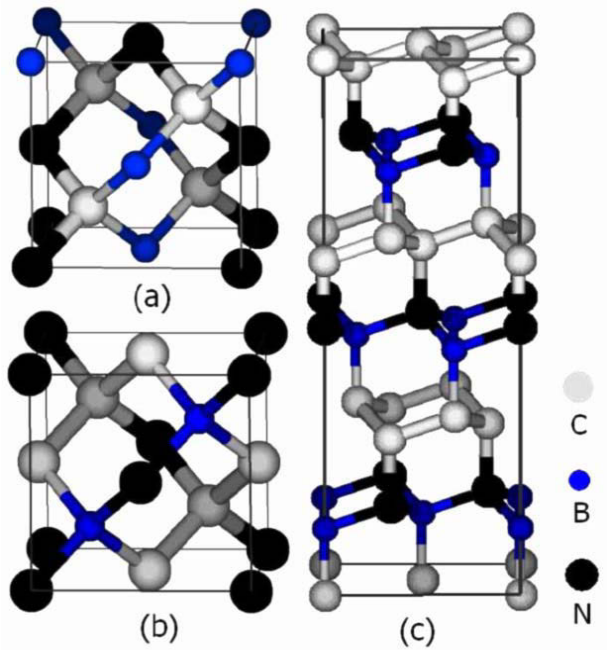

Figure 1.12: *Structural model of (a) chalcopyrite BC_2N, (b) orthorhombic BC_2N-1, (c) rhombohedral $BC_2N_{1\times1}$ superlattice. (from Ref.[38])*

In contrast, Chen et al. declared that even more stable structures than all previously proposed ones were predicted [38, 39]. They performed calculations on pseudo–diamond unit

cells with different numbers of atoms, i.e., less than 4, 8, and 12. They found that structures with low energy are mostly the C_2–BN superlattices along the [111] direction of the diamond cell. Figure 1.12c shows a representative structural model of such superlattices. They also calculated the ideal strength of these superlattices. All these superlattices are harder than c–BN, in contrast to the results from Sun's work [28], in which they found that their structures are less hard than c–BN according to the indication of ideal strength, as already mentioned above.

Besides the cubic structure, there are also plenty of works focusing on other symmetries of crystalline B–C–N materials. For example, hexagonal BC_2N [34], body–centered BC_2N [31], wurtzite BC_2N [33], and graphite–like BC_4N [34]. However, all these predicted structural models usually have lower hardness than that of the cubic ones. Therefore, they are not attractive like the cubic ones in view of the expected mechanical properties.

So far, theoretical efforts on the structure of cubic B–C–N materials can be classified into two kinds: (I) investigating the energetics and electronic structures of the $(BN)_n$–C_{2n} superlattice along 001, 110, and 111 crystal orientations [26, 27, 40-42]; (II) considering the c–BC_2N structure as ordered solid solution and searching for the most stable atomic arrangements within the diamond unit cell, typically within 8 ~ 16 atoms [28, 32, 38, 39, 43-45]. Almost all these structural models are based on the principle: search the optimal structure with the lowest formation energy.

1.3 Amorphous B–C–N Materials

1.3.1 Preparation Methods

1.3.1.1 Magnetron Sputtering Technique

The magnetron sputtering technique is one of the most frequently used methods to synthesize amorphous B–C–N materials. Yue et al. prepared ternary B–C–N thin films by the radio frequency sputtering method from a h–BN target in an atmosphere of argon (Ar) and methane (CH_4) [46]. By changing the CH_4 fraction of the reactive gases, B–C–N thin films

with different carbon concentrations were obtained. As revealed by the relationship of temperature and conductivity, B–C–N films obtained with 10% CH_4 exhibited semiconductor properties.

Lousa et al. reported the synthesis of B–C–N thin films by radio frequency magnetron sputtering from a sintered B_4C target [47]. The variations of film stress and hardness were presented as a function of N_2/Ar ratio. The stress in these B–C–N films can decrease from 5 GPa to 2 GPa as the incorporated nitrogen reached up to 30% into these films. The hardness characterized by nanoindentation showed less variation as the nitrogen content in these films is lower than 15%. But for higher nitrogen concentration, the hardness decreased down to ~ 12 GPa. Another similar work regarding internal stress was also reported. In that work, B–C–N thin films were deposited on silicon and fused silica by radio frequency reactive sputtering from the sintered h–BN target [48]. The internal stress was relieved via the exfoliation of these deposited B–C–N films off substrates. The way that stress relieved was determined by what kind of substrates was used, which can be interpreted by the bulkling–drived delamination theory.

1.3.1.2 Pulsed Laser Deposition (PLD)

Pulsed laser deposition (PLD) is another way of preparing amorphous B–C–N thin films. Wada et al. used the PLD technique to prepare B–C–N thin films [49]. They studied the effect of diverse laser wavelengths on bonding structures of their obtained films. They found that B–N and B–C bonds were very sensitive to different laser wavelengths. B–C–N films contained a large fraction of B–C bonds under the condition of deep–UV lasers. Another work based on plasma assisted pulsed laser deposition method showed the obvious effect of different substrates on the preparation of B–C–N thin films [50]. Phase separation into BN: C can be observed for B–C–N thin films deposited on silicon substrates. However, hybridized B–C–N films, not the products of phase separation, can be obtained on Ni substrates under nearly the same synthesis conditions as those films deposited on silicon substrates.

1.3.1.3 Ion Beam Assisted Deposition (IBAD)

The ion beam assisted deposition technique (IBAD) can be used to regulate the ion energy and individually control the ion flux. Thus the method provides an easy way to control the variations of chemical compositions.

Caretti et al. reported the synthesis of B–C–N films using the IBAD method from two independent molecular beams of B and C [51]. Prior to the deposition of ternary B–C–N films, they firstly attempted to prepare binary BN compounds because they mainly expected to obtain BC_xN compositions along C–BN line in the ternary B–C–N phase diagram. They found that the initial B/N atomic flux fixed at 1:1 from the B and the C molecular beam cannot guarantee the same B/N atomic ratio in the BN binary compounds. By exploring the relation between B/N relative fluxes and B/N atomic ratio in films, they found that the atomic flux of B/N close to 4 can give the B/N atomic ratio near to 1:1 in the BN binary films. Then carbon source was introduced with the fixed B/N atomic flux at ~ 4 and BC_xN films were successfully achieved.

Zhou et al. deposited B–C–N thin films by ion beam assisted deposition. The mechanical behaviors of the obtained B–C–N films were investigated as functions of acceleration voltage and ion current density [52]. They found that hardness and elastic modulus exhibited an initial increase followed by a decrease when the acceleration voltage was higher than 1.0 KV or the ion current density was lower than 90 $\mu A/cm^2$.

1.3.1.4 Chemical Vapor Deposition (CVD)

The chemical vapor deposition (CVD) method is based on chemical reaction to synthesize B–C–N thin films. This is different from the physical vapor deposition (PVD), which is usually related to the sputtering of various targets.

Hegemann et al. prepared B–C–N coatings by plasma assisted chemical vapor deposition (PA–CVD) by using pyridine–borane (PB) as a precursor [53]. The chemical compositions of their deposited B–C–N films were affected by both the precursor and applied bias voltages. At a low bias voltage, the chemical compositions of obtained B–C–N films were mainly affected

by the precursor. This is probably because the B–C–N films inherit the chemical information of the precursor fragments under the condition of low electron energy. At a high bias voltage (> – 65 V), the chemical compositions were largely affected by bias voltages. They can vary from the chemical composition B_2C_5N to $B_3C_7N_2$.

Ahn et al. deposited transparent B–C–N films by plasma assisted chemical vapor deposition from the precursors of trimethylborazine (TMB) and pyrrolidino diethylamine (PMB) [54]. The transparent B–C–N films have a high transmission in the UV–visible region (~ 90%). Sota et al. employed the remote plasma assisted chemical vapor deposition (RPA–CVD) to prepare B–C–N films [55]. They focused on the effect of the chemical bonding on the optical and electrical properties of their obtained B–C–N films. The optical bandgap and the bonding information in their films were characterized by transform infrared absorption (FTIR) and ultraviolet–visible light absorption. They found that the optical bandgap can be greatly improved by a large proportion of B–C, C = C, and C = N bonds. A strong relation between electrical conductivity and chemical bonding states was also observed, which can be attributed to the existence of π electrons from C = C and C = N bonds.

Besides plasma assisted chemical vapor deposition, thermal chemical vapor deposition (T–CVD) [56, 57] and hot filament chemical vapor deposition (HF–CVD) [58] are also reported to synthesize B–C–N films successfully.

1.3.2 Effect of Experimental Parameters

1.3.2.1 Bias Voltage

The bias voltage is one of the most important parameters for depositing B–C–N thin films. Many works have reported the preparations of B–C–N films by applying a bias voltage to substrates. Basically, the bias voltage is used to strengthen the bombardment of the substrate surface by high energy ions, which are generated in the plasma during the synthesis process of PVD and CVD. Correspondingly, surface morphologies, film structures and physical properties of deposited B–C–N films are also greatly influenced by the parameter.

Tsai attempted to use a very high bias voltage to deposit B–C–N films [59]. He found that the B–C–N films obtained at – 200 V have a RMS value of ~ 40 nm, and those ones obtained at – 400 V have lower RMS values (~ 20 nm). This indicates that the increment of the bias voltage can make the surface of B–C–N films smoother. In addition, the Raman characterization showed that the intensity of D and G bands were different for diverse bias voltages (– 200, – 300, and – 400 V). This reveals that the bias voltage can efficiently change the fraction of the dominated bonding states in these obtained B–C–N films.

Yap et al. prepared B–C–N films from the target of sintered graphite and BN by varying bias voltages from 0 to – 200 V [60]. The chemical compositions of prepared B–C–N films were obviously changed under different bias voltages. As the negative bias voltage increases from 0 to 200 V, the carbon atomic concentration in the deposited films decreased dramatically from ~ 76 at.% down to ~ 30 at.%. In contrast, nitrogen and boron fractions increased from ~ 10 at.% to ~ 33 at.%.

Zhou et al. prepared B–C–N films by radio frequency magnetron sputtering [61]. The effect of a bias voltage on the chemical composition, structure, and properties of B–C–N films was detailedly investigated. A high bias voltage corresponded to a low content of carbon. At a low bias voltage, a broad absorption between 1000 and 1600 cm^{-1} can be observed from IR spectra. This broad absorption peak can commonly be decomposed into different bonding states, such as the in–plane B–N stretching vibration, C–N, and B–C peaks. Raman spectra also showed one broad range between 1200 cm^{-1} and 1700 cm^{-1}, the typical area that D and G peaks are located. As the bias voltage increased, the intensities of these peaks decreased greatly. At a bias voltage of – 300 V, nearly no obvious adsorption peak can be observed from both IR and Raman spectra. In addition, mechanical properties of these B–C–N films, i.e., hardness and modulus, are proportional to the bias voltage, that is, the larger the bias voltage, the higher the hardness and the modulus.

1.3.2.2 Substrate Temperature

In general, heating substrate can provide more usable energy for the movement of energetic spices on substrates. Thus dense and homogenous films can be obtained. In addition,

chemical compositions, chemical bonding, and properties of B–C–N films are also proved to be greatly affected by various substrate temperatures.

Lei et al. prepared B–C–N films by the technique of radio magnetron sputtering under different substrate temperatures [62]. By XPS analysis, they found that the C1s spectrum was very sensitive to substrate temperature. A higher substrate temperature can result in the main peak of C1s shifting toward the lower bonding energy. Furthermore, more sp^3 bonding states among boron, carbon and nitrogen atoms can also be introduced in the obtained B–C–N films under higher substrate temperatures. Besides, optical properties of these deposited films were also affected by the parameter of substrate temperature. B–C–N films obtained at higher temperatures possessed larger optical bandgaps.

Chien et al. tried to unveil the relations between the hardness and the substrate temperature in B–C–N films [63]. The hardness of B–C–N films decreased as the substrate temperature increased. The elastic modulus also showed the similar trend. This indicates that harder B–C–N films can be obtained at lower substrate temperatures. In addition, the chemical composition also showed clear variations as the substrate temperature was changed from 75 to 400 ^{o}C.

1.3.2.3 Ion Energy

The ion energy is also one important parameter during the preparation of B–C–N films. Yang et al. prepared B–C–N films by dual ion beam sputtering deposition [64]. The surface roughness and the mechanical properties of their B–C–N films were correlated to ion energy. They showed the surface morphology of three representative B–C–N samples obtained at an ion energy of 200, 300, and 400 eV, respectively. Very clearly, the sample prepared at the ion energy of 400 eV had a higher roughness value than the one obtained at 200 eV. The microstructure was also affected by ion energy as revealed by the variations of the intensity of Raman peaks. In addition, a higher value of the ion energy corresponded to a lower hardness. As the ion energy increased from 200 to 400 eV, the hardness of these B–C–N films dropped greatly from ~ 30 to ~ 21 GPa. This clearly demonstrates the important role of the ion energy during the preparation of B–C–N films.

Ulrich used different ion energies to study the variation of the compressive stress in B–C–N films prepared by magnetron sputtering [65]. The compressive stress showed a Gaussian–like curve as a function of Ar^+ ion energy. That is, the compressive stress was small when the Ar^+ ion energy was low. As the Ar^+ ion energy reached up to a certain value, one main peak appeared. Afterwards, the compressive stress was weakened by the further increment of the Ar^+ ion energy.

Zhou et al. showed the effect of the ion acceleration voltage and current density on the surface roughness and mechanical properties of B–C–N films [52]. The surface roughness showed less effect by ion acceleration voltage and current density if the deposition rate was low. At higher voltage and current density, not clear trend was observed for the variations of the surface roughness. Hardness and Young's modulus of their deposited films showed the similar way as that of the surface roughness.

1.3.2.4 Gas Flow Ratio

The variation of gas flow ratio is one frequently used way for preparing B–C–N films. Various gases and their different flow ratios are employed in most of previous works. Lousa et al. studied the deposition rate, chemical composition, and structure of their deposited B–C–N films with different N_2/Ar ratios [47]. More N_2 in the gas composition corresponded to higher growth rate, higher nitrogen content, and lower boron and carbon concentrations. The adsorption peaks of FTIR were also sensitive to N_2 concentration. When the N_2 concentration increased from 1% to 10%, the broad adsorption peak around 1400 cm^{-1} shifted towards higher wavenumber. Besides, a new adsorption peak was generated at around 800 cm^{-1} as the N_2 concentration was higher than 4%. A clear adsorption region was observed at 1300 ~ 1600 cm^{-1} from the Raman characterization when the N_2 concentration was higher than 10%.

Hasegawa et al. studied the effect of the variation of B_2H_6 flow rate on the chemical compositions of B–C–N films prepared by electron beam excited plasma CVD [66, 67]. As the B_2C_6 flow continuously increased from 1 to 8 sccm, the boron content showed a monotonous increment while the carbon content responded in an opposite way. When more B_2C_6 flows were introduced, the main adsorption peak of FTIR shifted towards lower

wavenumber. This indicates that the bonding state in their obtained films is also affected by the variations of the B_2C_6 flow.

Chen et al. showed the surface morphology and mechanical properties of their B–C–N films prepared with different CH_4 flow rates [68]. The surface roughness of the B–C–N films synthesized with a low CH_4 flow rate was at least twice larger than that with a high CH_4 flow rate. This reveals that a higher CH_4 flow rate can make the surface of obtained B–C–N films smoother. Micro–hardness showed an initial increase followed by a decrease as the CH_4 flow rate increased from 0 to 40 sccm.

1.3.3 Structural Characterization

1.3.3.1 Infrared Reflection (IR)

The infrared reflection (IR) is one of the powerful tools to give qualitative information about the possible bonding characteristics in B–C–N films. In general, IR spectra are used to demonstrate whether obtained B–C–N films are real ternary compounds or just nominal mixtures of BN, graphite, or BC_x.

Figure 1.13 shows the IR spectra of B–C–N films with different carbon contents [69]. Two absorption peaks at 1370 cm^{-1} and 750 cm^{-1} are generally assigned to in–plane B–N stretching and out–of–plane B–N bending vibration, respectively. The peak located at 1200 cm^{-1}, 1300 cm^{-1}, 1600 cm^{-1}, and 2170 cm^{-1} are usually attributed to B–C, C–N, C = N, and C ≡ N, respectively. As the carbon content increases, the main absorption peaks at ~ 1290 cm^{-1} shift towards ~ 1380 cm^{-1}. The corresponding peak width increases from 315 cm^{-1} to 485 cm^{-1}. This indicates that B–N and carbon–rich B–C bonds are generated and real ternary B–C–N compounds are formed.

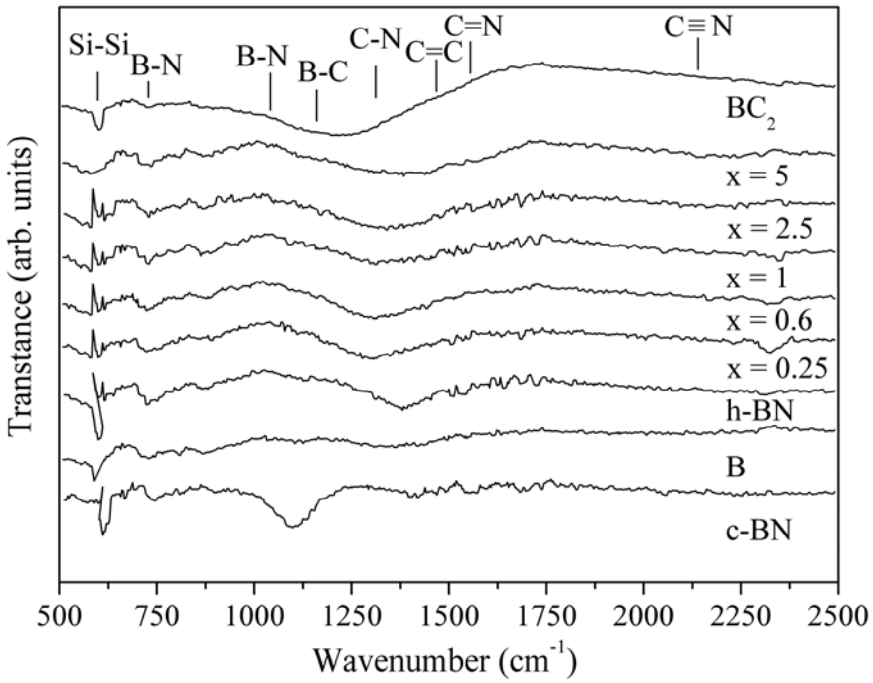

Figure 1.13: *IR spectra of B–C–N films with different carbon concentrations. IR spectra of c–BN, B, h–BN and BC_2 are also shown for comparison. (from Ref.[69])*

Figure 1.14 shows representative FTIR spectra of B–C–N films obtained by changing N_2/Ar gas flow ratio [47]. These spectra show obviously different features as the N_2/Ar flow ratio varies. Without the addition of N_2, the spectrum shows a broad absorption band locating at ~ 1100 cm^{-1}. This corresponds to the vibrations of B–C bonds generated from the sputtered B_4C target. As the N_2/Ar flow ratio increases, the absorption band shifts towards a high wavenumber. The obvious shift may be interpreted from the formation of B_4C: N film structure by the incorporation of N into B_4C, or perhaps from the overlap of the adsorption peaks at 1100 cm^{-1} and 1385 cm^{-1}. The IR spectra alone cannot give a decisive conclusion. Other analysis techniques like XPS need to be employed for further verification.

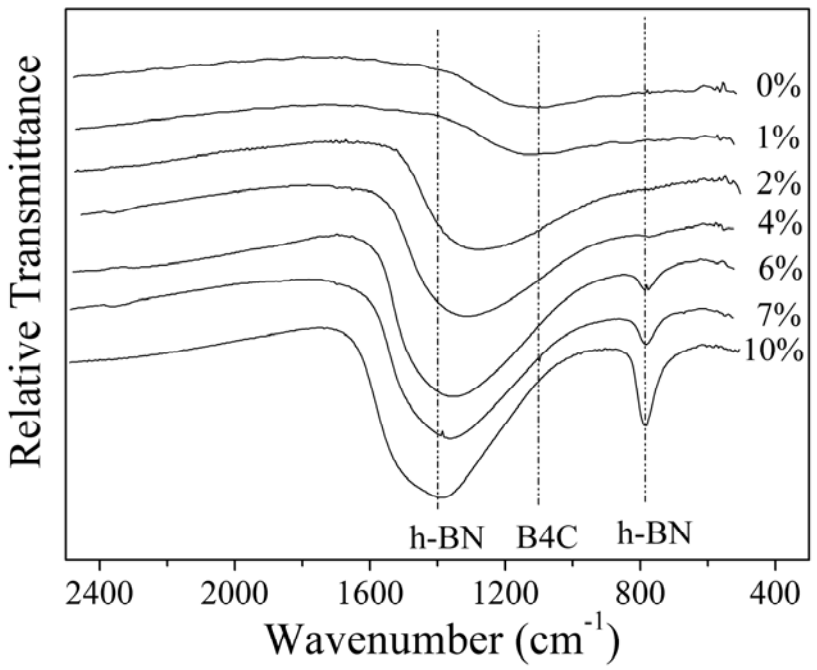

Figure 1.14: *FTIR spectra of B–C–N films obtained with different* N_2/Ar *gas flow ratios. (from Ref.[47])*

1.3.3.2 X–ray Photoelectron Spectroscopy (XPS)

The X–ray photoelectron spectroscopy (XPS) is frequently used to characterize the bonding information in B–C–N films. It is adopted to examine whether deposited B–C–N films are phase separated or real ternary compounds. And furthermore, the decomposition of the main peaks like B1s, C1s, N1s, and O1s can give the detailed information of different bonding states. From these decomposed peaks, we can have a better understanding of the relation between microstructures and properties in B–C–N films.

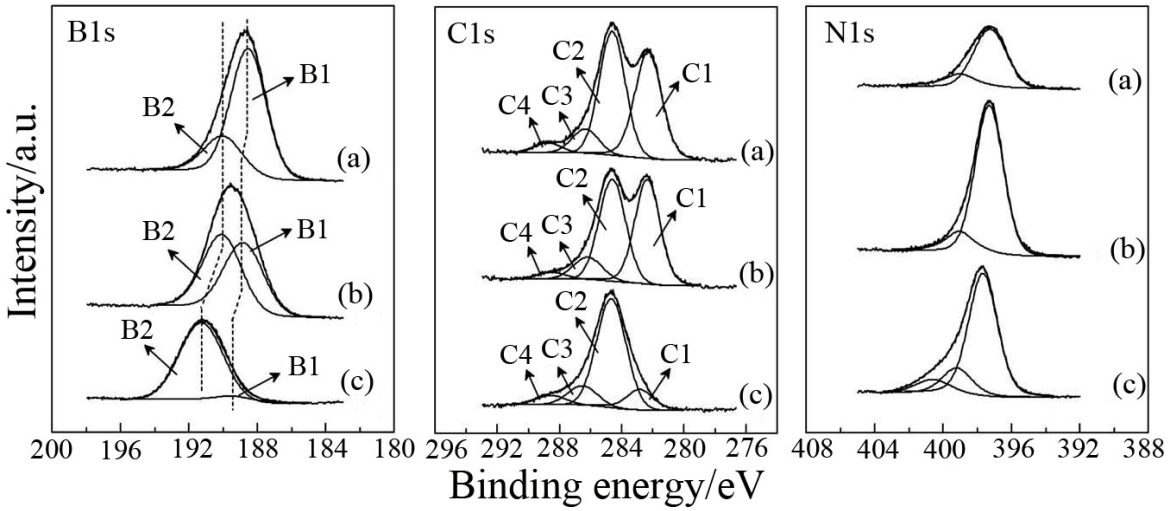

Figure 1.15: *XPS of B1s, C1s, and N1s peaks for B–C–N films deposited with different N_2 partial pressures (a) 2 Pa, (b) 5 Pa, and (c) 15 Pa. The main peaks of B1s, C1s, and N1s are decomposed into many small peaks. (from Ref.[70])*

Figure 1.15 shows the representative XPS spectra of B–C–N films obtained with different N_2 partial pressures [70]. The main peaks of B1s, C1s, and N1s spectra are affected by various N_2 partial pressures and shift toward higher binding energies. They are also broad and asymmetric. This reveals that there are different bonding states in such B–C–N films. The broadening B1s peaks indicates that boron atoms are in different bonding states. By decomposing the main peak of B1s, two small peaks can be obtained. One is located at 188.4 ~ 189.5 eV which corresponds to B–C bond. The other is at 190 ~ 191.3 eV which is attributed to B–N. The main peak of C1s can be decomposed into four component peaks, they are B–C (282.3 ~ 282.8 eV), C = C (284.6 eV), C–N (286.2 ~ 286.5 eV), and C–O (288.5 ~ 288.7 eV). The main peak of N1s can also be decomposed into different component peaks. The dominated peak at 397.3 ~ 397.7 eV can be assigned to B–N. The peak at ~ 400 eV is usually attributed to C = N and the peak at ~ 399 eV corresponds to C–N. In addition, a higher N_2 partial pressure results in the variations of bonding states. As the N_2 partial pressure increases, more N atoms are bonded to boron atoms. This leads to an individual decrement and increment of the B–C and B–N fractions. From XPS analysis, B–C–N films contain various B–N, B–C, and C–N bonding states. This means that the obtained films are ternary B–C–N compounds, not the mixture of separated phases.

1.3.3.3 X–ray Absorption Near–Edge Spectroscopy (XANES)

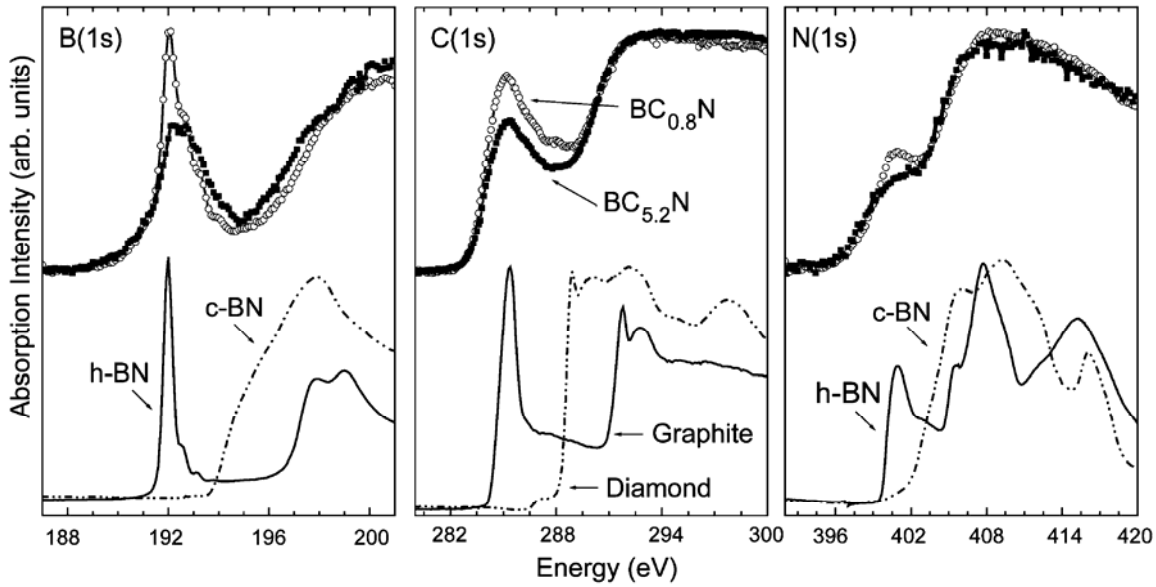

Figure 1.16: *XANES spectra of B1s, C1s, and N1s for ternary B–C–N films with low (white dots) and high carbon (black dots) content. The spectra of diamond, h–BN, c–BN and graphite are also shown for comparison. (from Ref.[69])*

The X–ray absorption near–edge spectroscopy (XANES) is another powerful tool to detect the local bonding structure in B–C–N films. The basic principle underlying XANES is the absorption of an X–ray photon by the core level of an atom and the subconsequent emission of a photoelectron.

Figure 1.16 shows the XANES spectra of B1s, C1s, and N1s for ternary BC_xN films with low (x = 0.8) and high (x = 5.2) carbon content [69]. The reference spectra of h–BN, c–BN, graphite and diamond are also shown for comparison. Seen from Figure 1.17, the π* peaks, centered at 192 eV, 285.4 eV and 401 eV for B1s, C1s, and N1s, correspond to the sp^2 bonding configurations such as in hexagonal BN and graphite. The σ* peaks are linked to sp^3 bonding states like that in diamond and c–BN. Compared with these reference spectra, the relative intensity of π*/σ* decreases as the carbon content increases, corresponding to higher sp^3 bonding configurations in B–C–N films. This indicates that the microstructures of B–C–N films experience the transition of bonding states towards a diamond–like structure.

1.3.4 Mechanical Properties

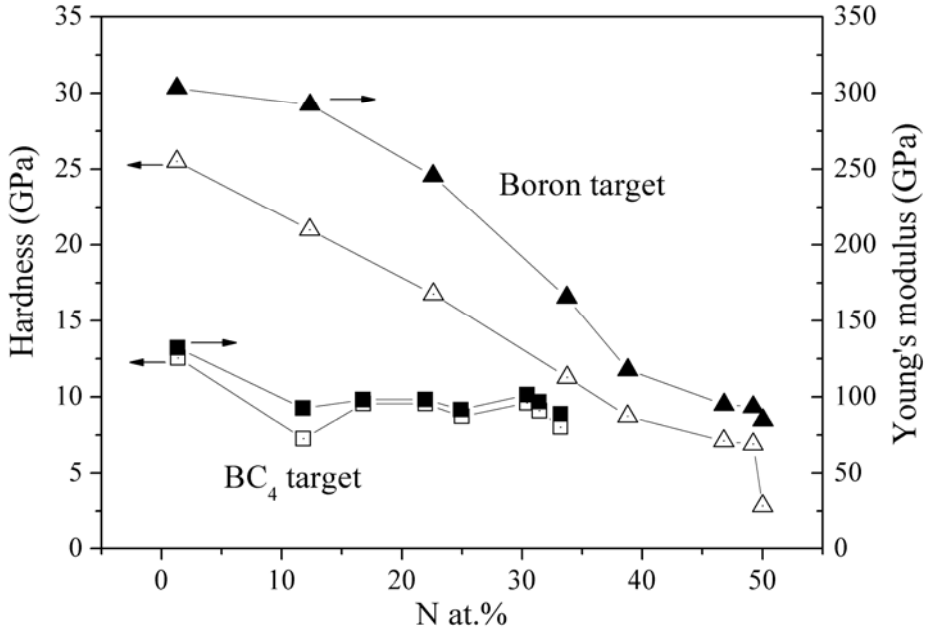

Figure 1.17: *Hardness and Young's modulus of B–C–N films deposited with boron (empty symbols) and BC_4 target (full symbols) as a function of the nitrogen content. (from Ref.[71])*

In principle, B–C–N films are expected to combine the excellent properties of diamond and c–BN. They can be taken as potential hard materials that can replace diamond and c–BN. Therefore, mechanical properties, mainly hardness and elastic modulus, are the chief aim to be controlled during the preparation of B–C–N films.

Figure 1.17 shows the variation of hardness and Young's modulus as a function of the nitrogen content in B–C–N films [71]. Films deposited from a B target have higher hardness than those from a BC_4 target. The highest value of hardness prepared from a boron target can reach ~ 30 GPa, revealing that B–C–N films can really be taken as hard materials. It can also be seen from Figure 1.17 that higher nitrogen content corresponds to lower hardness and Young's modulus. This indicates that a high nitrogen fraction in B–C–N films does not favor high hardness.

In general, films with high nitrogen content have diamond–like structure, such as c–BN, the predicted β–C_3N_4. For such cubic structures, they are usually obtained under extreme experimental conditions, such as high temperature high pressure, or PVD/CVD with high

substrate temperature. If such conditions are not satisfied, the superfluous nitrogen atoms in the B–C–N films are usually bonded to other atoms in the form of hexagonal or graphite–like structures. This is probably the reason why B–C–N films with high nitrogen content have low hardness values.

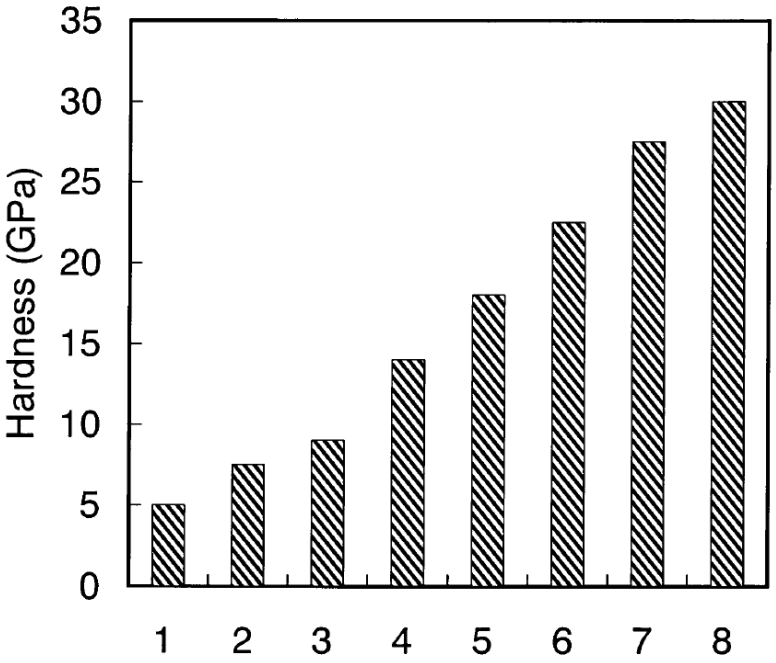

Figure 1.18: *Hardness of B–C–N films as a function of the B_2H_6 flow rate. (from Ref.[66])*

Figure 1.18 shows another representative dependence of mechanical properties in B–C–N films prepared by electron beam excited plasma CVD [66]. The hardness is expressed as a function of the gas flow rate. As a clear trend it can be seen that the hardness of B–C–N films monotonously increases as the B_2H_6 flow rate increases. Since the increment of B_2H_6 flow rate corresponds to higher boron content in B–C–N films, we can understand this phenomenon in the way that B–C–N films with higher boron content have higher hardness. The maximum value of hardness achieved within the range investigated is ~ 30 GPa, with the highest B_2H_6 flow rate of 8 sccm.

Besides hardness and Young's modulus, there are also plenty of works focusing on the tribological and wear properties of B–C–N films. Figure 1.19 shows one representative curve of friction coefficients in B–C–N films with different carbon contents [72]. It is recorded by sliding against steel GCr15 balls as a function of time. In general, the average friction

coefficient decreases from ~ 0.4 to ~ 0.2 as the carbon content increases from 26.9 wt.% up to 61.3 wt.%. XPS results show that B–C–N films with higher carbon contents have higher sp^2C–C and sp^2C–N fractions. It is probably because these bonds act as a self–lubrication medium, resulting in the decrement of the friction coefficient.

Figure 1.20 shows the variation of volume wear rate as a function of carbon content in B–C–N films [72]. Wear properties of B–C–N films can be improved by increasing the carbon content. Since the wear is related to many complex parameters, here the improvement of wear properties is probably associated with the higher hardness and lower friction coefficient for B–C–N films with more carbon content.

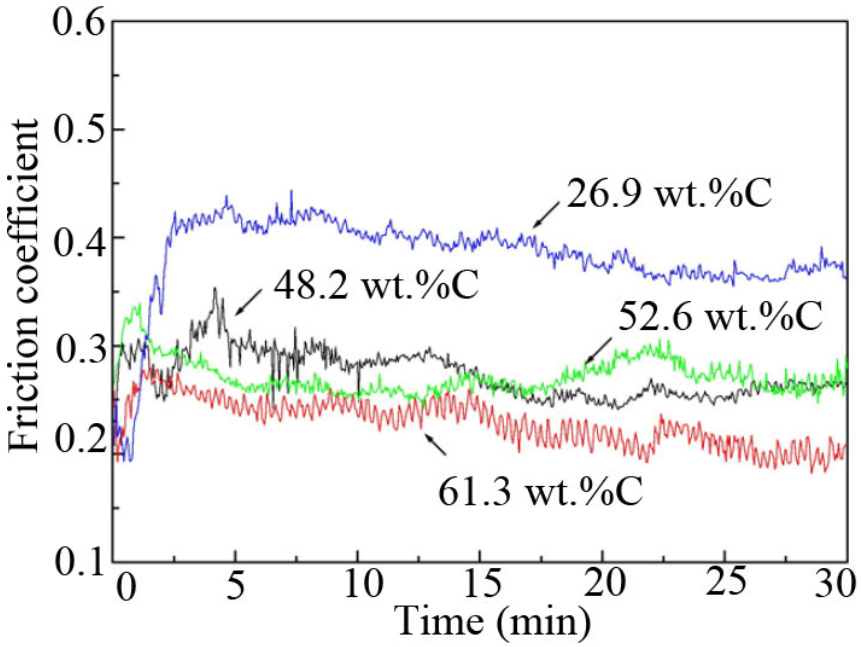

Figure 1.19: *Variations of friction coefficient of B–C–N films with different carbon content as a function of time. (from Ref.[72])*

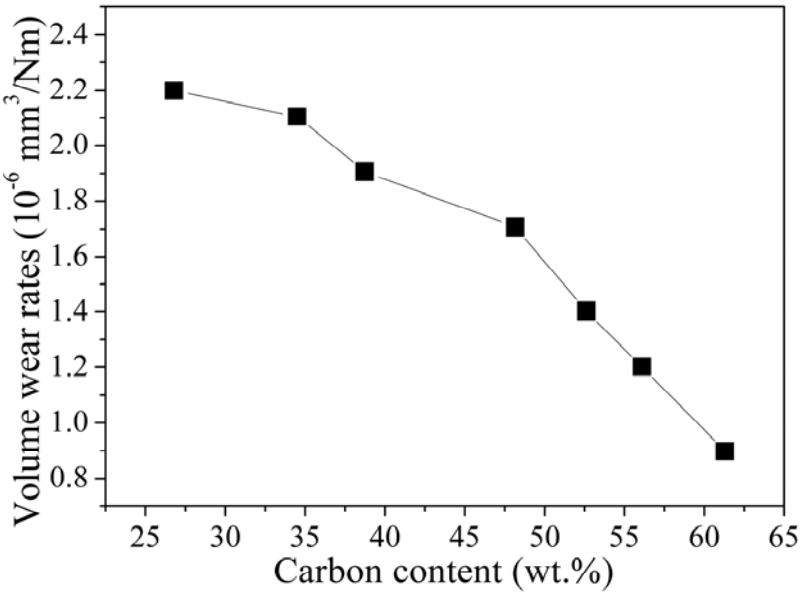

Figure 1.20: *Volume wear rates of B–C–N films as a function of carbon content (from Ref.[72]).*

1.3.5 Optical Properties

Ternary B–C–N materials are also expected to have excellent optical properties because both diamond and h–BN have high bandgap energies. In recent years, there are a few works focusing on the optical properties of B–C–N films. For example, Lei et al. reported the refractive index, visible light absorbance, and optical bandgap of B–C–N films as a function of substrate temperature [62]. B–C–N films obtained at high substrate temperature correspond to a low value of refractive index. This indicates that such B–C–N films have a better optical transparency.

Todi et al. reported the optical behavior of B–C–N films prepared by RF magnetron sputtering with different N_2/Ar flow ratios [73]. They found that a small amount of N_2 introduced into the sputtering chamber can obviously increase the transmittance of B–C–N films. But a further increment of the N_2 fraction gives no great change in the transmittance. They also observed that the optical bandgap of B–C–N films changes from 2.1 to 2.8 eV when the N_2 gas was introduced. As the N_2 fraction increases up to 75%, the bandgap shows an initial increase followed by a small decrease. No monotonous trend can be clearly observed between optical bandgap and the N_2/Ar flow ratio.

At present, the open issues for amorphous B–C–N films are as follows: (I) demonstrating whether B–C–N films deposited by various methods are real ternary compounds or they are just mechanical mixtures of separated phases. (II) Adhesion problem between B–C–N films and diverse substrates is still far away from industrial applications. B–C–N films are easily peeled off from substrates. This leads to the difficulty in the measurements of their mechanical properties. (III) It is difficult to obtain B–C–N films with a broad range of chemical compositions. (IV) A relation between mechanical properties and chemical compositions has not been developed. Therefore, it is still not clear which area of the ternary B–C–N phase diagram has better mechanical properties.

1.4 The Aim of This Work

For crystalline B–C–N materials, the main aim in this work is to predict the structures of crystalline BC_2N materials using one quite different way from previous theoretical works. After demonstrating the validity, we popularize our structural models to the compositions of BC_xN along the isoelectronic C–BN line. We attempt to explore whether B–C–N crystals with other chemical compositions have better mechanical properties than those of BC_2N. Furthermore, we extend our structural models to the ternary B–C–N phase diagram to search potential superhard phases in broader areas of chemical compositions. Thus, from the exploration of the composition point of BC_2N to the composition line of BC_xN along C–BN line, and then to the ternary B–C–N phase diagram, we can have a complete understanding of the relation between mechanical properties and chemical compositions. Besides the B–C–N systems, the validity of our structural models is also demonstrated for crystalline BC_x systems.

For amorphous B–C–N materials, we present a systematical investigation of the relation between mechanical properties and chemical compositions in the ternary B–C–N phase diagram. We expect that our theoretical results can provide useful information to guide experimental synthesis of amorphous B–C–N films with desired mechanical properties. We perform further experimental work on amorphous B–C–N films to demonstrate our theoretical results.

According to our aim in this work, this thesis is organized as follows: The theoretical background of density functional theory (DFT) is presented in Chapter 2. Chapter 3 includes how to produce our structural models in detail, demonstrate the validity of our structural models, and extend the model to BC_xN and then to $B_xC_yN_z$ in the ternary B–C–N phase diagram. Besides, our structural model is also extended to cubic BC_x system to demonstrate its transportability to other cubic systems. Chapter 4 is devoted to the theoretical prediction of mechanical properties in amorphous B–C–N materials. Chapter 5 is organized to confirm the theoretical results presented in Chapter 4 by our experimental work. Besides, the mechanism behind hardness and the substrate effect also includes Si–C–N systems. A short summary as well as an outlook is presented in Chapter 6.

2 Theoretical Background

2.1 Born–Oppenheimer Approximation

At the nonrelativistic level of approximation (which is sufficient for the lighter elements like B, C, and N) and neglecting the embedding of the polyatomic system in the environment (which would be needed for a deduction of the concept of the atomistic structure), the Hamiltonian for the many–body systems of a finite number of interacting particles (nuclei and electrons) is:

$$\hat{H} = -\frac{\hbar^2}{2m_e}\sum_i \nabla_i^2 - \sum_{i,I}\frac{Z_I e^2}{|r_i - R_I|} + \frac{1}{2}\sum_{i\neq j}\frac{e^2}{|r_i - r_j|} - \sum_I \frac{\hbar^2}{2M_I}\nabla_I^2 + \frac{1}{2}\sum_{I\neq J}\frac{Z_I Z_J e^2}{|R_I - R_J|}, \tag{2.1}$$

where the electrons with mass m_e are denoted by lower cases (*i, j*), and the nuclei with mass M and charge Z are presented by upper cases (*I, J*). The five terms on the right side of equation 2.1 are, in order, kinetic energy of electrons, interaction energy between electrons and nuclei, interaction energy between electrons, kinetic energy of nuclei, and repulsion energy between nuclei. Since the atomic nuclei are much heavier than the electrons (~ A·1823 times), electrons move in a very high speed whereas nuclei only vibrate comparatively slowly near their equilibrium positions. This leads to the result that electrons are almost adiabatic relative to the motion of the nuclei. The nuclei can only follow very slowly with the variation of the electrons. Therefore, nuclei can be considered as in quasi–stationary state with respect to the motion of the electrons [74]. Based on this consideration, the total wavefunction can be divided approximately into two parts:

$$\Psi(\mathrm{r}_i, \mathrm{R}_I) \approx \Phi(\mathrm{R}_I)\psi(\mathrm{r}_i, \mathrm{R}_I), \tag{2.2}$$

where $\psi(\mathrm{r}_i, \mathrm{R}_I)$ includes the effect of the nuclear motion in terms of the change of the electronic wavefunction with the parameters R_I for the nuclear positions. Then the Schrödinger equation can be given as:

$$\hat{H}\Psi(\mathrm{r}_i, R_I) = E\Psi(\mathrm{r}_i, R_I). \tag{2.3}$$

Putting equation (2.2) into (2.3):

$$\hat{H}\Phi(\mathrm{R}_I)\psi(\mathrm{r}_i, \mathrm{R}_I) \approx E\Phi(\mathrm{R}_I)\psi(\mathrm{r}_i, \mathrm{R}_I)\,. \tag{2.4}$$

Combination of equation (2.1) and equation (2.4) gives:

$$\begin{aligned}&\left[-\frac{1}{2}\sum_i \nabla_i^2 - \sum_{i,I}\frac{Z_I e^2}{|r_i - R_I|} + \frac{1}{2}\sum_{i\neq j}\frac{e^2}{|r_i - r_j|}\right]\Phi(\mathrm{R}_I)\psi(\mathrm{r}_i, \mathrm{R}_I) + \\ &\left[-\sum_I \frac{\hbar^2}{2M_I}\nabla_I^2 + \frac{1}{2}\sum_{I\neq J}\frac{Z_I Z_J e^2}{|R_I - R_J|}\right]\Phi(\mathrm{R}_I)\psi(\mathrm{r}_i, \mathrm{R}_I) \approx E\Phi(\mathrm{R}_I)\psi(\mathrm{r}_i, \mathrm{R}_I)\end{aligned}\,. \tag{2.5}$$

Putting the relations:

$$\nabla_i^2\Phi(R_I)\psi(r_i, R_I) = \Phi(R_I)[\nabla_i^2\psi(r_i, R_I)] \tag{2.6}$$

and

$$\begin{aligned}\nabla_I^2\Phi(R_I)\psi(r_i, R_I) = {} & \psi(r_i, R_I)\nabla_I^2\Phi(R_I) \\ & + 2[\nabla_I\psi(r_i, R_I)][\nabla_I\Phi(R_I)], \\ & + \Phi(R_I)\nabla_I^2\psi(r_i, R_I)\end{aligned} \tag{2.7}$$

into equation (2.5) gives:

$$\begin{aligned}&\left\{-\frac{1}{2}\sum_i \Phi(\mathrm{R}_I)\left[\nabla_i^2\psi(\mathrm{r}_i, \mathrm{R}_I)\right] + \left[-\sum_{i,I}\frac{Z_I e^2}{|r_i - R_I|} + \frac{1}{2}\sum_{i\neq j}\frac{e^2}{|r_i - r_j|}\right]\Phi(\mathrm{R}_I)\psi(\mathrm{r}_i, \mathrm{R}_I)\right\} + \\ &\left\{\begin{aligned}&-\sum_I \frac{\hbar^2}{2M_I}\left[\psi(r_i, R_I)\nabla_I^2\Phi(R_I) + 2[\nabla_I\psi(r_i, R_I)][\nabla_I\Phi(R_I)] + \Phi(R_I)\nabla_I^2\psi(r_i, R_I)\right] + \\ &\left[\frac{1}{2}\sum_{I\neq J}\frac{Z_I Z_J e^2}{|R_I - R_J|}\right]\Phi(\mathrm{R}_I)\psi(\mathrm{r}_i, \mathrm{R}_I)\end{aligned}\right\}. \\ &\approx E\Phi(\mathrm{R}_I)\psi(\mathrm{r}_i, \mathrm{R}_I)\end{aligned} \tag{2.8}$$

Rewriting equation (2.8) as:

$$\begin{aligned}&\Phi(\mathrm{R}_I)\left[-\frac{1}{2}\sum_i \nabla_i^2 - \sum_{i,I}\frac{Z_I e^2}{|r_i - R_I|} + \frac{1}{2}\sum_{i\neq j}\frac{e^2}{|r_i - r_j|}\right]\psi(\mathrm{r}_i, \mathrm{R}_I) + \\ &\psi(r_i, R_I)\left[-\frac{\hbar^2}{2}\sum_I \frac{1}{M_I}\nabla_I^2 + \frac{1}{2}\sum_{I\neq J}\frac{Z_I Z_J e^2}{|R_I - R_J|}\right]\Phi(R_I) + \\ &\left[-\sum_I \frac{\hbar^2}{M_I}[\nabla_I\psi(r_i, R_I)][\nabla_I\Phi(R_I)]\right] + \\ &\left[-\Phi(R_I)\sum_I \frac{\hbar^2}{2M_I}\nabla_I^2\psi(r_i, R_I)\right] \\ &\approx E\Phi(\mathrm{R}_I)\psi(\mathrm{r}_i, \mathrm{R}_I)\end{aligned}\,. \tag{2.9}$$

Neglecting the last two terms in equation (2.9) gives:

$$\left[-\frac{\hbar^2}{2m_e}\sum_i \nabla_i^2 - \sum_{i,I}\frac{Z_I e^2}{|r_i - R_I|} + \frac{1}{2}\sum_{i\neq j}\frac{e^2}{|r_i - r_j|}\right]\psi(\mathrm{r}_i, \mathrm{R}_I) = E_{el}(R_I)\psi(\mathrm{r}_i, \mathrm{R}_I) \tag{2.10}$$

and

$$\left[-\sum_I \frac{\hbar^2}{2M_I}\nabla_I^2 + \frac{1}{2}\sum_{I\neq J}\frac{Z_I Z_J e^2}{|R_I - R_J|} + E_{el}(R_I)\right]\Phi(\mathrm{R}_I) = E\Phi(\mathrm{R}_I)\,. \tag{2.11}$$

Equations (2.10) and (2.11) can be simplified as:

$$\left[\hat{H}_e + \hat{H}_{en}\right]\psi(\mathrm{r}_i, \mathrm{R}_I) = E_{el}(R_I)\psi(\mathrm{r}_i, \mathrm{R}_I) \tag{2.12}$$

for electrons with the parameter of nuclear coordinates R_I, and

$$\left[\hat{H}_n + E_{el}(R_I)\right]\Phi(\mathrm{R}_I) = E\Phi(\mathrm{R}_I)\,, \tag{2.13}$$

where the "Hamiltonian of electrons" $\hat{H}_e$ is the 1st plus 3rd term and $\hat{H}_{en}$ the 2nd term of equation (2.10), and the "Hamiltonian for the nuclei" $\hat{H}_n$ contains the 1st and 2nd term of equation (2.11). The mixed terms in equation (2.9), namely, the coupling between electrons and nuclei, are neglected. This is called adiabatic approximation or Born–Oppenheimer approximation. The Born–Oppenheimer approximation is one of the most important approximations in the field of molecular and solid state quantum mechanics [74]. It separates electronic and nuclear motions on the consideration that the nuclear mass is much larger than the electronic mass so that the nuclei can be taken as "stationary" particles, whose motions the electrons cannot "feel", thus providing an efficient way to solve Schrödinger's equation for complex interacting systems.

2.2 Hartree–Fock Theory

The Hartree–Fock (HF) approximation, also named the self–consistent field (SCF) approximation or mean field approximation, means that each electron moves in an average electrostatic field generated by all other electrons and the external (e.g. nuclear) field. It has been widely used for atoms, molecules, and condensed matter systems. This approximation started from the Hartree approximation [75], constructing N–electron wavefunction $\Psi(r)$ from the products of single–electron orbital functions $\psi(r)$ as:

$$\Psi(r_1, r_2, \cdots, r_N) = \psi_1(r_1)\psi_2(r_2)\cdots\psi_N(r_N). \tag{2.14}$$

This is based on the assumption that the electrons move independently, and can be distinguished as the 1st, 2nd,…, Nth one, and that their interactions are only due to Coulomb potential without relativistic spin–magnetic contributions. Using the wavefunction in equation (2.14), the expectation value of the Hamiltonian for many–body system can be expressed as:

$$E = \langle \psi | H | \psi \rangle = \sum_i \langle \psi_i | H_i | \psi_i \rangle + \frac{1}{2} \sum_{i,j} \langle \psi_i \psi_j | H_{ij} | \psi_i \psi_j \rangle, \tag{2.15}$$

providing that the single–electron orbital functions are orthonormal and normalized. According to the variational principle, the variation of E relative to the single–electron orbital function gives the single–electron Hartree equation:

$$\left[-\frac{1}{2}\nabla_i^2 + U_{ion}(r) + \sum_{j(\neq i)} \int dr' \frac{|\psi_j(r')|^2}{|r - r'|} \right] \psi_i(r) = E_i \psi_i(r), \tag{2.16}$$

in which the third term on the left–hand side of the equation (2.16) describes the electron ***i*** "feel" the mean field generated by the N–1 other electrons at the position ***r***. The *self–interaction* has been eliminated, i.e. each electron ***i*** does not feel its own contribution to the total electronic charge distribution. The essence of the Hartree equation is that the N–electron wavefunction is constructed from independent single–electron orbital functions.

Although the Hartree approximation can be numerically treated by self–consistently, it neglects the essential physics that electrons are indistinguishable Fermi particles and they should meet the basic prerequisite that the N–electron wavefunction must be antisymmetric when swapping any pair of particles:

$$\Psi(x_1, x_2, \cdots, x_N) = -\Psi(x_2, x_1, \cdots, x_N). \tag{2.17}$$

This can be solved by constructing a Slater determinant wavefunction to meet the anti–symmetry principle as:

$$\Psi = \frac{1}{\sqrt{N!}} \begin{vmatrix} \psi_1(x_1) & \psi_1(x_2) & \ldots & \psi_1(x_N) \\ \psi_2(x_1) & \psi_2(x_2) & \ldots & \psi_2(x_N) \\ \ldots & \ldots & \ldots & \ldots \\ \psi_N(x_1) & \psi_N(x_2) & \ldots & \psi_N(x_N) \end{vmatrix}, \tag{2.18}$$

where $\psi_i(x_j)$ is the single–electron orbital function and x_i includes the coordinates of both position and spin. Similar to solving the expectation value of the Hamiltonian for the Hartree equation together with the variational principle, the single–electron Hartree–Fock equation is given as:

$$\begin{aligned}&\left[-\frac{1}{2}\nabla_i^2+U_{ion}(r)\right]\psi_i(r)+\sum_{j(\neq i)}\int dr'\frac{\left|\psi_j(r')\right|^2}{\left|r-r'\right|}\psi_i(r)\\&-\sum_{j(\neq i)\|}\int dr'\frac{\psi_j^*(r')\psi_i(r')}{\left|r-r'\right|}\psi_j(r)=E_i\psi_i(r)\end{aligned}. \tag{2.19}$$

Comparing with the Hartree equation (2.16), there is one more term in the Hartree–Fock equation (2.19). It is the exchange term with the consideration of the anti–symmetry principle. The anti–symmetry condition is satisfied in the form of the last term on the left–hand side of equation (2.19).

Rewriting the third term on the left–hand side of equation (2.19) as:

$$\sum_{j(\neq i)}\int dr'\frac{\left|\psi_j(r')\right|^2}{\left|r-r'\right|}\psi_i(r)=\sum_j\int dr'\frac{\left|\psi_j(r')\right|^2}{\left|r-r'\right|}\psi_i(r)-\int dr'\frac{\left|\psi_i(r')\right|^2}{\left|r-r'\right|}\psi_i(r), \tag{2.20}$$

where the first term on the right–hand side of equation (2.19) is the interaction among all electrons, and the second one is the charge distribution of the electron ***i***. The fourth term on the left–hand side of equation (2.19) can be written as:

$$\begin{aligned}&\sum_{j(\neq i)\|}\int dr'\frac{\psi_j^*(r')\psi_i(r')}{\left|r-r'\right|}\psi_j(r)=\sum_{j\|}\int dr'\frac{\psi_j^*(r')\psi_i(r')}{\left|r-r'\right|}\psi_j(r)-\int dr'\frac{\psi_i^*(r')\psi_i(r')}{\left|r-r'\right|}\psi_i(r)\\&=-\int dr'\frac{\rho_i^{HF}(r,r')}{\left|r-r'\right|}\psi_i(r)-\int dr'\frac{\psi_i^*(r')\psi_i(r')}{\left|r-r'\right|}\psi_i(r)\end{aligned}, \tag{2.21}$$

where

$$\rho_i^{HF}(r,r')=-\sum_{j\|}\frac{\psi_j^*(r')\psi_i(r')\psi_i^*(r)\psi_j(r)}{\psi_i^*(r')\psi_i(r')}. \tag{2.22}$$

Putting equations (2.20)–(2.22) into equation (2.19) gives:

$$\left[-\frac{1}{2}\nabla_i^2+U_{ion}(r)-\int dr'\frac{\rho(r')-\rho_i^{HF}(r,r')}{\left|r-r'\right|}\right]\psi_i(r)=E_i\psi_i(r), \tag{2.23}$$

where

$$\rho(r') = \sum_j \left|\psi_j(r')\right|^2 . \tag{2.24}$$

For complex systems with many electrons, the term $\rho_i^{HF}(r,r')$ in equation (2.23) is generally averaged as:

$$\rho_i^{HF}(r,r') = \bar{\rho}^{HF}(r,r') = \frac{\sum_i \psi_i^*(r)\psi_i(r)\rho_i^{HF}(r,r')}{\sum_i \psi_i^*(r)\psi_i(r)} . \tag{2.25}$$

Definition of the effective potential as:

$$V_{eff}(r) = U_{ion}(r) - \int dr' \frac{\rho(r') - \bar{\rho}^{HF}(r,r')}{\left|r - r'\right|}, \tag{2.26}$$

then the single–electron Hartree–Fock equation can be simplified as:

$$\left[-\frac{1}{2}\nabla_i^2 + V_{eff}(r)\right]\psi_i(r) = E_i\psi_i(r) . \tag{2.27}$$

The Hartree–Fock equation is an extension of the Hartree equation. The difference between the two approximations is that the Hartree–Fock approximation constructs the wavefunction by Slater determinant not by the products of independent single–electron orbital functions. Therefore, the Hartree–Fock approximation [76-78] includes the anti–symmetry condition. However, the correlation effect, i.e. the avoiding of other nearby electrons due to two–electron Coulomb repulsion is neglected, which directly leads to failures, for instance that the jellium as predicted by the Hartree–Fock approximation is an insulating rather than a metallic system. Therefore, both exchange and correlation effects are expected to be necessarily incorporated into practical calculations, which can approximately be achieved by the density functional theory.

2.3 Density Functional Theory

2.3.1 Thomas–Fermi Theory

In the ground state, an assumed uniform electron density distribution with the number of electrons N over a volume V is:

$$\rho(r) = \frac{N}{V} = \frac{8\pi}{3h^3} p_F^3(r), \tag{2.28}$$

where ***r*** is a point in the volume V. The kinetic energy density t is:

$$t = \frac{T}{V} = \frac{1}{V}\int \frac{p^2}{2m} dN = \frac{8\pi}{2mh^3}\frac{p_F^5}{5}. \tag{2.29}$$

Combining equations 2.28 and 2.29 gives:

$$t = \frac{8\pi}{2mh^3}\frac{1}{5}\left[\frac{3h^3}{8\pi}\rho(r)\right]^{5/3} = \underbrace{\frac{3h^2}{10m}\left(\frac{3}{8\pi}\right)^{2/3}}_{C_K}\left[\rho(r)\right]^{5/3}. \tag{2.30}$$

The potential energy originating from the interaction with an external field and the electrostatic interaction of the electron density is:

$$U = e\int \rho(r) V_{ext}(r) dr + \frac{1}{2}e^2 \iint \frac{\rho(r)\rho(r')}{|r-r'|} dr dr'. \tag{2.31}$$

The total energy of an electron system, neglecting the self–interaction error, is:

$$E_{tot} = C_K \int \left[\rho(r)\right]^{5/3} dr + e\int \rho(r) V_{ext}(r) dr + e^2 \iint \frac{\rho(r)\rho(r')}{|r-r'|} dr dr'. \tag{2.32}$$

After minimization of the total energy with respect to $\rho(r)$ with the introduction of the Lagrange multiplier μ, the Thomas–Fermi equation [79, 80] can be given as:

$$\frac{5}{3} C_K \left[\rho(r)\right]^{2/3} + eV_{ext}(r) + e^2 \int \frac{\rho(r')}{|r-r'|} dr' - \mu = 0. \tag{2.33}$$

One of the most serious defects is that the Thomas–Fermi approximation does not reproduce any bonding between atoms. In addition, the classical treatment of the interactions between the electrons is oversimplified because of neglecting important quantum phenomena like exchange or the Coulomb correlation. Nevertheless, The Thomas–Fermi theory has been the origin of density functional theory (DFT). Its important contribution is that the electron density $\rho(r)$ is taken as the central variable rather than the commonly used wavefunction.

2.3.2 Hohenberg–Kohn Theorem

The work of Hohenberg and Kohn can be summarized into two classical theorems [81], which is the basis of the density functional theory. The first theorem states that *the ground*

state energy is a unique functional of the electron density distribution ρ(r). It follows that many–body wavefunctions are also determined by the density. According to the Schrödinger equation, all properties can then be determined. However, although the first theorem reveals that there exists such functional of electron density, the specific formulation of the functional is unknown. In other words, we know nothing else but the existence of such a functional. It is explicitly given through the solution of all possible Schrödinger equations.

The second theorem describes one important feature of the functional, that is, *minimizing the energy of the functional corresponds to the determination of the ground–state energy with the condition that the number of particles is kept constant*. If we knew the exact form of the functional, then we could vary the electron density to get the minimization of the energy from the functional. The energy functional can be expressed as:

$$E\left[\rho(r)\right] = F[\rho(r)] + E_{ext}\left[\rho(r)\right] + E_{N-N}\,, \tag{2.34}$$

in which $F[\rho(r)]$ is a functional that is not related to external field and expressed as:

$$F[\rho(r)] = T[\rho(r)] + \frac{1}{2}\iint \frac{\rho(r)\rho(r')}{|r-r'|}\,drdr' + E_{xc}[\rho(r)]\,. \tag{2.35}$$

The first two terms on the right–hand side of equation (2.35) are electron kinetic energy and the Coulomb interaction of non–interacting electrons including the physically nonexistent repulsion of each electron by itself. The complexity of the interaction among electrons is left in the third term $E_{xc}[\rho(r)]$, i.e., the exchange–correlation term. The second term on the right–hand side of equation (2.34) represents the interaction between electrons and external field, namely,

$$E_{ext}\left[\rho(r)\right] = \int \upsilon(r)\rho(r)dr\,, \tag{2.36}$$

where $\upsilon(r)$ is the local potential that is the same for all electrons. The last term on the right–hand side of equation (2.34) is the repulsion energy among atomic nuclei.

In fact, the existence of one electron definitely affects all other electrons. If one electron is at position ***r***, then the electron density at position ***r′*** is not the same for the case when no electron is at position ***r***. This indicates that the true Coulomb repulsion between particles

differs from the Coulomb interaction within a charge density continuum. Now we know, there are 1st the Coulomb exchange interaction correction (abbreviated as exchange interaction) between electrons with so-called parallel spins (the angle between them is "only" 70.5°) and 2nd the Coulomb correlation interaction correction (abbreviated as correlation interaction) between all electrons, where however the terms for anti–parallel spin electrons (with spin angle of 180°) usually dominate.

To get the energy functional, three issues have to be addressed: (I) how to determine the electron density; (II) how to determine the functional of kinetic energy; (III) how to determine the functional of exchange and correlation. Kohn and Sham presented the solution for the first two issues, which gives the famous Kohn–Sham equation. The third issue is usually solved by local density approximation.

2.3.3 Kohn–Sham Equations

Because nothing is known about the term for the kinetic energy of interacting particles, an important assumption is proposed by Kohn and Sham: *the original interacting many–body problem is replaced by an auxiliary independent–particle problem*. That is, the ground state density of the difficult interacting many–body system is chosen to be equal to that of some non–interacting system. In addition, the density function can be constructed by N individual electron wavefunctions (Kohn-Sham orbitals ψ). The independent–particle equations for the auxiliary system can be solved by numerical methods, leaving all the complex interacting terms incorporated into the exchange–correlation functional.

The density function is thereby:

$$\rho(r) = \sum_{i=1}^{N} |\psi_i(r)|^2 . \tag{2.28}$$

The kinetic energy term is approximated by:

$$T[\rho(r)] = T_s[\rho(r)] = \sum_{i=1}^{N} \int dr \psi_i^*(r)(-\frac{1}{2}\nabla^2)\psi_i(r) . \tag{2.29}$$

Replacement of the variation of energy functional $E[\rho(r)]$ with respect to the density $\rho(r)$ by

the variation of energy functional with respect to electron wavefunctions ψ, the Kohn–Sham equation can be obtained:

$$\left\{-\frac{1}{2}\nabla^2 + V_{KS}\left[\rho(r)\right]\right\}\psi_i(r) = E_i\psi_i(r), \tag{2.30}$$

where

$$\begin{aligned} V_{KS}\left[\rho(r)\right] &= \upsilon(r) + V_{coul}\left[\rho(r)\right] + V_{XC}\left[\rho(r)\right] \\ &= \upsilon(r) + \int dr' \frac{\rho(r')}{|r-r'|} + \frac{\delta E_{XC}\left[\rho(r)\right]}{\delta\left[\rho(r)\right]}. \end{aligned} \tag{2.31}$$

The core of the Kohn–Sham equation [82] is 1st that the kinetic energy term of interacting many–body system is approximated by the one of the non–interacting system, 2nd that the largest part of the Coulomb interaction of individual Fermionic electrons is described as the Coulomb interaction within a continuous charge distribution, and 3rd that all complex corrections to the kinetic energy and to the Coulomb potential energy due to the classical Coulomb correlations and due to the Fermionic behavior of electrons according to the Pauli principle are included into the so-called exchange–correlation functional $V_{XC}\left[\rho(r)\right]$. In practical calculations, the Kohn–Sham equation transforms the issue of the ground–state properties of a many–body system into an equivalent single–electron problem, which can be easily solved by numerical methods.

2.3.4 Exchange Correlation Functional

The simplest approach to approximate the effects of kinetics, exchange and correlation is to describe it by a simple function of the local electron density. Kohn and Sham presented the local density approximation (LDA). That is, the exchange–correlation energy $E_{xc}\left[\rho(r)\right]$ at a position (locally) can be approximated by the exchange–correlation energy in an uniform electron gas with the same electron density at the position. According to this approximation, the exchange–correlation energy is expressed as:

$$E_{xc}\left[\rho(r)\right] \approx \int \varepsilon_{xc}\left[\rho(r)\right]\cdot\rho(r)dr, \tag{2.32}$$

where $\varepsilon_{xc}\left[\rho(r)\right]$ is the exchange–correlation energy per electron of the uniform electron gas

with the density $\rho(r)$. The exchange–correlation potential is given by:

$$V_{xc}\left[\rho(r)\right]=\frac{\delta E_{xc}\left[\rho(r)\right]}{\delta\rho(r)}\approx\varepsilon_{xc}\left[\rho(r)\right]+\rho(r)\frac{\partial\varepsilon_{xc}\left[\rho(r)\right]}{\partial\rho(r)}. \tag{2.33}$$

For practical calculations, the exchange–correlation energy is generally divided into two parts, namely the exchange $\varepsilon_x\left[\rho(r)\right]$ and the correlation $\varepsilon_c\left[\rho(r)\right]$ including also the kinetic correction:

$$\varepsilon_{xc}\left[\rho(r)\right]=\varepsilon_x\left[\rho(r)\right]+\varepsilon_c\left[\rho(r)\right]. \tag{2.34}$$

The exchange energy is given by the Dirac functional:

$$E_x\left[\rho(r)\right]=-\frac{3}{4}\left(\frac{3}{\pi}\right)^{1/3}\int\rho(r)^{4/3}dr. \tag{2.35}$$

An analytic expression for the correlation energy is not known except for the high and low density limits. At present, the correlation energy of the homogenous gas can be calculated numerically to have great accuracy by Monte Carlo methods. The LDA has been demonstrated to be reasonably accurate for many ground–state properties, which is probably because of the short range of exchange and correlation effects in many solids. However, the LDA works not well for the calculations where specific effects play a role such as in atomic cores or in local d and f shells or in the case of delocalized (aromatic, resonating) bonds and so on. Fortunately, the density functional approximation often benefits from accidental error cancellation.

An improved method is the Generalized Gradient Approximation (GGA), with the addition of the gradient effect of electron density based on the consideration of the variations of electron density. There are several different parameterizations for GGA, such as PBE [83], RPBE [84], PW91 [85], WC [86], and PBESOL [87]. Among them, PBE and PW91 are the most frequently used ones. Besides LDA and GGA, there are also many other different types of functionals to treat the kinetic–exchange–correlation effect.

2.4 Pseudopotentials

As shown in equation (2.1), the Hamiltonian contains the interactions from electrons,

nuclei, and the interaction between electrons and nuclei. By solving the Schrödinger equation, the properties of solids, polymers, nanoparticles and molecules can be deduced. In general, the physical and chemical properties of hard solids are dominantly determined by covalent electrons, not so much by nuclei and core electrons. Furthermore, more plane waves are needed for core electron wave functions that are violently oscillating when approaching the nulcei. If the electron density to be treated in the cores can be replaced by smoother densities of node–less pseudo–wavefunctions, then the computational time can be greatly reduced with appropriate accuracy. If also the core electrons are not explicitly treated but taken over from frozen free atoms, generating an effective potential of the atomic cores, then the pseudopotential method is obtained. The introduction of a pseudopotential effectively reduces both the number of electrons and in addition the basis set size for the remaining valence electrons, thereby speeding up the calculations. It also includes relativistic and other effects into the effective pseudopotentials. At present, there are many different types of Pseudopotentials on the market. Among them, the two most effective and common methods are the norm–conserving pseudopotentials (NCPP) [88] and the ultrasoft pseudopotentials (USPP) [89].

For the norm–conserving pseudopotential (NCPP), the one–particle pseudo–wavefunctions beyond the chosen cut–off radius are the same as the all–electron one–particle wavefunctions. The main idea is that the wavefunctions inside the cut–off radius with violent oscillations are replaced by smooth node–less wavefunctions with slow oscillations. The total charge inside the cut–off radius is to be identical before and after the reconstructed wavefunctions to ensure that the scattering properties of the pseudopotential can be reproduced correctly. However, for strongly localized orbitals, the pseudopotentials still require large basis set with corresponding considerable computational time. The ultrasoft pseudopotentials (USPP) method, reinvented by Vanderbilt, is to make the pseudo–wavefunctions even smoother than the norm–conserving pseudopotential method. The method reduces the large basis set by removing the strongly attractive shielded core Coulomb potential together with orbital oscillations inside of the cut–off region causing the so-called strong kinetic Pauli repulsion. To recover the full charge during the construction of

the ultrasoft pseudopotential, the electron density needs to be augmented in the core regions. Therefore, the electron density can be divided into two parts: the soft part that can extend into one whole unit cell and the hard part that is localized inside the core regions.

2.5 Vienna *ab initio* Simulation Package (VASP)

The Vienna ab initio simulation package (VASP) [90] is a very complex package designed to perform ab initio quantum mechanical calculations using plane wave basis set. The method is based on pseudopotentials and projector augmented waves (PAW) to deal with the interaction between ionic cores and electrons, which greatly reduces the demand of the number of plane waves. Therefore, it performs almost as the fastest scheme, performing iterative matrix diagonalisations within RMM–DISS and efficient numerical methods, thus significantly cutting the computational time for large systems with approximate accuracy. It also introduces the local density approximation for the exchange and correlation functional and takes the free energy as the variational quantity.

Periodic boundary conditions are used in VASP to deal both with isolated systems such as atoms and molecules, one–dimension materials like nanowires, nanorods and nanotubes, two–dimension materials such as thin films and surfaces, and bulk materials, for example crystalline and amorphous materials. Therefore, it can perform broad calculations for various properties as follows: (I) Structural calculations: bond lengths, bond angles, lattice parameters, and effective atomic configurations. (II) State of equation. (III) Mechanical properties: bulk moduli, shear moduli, Young's moduli, elastic constants. (IV) Electronic structures: energy levels, charge densities, energy bands, densities of states. (V) Optical properties. (VI) Magnetic properties. (VII) Lattice dynamics. (VIII) Surface simulations. These calculations cover almost all the popular fields that are intensively investigated nowadays.

2.6 Computational Methods Employed in This Work

All theoretical calculations in this work are based on density functional theory and plane–wave pseudopotential technique. The interaction between atomic cores and valence

electrons in our investigated systems is treated by norm–conserving pseudopotentials for crystalline materials using the CASTEP code, and by ultra–soft pseudopotentials for amorphous ones as implemented in the VASP program. Throughout the work, the exchange–correlation interaction is described by the generalized gradient approximation (GGA) with the PW91 parameterization. To balance the computational time and the convergence of total energy and stress, different values of energy cutoff for the plane–wave basis are chosen according to the demands of the specific systems.

3 Theoretical Calculations on Crystalline B–C–N Materials

3.1 Crystalline BC_2N Materials*

Searching for novel superhard materials is a long–term goal for condensed matter physicists and material scientists [91]. The traditional superhard materials, diamond and c–BN as known, are composed of light elements (C, B, and N). This motivates investigators to attempt to synthesize superhard materials with light elements, based on the consideration that they can form extremely strong covalent bonds.

Based on such initial motivation, ternary B–C–N crystals with diamond–like structure have attracted great attention in the past two decades. They are expected to possess simultaneously the super hardness of diamond and the high–temperature inertness of c–BN. In particular, the discovery of the cubic BC_2N phase has stimulated numerous investigations on ternary B–C–N crystals. This is because the cubic BC_2N phase is the first one that is declared to have the hardness only next to diamond, even harder than c–BN. This exciting discovery encourages more works focusing on its microstructure because the microstructure, in principle, dominates any property of materials. Unfortunately, the structure of the cubic BC_2N phase has not been determined. Since the discovery of the phase, great controversy on the issues of the microstructure and mechanical properties has never been stopping from both the experimental and the theoretical aspects.

From the experimental perspective of view, most of the measured lattice constants of c–BC_xN obey Vegard's law as a linear interpolation of diamond and c–BN. In contrast, Solozhenko determined a lattice constant (3.642 Å) for a c–BC_2N crystal that is higher than for c–BN (3.617 Å). The bulk modulus of the c–$BC_{2.5}N$ samples from shock compression is 401 GPa, lying between those of diamond (443 GPa) and c–BN (368 GPa). On the contrary, bulk and shear moduli of the c–BC_2N crystal in Solozhenko's experiments are much lower than the c–BN values, even though the measured Vickers hardness for c–BC_2N is higher than

* Reference [5] in the list of publications

that of c–BN by 10 ~ 15 GPa.

As summarized in the first chapter, theoretic works can generally be classified into two kinds: the $(BN)_n(C_2)_n$ superlattice [26, 27, 40-42] and the ordered solid solution within the diamond lattice (typically with 8 ~ 16 atoms) [28, 32, 38, 39, 43-45]. In general, the structure with the lowest energy is highly symmetric with atoms well organized. That is why plenty of previous theoretical models have such typical characteristics. However, most of these theoretical works neglect one extremely important phenomenon revealed in experimental works. That is, in contrast to the ordered structures presumed in the theoretical calculations, XRD experiments [10, 12, 13, 18, 24] indicated the absence of the (200) diffraction peak in c–BC_2N crystals, implying that B, C, and N atoms were randomly distributed over the diamond lattice. Moreover, Hubble [19] observed a wide peak at 1325.7 cm^{-1} in the Raman spectrum of c–BC_2N. They speculated that C atoms were substituted randomly by B and N atoms in the diamond lattice.

Our work is based on these experimental evidences to propose structural models of cubic BC_2N phases. Note that our motivation is nearly completely different from previous theoretical works. We are not struggling to search the models with the lowest energy regardless of the observed experimental phenomena, but following the clues indicated by experimental findings. Based on this consideration, we propose our random solid solution model for cubic BC_2N crystals, in which B, C, and N atoms randomly occupy diamond lattice sites. The inconsistence of the lattice constant and mechanical properties, observed in experiments, can be understood by different degrees of atomic mixture in the c–BC_2N samples. The controversy over theoretical calculations can also be unified by our structural models via the parameter of degree of atomic mixture.

3.1.1 Structural Predication and Verification

The fundamental concept of the random solid solution model is that atoms are randomly distributed over lattice sites. For cubic BC_2N, that is, 16 boron atoms, 16 nitrogen atoms, and 32 carbon atoms are randomly occupying 64 atomic coordinates of 64–atom diamond supercell. During the process of random distribution, a bonding rule is introduced. That is, no

B–B or N–N bond is allowed since they are highly energetically unfavorable [27, 28, 92, 93]. They are also excluded by experimental IR, XPS, and NMR data [13, 14]. Under extreme conditions in experiments, these bonds will be broken or decomposed and exist in other forms of bonding states. This bonding rule is also frequently used in other theoretical calculations.

Except for B–B and N–N bonds, there are four types of bonding states in cubic BC_2N crystals, i.e., C–C, C–N, C–B, and B–N. The random distribution of B, C, and N atoms over the lattice sites can produce a huge number of possible configurations. Here we introduce a parameter, namely the degree of mixture χ, to classify all these possible structural models. It is defined in terms of the ratio of bond contents (C–C, C–N, C–B, and B–N) as:

$$\chi = \frac{N_{B-C} + N_{N-C}}{N_{C-C} + N_{B-C} + N_{N-C} + N_{B-N}}, \tag{3.1.1}$$

where N_{C-C}, N_{B-C}, N_{N-C}, N_{B-N} are the numbers of C–C, C–N, C–B, and B–N bonds. Figure 3.1.1 shows representative structures of cubic BC_2N with different degree of mixture χ. By definition, $\chi = 1$ corresponds to a complete mixing of two FCC sublattices by BN and C_2, while small χ denotes severe phase separation of diamond and c–BN. Hence, χ actually describes the degree of BN–C_2 mixture in the B–C–N random solid solutions. As we will show below, χ is also the key parameter that determines the lattice constants and physical properties of c–BC_2N solid solutions.

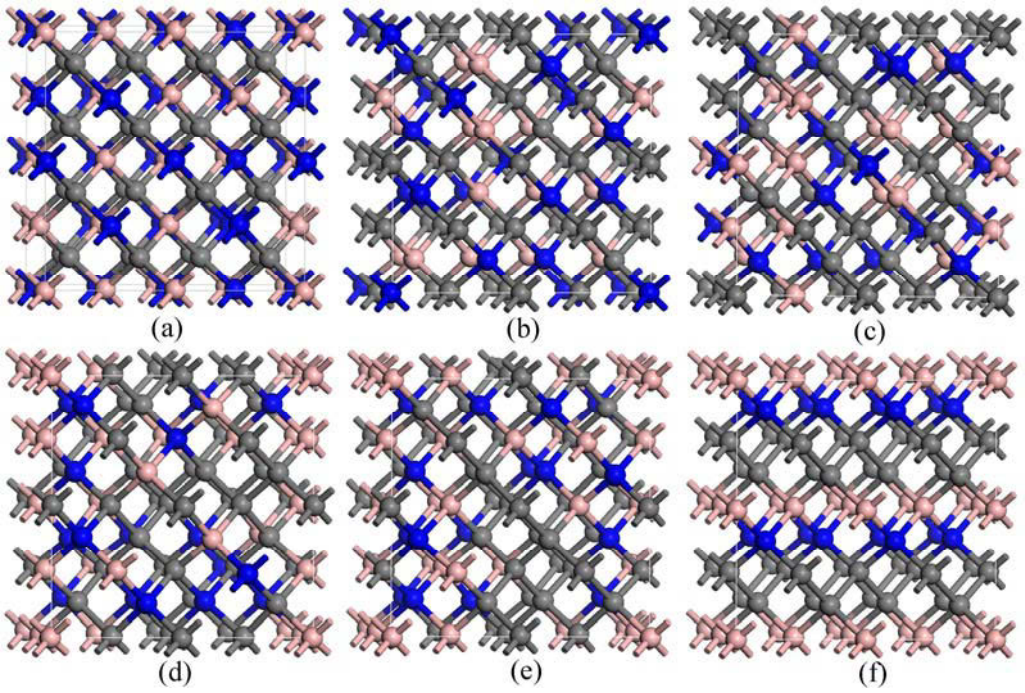

Figure 3.1.1: *Representative structures of cubic BC_2N phase predicted by random solid solution model with different degree of mixture. Models (a) ~ (f) corresponds to the degree of mixture χ equal to 1=64/64, 0.8125=52/64, 0.671875=43/64, 0.53125=34/64, 0.34375=22/64, and 0.21875=14/64, respectively. Boron, carbon, and nitrogen atoms are shown by pink, grey, and blue colors, respectively.*

Different kinds of configuration correspond to different degrees of atomic mixture. After classification of all produced structures, there exist many different values of the degree of mixture. Therefore, the configurational distribution can be correlated with the degree of mixture. Here the statistic distribution of χ counted from a large number of random configurations is displayed in Figure 3.1.2. One can see that χ distributes in a narrow range with FWHM $\approx$ 0.05. The left side of the curve corresponds to the case that B, C, and N atoms are distributed over the crystal lattice more orderly. In contrast, the case on the right side corresponds to more randomly atomic arrangements. The maximum peak at $\chi_0 \approx 0.8125 = 52/64$ corresponds to the most probable degree of mixture for c–BC_2N solid solution.

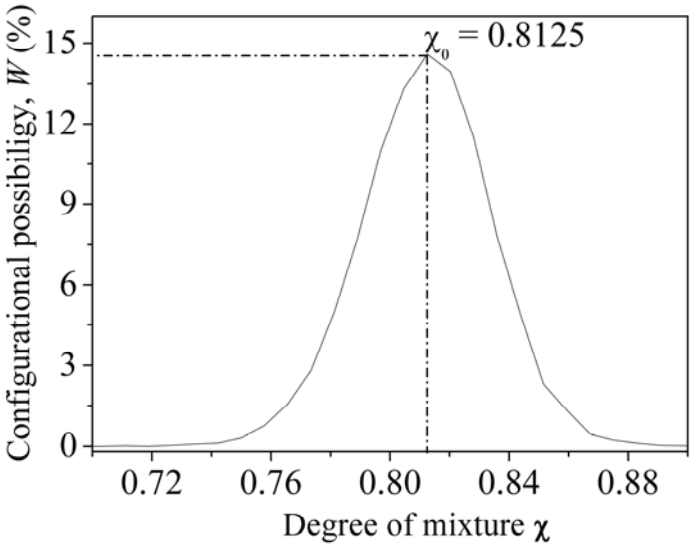

Figure 3.1.2: *Statistic distribution of degree of mixture (χ) for c–BC_2N counted from 2.5×10^6 random configurations. The maximum peak at $\chi_0 = 0.8125$ is labeled.*

3.1.2 Computational Details

We have considered a number of representative c–BC_2N random configurations with different χ values (from 0.22 to 1). Each of these crystal structures was fully optimized. Their mechanical properties were computed by using density functional theory and the plane–wave pseudopotential technique as implemented in the CASTEP program [94]. The ion (i.e. atomic core)–valence-electron interaction was modeled by norm–conserving pseudopotentials [88]. An energy cutoff of 1000 eV was used for the plane–wave basis to ensure converge of the total energy and stress. The generalized gradient approximation (GGA) with the PW91 parameterization was adopted to describe the exchange–correlation correction to the interaction [95]. The Brillouin zone of the reciprocal space was sampled by a 2 × 2 × 2 grid. As shown in Table 3.1.1, the present computational method is able to reproduce the lattice parameters (~ 1% deviation) and elastic properties of diamond and c–BN crystals quite well.

Table 3.1.1. *Lattice constant (a), bulk modulus (B), isotropic (Voigt–Reuss–Hill average [96]) shear modulus (G), Young's modulus (E), Poisson's ratio (ν), and Vickers hardness (H_v) of diamond, c–BN, and c–BC_2N (with the most probable degree of mixture) from the present calculations compared with experiments (% differences in parentheses).*

	a (Å)	*B* (GPa)	*G* (GPa)	*E* (GPa)	ν	H_v (GPa)
Diam.	3.531	444	546	1162	0.064	93.6
	(–0.036)	(+1)	(+13)	(+21)	(–0.067)	(–2.4)
Expt.	3.567	443	533	1141	0.071	96±5
c-BN	3.596	381	405	897	0.108	64.5
	(0.020)	(+13)	(+0)	(+8)	(+0.011)	(+1)
Expt.	3.616	368	405	889	0.097	63±5
BC_2N	3.614	351	393	859	0.092	72
	(–0.028)	(+92)	(+155)	(+312)	(–0.056)	(–4)
Expt.	3.642	259	238	547	0.148	76±4
Ave. Dev.	–1%	+20%	+35%	+25%	±25%	±4%

3.1.3 Results and Discussion

3.1.3.1 Formation Energy

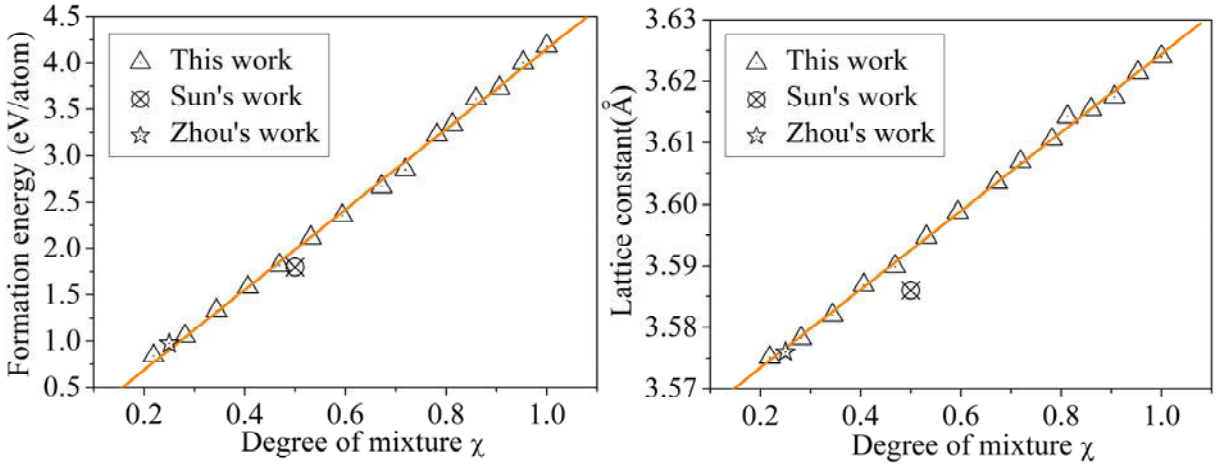

Figure 3.1.3: *Formation energy and lattice constant for c–BC_2N crystals as a function of χ. Both sets of data are fitted to a linear relation (orange lines). Results for some previous ordered structures are included. Sun's work is from Ref.[28] and Zhou's work is from Ref.[32].*

The formation energy is defined by the energy difference between c–BC_2N and the summation of diamond and c–BN. Figure 3.1.3 shows the formation energy and the lattice constant as a function of χ. The formation energy rises linearly with increasing degree of

mixture. This indicates that mixing BN and diamond into a BC_2N alloy is unfavorable due to the positive formation energies (0.84 ~ 4.18 eV/atom). From the energetic point of view, crystalline c–BC_2N is metastable and tends to separate into diamond and c–BN phases. Therefore, it is not surprising that previously proposed low–energy crystal structures for c–BC_2N were either $(BN)_n(C_2)_n$ superlattices or ordered structures with significantly local BN–C_2 phase separation [27, 32, 38, 39]. With our random solid solution model and a sufficiently large supercell, it is always possible to find some particular configurations with very low formation energy but serious phase separation (small χ).

However, formation energy is not the only factor for determining the most favorable crystal structure of c–BC_2N. Under experimental high–temperature conditions, the positive formation energy of c–BC_2N can be compensated by the contribution ΔU from the configuration entropy to free energy, which is described by

$$\Delta U = -k_B T \ln W , \tag{3.1.2}$$

where U is the free energy, k_B is the Boltzmann constant, T is the temperature, and W represents the configurationally possibility displayed in Figure 3.1.2. The synthesis temperature of cubic BC_2N crystals can be as high as 2500 K in experiments [24, 25, 91]. According to this temperature, the contribution of configuration entropy to the free energy is about 0.41 eV for W = 14.6% and 1.99 eV for W = 0.01%. The low free energy corresponding to the high configuration probability should at least partially balance the positive formation energy (e.g., 3.34 eV for χ_0 = 0.8125) of the c–BC_2N solid solution.

3.1.3.2 Lattice Parameter

Within our random solid solution model, the lattice constant of c–BC_2N increases linearly with χ (Figure 3.1.3). This effect is related to the reduced ionicity found by Mulliken analysis. For example, the average on–site charge on B (N) atoms drops from 0.59 (– 0.54) e for χ = 0.22 to 0.41 (– 0.30) e for χ = 1. The reduced ionicity with increasing BN–C_2 mixture in the solid solution would slightly weaken the contribution of Coulomb attraction in the B–N interatomic bonding and then expand the lattice a little. As a consequence, the elastic moduli will decrease with increasing χ. This has been confirmed by our first–principles calculations.

At high degree of mixture ($\chi \geq 0.55$), the lattice constant of c–BC_2N is larger than that of c–BN. This is contradictory to the prediction of Vegard's law but agrees with Solozhenko's experimental observation [18]. The lattice constant of c–BC_2N solid solution at χ_0 is larger than the c–BN value by 0.018 Å, comparable to the measured difference of 0.026 Å [18]. It is noteworthy that other previous experiments obtained different values of the lattice constants, i.e., 3.602 Å by Knittle [24] and 3.595 Å by Zhao [20], both roughly obeying Vegard's law. With our model, such discrepancy in the lattice constant of c–BC_2N can be explained by different degrees of mixture that is sensitive to the synthesis conditions.

3.1.3.3 Elastic Modulus

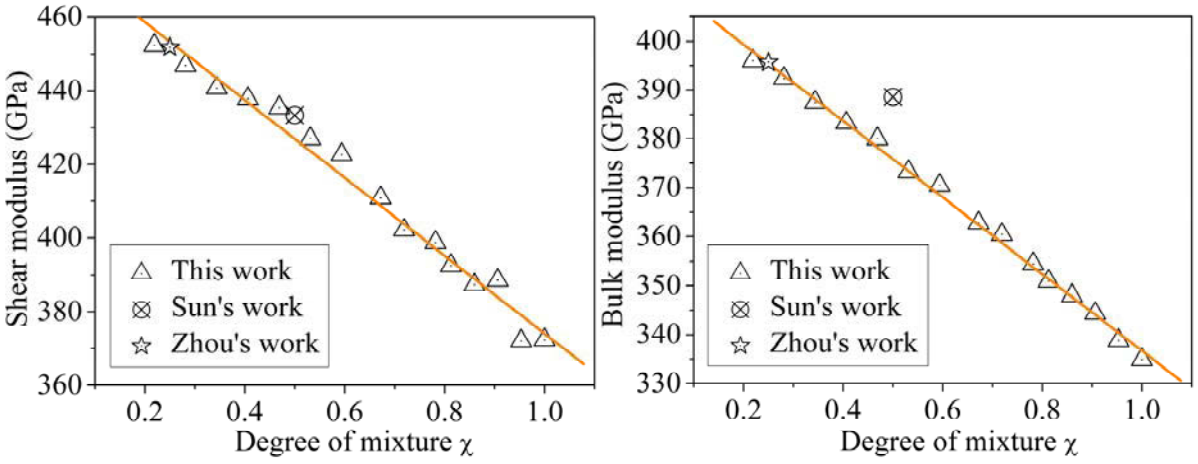

Figure 3.1.4: *Shear modulus and bulk modulus for c–BC_2N crystals as a function of χ. Both sets of data are fitted to linear relations (orange lines). Results for some previous ordered structures are included [28, 32]. Sun's work is from Ref.[28] and Zhou's work is from Ref.[32].*

The theoretical bulk modulus and (isotropic) shear modulus as a function of χ are shown in Figure 3.1.4. Both of them decrease with increasing degree of mixture. This trend can be related to the expanded lattice constant and the reduced on–site charge with increasing χ. At $\chi_0 = 0.8125$, our calculations predicted that B = 351 GPa and G = 393 GPa, lower than the theoretical values of c–BN (B = 381 GPa, G = 405 GPa). Similar behavior was found for Young's modulus E, which is proportional to the shear modulus approximately according to $E = 2.076\ G$. Our present results for c–BC_2N with the most probable χ_0 agree qualitatively with

the experiment by Solozhenko et al. [25, 97], although the theoretical moduli are still far higher than the measured data. Indeed, the experimental measurements were done on polycrystalline nano–grain samples instead of the perfect bulk crystal assumed in our theoretical calculations. Moreover, the Poisson's ratio (ν = 0.148) obtained in Ref. [25] is significantly larger than those of diamond (0.071) and c–BN (0.097), whereas our theoretical ν lies between the diamond and BN values. Meanwhile, the bulk modulus of 401 GPa for $BC_{2.5}N$ samples from shock compression is higher than that of c–BN [15].

According to our model, this may correspond to the solid solutions with low degree of mixture (e.g., $\chi \leq 0.3$) due to the short duration time in the shock compression process. For the purpose of comparison, in Figures 3.1.3 and 3.1.4 we have also included the theoretical results for two typical ordered crystal structures of c–BC_2N obtained using the same computational scheme [23, 28, 32]. The lattice constants, formation energies, and elastic moduli for these ordered structures basically fit well to the χ–dependent trends predicted by the random solution model. Generally speaking, any ordered structure can be viewed as a specific situation within the random model. Regardless the detailed B, C, and N atomic arrangement, the essential physics related to the degree of mixture would still be valid.

3.1.3.4 Hardness

Based on the bond populations and on–site charges from first–principles calculations, we evaluated the Vickers hardness (H_v) of c–BC_2N crystals using a semiempirical formula developed by Tian's group [98]. The semiempirical formulas are mainly based on three factors, electronic density, bond length, and degree of covalent bonding, to determine the hardness of polar covalent crystals, which is described as:

$$H_v = \left[\prod^{\mu} \left(H_v^{\mu} \right)^{n^{\mu}} \right]^{1/\sum n^{\mu}}, \tag{3.1.3}$$

where H_v^{μ} represents the hardness of a binary compound and defined as:

$$H_v^{\mu} = 350 \left(N_e^{\mu} \right)^{2/3} e^{-1.191 f_i^{\mu}} \Big/ \left(d^{\mu} \right)^{2.5}. \tag{3.1.4}$$

N_e^{μ} is the number of valence electrons and expressed as:

$$N_e^{\mu} = \left(n_e^{\mu}\right)^* \Big/ v_b^{\mu} , \tag{3.1.5}$$

in which the number of valence electrons per bond and the bond volume are expressed as:

$$\left(n_e^{\mu}\right)^* = \left[\left(Z_A^{\mu}\right)^* \Big/ N_{CA} + \left(Z_B^{\mu}\right)^* \Big/ N_{CB}\right], \tag{3.1.6}$$

and

$$v_b^{\mu} = \left(d^{\mu}\right)^3 \Big/ \sum_{\nu} \left[\left(d^{\nu}\right)^3 N_b^{\nu}\right]. \tag{3.1.7}$$

As shown in Figure 3.1.5, the theoretical H_v ranges between 65 GPa and 75 GPa and decreases with increasing degree of mixture. At the most probable χ, the hardness of the c–BC_2N solid solution (H_v = 66.5 GPa) reaches about 77% of the diamond's value (93.6 GPa) [98] and is higher than that of c–BN by 2 GPa. This agrees well with the experiments, that is, the measured H_v of c–BC_2N is about 79% [25, 28] or 73% [20] of the diamond's hardness and is 10 ~ 15 GPa higher than for c–BN [18, 20]. Most previous calculations on the hardness of c–BC_2N predicted similar values [32, 98, 99]. Indeed, it was found that the Vickers hardness is insensitive to the details of atomic arrangements in the crystal [99]. In all situations, c–BC_2N possesses larger hardness than c–BN, making it an excellent candidate as a superhard material.

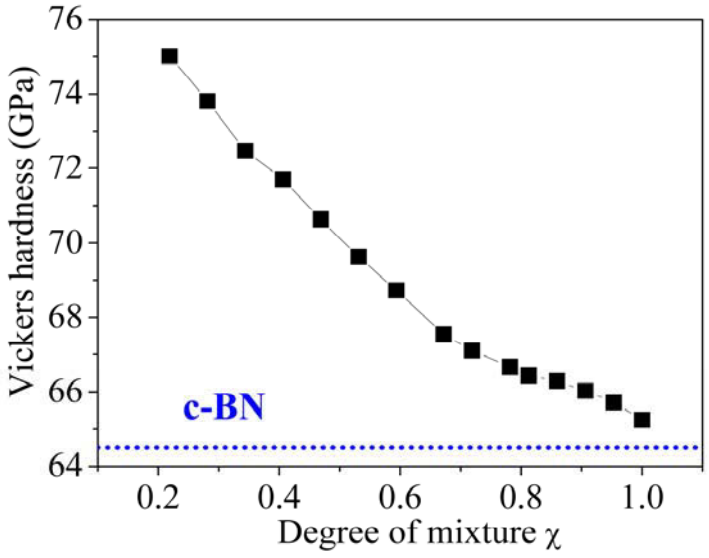

Figure 3.1.5: *Vickers hardness for c–BC_2N crystals as a function of χ. Dotted line shows theoretical value of c–BN.*

3.1.3.5 Ideal Strength*

However, for hardness measurements in experiments, the measured values of hardness are usually integrated values over large areas of samples under the indenter. This inevitably incorporates other factors such as defects in crystals. It is not the true value of hardness of pure and singular phases. Another mechanical parameter, ideal strength, can give a real examination of pure phases. For the investigation of the ideal strength of cubic BC_2N crystals, there are already numerous works focusing on this topic. However, tensile properties for different structural models show great discrepancies. In a previous theoretical study, Zhang et al. simulated the tensile strength of c–BC_2N crystals with two structural models, BC_2N-1 and BC_2N-2 [29]. They found that the tensile strength and the critical strain for the BC_2N-1 structure along the [111] direction are 79 GPa and 12%, respectively. In contrast, the BC_2N-2 structure has a lower tensile strength down to 56 GPa and the corresponding critical strain drops to 8%. Taking a typical error of ~ 10% for the tensile strength, the obvious discrepancy of 23 GPa, which is far beyond the systematic error of DFT, clearly indicates that some other underlying factors might be responsible for this great difference of tensile strengths between the two structures. Here we attempt to explain these discrepancies in terms of the atomic arrangements (B, C, and N) within the same crystal structure (c–BC_2N). Using first–principles calculations, we revealed that diverse degrees of mixture in the c–BC_2N crystal may lead to distinctly different values of tensile strength, which may be the underlying mechanism for the above mentioned discrepancies.

In general, the failure mode of c–BC_2N crystals is considered to be dominated by the tensile strength in the [111] direction [29, 100]. Therefore, tensile strengths along the [111] direction for c–BC_2N crystals with four types of degree of mixture were calculated. Using the computational method developed in Ref. [101, 102] and described in Ref. [39], the tensile stress was calculated by incrementally deforming the lattice vector along the [111] direction. At each step, both the lattice vectors orthogonal to the applied strain and the internal coordinates were completely relaxed. At each strain step, the optimized coordinates were used as input for the following step in order to ensure continuous deformation.

* Reference [4] in the list of publications

The structural models of c–BC_2N crystals with four types of degree of mixture are described as follows: Str-1 shown in Figure 3.1.6a with the structural parameter $\chi = 1$ corresponds to a complete mixing of B, C, and N atoms in the c–BC_2N lattice. In other words, no C–C or B–N bond is contained in Str-1. For Str-2, the parameter χ decreases to 0.781 (Figure 3.1.6b) and some C–C and B–N bonds emerge. The mixing degree further reduces in Str-3 ($\chi = 0.531$) and random agglomerations in local areas of the c–BC_2N crystal can be seen (Figure 3.1.6c). Meanwhile, embryos of diamond and c–BN are formed in the tetra–coordinated lattice structure. As these embryos grow orderly, alternatives of diamond and c–BN layers appear with high symmetry in Str-4 with a structural parameter $\chi = 0.5$ (Figure 3.1.6d).

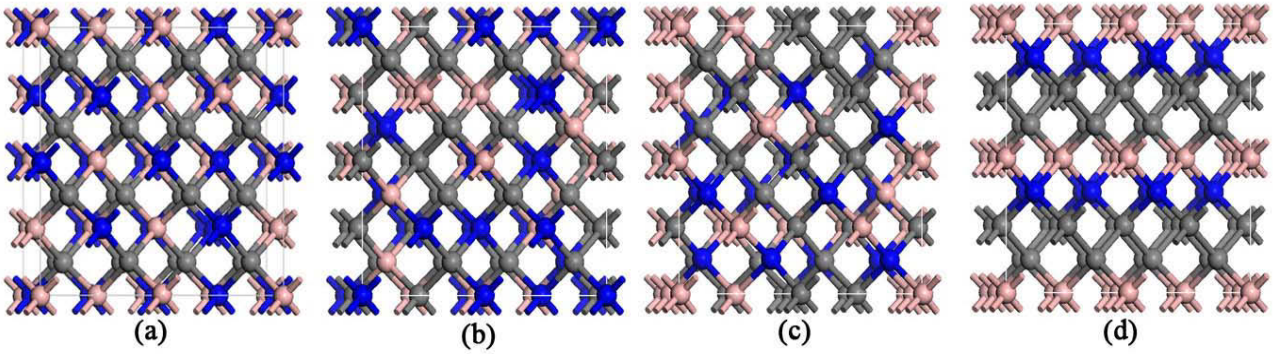

Figure 3.1.6: *Four types of c–BC_2N crystals with different structural parameter χ. (a) Str-1 with $\chi = 1$; (b) Str-2 with $\chi = 0.781$; (c) Str-3 with $\chi = 0.531$; (d) Str-4 with $\chi = 0.5$. Carbon: gray; nitrogen: blue; boron: light pink.*

Table 3.1.2. *Calculated lattice constant (a), bulk modulus (B), Young's modulus (E), Vickers hardness (H_v), and ideal tensile strength (T_s) for diamond and c–BN crystals from our calculations compared with previous experimental and theoretical results.* [a]*Ref.[24];* [b]*Ref.[98];* [c]*Ref.[29].*

Str.	a (Å)	B (GPa)	E (GPa)	H_v (GPa)	T_s (GPa)
Diamond	3.531	445	1159	94	90
Ref.	3.567[a]	443	1143[a]	96[b]	93[c]
c-BN	3.596	381	897	65	63
Ref.	3.616[a]	368[a]	889[a]	63[b]	63[c]

First, calibration calculations were performed to verify the accuracies of our

computational scheme. The results are summarized in Table 3.1.2. The deviations of both lattice constants and elastic moduli between theoretical and experimental results [24, 103] are less than 1% and 5%, respectively. Besides, Figure 3.1.7a compares the tensile strength and critical strain of diamond, c–BC_2N, and c–BN with previous theoretical work [29]. The critical strains determined from our calculations are exactly the same as those from previous works. The corresponding tensile strengths deviate by approximate 3%. Such small deviations can be attributed to the difference in the specific settings of DFT calculations. Overall speaking, our present scheme is able to reproduce previous experimental and theoretical results quite well.

Figure 3.1.7b shows stress–strain curves for the four types of c–BC_2N crystals. Distinct differences of both tensile strength and critical strain can be clearly seen, although these crystals share the same stoichiometry and the same diamond–like crystal structure. For example, for Str-1 the calculated tensile strength is 27 GPa and the critical strain is 5%. In contrast, the tensile strength for Str-4 reaches up to 77 GPa with the critical strain of 12%. In the following paragraph, the variations of tensile strength are detailedly discussed as a function of the degree of mixture χ.

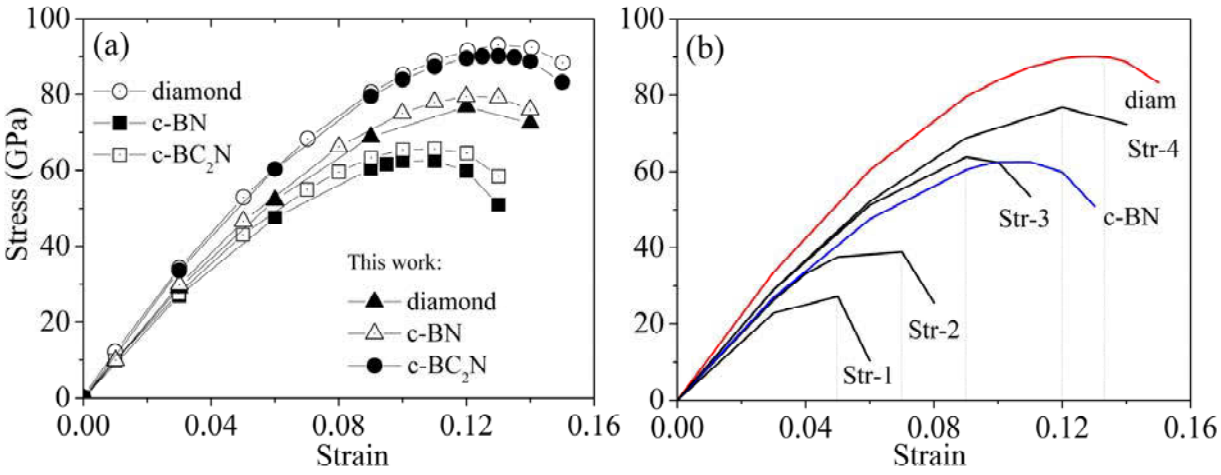

Figure 3.1.7: *Relationship of stress and strain in cubic BC_2N crystals with different degree of mixture, namely, Str-1 with χ = 1; Str-2 with χ = 0.781; Str-3 with χ = 0.531; Str-4 with χ = 0.5. The results of diamond, c–BN, and c–BC_2N (model from other publications) are also shown in Figure 3.1.7a for comparison.*

As shown in Figure 3.1.7b, Str-1 with $\chi = 1$ (without any C–C or B–N bond) collapses at a strain of 6% with an ideal tensile strength of 27 GPa. However, as χ reduces to 0.781, the tensile strength increases up to 39 GPa with the critical strain of 7%. As the parameter χ further decreases, local regions of the c–BC_2N crystal are dominated by embryos of diamond and c–BN. Both tensile strength and critical strain increase up to 64 GPa and 9%, respectively. This reveals an enhancement in the tensile capacity of c–BC_2N crystal. This is similar to the situation where nano–scale diamond and c–BN grains are embedded in a matrix of diamond–like structures [20]. Reduction of the degree of mixture to $\chi = 0.5$ in the c–BC_2N crystal (Figure 3.1.6d) further increases the tensile strength to 77 GPa and the critical strain to 12%. The relationship between χ and tensile strength for the four types of c–BC_2N crystal are shown in Figure 3.1.8. Clearly, the variations of the structural parameter χ directly result in distinct differences of the tensile strength.

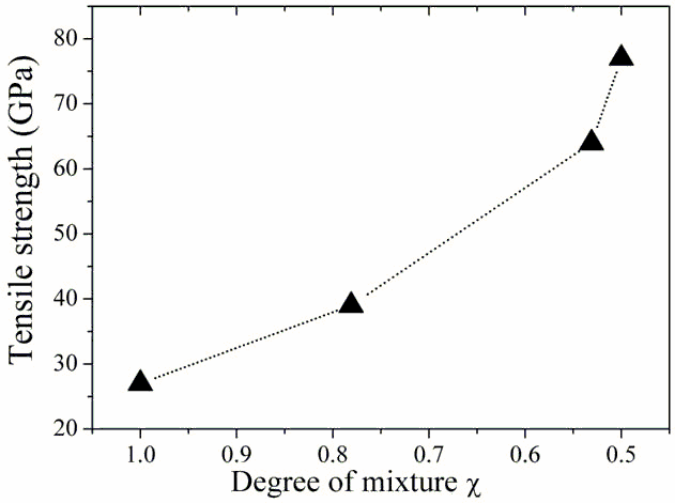

Figure 3.1.8: *Tensile strength of the four c–BC_2N crystals as a function of degree of mixture.*

The effect of the structural parameter χ on ideal strength of the c–BC_2N crystals can be summarized as follows. Larger χ means that B, C, and N atoms distribute more uniformly on the host lattice of diamond–like structures, which corresponds to the expanded lattice constant and the reduced on–site charge. Therefore, c–BC_2N crystals with uniform atomic distributions exhibit "soft" mechanical properties. On the other hand, smaller parameter χ denotes that C–C and B–N segregations emerge in partial regions in the c–BC_2N crystal lattice. They can contract the c–BC_2N lattice and then enhance the ability of resisting external loading.

Since χ can modify the ideal strength of c–BC_2N crystals, we further discuss under which conditions the structural parameter can vary. It is known that the temperature for nucleation and growth of c–BN is 250 ~ 900 ^oC [104, 105]. The temperature for diamond growth is usually located at 800 ~ 1050 ^oC [106]. By contrast, the temperature for c–BC_2N crystal growth is higher than 2000 K [18, 24]. This means that before approaching the temperature for c–BC_2N crystal growth, small domains of diamond and c–BN as prototype structures may be formed under appropriate thermodynamic fluctuations. This corresponds to small values of the structural parameter χ. Higher energetic conditions may spur B, C, and N atoms to occupy the lattice sites more randomly, forming a uniformly atomic mixing of c–BC_2N crystals with larger χ. Therefore, thermodynamic fluctuation may be responsible for the various structural parameter χ. In turn, variations of the degree of mixture χ under different synthesis conditions may account for why c–BC_2N crystals exhibit different Vickers hardness measured in experiments.

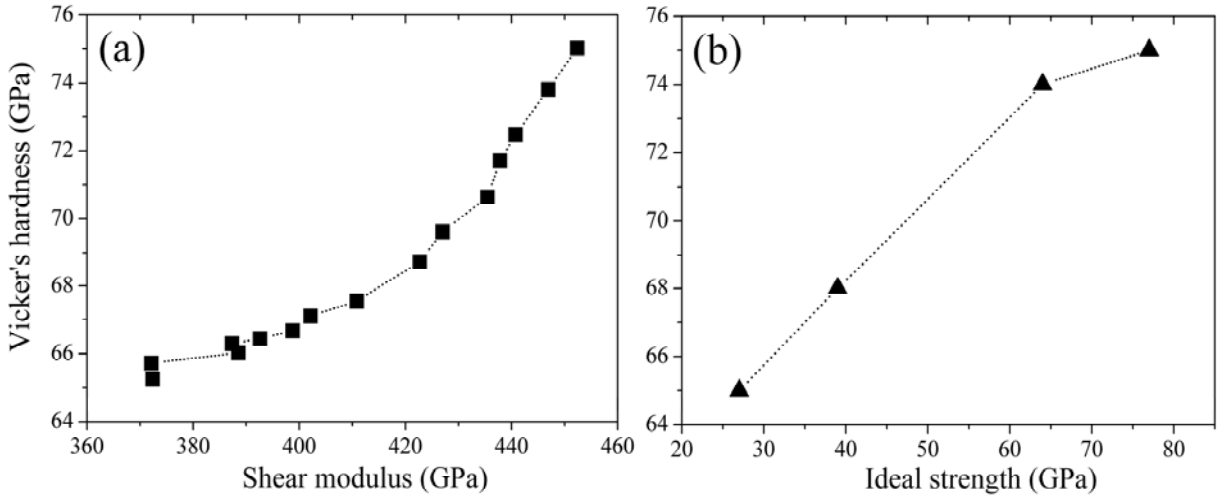

Figure 3.1.9: *Relations between hardness and shear modulus (a) and ideal strength (b) in cubic BC_2N crystals.*

3.1.3.6 Relations of Mechanical Parameters

For theoretical calculations, the mechanical parameters, bulk modulus, shear modulus, Young's modulus etc., are usually evaluated under the condition that they are based on equilibrium structural models. However, for hardness measurements, there are commonly

associated with structural deformation following the process of strain and stress under non–equilibrium conditions. Whether the relation between these mechanical parameters and hardness can be built or not is still to be investigated. Here for such kinds of cubic BC_2N crystals, we attempt to extract their correlations to check their behaviors.

Figure 3.1.9 shows the relations of hardness and shear modulus, hardness and ideal strength. It can be seen from Figure 3.1.9 that high shear modulus and ideal strength correspond to high hardness. This means that for such kinds of materials both the ideal strength and the shear modulus can give roughly evaluation of hardness. In other words, they present direct proportions even though they are not linear relations. Figure 3.1.10 shows the relationship of shear modulus, hardness, and Young's modulus. A similar trend can also be seen as that shown in Figure 3.1.9. Therefore, the empirical rule can still work in these kinds of covalent BC_2N crystals. That is, high hardness of cubic BC_2N crystals is related to high bulk modulus, shear modulus, Young's modulus, and tensile strength.

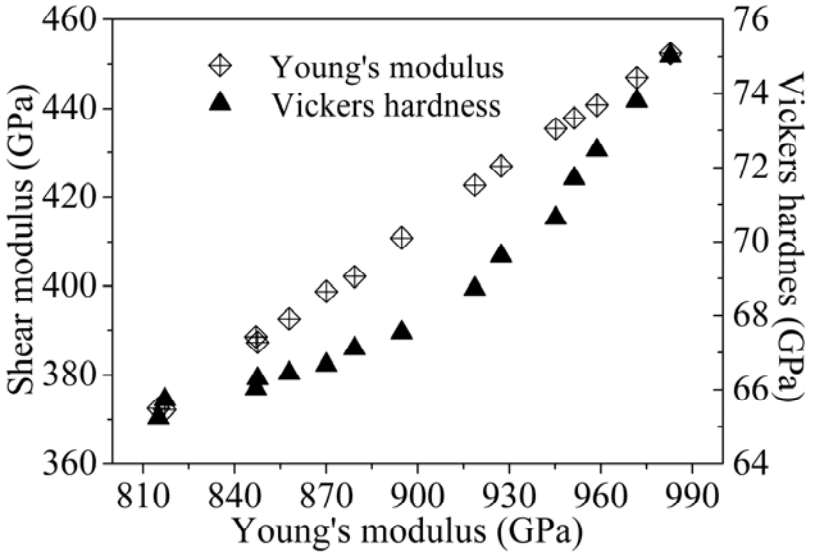

Figure 3.1.10: *Relations between shear modulus, hardness, and Young's modulus in cubic BC_2N crystals.*

3.1.4 Summary

To summarize, within a random solid solution model based on the diamond lattice, the formation energies, lattice constants, and elastic properties of BC_2N crystals were calculated

by using first–principles methods. We found that the degree of BN–C_2 mixture defined by the ratio of bond contents is the key for lattice parameter, relative stability, and physical properties in the BC_2N solid solutions. BC_2N crystals with the most probable degree of mixture possess larger lattice parameters and less elastic moduli with respect to c–BN. The high formation energy can be compensated by the contribution of configuration entropy under high–temperature conditions. The random solid solution model for c–BC_2N alloys allows nearly homogeneous mixing between the diamond and BN phases. This provides a new perspective for understanding the structure and physical properties of B–C–N systems. The experimental controversies on lattice constant and mechanical properties can be explained by different degrees of mixture, which are related to specific synthesis conditions. Considering the statistical distribution of the degrees of mixture and the contribution of configuration entropy to the free energy, c–BC_2N crystals may possess a larger lattice constant and less bulk/shear modulus with respect to c–BN. The high hardness makes this material promising in a variety of applications.

The tensile strength of c–BC_2N crystals can vary drastically from 27 GPa for a large χ = 1 to 77 GPa for a small χ = 0.5, resulting in the remarkable variation of tensile strength. It is also noteworthy that the magnitude of hardness fluctuation (~ 10 GPa) is also comparable to the experimental difference (~ 14 GPa). Thus, atomic–scale characterization of c–BC_2N crystal structures by the variations of the degree of C/BN mixture may unveil the discrepancy of the measured Vickers hardness in experiments, and uncover the obvious differences of tensile strength described in theoretical calculations.

3.2 Crystalline BC_xN Materials*

Covalent crystalline B–C–N materials, composed of B, C, and N light elements, are ranked as the potential superhard materials that can substitute for the traditional diamond and c–BN. In particular, cubic BC_2N crystals are found to have exceptionally high hardness [18]. They are taken as the second hardest materials ever known, only next to diamond. The extreme properties have attracted broad attention to explore their potential industrial applications. However, cubic BC_2N crystals are extremely difficult to obtain in practice. So far, there are only a few reports that declare the successful synthesis of such cubic crystals with measurable hardness. Nevertheless, during the process of the synthesis of cubic BC_2N phases, a common phenomenon is observed. That is, other compositions along the isoelectronic C–BN line can also be obtained. Since all these compositions are distributed along the C–BN isoelectronic line, this motived us to get the basic idea that crystalline BC_xN except for BC_2N may also be potential superhard materials. Therefore, we extended our random solid solution model from the composition BC_2N to those ones (BC_xN) that are distributed along the iso–electronic C–BN line to explore possible chemical compositions with superhard properties.

In previous experiments, crystalline BC_xN (x = 1, 2, 2.5) of cubic phase have been prepared using different techniques such as ball milling [20] and shock–compression [13]. These synthesized cubic–BC_xN solids usually possess high hardness that can be comparable to c–BN [24]. So far, little is known about those compositions with higher carbon contents (x > 2) on the isoelectronic line of BC_xN. Intuitively, incorporating a small amount of boron and nitrogen into the diamond lattice can tune its electronic properties without downgrading its superior mechanical properties remarkably [107]. Therefore, it would be interesting to study BC_xN crystals beyond BC_2N, in particular, those carbon–rich ones with $x > 2$.

For a ternary alloy mixed from two component crystals, it is often assumed that Vegard's law [108] holds for the lattice parameters and maybe also applies to physical properties. The

* Reference [1] in the list of publications

small lattice mismatch [40] of diamond and c–BN (≈ 1%) implies that the lattice parameters of c–BC_xN would satisfy Vegard's law. However, the measured lattice parameters for x = 1, 2, and 2.5 clearly deviate from the ideal mixing of diamond and c–BN [13, 18, 24]. Furthermore, bulk moduli of BC_2N and BCN crystals measured by Tkachev [25] and Knittle [24] also show distinct deviation from Vegard's predictions. These results suggest that the structures and physical properties of c–BC_xN cannot simply be understood by an ideal mixing of diamond and c–BN. Obviously, the chemical compositions and the detailed atomic arrangements [13] play a vital role. However, direct experimental determination of the atomic occupation within the crystal lattice is very difficult [13, 26]. In addition, at present crystalline BC_xN materials with large yield still have not been obtained. Thus, theoretical calculations [27, 28, 109] provide the opportunity to elucidate the structural and physical properties of c–BC_xN crystals, hopefully guiding experimental works to intentionally synthesize specific compositions that have high hardness.

Here we extended the random solid solution model from BC_2N to c–BC_xN with higher and lower carbon contents. Thus BC_xN crystals with different compositions ($0.21 < x < 19.28$) can be systematically investigated along the C–BN isoelectronic line on the ternary phase diagram. The structural stabilities, elastic and electronic properties of c–BC_xN are discussed in detail. The computational results showed that the lattice parameters and physical properties of c–BC_xN are not a linear interpolation between those of diamond and c–BN, in agreement with previous experimental [13, 18, 24] and theoretical findings [93, 110].

The random solid solution model for c–BC_xN crystals was based on the following considerations. Firstly, the structural similarities [28] and small lattice mismatch [40] between diamond and c–BN indicate the possibility of forming $(BN)C_x$ solid solution in the B–C–N systems. Secondly, the model is proposed according to experimental evidences that B, C, and N atoms are distributed evenly on the diamond lattice [10, 13, 18]. Thirdly, no B–B or N–N bond, which is highly energetically unfavorable, is allowed [13, 27, 28]. We consider nine compositions of c–BC_xN, namely, $BC_{0.21}N$, $BC_{0.46}N$, $BC_{0.91}N$, $BC_{1.37}N$, BC_2N, $BC_{2.92}N$, $BC_{4.4}N$, $BC_{8.67}N$, and $BC_{19.28}N$. Four compositions ($x < 2$) have lower carbon contents while another four ($x > 2$) have higher ones compared with that of BC_2N ($x = 2$). All these

compositions are described on a ternary B–C–N phase diagram in Figure 3.2.1 to give a direct impression where they are located.

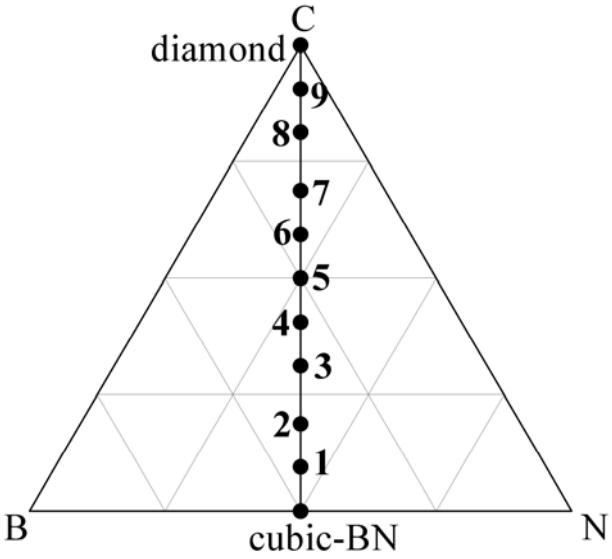

Figure 3.2.1: *Distribution of the nine investigated compositions of c–BC_xN crystals along the C–BN isoelectronic line. Numbers 1–9 represent $BC_{0.21}N$, $BC_{0.46}N$, $BC_{0.91}N$, $BC_{1.37}N$, BC_2N, $BC_{2.92}N$, $BC_{4.4}N$, $BC_{8.67}N$, and $BC_{19.28}N$, respectively. The positions of diamond and c–BN are also shown.*

A series of 64–atoms supercell structures, based on the random solid solution model, were constructed by randomly substituting boron and nitrogen atoms for carbon in the diamond lattice to meet the BC_xN stoichiometry and the basic bonding rule (no B–B and N–N bonds) [93]. For each composition, a number of random configurations can be obtained, in which the BN and C crystals are mixed in different fashions. They are classified by the degree of mixture for all these generated structures. In principle, there are many possible choices of χ. For each composition, we have counted the statistical distribution of χ from a large number of random configurations (2.5×10^6) and determined the most probable χ values for different compositions (shown in Figure 3.2.2).

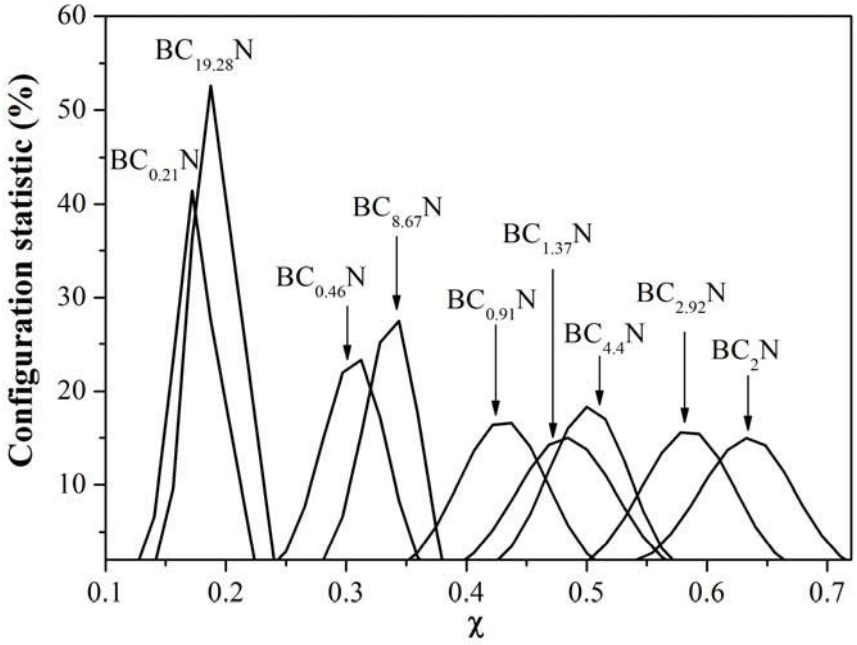

Figure 3.2.2: *Configuration statistics of the nine compositions of c–BC_xN crystals along the C–BN isoelectronic line.*

Starting from the random solid solution structures with the most likely χ constructed for each BC_xN crystal ($0.21 < x < 19.28$), first–principles calculations have been performed using density functional theory (DFT) and the plane–wave basis and pseudopotential techniques implemented in the CASTEP program [94, 111]. The ion–electron interaction was described by norm–conserving pseudopotentials [112]. A cutoff of 1000 eV was used for the plane–wave basis to ensure converge of total energy and stress. The exchange–correlation interaction was described by the PW91 functional in the generalized gradient approximation (GGA) [113]. During the geometry optimization and elastic constant calculations, the Brillouin zone of the reciprocal space was sampled by a 2 × 2 × 2 **k**–point mesh, and the **k**–point mesh was increased to 4 × 4 × 4 to compute the electronic structures and band gaps.

The lattice parameters, bulk moduli, shear moduli, and electronic band gaps for diamond and c–BN crystals from our calculations are compared with the experimental data in Table 3.2.1. Our theoretical calculations underestimate the lattice constants by about 0.5% to 1%. The deviation between theory and experiment is within 3% for the elastic moduli. For each composition of c–BC_xN, three representative structures (with the most probable χ) were

studied. The average results for the three systems are used to avoid fluctuations due to the arbitrary choice of random configurations.

Table 3.2.1. *Lattice constants a_0 (Å), bulk moduli B (GPa), shear moduli G (GPa), and band gaps (eV) of diamond and c–BN from previous experiments and present theoretic calculations.* [a]*Ref.[24];* [b]*Ref.[103];* [c]*Ref.[93].*

		Lattice constant	Bulk modulus	Shear modulus	Band gap
diamond	Theo.	3.531	444	544	4.68
	Expt.	3.567[a]	443[a]	534[b]	5.5[c]
c-BN	Theo.	3.596	378	399	4.86
	Expt.	3.617[a]	368[a]	405[b]	6.1[c]

3.2.1 Crystal Structure and Stability

In each cubic BC_xN crystal, the carbon mass content C% can be related to the stoichiometry x as following:

$$C\% = \frac{x \cdot M_C}{M_B + x \cdot M_C + M_N} \times 100\% , \qquad (3.2.1)$$

where M_B, M_C, and M_N is the mole mass of boron, carbon, and nitrogen atoms, respectively. Figure 3.2.3 shows the computed formation energy as a function of C%. One can see that all c–BC_xN crystals have positive formation energy. In other words, they are all metastable structures and they can be separated into two phases (diamond and c–BN) [11, 12, 27, 93]. Starting from the c–BN, the formation energy first increases with C% and approaches a maximum value of 0.58 eV/atom at the middle composition of BC_2N. Then, it gradually drops towards zero at the diamond limit in the carbon–rich region (x > 2). Hence, the formation of c–BC_2N crystal is the most difficult from the thermodynamic point of view. Since the most difficult one (BC_2N) can be successfully obtained in experiments, then the other compositions beyond BC_2N should, in principle, also be obtained. Comparing the formation energy of the carbon–poor compositions with those carbon–rich ones, i.e., c–$BC_{0.21}N$ vs. c–$BC_{19.28}N$, c–$BC_{0.46}N$ vs. c–$BC_{8.67}N$, c–$BC_{0.91}N$ vs. c–$BC_{4.4}N$, and c–$BC_{1.37}N$ vs. c–$BC_{2.92}N$, the former ones are slightly more stable because of lower formation energies. This suggests that the incorporation of a small amount of carbon into BN crystal is easier than the inverse process.

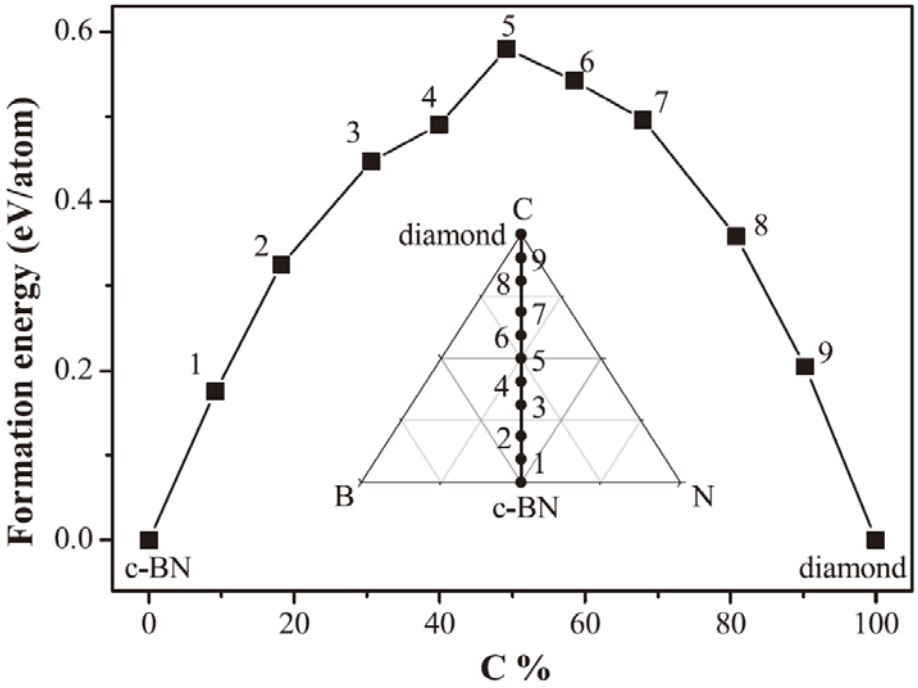

Figure 3.2.3: *Formation energies of c–BC_xN crystals as a function of the C%. The digits 1–9 represent the compositions of c–$BC_{0.21}N$, c–$BC_{0.46}N$, c–$BC_{0.91}N$, c–$BC_{1.37}N$, c–BC_2N, c–$BC_{2.92}N$, c–$BC_{4.4}N$, c–$BC_{8.67}N$, and c–$BC_{19.28}N$, respectively. Insert plot: location of the nine compositions along the C–BN isoelectronic line on the B–C–N ternary phase diagram.*

The relationship between the lattice parameters and the carbon content C% is shown in Figure 3.2.4. For BC_xN crystals with $x \leq 2$, the theoretical lattice parameters are larger than that of c–BN. This lattice expansion effect can be related to the weakening of ionicity of the original BN crystal. From the Mulliken analysis of our calculations, the amount of charge transfer between boron and nitrogen is 0.64 electrons for the pure c–BN crystal, while the amount of charge transfer reduces with increasing carbon content and it is about 0.44 electrons for BC_2N.

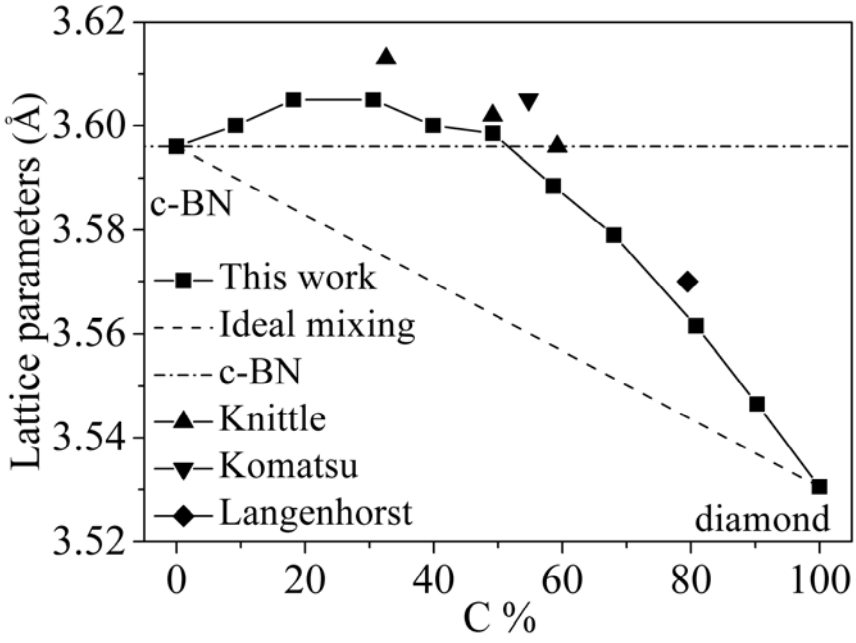

Figure 3.2.4: *Lattice parameters for c–BC_xN with x = 0.21, 0.46, 0.91, 1.37, 2, 2.92, 4.4, 8.67, and 19.28 as a function of the C%. The dash line represents the ideal mixing by Vegard's law. The dash–dotted line represents the lattice constant of c–BN. Some previous experimental values are also shown for comparison [13, 24, 114].*

Obviously, the lattice parameters for all BC_xN compositions are away from Vegard's line by ideal mixing of diamond and c–BN, but in excellent agreement with experimental observations. For example, the measured lattice parameters [24] for the composition of $C_{0.6}(BN)_{0.4}$, $C_{0.5}(BN)_{0.5}$, and $C_{0.33}(BN)_{0.67}$ were 3.596 ± 0.003 Å, 3.602 ± 0.003 Å, and 3.613 ± 0.003 Å, respectively. The corresponding theoretical values are 3.604 Å, 3.599 Å, and 3.588 Å, with discrepancies to experiment by only 0.25%, 0.01%, and 0.21%, respectively, while the 2σ value of the experimental accuracy is 0.17%. For the $BC_{2.5}N$ and BC_8N crystals, the theoretical lattice constants are 3.593 Å and 3.563 Å, respectively. They are slightly lower than the experimental values [13, 114] of 3.605 Å and 3.57 Å by only 0.33% and 0.2%.

3.2.2 Mechanical Properties

Figure 3.2.5 shows the theoretical bulk and shear moduli as functions of C%. Again, both curves deviate from those of ideal mixing, indicating that bulk and shear moduli of c–BC_xN are not simple interpolations of those of diamond and c–BN. The computed bulk/shear

modulus for BC_xN crystal first decreases with C% monotonically from diamond to $BC_{1.37}N$ (C% = 39.9%). Then it drops rather slowly (with some weak oscillations) to BCN (C% = 32.6%). Finally, it rises to the value of c–BN. Along the C–BN isoelectronic line in the ternary phase diagram, there is no local maximum of either bulk or shear modulus.

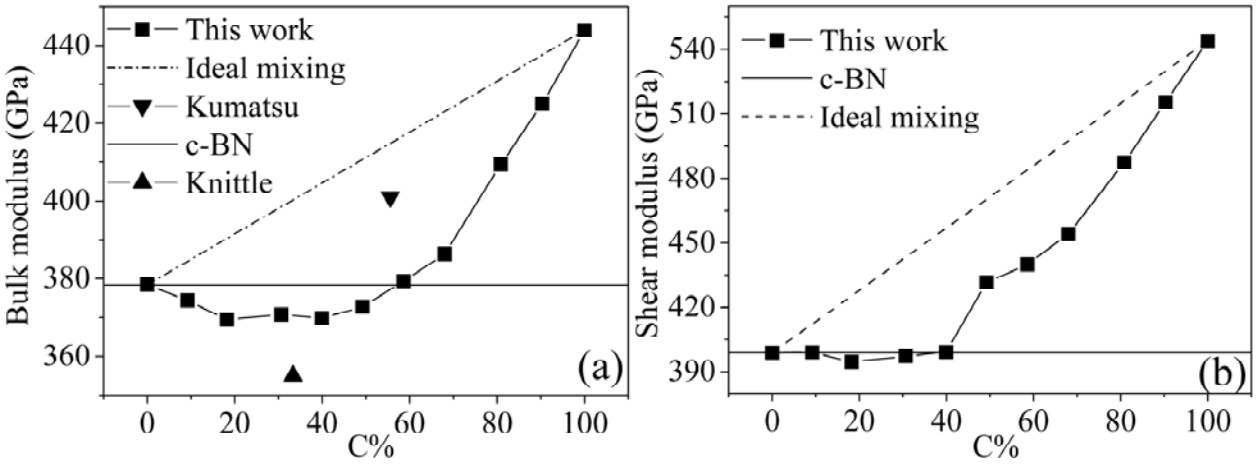

Figure 3.2.5: *(a) Bulk modulus and (b) shear modulus of c–BC_xN crystals (x = 0.21, 0.46, 0.91, 1.37, 2, 2.92, 4.4, 8.67, and 19.28) as a function of C%. The dashed lines represent the ideal mixing of diamond and c–BN by Vegard's law. The black lines represent that of c–BN. Some previous experimental values are also shown for comparison [13, 24].*

In general, BC_xN crystals with $x < 2$ have similar bulk modulus as that of BC_2N, while the shear modulus for BC_xN crystals with $x < 2$ shows observable lower than that of BC_2N. BC_xN crystals with $x > 2$ have higher bulk and shear modulus than that of BC_2N. This means that BC_xN crystals with $x > 2$ are harder than BC_2N. Please note that the previous publication has already declared that the cubic BC_2N crystal is the second hardest materials ever found. We also show in the last section that the hardness has some direct relations with bulk and shear modulus. Therefore, we expect that BC_xN crystals with $x > 2$ should also have higher hardness than BC_2N. This is even encouraging finding because there are some new BC_xN crystals: (I) they are easier to be formed according to the formation energy comparing with that of BC_2N; (II) they are harder than BC_2N, which is declared as the second hardest material. Unfortunately, the calculated hardness is not as we expected (as shown in Figure 3.2.6). But still amazingly, the hardness of the composition BC_2N is lower than that of the other compositions.

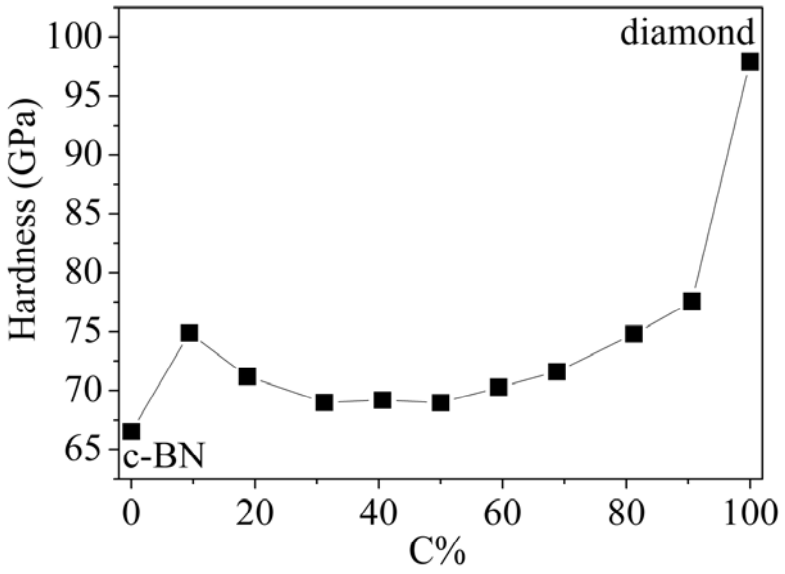

Figure 3.2.6: *Hardness of the nine cubic BC_xN as a function of carbon content. The values of diamond and c–BN are also shown for comparison.*

In a previous experiment by Knittle et al. [24], the bulk modulus of BCN was 355 ± 19 GPa. It is close to our theoretical value of B = 370.1 GPa for $BC_{0.91}N$. For BC_2N, our theoretical bulk modulus is 372.7 GPa, lower than that of c–BN (B = 378.4 GPa). For comparison, Solozhenko et al. [18] obtained an even lower bulk modulus of 259 ± 22 GPa in experiments. As shown in Figure 3.2.5, incorporating little amount of carbon (boron/nitrogen) atoms into the c–BN (diamond) lattice effectively reduces the hardness of the host lattice. Compared to the BC_2N crystal, our present theoretical results suggest that the carbon–rich BC_xN materials ($x > 2$) possess better mechanical properties and are easier to be formed. On the contrary, even with lower formation energies, the compositions on the carbon–poor side are less attractive due to the lower elastic modulus (see Table 3.2.2 and Figure 3.2.3). In experiment, synthesis of cubic BC_8N phase has been reported under high–temperature and long–annealing conditions [114]. According to the present theoretical results, we anticipate the experimental preparation of other BC_xN compositions with higher carbon contents, which are promising as candidate superhard materials with higher chemical stability with regard to diamond.

Table 3.2.2. *Carbon contents (C%), most probable degree of mixture (χ), lattice parameters, formation energies, bulk moduli (B), and shear moduli (G) for cubic BC_xN crystals with x =*

0.21, 0.46, 0.91, 1.37, 2, 2.92, 4.4, 8.67, and 19.28.

	$BC_{0.21}N$	$BC_{0.46}N$	$BC_{0.91}N$	$BC_{1.37}N$	BC_2N	$BC_{2.92}N$	$BC_{4.4}N$	$BC_{8.67}N$	$BC_{19.28}N$
C %	9.2	18.2	30.6	39.9	49.2	58.6	68.0	80.8	90.3
χ	0.172	0.313	0.438	0.484	0.625	0.578	0.5	0.344	0.188
a_0	3.600	3.603	3.603	3.600	3.599	3.589	3.579	3.561	3.547
E_f	0.18	0.32	0.45	0.49	0.58	0.54	0.5	0.36	0.2
B	374.4	369.5	370.1	369.8	372.7	379.4	386.4	409.4	425
G	399.1	394.6	397.3	399.2	431.6	440	454.1	487.4	515.5

3.2.3 Electrical Properties

Compared with the experimental values of c–BN (6.1 eV) and diamond (5.5 eV) [93], the calculated band gaps for c–BN (4.86 eV) and diamond (4.68 eV) are lower by about 20% and 15%, respectively. The underestimation of band gap is a well–known deficiency of standard DFT methods, mainly due to the self–interaction–error. However, this systematical error should not affect the variation behavior of the band gap due to the effects of crystal structure and composition. The calculated band structures for all c–BC_xN crystals show a direct band gap with both the conduction–band minimum and the valance–band maximum at the Γ point. Figure 3.2.7 displays the variations of band gap for BC_xN crystals with different compositions.

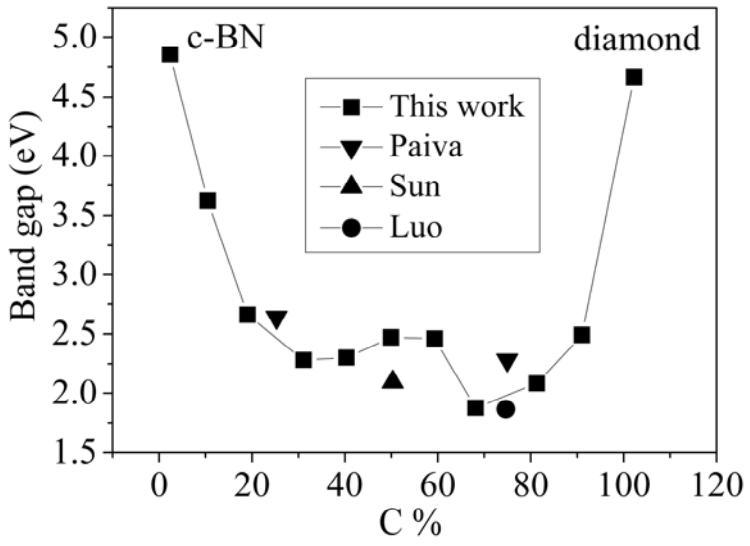

Figure 3.2.7: *Band gap as a function of the C% for c–BC_xN crystals (x = 0.21, 0.46, 0.91,*

1.37, 2, 2.92, 4.4, 8.67, and 19.28). Previous theoretical values are also shown for comparison [28, 109, 115].

The gaps for all BC_xN crystals are significantly lower than those of diamond and c–BN. Except for $BC_{0.21}N$ with the band gap of 3.72 eV, the band gaps for most of the BC_xN crystals lie between 2 eV and 3 eV, showing some composition–dependent variations. This is obviously away from the prediction of Vegard's law, which was found to be valid for many other ternary alloys like Cd–Zn–Te [116, 117], Ga–As–N [118], and In–Ga–As [119]. The present results are in accordance with a previous calculation of the cubic $(BN)_xC_{2(1-x)}$ by Lambrecht et al. [93]. They argued that the contribution of the C component to the valance–band maximum and the B component to the conduction–band minimum results in gap reduction. Pasva and Azevedo [115] also observed a similar effect of gap narrowing in the ordered $(BN)_xC_{2(1-x)}$ alloys. Further analysis of the electronic density of states revealed that the valance–band maximum and conduction–band minimum are mainly contributed by the carbon and boron atoms, respectively, in agreement with previous studies [93, 115]. Such significant narrowing of band gap implies a tunable band gap via controlling the composition, which makes these BC_xN alloys useful for optoelectronic applications.

3.2.4 Summary

To sum up, inspired by the successful application of the random solid solution model on c–BC_2N crystal, we extended our model from BC_2N to BC_xN ($0.21 < x < 19.28$) alloys along the C–BN isoelectronic line. Their structural stabilities, mechanical and electronic properties were systematically studied. The computed lattice parameters and bulk moduli are consistent with available experimental data. Significant deviations of structural and physical parameters from Vegard's law indicate that BC_xN alloys are not simply the linear interpolation of diamond and c–BN via ideally mixing. The bulk and shear moduli of c–BC_xN are evidently lower than those of diamond, revealing that a superhard phase does not exist on the C–BN isoelectronic line. Nevertheless, the carbon–rich BC_xN crystals may still be attractive due to their better structural stabilities and mechanical properties with regard to the intensively investigated c–BC_2N. Outside the C–BN isoelectronic line, we expect that the ternary alloys

along the BN–C_3N_4 line may also lead to new superhard materials. The computed band gaps are substantially lower than those of diamond and BN. Compared with BC_2N, the BC_xN solids with higher carbon content ($x > 2$) exhibit better structural stability and higher elastic moduli, making them more attractive as potential superhard materials.

3.3 Crystalline $B_xC_yN_z$ Materials*

Crystalline BC_2N materials have attracted great interest due to their extreme hardness. They are declared to be comparable to c–BN or even higher than c–BN, only behind diamond. However, our theoretical results shown in the last section indicate that cubic BC_2N crystals are actually not the second hardest material. The crystalline BC_xN, especially those with $x > 2$, has higher hardness than cubic BC_2N crystals. Unfortunately, only a few compositions, i.e. BC_4N, BC_6N, and BC_8N, are obtained in the form of crystalline phases in experiments. Furthermore, indenter cannot be performed to measure their hardness because large bulk materials of these compositions have not been successfully produced so far.

At present, almost all crystalline B–C–N ever synthesized are distributed along the C–BN isoelectronic line in the phase diagram. Beyond the isoelectronic line, little is known about the structural and mechanical properties of crystalline B–C–N materials. In the last section, we have shown that the extension of our model from BC_2N to BC_xN along the C–BN isoelectronic line. Even harder compositions than BC_2N can be obtained. This reminds us that the compositions $B_xC_yN_z$ beyond the C–BN isoelectonic line may also contain some novel crystalline phases with super hardness. Therefore, it is worth to explore the unknown chemical compositions beyond the C–BN isoelectronic line. In addition, several discovered superhard phases, diamond, c–BN, c–BC_5, β–C_3N_4, as shown in Figure 3.3.1, are all located in the ternary B–C–N phase diagram. Their hardness shows no clear trend. It is the irregular distribution of hardness that simulates us to explore the compositions beyond the C–BN isoelectronic line in the ternary B–C–N phase diagram.

* Reference [8] in the list of publications

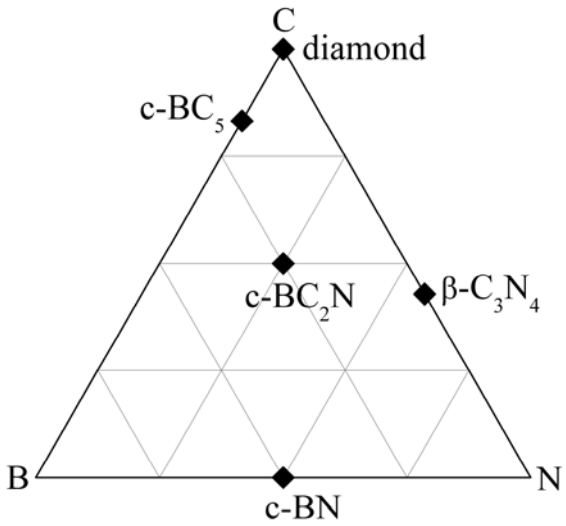

Figure 3.3.1: *Some superhard phases that have been successfully synthesized in experiments or predicted by theoretical calculations in the ternary B–C–N phase diagram.*

At present, it is still challenging to synthesize such materials in a wider compositional range in experiments. Such intractable problems can be tackled by atomistic simulation based on first–principles approaches. So far, there have already been some theoretical efforts devoted to the crystalline $B_xC_yN_z$ phases. However, almost all of these works focus on BC_xN compositions along the C–BN isoelectronic line [32]. For other compositions considered in previous works, they usually possess layered [120, 121] or tetragonal [121] crystal structures rather than diamond–like ones. Consequently, they have lower hardness values with regard to the sp^3 diamond–like phases. Here based on diamond–like structure, B–C–N compositions in a wider range are considered in the phase diagram, aiming to discovering potential superhard phases beyond the C–BN isoelectronic line. Besides, the thermodynamic stabilities of these compositions are also investigated, giving a general picture of the distributions of phase stability in the ternary B–C–N phase diagram.

3.3.1 Structural Model and Selected Area

The 64–atom supercell of diamond lattice is taken as the template for crystalline B–C–N systems. Then, certain numbers of C atoms in the 64–atom supercell C are randomly substituted by B and N atoms to meet the stoichiometry of $B_xC_yN_z$. Obviously, the current diamond–based template is not suitable for modeling those compositions with too high B and

N contents. This is because of the intrinsic difference in the structures and chemical bonding between the elementary carbon (diamond phase) and boron or nitrogen solids. Basically, B–C–N compositions near the vertex angle of pure boron should be based on the main structure of pure boron. However, the genuine structure of boron has still not been determined so far. Therefore, these compositions cannot be considered based on our models. For the vertex angle of pure nitrogen, to the best of our knowledge there is no stable structure for pure nitrogen solid at normal pressure. Thus these compositions can also not be achieved. For the vertex angle of pure carbon, there are so many different types of crystal such as diamond, graphite, graphene, and carbon tubes. Among them, the most expected one is the diamond, the hardest one. That is why the diamond structure is used as the template to investigate B–C–N systems.

Here we mainly focus on the carbon–rich compositions in which both B and N contents are less than 35 at.%, corresponding to the upper rhombus in the ternary B–C–N phase diagram. More specifically, we divided the XYZ axis of the B–C–N phase diagram by a proportion of 5%. A series of intersections were generated in the phase diagram, as shown in Figure 3.3.2. Within the upper rhombus of the phase diagram, the compositions located at each intersection were selected for first–principles calculations. Those compositions outside the intersections can be approximated by weighted average from the neighboring intersections.

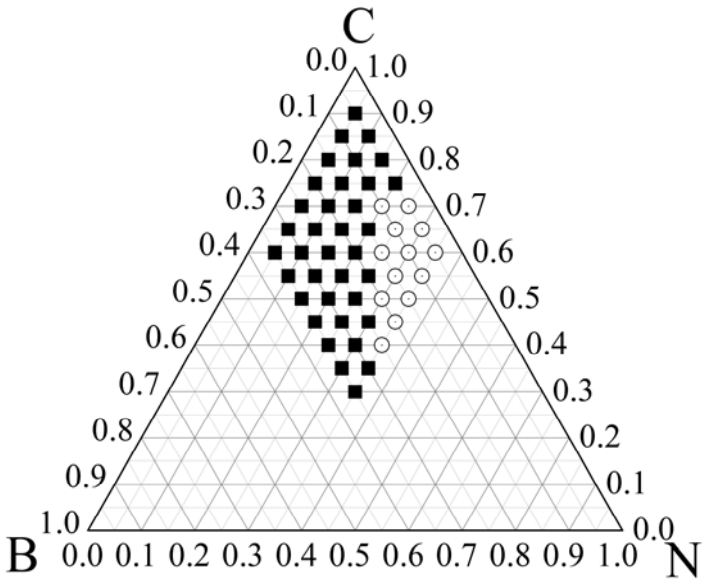

Figure 3.3.2: *Compositions located at each intersection were selected for first–principles calculations as indicated by solid square circles and hollow circles. The compositions denoted by hollow circles are the ones that their structures are seriously deformed after geometrical optimization. Therefore they are not considered as further mechanical calculations.*

In principle, there are a huge number of random configurations for each composition after randomly replacing C atoms with B or N. the degree of mixture χ is used to classify all these possible structures. For each composition, the supercell structures were constructed according to the most probable χ values selected from statistic distribution of 2×10^6 random configurations.

3.3.2 Structure Transformation

Upon optimization, some of the B–C–N crystals are not able to retain the initial sp^3 diamond–like lattices. They transform into layered graphite–like structures. In other words, these cubic structures are not stable for these compositions. One representative layered structure after optimization is shown in Figure 3.3.3a. On the upper rhombus in the ternary B–C–N phase diagram, there are totally thirteen such intersection points which prefer layered structures rather than cubic diamond lattice. These compositions locate on the N–rich area, the right side of C–BN isoelectronic line. In other words, the present theoretical results indicate that superhard B–C–N cubic phase with sp^3 hybridization cannot be synthesized in certain nitrogen–rich composition region. That is why it is challenging to obtain N–doped diamond because doping nitrogen into diamond usually destroys its structure. In addition, experimentally synthesized crystals (like BC_3N and BC_8N [114], BC_2N [29]) fall in the range of the rest thirty–six composition points with stable cubic lattice structures (Figure 3.3.2).

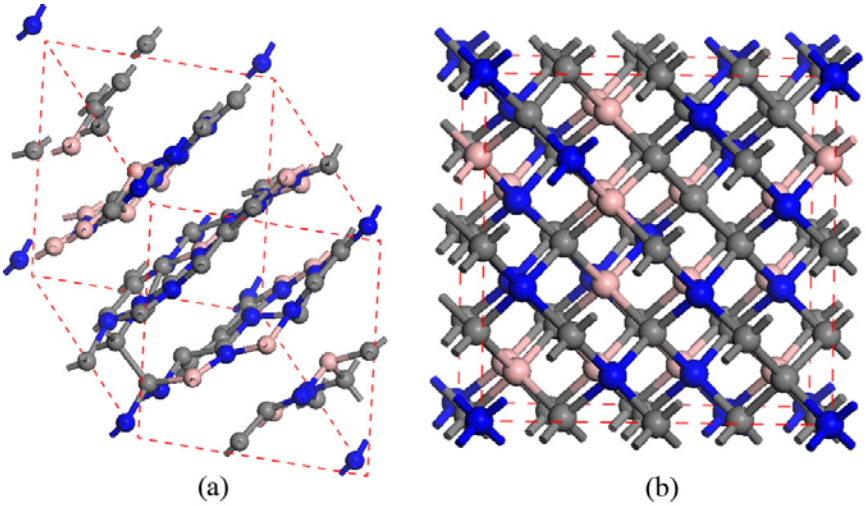

Figure 3.3.3: *Representative structures of B–C–N crystals after geometry optimization. (a): $B_6C_{45}N_{13}$ with layered structure; (b): $B_6C_{52}N_6$ with diamond–like cubic structure. Boron: pink; carbon: grey; nitrogen: blue.*

3.3.3 Lattice Parameter and Structural Stability

3.3.3.1 Lattice Constant

The predicted lattice constants for $B_6C_{52}N_6$ (3.563Å) agree with the nearby composition of BC_8N (3.572 Å) [114], a cubic phase obtained in experiments. Besides, the lattice constants of B–C–N crystals within the range of our investigations are shown in Figure 3.3.4 as a function of C at.% with diverse fixed boron and nitrogen concentrations. In general, the lattice constant increases as the carbon content increases for the compositions with the boron content fixed (Figure 3.3.4a). Furthermore, compositions with higher boron content correspond to larger lattice constant. For example, the lattice constant shows near the linear trend as a function of carbon content for the compositions with the boron content fixed at 35 at.%. This is easily to be understood since the atomic radius of boron is larger than that of carbon and nitrogen atoms. If there are higher boron contents in B–C–N crystals, the lattice constant can be expanded. But if the boron concentration is low, the linear trend is not clear, especially at the range of the low carbon content.

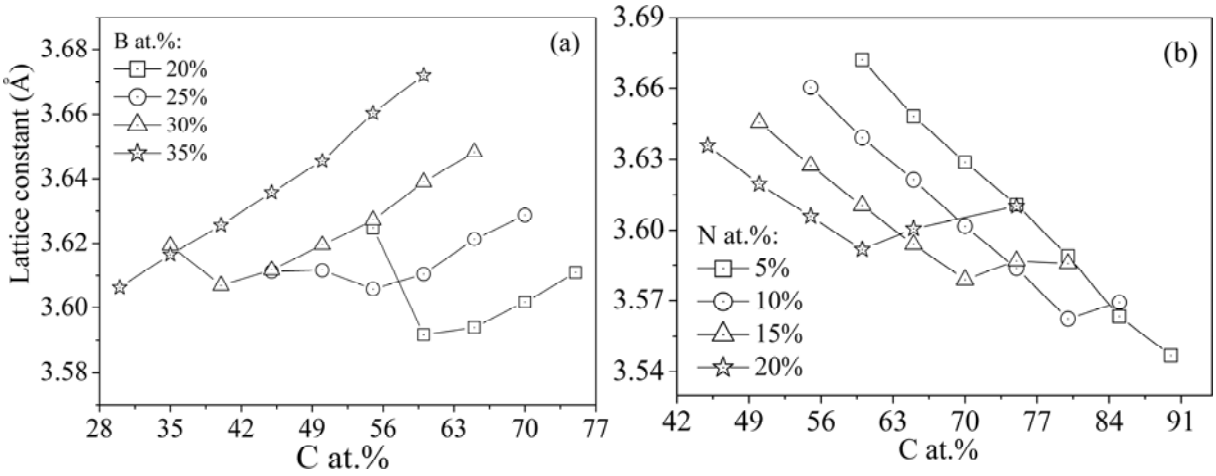

Figure 3.3.4: *(a) Lattice constant as a function of C content in the B–C–N crystals with fixed B content of 20 at.%, 25 at.%, 30 at.%, and 35 at.%; (b) Lattice constant as a function of C content in the B–C–N crystals with fixed N content of 5 at.%, 10 at.%, 15 at.%, and 20 at.%.*

If the nitrogen concentration is fixed, the relation between the lattice constant and the C% shows the opposite trend comparing with that shown in Figure 3.3.4a. As shown in Figure 3.3.4b, compositions with higher nitrogen concentration correspond to smaller lattice constant. As well, the linear trend becomes weaker as the fixed nitrogen content is higher. In contrast, the linear trend is clear as the nitrogen concentration is low. For example, for the compositions with the nitrogen content fixed at 5 at.%, the lattice constant shows nearly linear decrement as the carbon content increases. This indicates that the boron and the nitrogen play the opposite role in affecting the lattice constant. This is probably because of the different atomic radius among B, C, and N atoms.

3.3.3.2 Formation Energy

The formation ability of a crystal $B_xC_yN_z$ solid with given composition can be related to its formation energy (E_f), which is defined by:

$$E_f = E_{B_xC_yN_z} - (xE_{\alpha-B_{12}} + yE_{graphite} + zE_{N_2})/(x+y+z), \quad (3.3.1)$$

where $E_{B_xC_yN_z}$, $E_{(\alpha-B_{12})}$, E_{N_2}, and $E_{graphite}$ denote the total energy per atom for $B_xC_yN_z$ solid, α–B_{12} crystal, gaseous N_2 molecule, and crystalline graphite, respectively. By definition, negative E_f means that the formation of this system is exothermic, whereas positive E_f

corresponds to endothermic formation.

On the B–C–N ternary diagram, the computed formation energies of the crystalline B–C–N solids exhibit similar trend as the amorphous B–C–N solids, despite the absent composition points with layered structures. Compared with other composition, the compositions within the area of B: 15 ~ 35 at.%; C: 30 ~ 55 at.%; N: 15 ~ 35 at.% are easier to form. It is noteworthy that the experimentally synthesized BC_2N and $BC_{2.5}N$ compositions [15] are inside this area, which provides a sound support of our theoretical prediction. Furthermore, the compositions in the area with relatively lower formation energy should be the target compositions for the future experimental synthesis of BCN crystals.

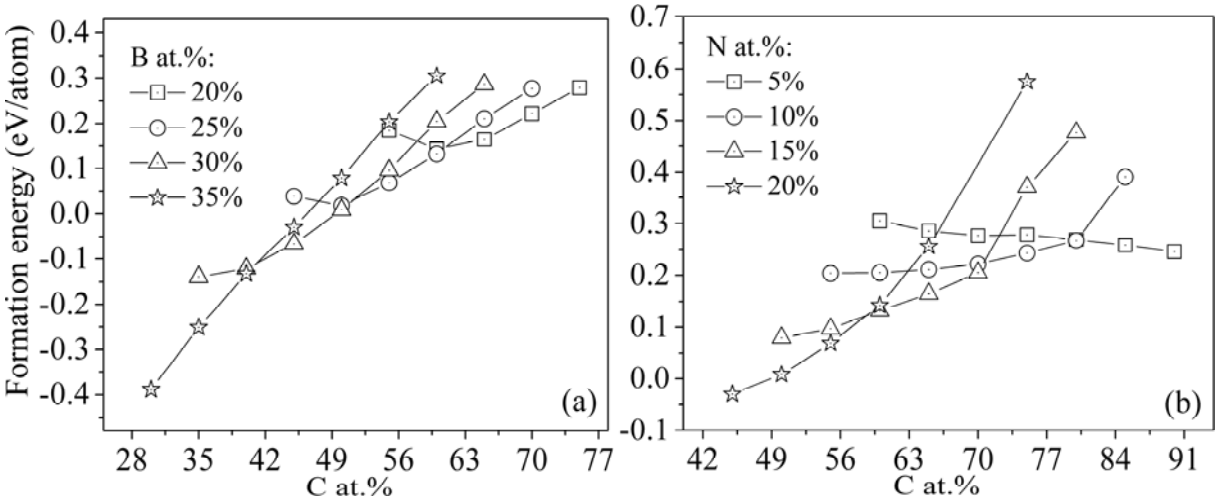

Figure 3.3.5: *(a) Formation energy as a function of C content in the B–C–N crystals with fixed B content of 20 at.%, 25 at.%, 30 at.%, and 35 at.%; (b) formation energy as a function of C content in the B–C–N crystals with fixed N content of 5 at.%, 10 at.%, 15 at.%, and 20 at.%.*

The dependence of formation energy on the B, C and N contents is displayed in Figure 3.3.5. As shown in Figure 3.3.5a, the formation energy of the compositions rises as the C content increases, whereas the B contents have only little influence. The dependence of formation energy on the N content is different. We can see from Figure 3.3.5b that the formation energy increases substantially as the C content rises for 20 at.% of N. However, the upward trend becomes less remarkable as the N content increases. When the N content reaches 5 at.%, the formation energy remains steady no matter how the C content varies.

3.3.4 Mechanical Parameters

3.3.4.1 Young's Modulus

Young's modulus is one of the most important mechanical properties of a material. It describe the ability of the elastic deformation of materials, and it has a nearly linear dependence with the Vickers hardness (H_v) for covalent solids [122, 123]. The isotropic Young's modulus can be evaluated by bulk modulus and shear modulus using the following formula:

$$E = 9BG/(3B+G)\,. \tag{3.3.2}$$

Similar to the case of amorphous B–C–N solids [122], our theoretical results reveal that the compositions with relatively higher value of Young's modulus mainly locate along the C–BN isoelectronic line on the phase diagram. Among all composition considered, the one with highest carbon content near the C vertex of ternary phase diagram possess highest Young's modulus of 1141 GPa. The c–BC_2N composition, which attracted great attention during the past decade, owns a Young's modulus of 924.9 GPa, rather close to the experimental data of 980 GPa [97].

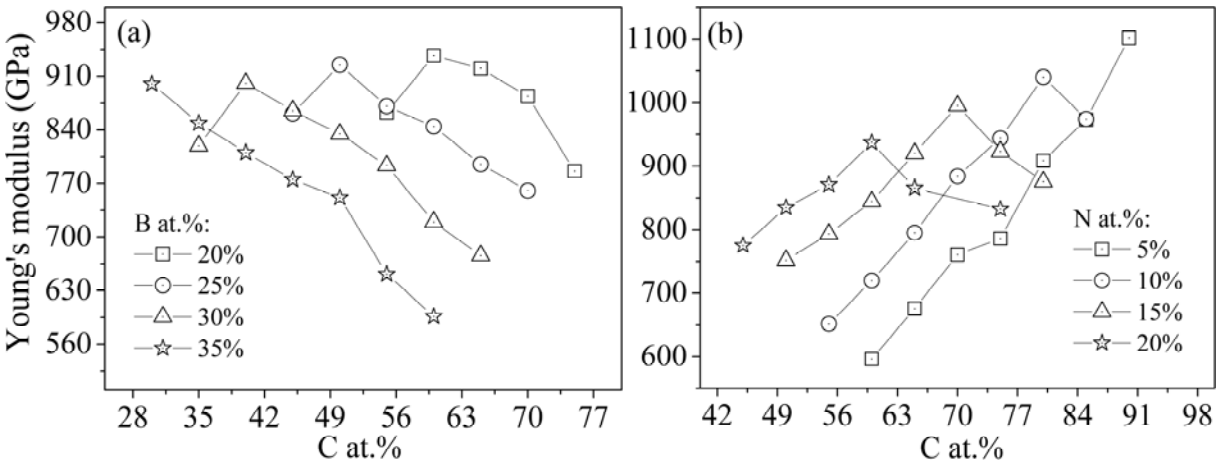

Figure 3.3.6: *(a) Young's modulus as a function of C content in the B–C–N crystals with fixed B content of 20 at.%, 25 at.%, 30 at.%, and 35 at.%; (b) Young's modulus as a function of C content in the B–C–N crystals with fixed N content of 5 at.%, 10 at.%, 15 at.%, and 20 at.%.*

The detailed variation of Young's modulus with B, C and N contents is depicted in Figure

3.3.6. One can see from Figure 3.3.6a that the Young's modulus show declined trend as the C content increases. The compositions with higher B content possess lower Young's modulus. On the contrary, for a given N content the Young's modulus rises with increasing carbon content (see Figure 3.3.6b). The N–richer compositions correspond to higher Young's modulus. In previous experiment [124], it was shown that the N–rich system like BC_3N_3 would transform into tetrahedral and rhombohedral structures rather than the diamond–like cubic one, although its mechanical properties like bulk modulus (405.3 GPa for rh–BC_3N_3) are excellent.

3.3.4.2 Bulk Modulus

Figure 3.3.7 shows the variations of bulk modulus as a function of carbon content with relative to different boron and nitrogen fractions in c–$B_xC_yN_z$ crystals. If the boron content in c–$B_xC_yN_z$ crystals is fixed (Figure 3.3.7a), the overall trend for bulk modulus roughly increases as the carbon fraction increases. For c–$B_xC_yN_z$ crystals with the same carbon content, higher boron content corresponds to larger bulk modulus when the carbon content is lower than 60 at.%. But if the carbon content is higher than 60 at.%, the bulk modulus presents the opposite trend, that is, higher boron content is related to lower bulk modulus. This is probably because the boron content dominates the bulk modulus of c–$B_xC_yN_z$ crystals with low carbon content. When c–$B_xC_yN_z$ crystals have high carbon content, the carbon content takes over the role to dominate the bulk modulus.

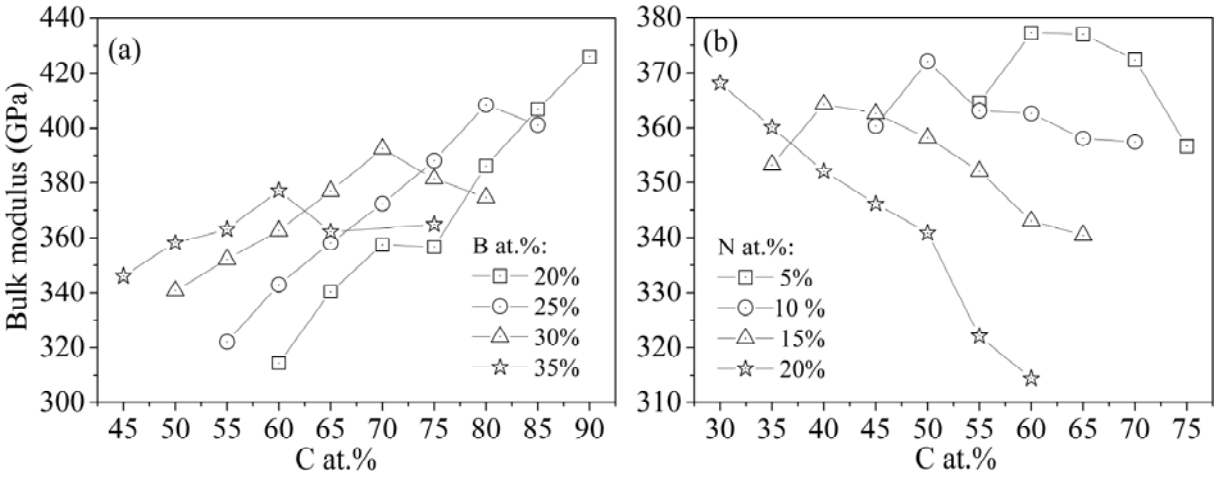

Figure 3.3.7: *(a) Bulk modulus as a function of C content in the B–C–N crystals with fixed B*

content of 20 at.%, 25 at.%, 30 at.%, and 35 at.%; (b) Bulk modulus as a function of C content in the B–C–N crystals with fixed N content of 5 at.%, 10 at.%, 15 at.%, and 20 at.%.

As shown in Figure 3.3.7b, the nitrogen content is fixed. The role of boron content in affecting the bulk modulus of c–$B_xC_yN_z$ crystals is checked as a function of carbon content. The bulk modulus shows roughly the opposite trend with relative to Figure 3.3.7a. For example, when the nitrogen content is fixed at 20 at.% (shown in Figure 3.3.7b), a clear trend can be observed that the bulk modulus decreases as the carbon content increases. This corresponds to the decrement of boron content since the total fraction for boron and carbon is kept at 80 at.%. This means that when the nitrogen content is high in c–$B_xC_yN_z$ crystals, the introduction of boron content can improve the properties of uniform compression. But for low nitrogen content, no clear trend can be found. This is very interesting phenomenon because the bulk modulus is normally high if the carbon content is high. But here we can see that the association of nitrogen and boron content can break the empirical rule to give a new understanding of the bulk properties.

3.3.4.3 Shear Modulus

Shear modulus show the opposite way comparing with bulk modulus. That is, when the boron content is fixed with certain values (20 at.%, 25 at.%, 30 at.%, and 35 at.%), the shear modulus decreases as the carbon content increases. The boron content fixed at 35 at.% in Figure 3.3.8a shows the clear trend. This means that even for the diamond–like structure, the shear modulus does not always increases with higher carbon contents. The nitrogen and boron content can also balance the role of carbon content in determining the shear properties of B–C–N crystals. Figure 3.3.8b shows the case that the nitrogen content is fixed. Overall speaking, when the nitrogen content is fixed, the boron role is not so crucial. The shear modulus shows increment as the carbon content increases.

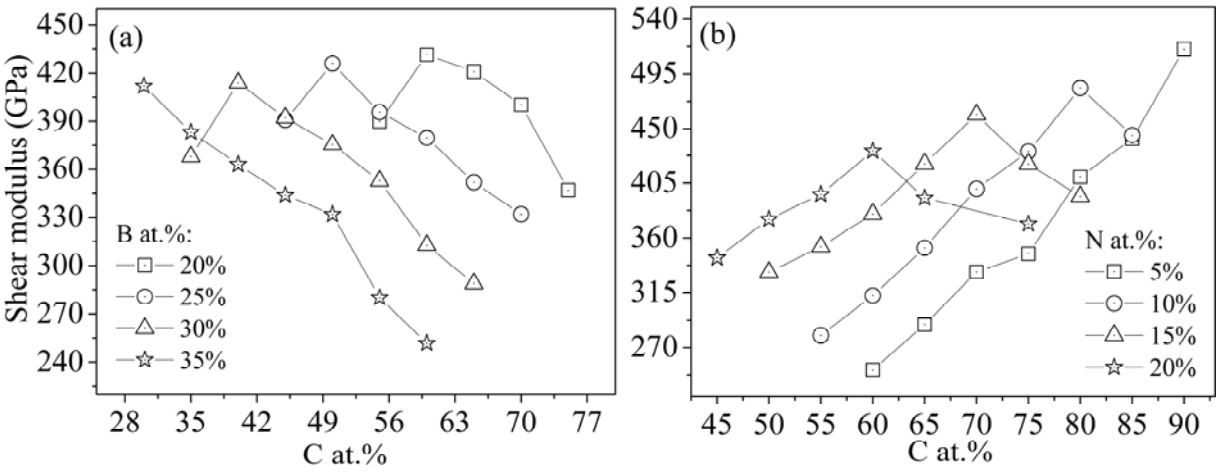

Figure 3.3.8: *(a) Shear modulus as a function of C content in the B–C–N crystals with fixed B content of 20 at.%, 25 at.%, 30 at.%, and 35 at.%; (b) Bulk modulus as a function of C content in the B–C–N crystals with fixed N content of 5 at.%, 10 at.%, 15 at.%, and 20 at.%.*

3.3.4.4 Poisson's Ratio

Poisson's ratio describes the ability of the lateral extension or contraction under the condition of axial loading. As shown in Figure 3.3.9a, the Poisson's ratio decreases as the carbon content increases when the boron content is fixed. This indicates that high carbon content can prohibit the ability of lateral deformation. When the nitrogen content is fixed (shown in Figure 3.3.9b), the Poisson's ratio shows the opposite trend with relative to Figure 3.3.9a. Again, this means that the boron role is not crucial in dominating the Poisson's ratio comparing with the carbon role.

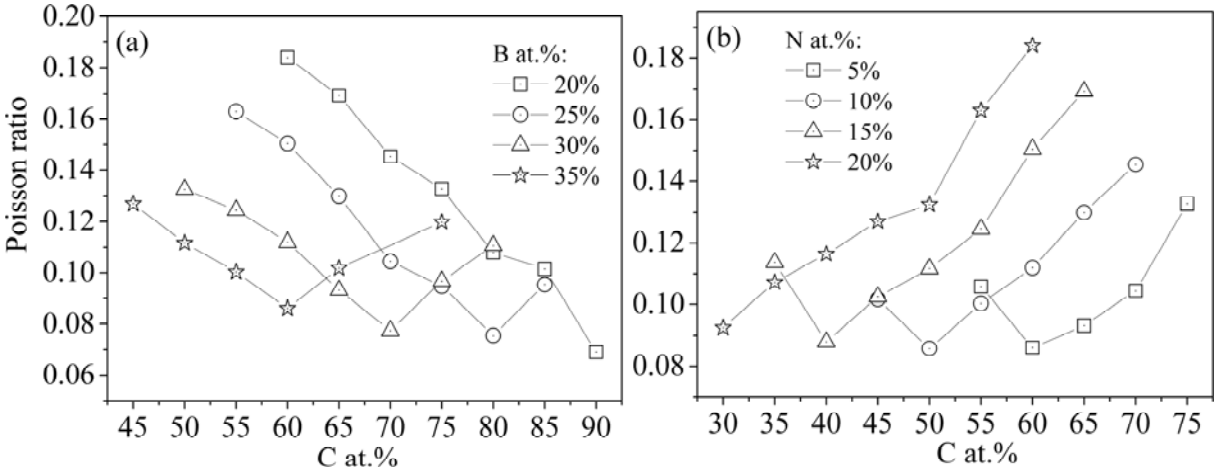

Figure 3.3.9: *(a) Poisson ratio as a function of C content in the B–C–N crystals with fixed B*

content of 20 at.%, 25 at.%, 30 at.%, and 35 at.%; (b) Poisson ratio as a function of C content in the B–C–N crystals with fixed N content of 5 at.%, 10 at.%, 15 at.%, and 20 at.%.

3.3.4.5 Vickers Hardness

We now discuss the Vickers hardness of the ternary B–C–N systems, which was evaluated by an semi–empirical formula developed by Tian's group [98] based on bond populations and on–site charges. All stable compositions in the upper rhombus of phase diagram possess Vickers hardness of > 40 GPa. Thus they can be considered superhard materials.

Again, hardest compositions are found in the C–rich area. Table 3.3.1 summarizes the theoretical results for those with sufficiently high Vickers hardness. The Vickers hardness of c–BC_2N crystal synthesized by Solozhenko et al. was reported to be 76 GPa, lying between the hardness of diamond (96 GPa) and c–BN (66 GPa) [99]. Obviously, these compositions selected in Table 1 possess appreciable Vickers hardness of 74 ~ 78 GPa, which is higher than c–BN, lower than diamond, and comparable to c–BC_2N [18]. Previous first–principles calculations [39] predicted a Vickers hardness of 68 GPa for the BC_4N crystal, which is consistent with our present result (72 GPa), in spite of the different structural model and computational methods used.

Table 3.3.1. *Compositions with higher Vickers hardness (H_v) in the selected areas of the B–C–N phase diagram.*

Composition	$B_3C_{58}N_3$	$B_3C_{54}N_7$	$B_3C_{51}N_{10}$	$B_3C_{48}N_{13}$	$B_6C_{54}N_4$	$B_6C_{52}N_6$
H_v (GPa)	77.5	77.1	76.2	75.8	74.9	74.6

The detailed variation of the Vickers hardness with different B, C and N contents is shown in Figure 3.3.10. For given boron concentration, the Vickers hardness drops as the C content increases. The trend is more pronounced in case of the high–boron concentration like 35 at.% (see Figure 3.3.10a). As shown in Figure 3.3.10b, for a certain amount of N content, the Vickers hardness shows a completely opposite trend, that is, it rise rapidly with increasing C content. Meanwhile, with the same amount of carbon, the theoretical Vickers hardness

increases with nitrogen percentage but decreases with boron concentration.

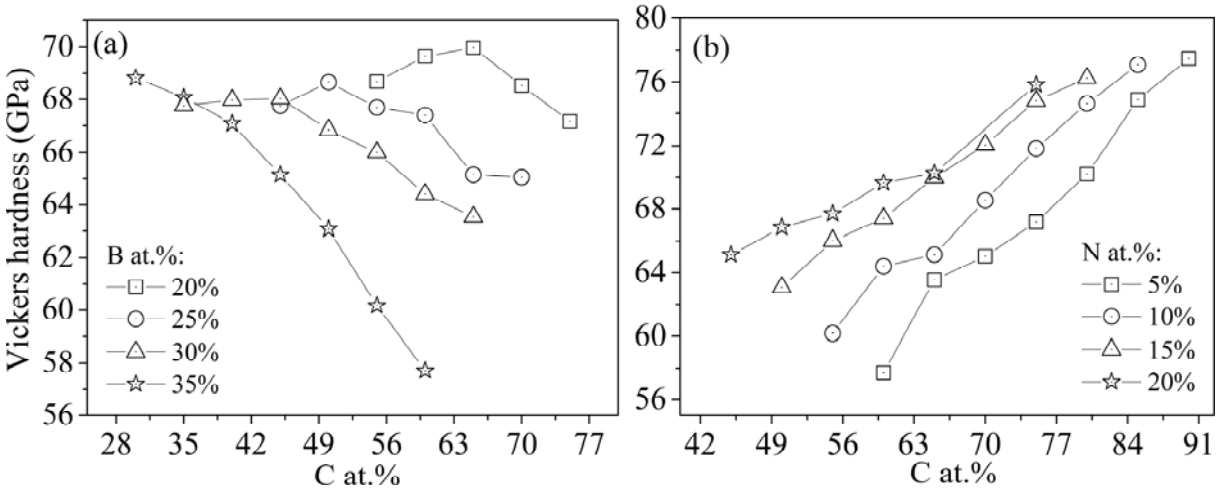

Figure 3.3.10: *(a) Vickers hardness as a function of C content in the B–C–N crystals with fixed B content of 20 at.%, 25 at.%, 30 at.%, and 35 at.%; (b) Vickers hardness as a function of C content in the B–C–N crystals with fixed N content of 5 at.%, 10 at.%, 15 at.%, and 20 at.%.*

3.3.4.6 Ductility

As an important aspect for the mechanical behaviors of a solid, the ductility describes the ability to change shape without fracture. It is necessary to explore the ductile properties of B–C–N materials because low ductility (corresponding to high brittleness) may affect their potential applications even though they possess high hardness.

In previous first–principles studies [125-127], the ratio of bulk and shear modulus (B/G) have been used to characterize the ductile behavior of materials. An approximate critical value of B/G for the ductile–brittle transition has been proposed [128]: a material behaves in a ductile manner when its ratio of B/G is greater than 2.0; otherwise, it is brittle.

From our calculations, the B/G ratio for all compositions considered range between 0.8 and 1.3, indicating that all B–C–N crystals are indeed brittle. For comparison, the highest B/G predicted for amorphous B–C–N solid can reach up to 2.25 (ductile) [122], although the lowest value for the B/G ratios are almost the same (0.84 for amorphous B–C–N and 0.83 for crystalline one). Along the C–BN isoelectronic line, most compositions possess a low ratio of

B/G, whereas the B–rich compositions exhibit relatively higher ratios of B/G around 1.25.

The detailed trend of B/G ratio with B, C, or N content is shown in Figure 3.3.11. Overall speaking, the trend of B/G ratio is opposite to the trends of Young's modulus or Vickers Hardness. For a given B content, the B/G ratio becomes higher as the C content increases (see Figure 3.3.11a). On the other hand, the B/G ratio for a fixed N content usually drops with increasing C content. With the same at.% of carbon, the B/G ratio generally increases with B content but decreases with N content, with some exceptions at high N concentrations (15 at.% or 20 at.%).

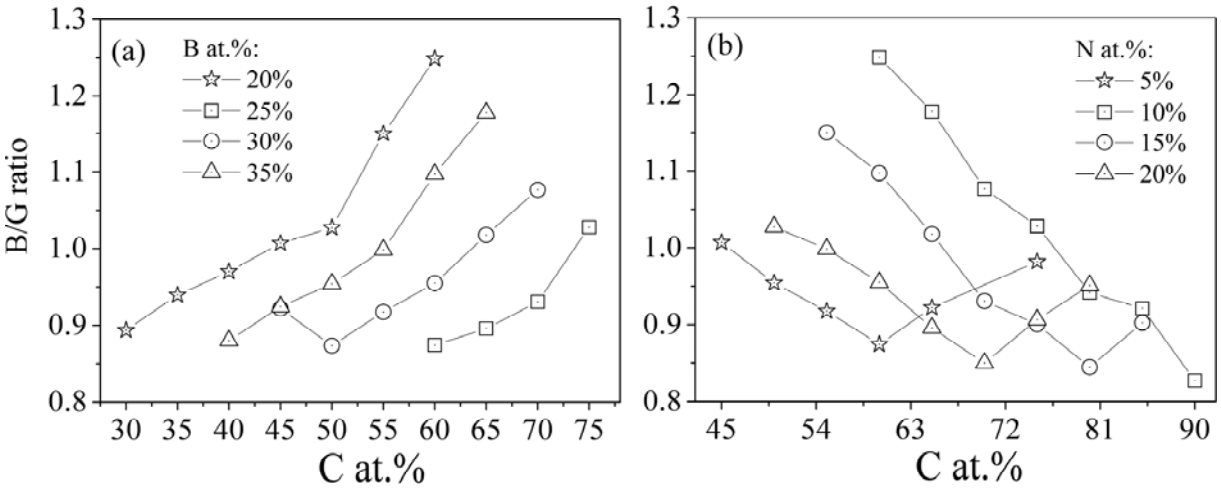

Figure 3.3.11: *(a) B/G ratio as a function of C content in the B–C–N crystals with fixed B content of 20 at.%, 25 at.%, 30 at.%, and 35 at.%; (b) B/G ratio as a function of C content in the B–C–N crystals with fixed N content of 5 at.%, 10 at.%, 15 at.%, and 20 at.%.*

3.3.4.7 Cauchy Pressure

Cauchy pressure, defined as the difference between the two elastic constants C_{12}–C_{44}, can also be used to describe the metallic character of atomic bonding, namely, ductibility or brittleness. Positive values mean materials are ductile while negative ones denote materials are brittle. Figure 3.3.12 shows the Cauchy pressure as a function of carbon content with different boron and nitrogen fixed fractions. All the values of the Cauchy pressure are negative, indicating that such c–$B_xC_yN_z$ crystals present the brittle properties of semiconductors.

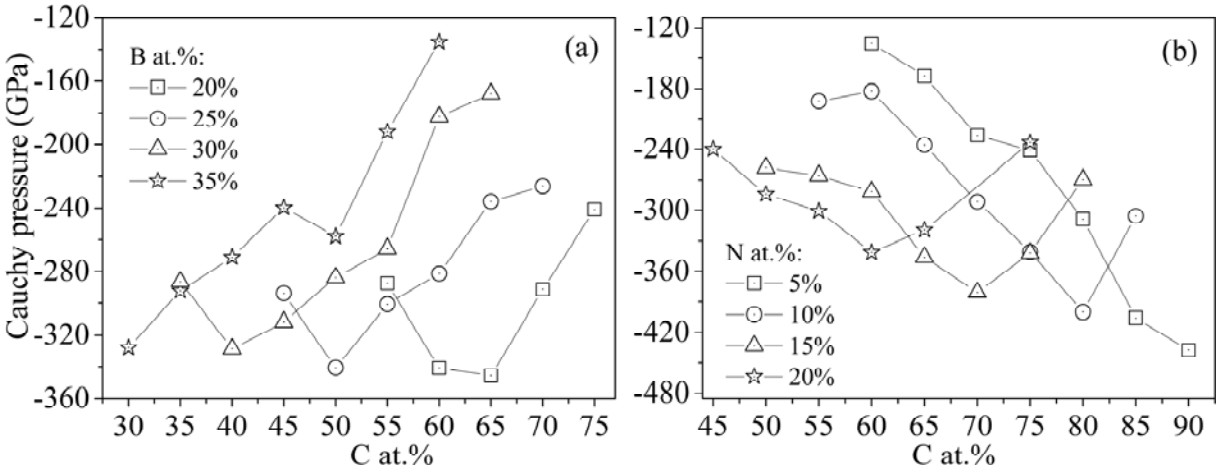

Figure 3.3.12: *(a) Cauchy pressure as a function of C content in the B–C–N crystals with fixed B content of 20 at.%, 25 at.%, 30 at.%, and 35 at.%; (b) B/G ratio as a function of C content in the B–C–N crystals with fixed N content of 5 at.%, 10 at.%, 15 at.%, and 20 at.%.*

If the boron content is fixed (Figure 3.3.12a), the overall trend for Cauchy pressure is increasing as a function of carbon content, indicating the increment of brittle properties. For the same carbon content for example 60 at.% (Figure 3.3.12a), the higher boron content indicates larger Cauchy pressure corresponding to higher brittle properties. While if the nitrogen content is fixed, the opposite trend can be found in Figure 3.3.12b. That is, the Cauchy pressure decreases as the carbon content increases. In other words, the interesting phenomenon shows that the boron role can improve the ductile properties of c–$B_xC_yN_z$ crystals. This reveals that we cannot say exactly the role of different elements whether their introduction can improve or weaken the brittle/ductile properties. The brittle/ductile properties of c–$B_xC_yN_z$ crystals are determined by the integration of boron, carbon, and nitrogen fractions.

3.3.5 Summary

Mechanical properties and formation energies of the possible crystalline phases on the upper rhombus of the B–C–N ternary diagram were systematically studied using first–principles calculations. Upon structural relaxation, most N–rich compositions on the right side of rhombus do not have a stable cubic sp^3 phase. We found that the compositions with high Vickers hardness (~ 75 GPa) are located in the C–rich area (70 at.% ~ 90 at.%),

whereas the B–rich compositions (30 at.% ~ 35 at.%) possess better ductility and C–poor area (30 at.% ~ 50 at.%) in the diagram has ideal formation energies. In particular, the area within B: 25 ~ 35 at.%; C: 45 ~ 55 at.%; N: 5 ~ 20 at.% has the relatively lower formation energy, good ductility, and intermediate hardness (~ 66 GPa), which might be synthesized and have some technological applications. Our theoretical results provide valuable guidance for intentionally synthesizing $B_xC_yN_z$ materials with desirable mechanical properties. Some experiments on the compositions beyond the isoelectronic line of the ternary diagram are anticipated in the near future.

3.4 Crystalline BC_x Materials*

So far, based on the parameter of the degree of mixture to search possible structures, the random solid solution model has been successfully applied to cubic BC_2N, cubic BC_xN, and cubic $B_xC_yN_z$ crystals with reasonable accuracy. Beyond such kinds of crystalline B–C–N materials, it is still unknown whether the model can be extended to other covalent materials that are synthesized under similarly extreme conditions (shock–wave compression or HPHT) like that of the crystalline B–C–N materials.

Recently, a novel superhard phase, cubic BC_5, has been obtained under HPHT conditions (24 GPa, ~ 2200 K). This crystal exhibits extreme Vickers hardness of 71 GPa, high toughness (9.5 $MPa.m^{0.5}$), and high thermal stability (1900 K) [129, 130]. All these excellent properties rank the crystal as one kind of promising superhard materials for potential industrial applications. However, the detailed crystal structure is still unknown. Since the BC_5 crystal has also the cubic–like structure, thus we can use this novel superhard phase to verify our random solid solution model whether it can be extended to such kinds of covalent crystalline BC_x materials. Before the extension of our model, we present the general introduction of the state of art on such kinds of crystalline BC_x materials.

The applications of diamond are limited by its poor oxidation resistance and reaction with ferrous metals [131]. Doping a small amount of boron content into diamond can improve the oxidation resistance [132], reduce the energy bandgap [133] and increase the superconducting transition temperature (T_c) [130, 134-138] of the original diamond crystals. Therefore, diamond–based BC_x crystals with typically boron concentrations between 2.4×10^{20} and 1.4×10^{22} cm^{-1} (0.16 ~ 7.1 at.%) have attracted significant attention over the past few years. Under high pressure and high temperature (HPHT) conditions, Solozhenko et al. [129] recently synthesized cubic BC_5 crystals, which have indeed the highest boron concentration in BC_x crystals achieved so far. The BC_5 crystals exhibit a superior hardness of 71 GPa and a high T_c of 45 K. Since the atomic numbers and sizes of B and C are very close, it is very difficult to analyze the detailed atomic arrangement in the BC_5 crystals [139]. Hence the crystal structure

* Reference [3] in the list of publications

of BC_5 has not yet been well determined.

Theoretically, different models have been suggested as the possible crystal structures of BC_5 [131, 139-143]. For example, superlattice–like heterostructures with one B layer and five C layers arranged alternately along different crystal orientations were proposed [139, 140, 142]. However, within these heterostructure models, significant weakening of the B–C bonds adjacent to the boron layers would result in low intrinsic shear strength, in contrast to the high value of hardness measured in experiment [129]. Therefore, Zhang et al. [144] concluded that the heterostructure models are not suitable for the c–BC_5 crystal. Although there is no perfect model for the crystal structure of BC_5 yet, it is generally considered that theoretical results are close to the experiment when B atoms are distributed randomly in the diamond lattice [139, 141]. Furthermore, according to the experimental NMR data for B–doped diamond with a boron concentration of about 2.8 at.%, Ekimov et al. [145] found that B atoms are distributed evenly in the diamond lattice. Raman scattering analysis by Zinin et al. [146] also suggested a random distribution of B atoms in the diamond–based BC_x crystals.

Despite the above efforts on the structural properties of the BC_x crystals, much less is known about the effect of boron concentration on their structural stability and mechanical properties. In particular, from the materials design point of view, it is desirable to find out an appropriate range of boron concentration that is able to balance the stability, hardness and ductile/brittle properties of cubic BC_x crystals. Here we introduced the random solid solution model for cubic BC_5 crystals and assessed its validity by comparing the simulated XRD pattern and lattice parameter with the experimental data. Within this model, the effects of boron concentration and ratio of B–B bonds on the structural stability and mechanical properties of BC_x ($1 < x < 63$) crystals were investigated using first–principles methods.

3.4.1 Structural Model and Computational Accuracy

Three representative structures of BC_x crystals with different boron concentrations are shown in Figure 3.4.1. For each composition, three structures were used. The average results were presented to avoid fluctuations due to the random choice of configurations. The geometry optimizations and the consequent elastic constant calculations on the crystalline

BC_x systems were performed using a series of 64–atom cubic supercells. The elastic constants of cubic BC_x crystals were computed using the finite strain technique based on homogeneous deformation of the unit cell, as implemented in the CASTEP program. With the computed elastic constants, the bulk modulus and (isotropic) shear modulus of each crystal were then evaluated using the Voiget–Reuss–Hill average scheme [96]. The computed bulk modulus and shear modulus of the diamond crystal are B = 443.8 GPa and G = 544.1 GPa, respectively, in good agreement with the experimental values of B = 443 GPa and G = 534 GPa [147].

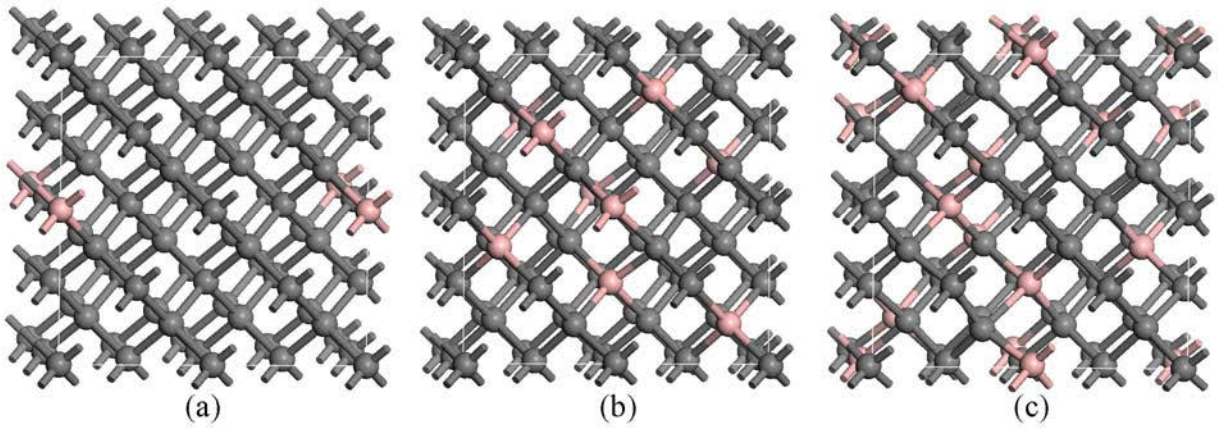

Figure 3.4.1: *Representative cubic BC_x structures with different boron concentrations. (a) BC_{63}; (b) $BC_{8.1}$; (c) $BC_{4.8}$. Boron: pink; carbon: grey.*

3.4.2 Crystal Structure

The crystal structure of cubic BC_x was described by our random solid solution model, in which a certain number of boron atoms randomly substitute the carbon atoms in the diamond lattice to meet the BC_x stoichiometry. A typical 216–atom supercell structure of cubic BC_5 from fully DFT relaxation is shown in Figure 3.4.2a. The validity of our structural model can be assessed by comparing the simulated XRD pattern with the measured data [129]. As shown in Figure 3.4.2b, the (111) and (220) diffraction peak positions from our simulations agree well with experiments, with a discrepancy less than 0.05%.

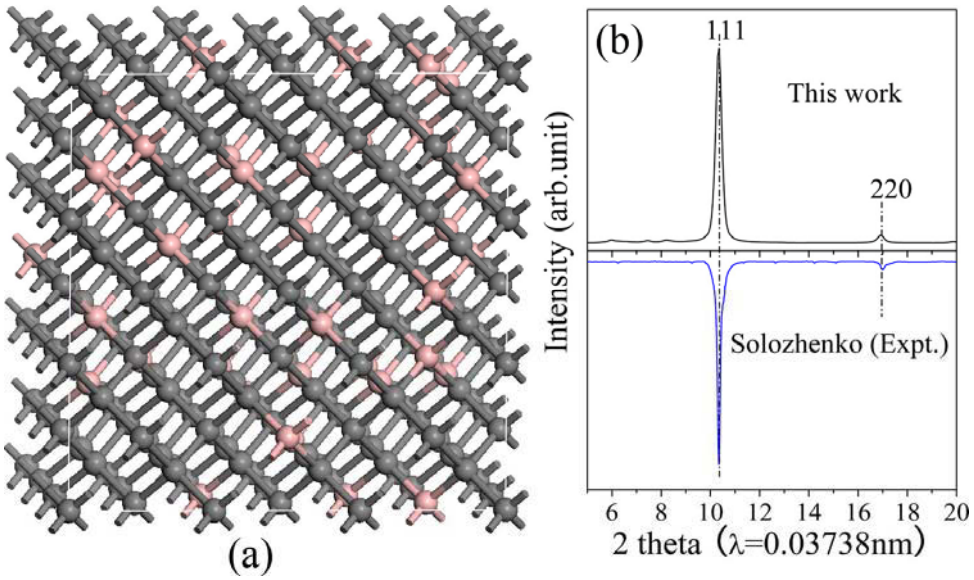

Figure 3.4.2: *(a) Random solid solution model for cubic BC_5 crystal within a 216–atom super cell. Carbon: light gray, boron: dark gray. (b) Simulated XRD pattern (upper plot) compared with experimental one (lower plot) [129].*

Previous studies also used the simulated XRD pattern to evaluate their models [139, 141]. Their simulated 111 and 220 peak positions show deviations from the experiment of approximately 1.43% and 1%, respectively. Comparing with their simulated patterns, our results show better agreement with the experimental one [129]. In addition, we have generated six random solid solution structures (within a 216–atom supercell) for BC_5 crystals. The simulated XRD patterns for all of them are nearly identical, suggesting that B atoms distribute randomly within the diamond lattice. Moreover, the theoretical lattice constant of the BC_5 crystal (3.598 Å) is also very close to the experimental value of 3.597 Å measured by SAED or 3.635 Å from angle–dispersive x–ray diffraction [129]. Such excellent agreements clearly demonstrate that the random solid solution model is appropriate for describing the cubic BC_5 and maybe other BC_x crystals.

3.4.3 Structural Stability

Within the random solid solution model, the structural stabilities of the BC_x crystals of different compositions (i.e., $1 < x < 63$) can be characterized by the formation energy (E_f) defined as:

$$E_f = E_{\mathrm{B}_m\mathrm{C}_n} - \left(mE_{(\alpha-B_{12})} + nE_{graphite} \right) \Big/ \left(m+n \right), \tag{3.4.1}$$

where $E_{\mathrm{B}_m\mathrm{C}_n}$, $E_{(\alpha-B_{12})}$ and $E_{graphite}$ represent the total energy per atom of cubic $\mathrm{B}_m\mathrm{C}_n$, α–B_{12} and graphite crystals, respectively. All theoretical results are summarized in Table 3.6.

Table 3.6. *Theoretical formation energy (E_f) (eV/atom), bulk modulus (B) (GPa), isotropic shear modulus (G) (GPa), Young's modulus (E) (GPa), ratio of bulk modulus and shear modulus (B/G), Cauchy pressure ($C_{12} - C_{44}$) (GPa) and Poisson's ratio (ν) for BC_x crystals with different boron concentrations. C_B ($\times 10^{21}$ cm^{-3}) denotes the number of B atoms per unit volume. The theoretical values of diamond are also shown for comparison.*

Str.	B (at.%)	C_B	E_f	B	G	E	C_{12}–C_{44}	B/G	ν
BC	50	76	0.51	287.8	295.3	660.1	–282.7	0.975	0.118
$BC_{4.8}$	17.19	29.4	0.32	375.1	358.8	816.2	–253.8	1.045	0.137
$BC_{6.1}$	14.06	24.4	0.3	386.6	382.9	863.6	–261.2	1.01	0.128
$BC_{8.1}$	10.94	19.2	0.28	404.5	445.0	976.8	–361.9	0.909	0.098
$BC_{11.8}$	7.81	13.8	0.26	414.0	465.9	1016.4	–391.7	0.889	0.091
$BC_{20.3}$	4.69	8.4	0.23	426.6	485.2	1055.5	–325.4	0.879	0.088
BC_{63}	1.56	2.8	0.21	440.4	485.3	1064.8	–282.3	0.907	0.097
Diam.	–	–	–	443.8	544.1	1158.8	–466.0	0.816	0.064

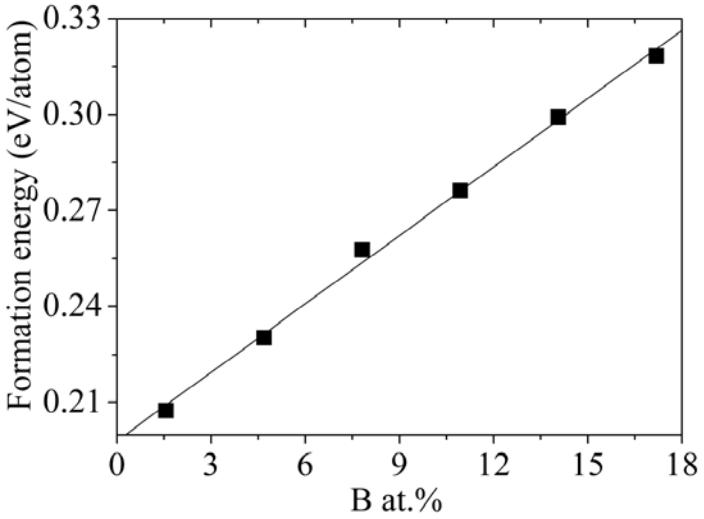

Figure 3.4.3: *Formation energy of cubic BC_x crystals as a function of boron concentration.*

The computed formation energy is plotted as a function of boron concentration in Figure

3.4.3. One can see that the formation energy of BC_x crystals increases as the boron concentration increases. In other words, doping diamond crystals with boron content is endothermic and the doped system becomes less stable as boron concentration increases. As the boron concentration in BC_x crystals approaches 4.69 at.% (about 8.4×10^{21} cm^{-3}), the corresponding formation energy is as high as 0.23 eV/atom. In fact, the boron concentration in most synthesized BC_x crystals is lower than 8.4×10^{21} cm^{-3} [145, 148-150]. Until recently, a high boron concentration of up to 16.7 at.% (~ 2.8×10^{22} cm^{-3}) has been achieved [129]. However, such a boron concentration is still far away from the ultimate boron concentration (50 at.%) of the cubic BC crystal, in which the B and C atomic layers are arranged alternately and there is still no B–B bond.

The difficulty in synthesizing BC_x crystals with higher boron concentrations (> 16.7 at.%) is probably related to the B–B bonds introduced in the starting materials (or precursors) as the boron concentration exceeds a certain value. Typically, the precursors for preparing cubic BC_x crystals are synthesized by chemical vapor deposition using different gas sources and they have graphite or turbostatic structures [129, 146]. Previous experiments [151] revealed that a number of B–B bonds will be introduced and become dominant in such precursors as the boron concentration increases up to 23 at.% or more.

Based on the reported value of boron concentration (23 at.%) [151], we constructed several structural models for the cubic BC_x crystal with the composition $BC_{3.3}$ (23.3 at.%), in which B–B bonds of different ratios (0%, 2.3%, 4.7% and 7%) were introduced as shown in Figure 3.4.4.

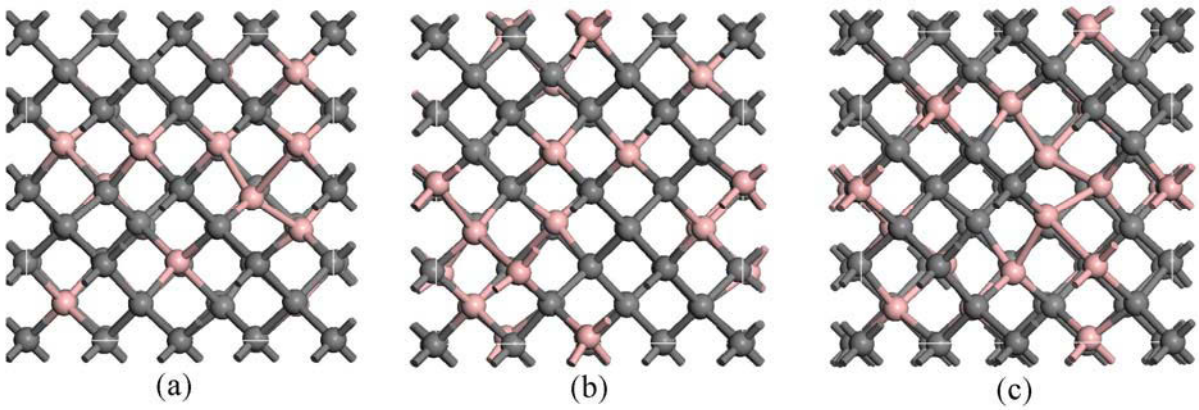

Figure 3.4.4: *Representative structures of cubic $BC_{3.3}$ with different B–B bond concentrations. (a) B–B% = 2.3%; (b) B–B% = 4.7%; (c) B–B% = 9%.*

After geometry optimization, the formation energies of all these structures were calculated to characterize their relative structural stabilities. Taking the system without B–B bonds (0% ratio) as reference, the cubic $BC_{3.3}$ crystals with a B–B bond ratio of 2.3% and 4.7% are only slightly higher in energy by 0.005 and 0.008 eV/atom, respectively. However, increasing the B–B bond ratio up to 7% would greatly increase the energy difference to 0.83 eV/atom. This implies substantial structural instability. The corresponding formation energy (as high as 1.17 eV/atom) of this system also clearly demonstrates that a B–B bond ratio up to 7% evidently aggravates the structural stability of cubic $BC_{3.3}$.

According to the experimental observation [151], we infer that more B–B bonds will be introduced when the boron concentration in the starting materials is higher. Hence, the B–B bonds will further increase the formation energies and deteriorate the structural stabilities of BC_x crystals. Since B–B bonds are unstable with high energies, they would probably be broken during the structural transformation under HPHT conditions. Consequently, these very unstable structures would be decomposed into other compositions with low boron concentration. Indeed, a previous experiment observed that graphite–like BC_3 (with 25 at.% boron content) was decomposed into BC_x crystals with low boron concentration of about 1.8 at.% and other boron carbides under high pressure (20 GPa) and high temperature (2200 K) conditions [152].

In fact, the graphite–like BC_3 precursor was prepared using similar methods as described in the previous work [151]. With such a high boron concentration (25 at.%), B–B bonds are very likely present in their precursors. During the transformation under HPHT conditions, graphite–like $BC_{1.6}$ (B%: 38.5 at.%) materials were also segregated into a mixture of diamond, boron carbide and boron [153]. The present results indicate the crucial role of B–B bonds in deteriorating the structural stability of cubic BC_x crystals with high boron concentration. The B–B bond ratio in precursors may be responsible for the difficulty in synthesizing BC_x crystals with high boron concentrations. Therefore, we suggest that controlling the B–B bond

ratio in the precursor materials to be as low as possible is a practicable route to synthesize BC_x with high boron concentrations.

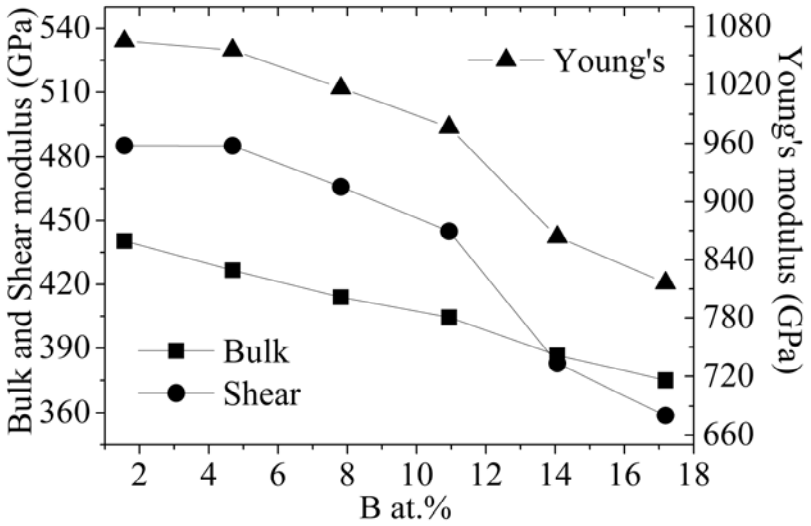

Figure 3.4.5: *Bulk modulus, shear modulus and Young's modulus as a function of boron concentration for BC_x crystals.*

3.4.4 Mechanical Properties

Within the present structural model, we further discuss the mechanical properties of the BC_x crystals. The bulk modulus, shear modulus and Young's modulus were plotted as a function of boron concentration in Figure 3.4.5. All of them decrease as boron concentration increases, indicating that more boron content will degrade the hardness of BC_x crystals.

The relationship between the characteristic ductility parameters and the boron concentration is shown in Figure 3.4.6. All the *B/G* values are lower than 2, indicating that the current cubic BC_x crystals are mainly brittle. With regard to the pristine diamond, doping a small amount of boron atoms would significantly improve the ductility of the crystal. However, further increasing the boron concentration does not continuously enhance the crystal ductility. As shown in Figure 3.4.6, at a boron concentration of about 4.7 at.%, a local minimum of the *B/G* curve is found.

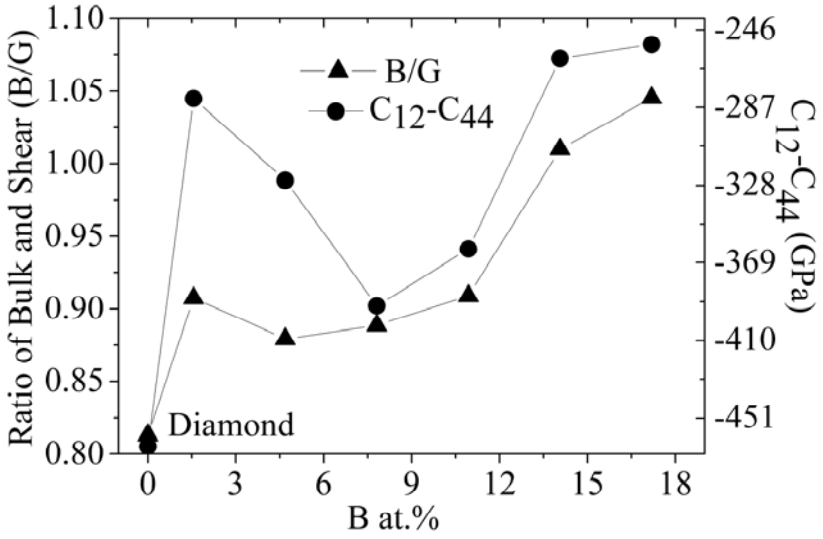

Figure 3.4.6: *Ratio of bulk modulus and shear modulus (B/G) and Cauchy pressure (C_{12}–C_{44}) as a function of boron concentration.*

A similar trend can be seen from the curve of Cauchy pressure (C_{12}–C_{44}), in which a local minimum of C_{12}–C_{44} is found at about 7.8 at.%. In other words, the BC_x crystals with boron concentrations below 4.7 at.% or above 7.8 at.% possess better ductility. However, BC_x crystals with boron concentrations > 7.8 at.% have higher formation energies and lower hardness, compared with those with boron concentrations < 4.7 at.%. Therefore, the boron concentration between 1.6 and 4.7 at.% ($2.8 \times 10^{21} \sim 8.4 \times 10^{21}$ cm^{-3}) in BC_x crystals is an optimal choice for mechanical properties from the perspectives of hardness, ductility and formation energy.

3.4.5 Summary

We extended the random solid solution model to the novel superhard phase: cubic BC_5. The simulated lattice constant and XRD pattern for BC_5 reproduce experimental data satisfactorily. The excellent agreement with the experiment verified the reasonability of the extension of our model. Extending the model to other compositions (BC_x) ($1 < x < 63$) beyond BC_5, the effects of boron concentration and B–B bonds on the structural stabilities and mechanical properties of BC_x crystals were systematically investigated using first–principles methods. We found that the formation energy increases with boron concentration, which can explain why it is difficult to obtain BC_x crystals with higher boron content. Furthermore, BC_x

crystals with higher boron content possess poorer mechanical properties. In addition, the ratio of B–B bonds has an evident effect on the structural stability of the cubic BC_x crystals. For precursor materials with sufficiently high boron concentrations, the existence of a large number of B–B bonds would hamper the formation of cubic BC_x crystals with higher boron concentrations under HPHT conditions. In other words, controlling B–B bonds in the precursor materials as low as possible might be a practicable route for the synthesis of boron rich BC_x materials. Judging by the formation energy, hardness and ductility, a boron concentration between 2.8×10^{21} and 8.4×10^{21} cm^{-3} (1.56 ~ 4.69 at.%) is a compromise choice to balance the structural stabilities and mechanical properties of BC_x crystals.

4 Theoretical Calculations on Amorphous B–C–N Materials

Crystalline B–C–N materials with cubic structure are usually synthesized under extreme conditions such as shock wave compression and high pressure high temperature (HPHT). Such crystalline materials are very sensitive to experimental conditions, thus they are quite difficult to be obtained. Once the experimental conditions exceed the range in which cubic phases stably exist, corresponding cubic structures will transform into other ones that are more stable, such as hexagonal or graphite–like ones. Overall speaking, it is still challenging to obtain cubic B–C–N materials due to their narrow synthesis conditions. Besides, the extreme techniques for the preparation of cubic B–C–N structures also limit their potential industrial applications based on the consideration of saving energy and reducing costs.

People attempted to synthesize crystalline B–C–N materials by common methods, such as PVD, CVD and PLD. Amorphous B–C–N materials, not crystalline ones, are most frequently obtained. These amorphous B–C–N materials also have good mechanical and electrical properties. Therefore, they are also intensively investigated. However, chemical compositions of amorphous B–C–N materials in a very broad range are not easy to be obtained. In general, the chemical compositions obtained are in a very narrow range even different experimental parameters are changed, such as gas flow ratio, sputtering power, bias voltage and substrate temperature. In addition, adhesion problems are still a big issue in amorphous B–C–N films. Amorphous B–C–N thin films are easily to be peeled off from silicon or other substrates. Therefore, nanoindentation cannot be further performed to examine the mechanical properties of these films. This is the reason why there are only few publications focusing on the mechanical properties of amorphous B–C–N thin films.

Theoretical calculations provide an efficient way to establish the relation between chemical compositions and mechanical properties of amorphous B–C–N films. The chemical composition of B–C–N materials can be arbitrarily designed by theoretical approach. The corresponding mechanical properties can also be calculated. In particular, to the best of our knowledge, there has been no theoretical study to address this important issue so far. Here we

focus on this issue and use first–principles calculations to study the variations of Young's modulus, ductility, and formation energy in the upper rhombus of the ternary B–C–N phase diagram. We build the connection between chemical compositions and mechanical properties, and provide a theoretical guidance to the experimental preparations of B–C–N films with desirable mechanical properties.

4.1 Structural Model*

Practical applications of amorphous B–C–N films usually require sufficiently high hardness. This requires a substantial amount of sp^3 bonding states in these kinds of materials. Previously, Martinez et al. [154] reported the synthesis of a tetrahedral amorphous carbon (ta–C) film. The film has a high mass density of 3.2 g/cm^3 and contains a large amount of sp^3 bonding states (84 ~ 88%). The corresponding hardness reaches up to ~ 45 GPa. Similar to ta–C, the B–C–N films investigated here should also have a high fraction of sp^3 hybridization, which can be treated as potentially useful materials in various fields.

Firstly, we constructed a template for amorphous B–C–N systems using a 216–atom cubic supercell. The template has a mass density of ~ 3.3 g/cm^3 and a sp^3 content of ~ 88%. The number of atom (216 carbon atoms) and the mass density (3.3 g/cm^3) are taken as the input parameters for molecular dynamics simulations. These carbon atoms were randomly put into a cubic supercell with the desired density. Afterwards, the cubic supercell was treated by quenching from 4000 K to 300 K with an interval of 100 K for each step. The inter–atomic interaction was modeled by empirical Tersoff potential [155]. At each temperature, the constant–temperature molecular dynamics within the NVT ensemble lasted 1ns with a time step of 1 fs. Hence, the total simulation time reaches 38 ns. The ultimate annealed structure of the template is shown in Figure 4.1. Based on the template, $B_xC_yN_z$ materials with different compositions were obtained by randomly replacing certain numbers of C atoms in the 216–atom supercell of ta–C with B and N atoms. Figure 4.2 shows some representative structural models of amorphous B–C–N materials with different chemical compositions. Thus we can have an intuitive impression of amorphous B–C–N materials at the atomic level.

* Reference [2] in the list of publications

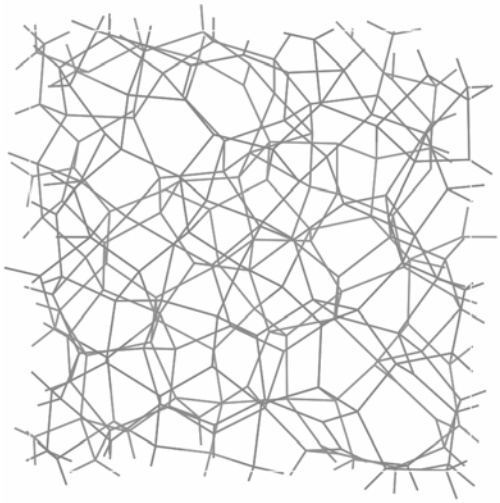

Figure 4.1: *Structural model of ta–C with 216 carbon atoms with a density of ~ 3.3 g/cm^3 annealed from MD simulations.*

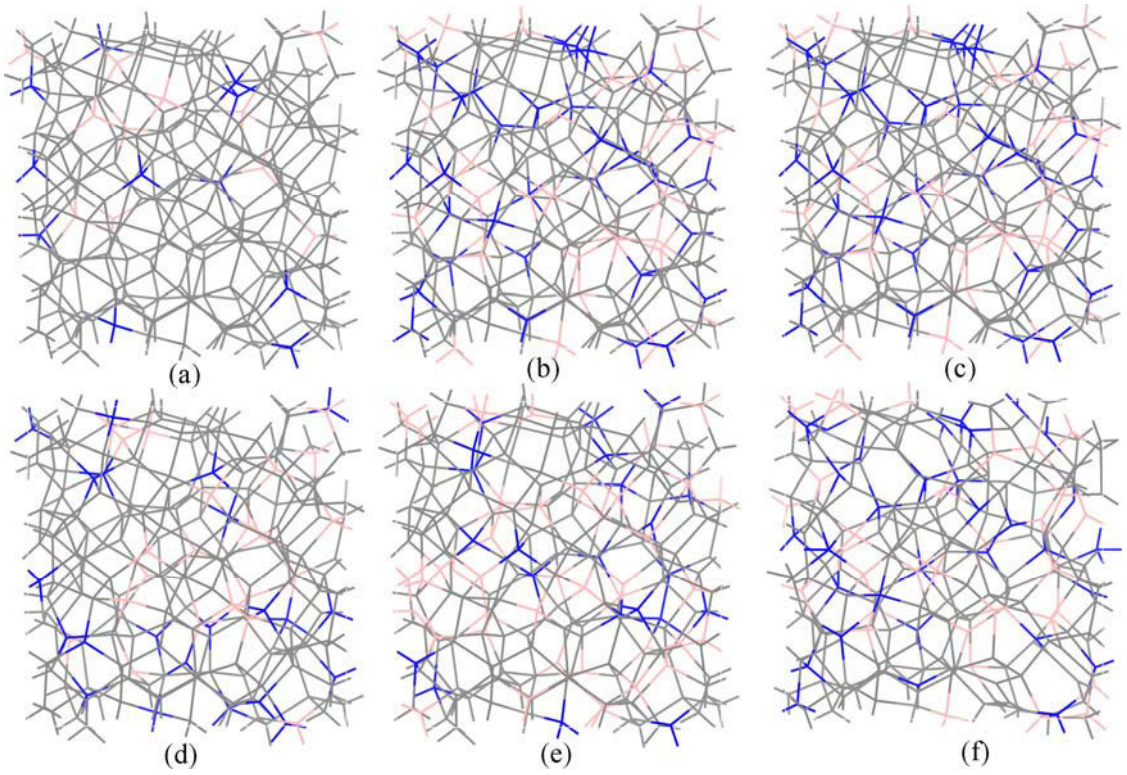

Figure 4.2: *Representative structural models of amorphous B–C–N materials with different chemical compositions. (a) $B_{0.051}C_{0.948}N_{0.051}$; (b) $B_{0.102}C_{0.847}N_{0.051}$; (c) $B_{0.051}C_{0.847}N_{0.102}$; (d) $B_{0.102}C_{0.796}N_{0.102}$; (e) $B_{0.199}C_{0.699}N_{0.102}$; (f) $B_{0.153}C_{0.699}N_{0.148}$. Different colors correspond to different atoms, in which boron is pink, carbon is grey, and nitrogen is blue.*

Obviously, the current ta–C template is not suitable to model those compositions with

high B and N contents due to the intrinsic difference in the structures and chemical bonding between the carbon (of diamond phase) and the boron or nitrogen solids. Hence, we mainly focus on the carbon–rich compositions in which both B and N contents are less than 35 at.%, corresponding to the upper rhombus in the ternary B–C–N phase diagram (see Figure 4.3). Then we divided the XYZ axes of the B–C–N phase diagram by a proportion of 5%, and generated a series of intersection points on the phase diagram. On the upper rhombus of the phase diagram, the compositions at the intersection points were selected for calculations. The properties for the compositions between these points, inside of a triangle composed of three neighboring intersection points, were obtained via the method of the linear interpolation.

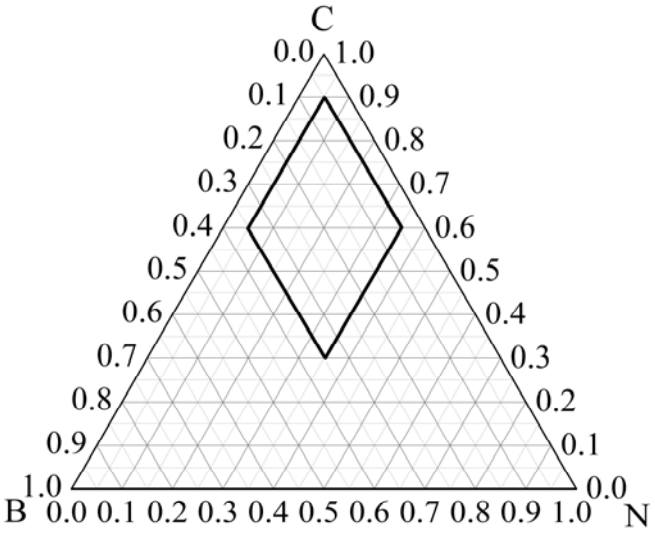

Figure 4.3: *The area of the upper rhombus as marked by black lines in the ternary B–C–N phase diagram. The chemical compositions in this area were chosen for investigation.*

In principle, a large number of random configurations for each composition can be obtained from the random replacement of C atoms by B and N atoms. Here the degree of mixture χ was also used to classify all produced structures. For each composition, the supercell structures were constructed according to the most probable χ values selected from statistic distribution of 2×10^4 random configurations. Figure 4.4 shows several representative configurational possibilities of amorphous B–C–N materials with different chemical compositions as a function of the degree of mixture.

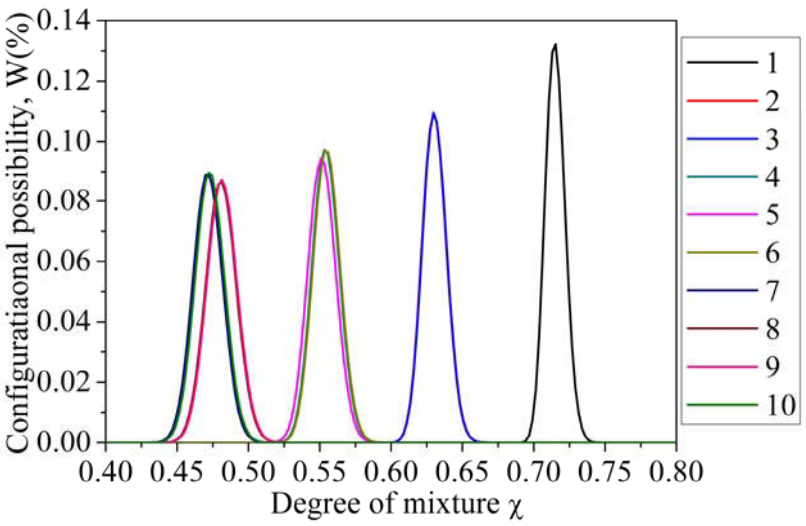

Figure 4.4: *Representatively configurational possibility of amorphous B–C–N materials with different chemical compositions as denoted by numbers as a function of degree of mixture χ. (1)* $B_{0.051}C_{0.898}N_{0.051}$*; (2)* $B_{0.102}C_{0.847}N_{0.051}$*; (3)* $B_{0.051}C_{0.847}N_{0.102}$*; (4)* $B_{0.148}C_{0.801}N_{0.051}$*; (5)* $B_{0.102}C_{0.796}N_{0.102}$*; (6)* $B_{0.051}C_{0.801}N_{0.148}$*; (7)* $B_{0.213}C_{0.736}N_{0.051}$*; (8)* $B_{0.148}C_{0.75}N_{0.102}$*; (9)* $B_{0.102}C_{0.75}N_{0.148}$*; (10)* $B_{0.051}C_{0.75}N_{0.199}$*.*

4.2 Computational Detail

First–principles calculations were performed using density functional theory (DFT) and the plane–wave pseudopotential technique implemented in the VASP program [90]. The ion–electron interaction was described by ultra–soft pseudopotentials [89]. A high energy cutoff of 650 eV was used for the plane–wave basis to ensure well converge of total energy within 1×10^{-4} eV/atom and stress within 1×10^{-3} eV/Å. The exchange–correlation interaction was described by the generalized gradient approximation (GGA) with PW91 parameterization [113]. Brillouin zone of the reciprocal space was sampled by the Γ point.

The bulk modulus (*B*) was directly fitted from the derivative of Pressure–Volume (*P–V*) relationship under hydrostatic compression. The elastic constant of the quasi–cubic supercell was computed using a finite strain method. The isotropic shear modulus (G) was evaluated by Voigt–Reuss–Hill average scheme. The isotropic Young's modulus (*E*) was calculated from bulk modulus *B* and shear modulus *G*. For each composition, three representative supercell structures were considered. Their average result was used to reduce the fluctuations due to the

arbitrary choice of random configurations.

4.3 Structural Stability*

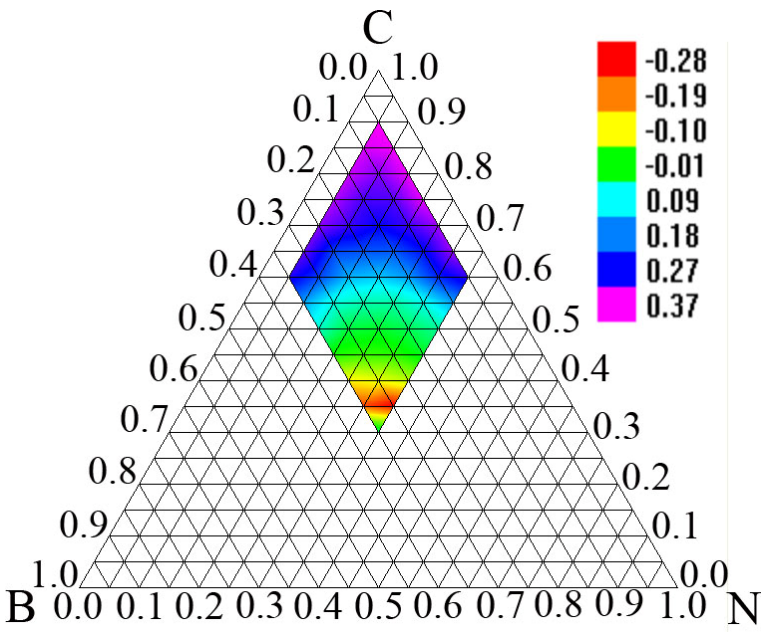

Figure 4.5: *Distribution of formation energy (eV/atom) on the upper rhombus of the ternary B–C–N phase diagram using full spectrum. Lower values of the formation energy mean that the corresponding compositions are easier to form.*

The formation ability of an amorphous $B_xC_yN_z$ solid with given composition can be evaluated by its formation energy (E_f), which has been defined in previous chapter. The computed results were mapped on the ternary B–C–N phase diagram (Figure 4.5) using numerical interpolation. Interestingly, the distribution of formation energies is nearly symmetric along the C–BN iso–electronic line on the B–C–N phase diagram. On the upper (purple) area with B and N contents lower than 7 at.%, the B–C–N solids possess rather high positive E_f values (0.27 ~ 0.37 eV/atom). This indicates that $B_xC_yN_z$ compositions in this area cannot easily form. As the B and N contents increase, the E_f value decreases. As seen from Figure 4.5, in those B–C–N systems dominated by a high proportion of sp^3 bonding state, their atomic structures are not stable if too much carbon content is involved. In contrast, when certain amount of B and N atoms is introduced, they become more stable. This reveals the

* Reference [7] in the list of publications

distinct effect of B and N content on the stability of such systems. Our calculation revealed that the area with 15 ~ 35 at.% of B, 30 ~ 53 at.% of C, and 15 ~ 35 at.% of N has negative formation energies. This result suggests that the $B_xC_yN_z$ solids in this composition region are easier to form with regard to other areas in the ternary B–C–N phase diagram.

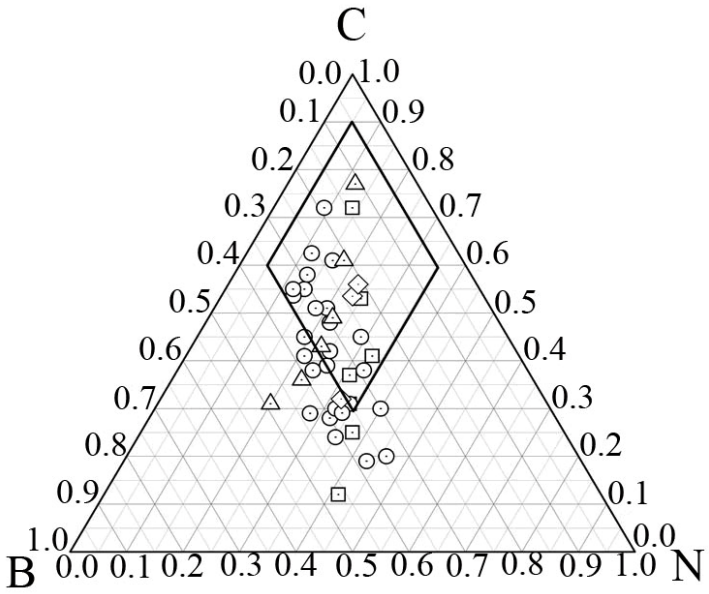

Figure 4.6: *$B_xC_yN_z$ compositions synthesized in previous experiments [156-159]. Most compositions locate in the area with negative formation energy, confirming our theoretical prediction.*

For comparison, Figure 4.6 collects a large number of $B_xC_yN_z$ compositions that have been synthesized in previous experiments by various methods [156-159]. Clearly, most of them fall in the region of negative formation energy (B: 15 ~ 35 at.%; C: 30 ~ 53 at.%; N: 15 ~ 35 at.%). In other words, our theoretical calculations are able to predict the dependence of the formation ability of $B_xC_yN_z$ solids on their chemical compositions. Note that our structural models contain mainly sp^3 contents (~ 88%), whereas the experimentally synthesized B–C–N films typically include a larger proportion of sp^2 components. In addition, there have been some experimentally synthesized $B_xC_yN_z$ compositions with high boron atomic concentrations that are outside the upper rhombus of ternary B–C–N phase diagram. Hence they cannot be simulated by our present model, which is originated from the ta–C template. Nevertheless, with respect to those experimental compositions located in the upper rhombus, the general trend of formation ability on the ternary B–C–N phase diagram revealed by our theoretical

simulations should still be valid.

In previous studies, it has been demonstrated that B–C–N films with compositions in the region of B: 15 ~ 35 at.%; C: 30 ~ 53 at.%; N: 15 ~ 35 at.% are accessible via tuning some key experimental parameters, e.g., the gas flow [157], substrate temperature [156], and microwave power [160] in CVD experiments, the powers applied to targets [158], and bias voltage [61] in magnetron sputtering experiments, the ratio of molecular fluxes of B, C, and N in ion beam assisted deposition (IBAD) experiments [159].

4.4 Mechanical Properties*

4.4.1 Young's Modulus

Despite the tremendous efforts of synthesizing B–C–N materials in experiments, the correlation between mechanical properties (in particular, the hardness) and chemical composition is still unclear yet. Nevertheless, the correlation is essential for achieving superhard B–C–N materials. Currently, the first–principles DFT calculations cannot directly compute the Vickers hardness (H_v) of a solid. In Figure 4.7, we collected a large number of experimental data of E and H_v from previous works based on amorphous B–C–N films [61, 71, 156, 158, 161-168]. A nearly linear dependence between Young's modulus and Vickers hardness ($E \approx 14.6H_v$) can be seen clearly. This allows us to roughly estimate the Vickers hardness of B–C–N solids using elastic moduli (B, G, and E) from first–principles calculations.

* Reference [7] in the list of publications

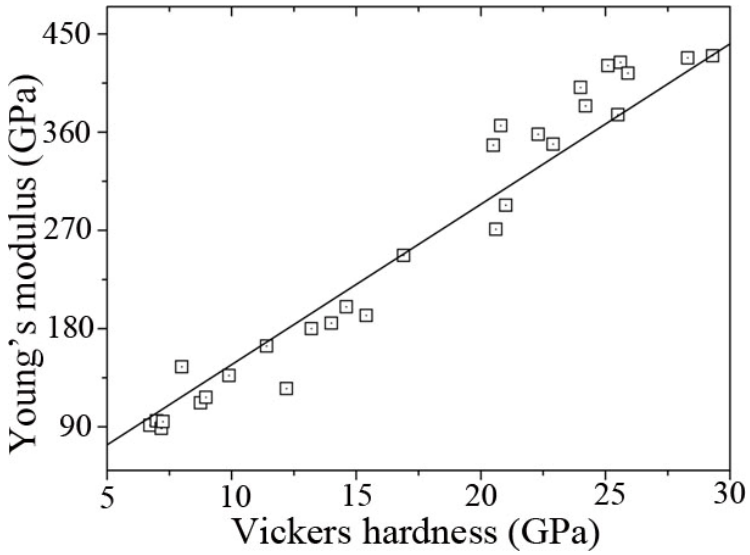

Figure 4.7: *Young's modulus versus Vickers hardness for amorphous B–C–N films. All these data are from previous experiments [61, 71, 156, 158, 161-168]. The straight line gives an approximate linear relationship as:* $E \approx 14.6H_v$.

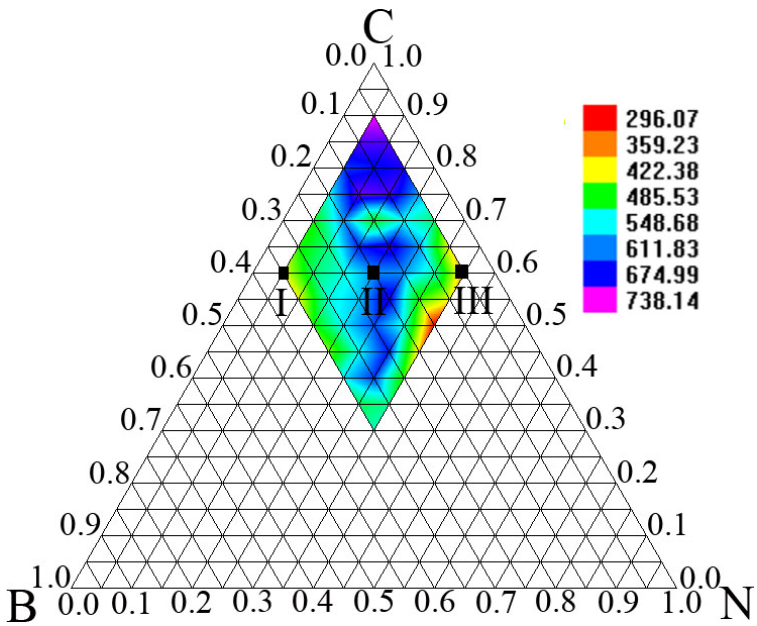

Figure 4.8: *Distribution of Young's modulus on the upper rhombus of the ternary B–C–N phase diagram using full spectrum. The superhard area (in purple and blue) shows a zonal distribution along the C–BN isoelectronic line. Compositions I, II and III are chosen as representative ones, shown in Figure 4.8 to interpret the distributions of Young's modulus.*

Figure 4.8 shows the distribution of Young's modulus on the upper rhombus of the ternary B–C–N phase diagram. In general, the carbon–rich compositions closer to the C vertex

possess higher Young's modulus (and hardness) since they are relatively closer to the original ta–C template. More importantly, the $B_xC_yN_z$ compositions along the C–BN isoelectronic line exhibit rather high values of Young's modulus (670 ~ 730 GPa) or Vickers hardness (45 ~ 50 GPa) that are comparable to those on the carbon–rich vertex. Therefore, superhard B–C–N solids (with hardness higher than 40 GPa) can be achieved in the zonal area along the C–BN isoelectronic line even with lower carbon contents.

4.4.2 Mechanism Interpretation

Previous work has demonstrated that B–C and C–N bonds are weaker than C–C and B–N bonds in the B–C–N systems [29]. In other words, breaking the B–C and C–N bonds is relatively easier than breaking the C–C and B–N bonds. Here three representative compositions, namely, **I** ($B_{0.347}C_{0.602}N_{0.051}$), **II** ($B_{0.199}C_{0.602}N_{0.199}$) marked in Figure 4.8 and **III** ($B_{0.051}C_{0.602}N_{0.347}$), are chosen to interpret the distributions of Young's modulus. The boron atoms in the optimized structure of composition **I** mainly form B–C bonds. Similarly, N atoms in system **III** mainly form N–C bonds. On the contrary, B, C and N atoms in the system **II** mainly exist in the form of C–C and B–N bonds. This means that it is not easy to deform structure **II** with relative to structure **I** and **III** under external loading. Indeed, B–C bonds in structure **I** and C–N bonds in structure **III**, as shown in Figure 4.9, are obviously changed (elongated or compressed) under 2.5% structural deformation. By contrast, B–N and C–C bonds in composition **II** show no obvious variation. This indicates that structures with more C–C and B–N bonds have better resistance to external loading. For such structures, their compositions are generally located along the isoelectronic C–BN line. That is why structures with the compositions distributed along the isoelectronic C–BN line have better mechanical properties comparing with other areas in the upper rhombus of the ternary B–C–N phase diagram.

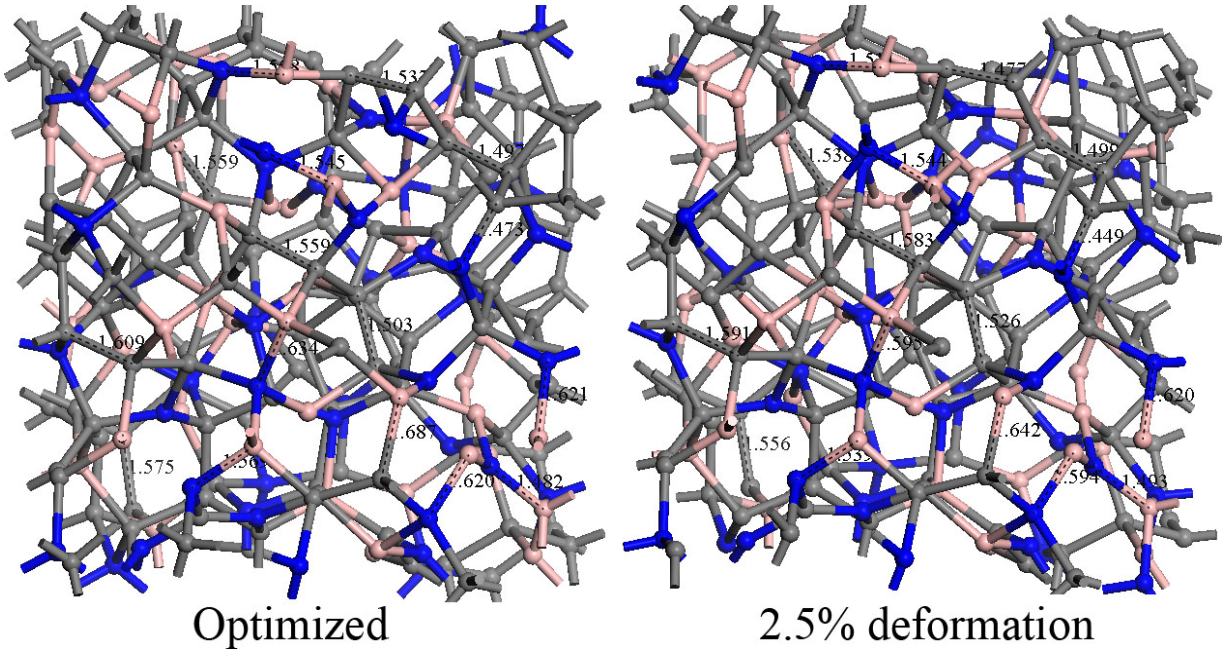

Figure 4.9: *Variations of one representative structure, with the composition II shown in Figure 4.8, after structure deformation. Left panel is the optimized structures and right panel is the deformed structures after applying 2.5% deformation on the optimized ones.*

It is noteworthy that the present theoretical hardness values cannot be compared directly with experimental hardness since our structural models typically contain higher sp^3 contents than the $B_xC_yN_z$ films synthesized in experiments. Besides, the experimentally measured hardness is affected by many factors such as film quality and local defects. Nevertheless, the theoretical prediction for the distribution of hardness in the ternary B–C–N phase diagram provides valuable guidance for purposely synthesizing B–C–N films with high hardness. In experiments, the B–C–N films with compositions in the zonal area of Figure 4.8 can be obtained by controlling carbon molecular beams using IBAD technique [159, 169]. If other experimental conditions that are in favor of sp^3 bonding (e.g., high substrate temperature [62]) can be realized, amorphous B–C–N films with excellent hardness (≥ 40 GPa) should be achieved according to our theoretical prediction.

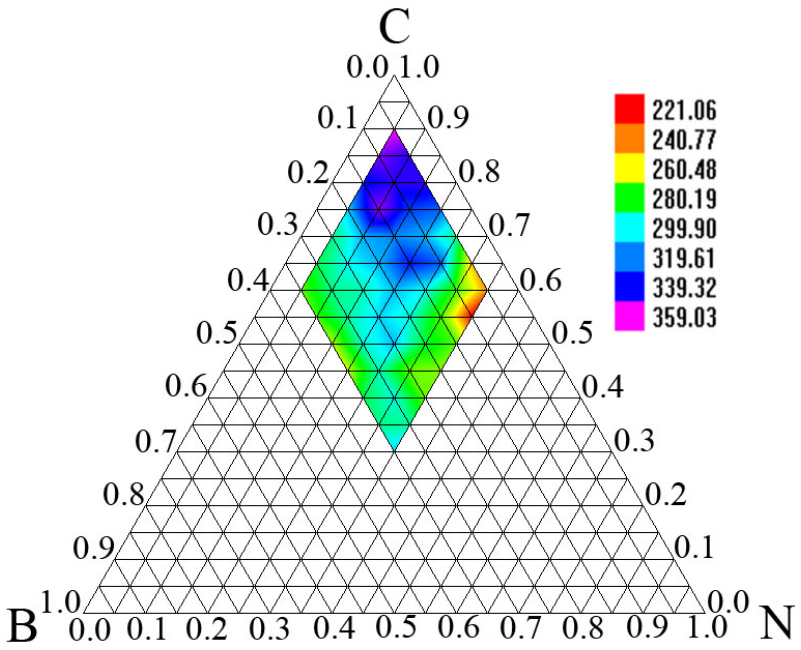

Figure 4.10: *Distribution of bulk modulus on the upper rhombus of ternary B–C–N phase diagram using full spectrum.*

4.4.3 Bulk Modulus

Figure 4.10 shows the distribution of bulk modulus on the upper rhombus of the ternary B–C–N phase diagram. In general, B–C–N compositions, distributed along the C–BN isoelectronic line, have higher bulk modulus comparing those located both sides of the corresponding isoelectronic line. The area that B–C–N compositions have the highest bulk modulus corresponds to the compositions with higher carbon concentration. It is not difficult to understand because the compositions with high carbon content are close to ta–C, therefore, they have higher bulk modulus comparing with other areas. Interestingly, the area with low bulk modulus does not correspond to those compositions with low carbon content. On the contrary, the area with the lowest bulk modulus is located at the range of N at.%: ~ 35 at.% and C at.%: 55 ~ 65 at.%. Furthermore, the compositions in this area have the highest nitrogen concentration within the range of our investigation. This indicates that amorphous B–C–N materials with higher nitrogen concentration can commonly weaken their bulk modulus. But of course boron and carbon concentrations in amorphous B–C–N materials can also determine the variation of the bulk modulus besides nitrogen concentration. These three quantities together control the changes of the bulk modulus.

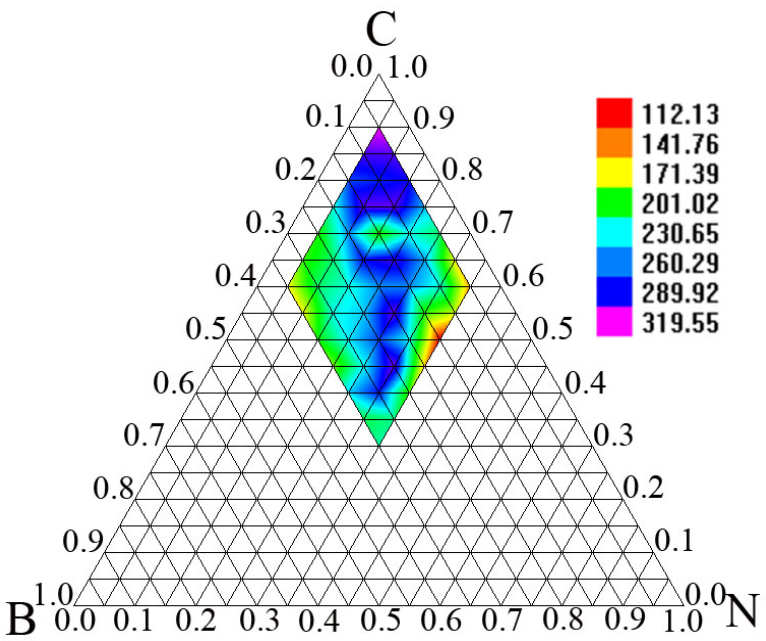

Figure 4.11: *Distribution of shear modulus on the upper rhombus of ternary B–C–N phase diagram using full spectrum.*

4.4.4 Shear Modulus

As shown in Figure 4.11, shear modulus also shows a similar trend as bulk modulus. That is, compositions along the C–BN isoelectronic line have higher values of shear modulus, and the area that compositions are close to the vertex angle of carbon has the highest values of shear modulus. As well, the area with the lowest shear modulus also corresponds to the highest nitrogen concentration. This means that higher nitrogen content is usually related to lower bulk and shear moduli. The difference from bulk modulus is that the area with the lowest shear modulus shifts towards a bit higher boron concentration comparing with the area that has the lowest bulk modulus as shown in Figure 4.10.

4.4.5 Ductility

In addition to the hardness, the ductility, defined as the ability to change shape without fracture, is also important for the mechanical behaviors of a material. It is necessary to explore the ductile properties of B–C–N materials. This is because low ductility (corresponding to high brittleness) may affect their potential applications even though they

possess extreme hardness. In Figure 4.12, we mapped the distribution of ductility on the B–C–N phase diagram. Within the composition range investigated, most $B_xC_yN_z$ solids exhibit better performance of resistance to stress cracking (namely, ductility), compared with ta–C (B/G ~ 1.0) and pristine diamond (B/G ~ 0.83). Remarkably, the $B_xC_yN_z$ materials in the area of B: 13 ~ 17 at.%; C: 48 ~ 52 at.%; N: 33 ~ 35 at.% have unexpected larger B/G values (B/G > 2.0), implying that their ductility is even better than some metals like TiCrN and Fe–Mg alloys [170, 171]. On the other hand, the composition area around the $B_{0.25}C_{0.45}N_{0.3}$ (B: 12 ~ 18 at.%; C: 42 ~ 48 at.%; N: 27 ~ 31 at.%) exhibits the lowest ductility ($B/G \approx 0.84$). After comparison of the ductility of these two compositions (i.e., $B_{0.25}C_{0.45}N_{0.3}$ and $B_{0.15}C_{0.5}N_{0.35}$), it can be deduced that properly decreasing B at.% or increasing N at.% may improve the ductile properties of B–C–N materials.

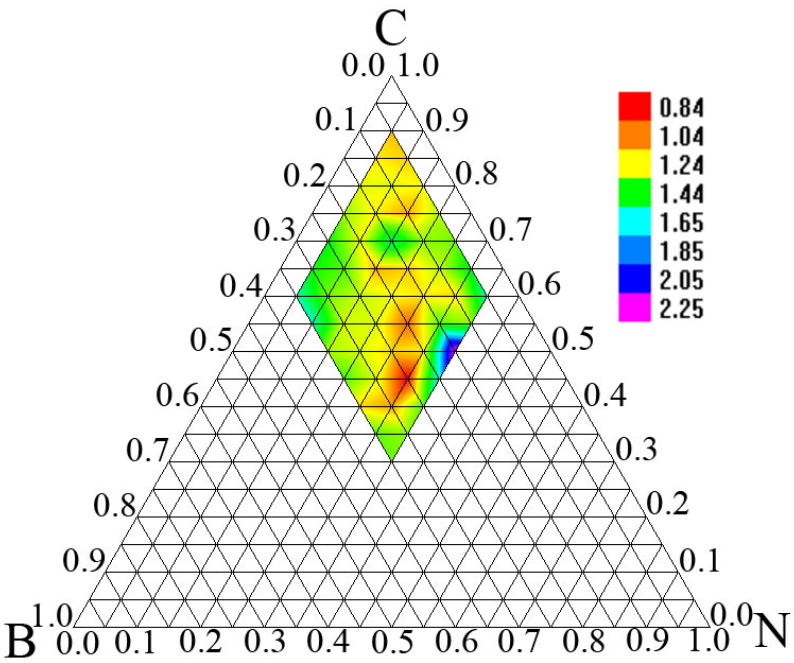

Figure 4.12: *Distributions of ductile property (characterized by B/G ratio) on the upper rhombus of the ternary B–C–N phase diagram using full spectrum. The area of B: 13 ~ 17 at.%; C: 48 ~ 52 at.%; N: 33 ~ 35 at.% (in blue and purple) exhibit higher ductility (B/G > 2.0).*

The theoretical results in Figures 4.8 and 4.12 together show that the area with excellent ductile properties has lower Young's modulus. Meanwhile, the zonal area along the C–BN isoelectronic line with higher hardness exhibits poor ductility. Hence, $B_xC_yN_z$ compositions

cannot possess extreme hardness and superior ductile properties simultaneously. As a compromise, according to our theoretical prediction the composition area within B: 15 ~ 30 at.%; C: 50 ~ 60 at.%; N: 20 ~ 30 at.% has appreciable Vickers hardness (37.6 ~ 46.2 GPa), good ductility (1.04 ~ 1.24) and low formation energies (–0.01 ~ 0.09 eV/atom), which might be potentially useful for future applications.

4.5 Summary

Based on ta–C structural model and first–principles calculations, the relationship between chemical compositions and mechanical properties of amorphous $B_xC_yN_z$ solids is fully understood on the ternary B–C–N phase diagram. Meanwhile, structural stabilities of these designed chemical compositions are also examined by the calculation of formation ability. Along the C–BN isoelectronic line, the formation energy show symmetric distributions, in which the compositions in the range of B: 15 ~ 35 at.%; C: 30 ~ 55 at.%; N: 15 ~ 35 at.% is relatively easier to form due to their negative formation energies. Most of the $B_xC_yN_z$ compositions synthesized in experiments are located in this area, showing the validity of our theoretical prediction. The Young's modulus and the ratio of bulk modulus and shear modulus (B/G) show zonal distributions along the C–BN isoelectronic line. The estimated Vickers hardness reaches as high as 45 ~ 50 GPa. Amazingly, for some peculiar compositions (B: 13 ~ 17 at.%; C: 48 ~ 52 at.%; N: 33 ~ 35 at.%), B–C–N solids exhibit certain ductile characteristic that is comparable to metals. As a compromise, B–C–N solids possess excellent hardness, good ductility, and good formation ability on the phase area (B: 15 ~ 30 at.%; C: 50 ~ 60 at.%; N: 20 ~ 30 at.%). These theoretical results provide valuable guidance for intentionally synthesizing $B_xC_yN_z$ materials with desirable mechanical properties for potential industrial applications.

5 Experimental Synthesis of Si, B, C and N-based Amorphous Materials

5.1 Amorphous B–C–N Materials*

In this chapter, experimental works of amorphous B–C–N materials were performed to demonstrate our theoretical results shown in the last chapter. As exhibited in the last chapter, the relation of chemical compositions, structural stabilities and mechanical properties has been built for amorphous B–C–N materials from our theoretical calculations.

With the aim of confirming our theoretical results, the experimental works here can be carried out as follows. The microstructure information of B–C–N samples can be characterized by various techniques such as infrared radiation (IR) and X–ray photoelectron spectroscopy (XPS). The mechanical properties, generally Young's modulus and hardness, can be evaluated by nanoindentation. The structural stabilities are based on the fact that whether amorphous B–C–N samples can be successfully obtained under certain experimental conditions. Therefore, chemical composition, structural stabilities and mechanical properties of amorphous B–C–N samples can also be correlated from the perspective of experiments. Thus the reasonability of theoretical results can be corroborated by comparing experimental results with theoretical ones.

To verify the structural stabilities, plenty of experimental works need to be performed to prepare amorphous B–C–N samples under diverse experimental conditions. Then we examine whether they can be successfully obtained under corresponding experimental conditions and whether they can exist stably when exposed to the atmosphere. Based on this consideration, diverse experimental parameters, i.e., gas flow ratio, working pressure, substrate temperature, bias voltage applied to substrate, sputtering power etc., were changed to prepare amorphous B–C–N samples by using magnetron sputtering technique. With regards to chemical

* References [9, 10] in the list of publications

compositions and microstructures, IR and XPS were employed to examine the bonding information and compositions in amorphous B–C–N samples. For mechanical properties, nanoindentation was used to collect the information of loading and displacement for further evaluation of hardness and Young's modulus.

5.1.1 Preparation Method

Magnetron sputtering was used to prepare amorphous B–C–N materials. The basic principle of magnetron sputtering is shown in Figure 5.1.1. Energetic ions excited by electrons under electric field move towards targets and impinge with targets. After energy exchange of energetic ions with atoms from targets, parts of the atoms from targets gain energy and impinge again with other atoms in targets, therefore forming cascade collision inside of targets. During the process, atoms near the surface of targets obtain enough energy to be continuously sputtered out, and then deposit on substrates to form films.

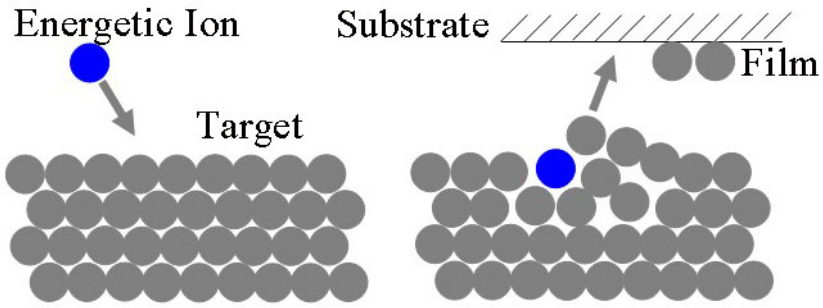

Figure 5.1.1: *Schematic plot of the basic principle of magnetron sputtering technique.*

The specific experimental conditions are shown as follows. All amorphous B–C–N films are deposited on silicon (100) substrate by radio frequency (13.56 MHz) reactive magnetron sputtering. High purity graphite (99.999%) and boron (99.9%) disks of 75 mm diameter and 5 mm thickness were used as targets in the mixed atmosphere of methane (CH_4), nitrogen (N_2) and argon (Ar) as the reactive gas. The deposition time was kept at 2 h. The base vacuum was below 5.3×10^{-6} Torr. The silicon substrates were dipped in a 5% hydrofluoric acid solution, ultrasonically cleaned in acetone, ethanol, and deionized water in sequence. Afterwards, they were dried up with nitrogen gas. Prior to deposition, the vacuum chamber was baked for 24 h

to reduce the moisture absorbed on the surface of vacuum chamber. The silicon substrate is sputter–cleaned in argon discharge with a bias voltage of – 750 V for about 15 min. The targets were pre–sputtered for about 30 min with a RF power of 100 W to remove the surface contamination and oxidation. During the deposition, the substrate holder was rotated uniformly to lower the inhomogeneity of both compositions and qualities of B–C–N films.

5.1.2 Experimental Parameters

Numerous experiments have been tried to prepare B–C–N films by magnetron sputtering methods under different experimental parameters. Among them, a number of amorphous B–C–N samples with different chemical compositions were successfully obtained. They are described as follows.

Samples #1–3 were obtained by sputtering the targets of boron and graphite under the atmosphere of $CH_4/N_2/Ar$ at room temperature. The fixed parameters were sputtering power (130 W for both targets). The gas flow ratio of $CH_4/N_2/Ar$ was 0/5/10 with the unit of sccm. No bias voltage was applied to substrate holder. The changed parameter was working pressure during the process of deposition. They were 0.5 Pa, 1.0 Pa, and 1.5 Pa, corresponding to samples #1–3, respectively. Samples #4–6 were prepared under different gas flow ratios of $CH_4/N_2/Ar$, i.e., 0/1/10, 0/5/10, 0/10/10, respectively. The fixed parameters were the sputtering power of both boron and graphite targets (130 W), the substrate temperature (400 ^oC), and the working pressure (1.0 Pa).

Samples #7–9 were synthesized under different sputtering powers of boron targets, which are 130 W, 200 W, and 260 W, respectively. Meanwhile, the sputtering power of graphite (130W), the substrate temperature (400 ^oC), the gas flow ratio of $CH_4/N_2/Ar$ (0/1/10), and the working pressure (1.0 Pa) were fixed during the deposition. Samples #10–13 were prepared by synchronously changing the sputtering power of boron and graphite, that is, 80 W, 100 W, 140 W, and 200 W, respectively. The fixed parameters were the substrate temperature (400 ^oC), the gas flow ratio of $CH_4/N_2/Ar$ (0/1/10), and the working pressure (1.0 Pa).

Samples #14–16 were synthesized by changing the substrate temperature. They are 25 ^oC,

200 ^{o}C, and 400 ^{o}C, respectively. The fixed parameters were the sputtering power (130 W), the gas flow ratio of CH_4/N_2/Ar (0/1/10), and the working pressure (1.0 Pa). Samples #17–19 were prepared by introducing CH_4 to replace the carbon source from the graphite target. The corresponding gas flow ratio was 2/10/20, 6/10/20, and 10/10/20, respectively. The sputtering power of boron target (130 W), the substrate temperature (25 ^{o}C), the working pressure (1.0 Pa), and the bias voltage (– 150 V) were kept constant during the preparation.

Samples #20–22 were prepared by using different bias voltages, namely, – 75 V, – 150 V, and – 200 V, respectively. The fixed parameters during the deposition process were the sputtering power of both boron and graphite targets (130 W), the substrate temperature (25 ^{o}C), the gas flow ratio of CH_4/N_2/Ar (0/5/10), and the working pressure (1.0 Pa), respectively. Samples #23–26 were also prepared under different bias voltages but with different substrate temperatures from those samples #20–22. The applied bias voltages were respectively 0 V, – 75 V, – 150 V, and – 200 V.

5.1.3 Chemical Compositions

The successful prepared samples were further characterized by XPS (ESCALAB250) to obtain the relative chemical compositions. Atomic concentrations were corrected by the corresponding sensitivity factors of 0.159, 0.296, 0.477 and 0.711 for B, C, N and O elements. After characterization by XPS, some samples have very near chemical compositions. The chemical compositions for B–C–N samples #1–26 are $B_{0.136}C_{0.653}N_{0.211}$, $B_{0.102}C_{0.633}N_{0.265}$, $B_{0.099}C_{0.629}N_{0.272}$, $B_{0.262}C_{0.47}N_{0.268}$, $B_{0.199}C_{0.544}N_{0.267}$, $B_{0.181}C_{0.568}N_{0.251}$, $B_{0.308}C_{0.437}N_{0.255}$, $B_{0.172}C_{0.619}N_{0.209}$, $B_{0.162}C_{0.643}N_{0.275}$, $B_{0.232}C_{0.515}N_{0.253}$, $B_{0.262}C_{0.478}N_{0.26}$, $B_{0.292}C_{0.433}N_{0.275}$, $B_{0.306}C_{0.419}N_{0.275}$, $B_{0.19}C_{0.571}N_{0.239}$, $B_{0.274}C_{0.488}N_{0.238}$, $B_{0.308}C_{0.437}N_{0.255}$, $B_{0.134}C_{0.668}N_{0.198}$, $B_{0.076}C_{0.802}N_{0.122}$, $B_{0.042}C_{0.875}N_{0.082}$, $B_{0.176}C_{0.551}N_{0.243}$, $B_{0.187}C_{0.551}N_{0.243}$, $B_{0.183}C_{0.557}N_{0.243}$, $B_{0.194}C_{0.532}N_{0.251}$, $B_{0.212}C_{0.51}N_{0.253}$, $B_{0.215}C_{0.503}N_{0.259}$, $B_{0.219}C_{0.499}N_{0.257}$, respectively. Experimental parameters together with chemical compositions were summarized in Table 5.1.1.

Table 5.1.1. *Amorphous B–C–N samples prepared under different experimental parameters.*

The chemical compositions characterized by XPS are also shown in the Table. B: boron sputtering power (W); C: carbon sputtering power (W); T: substrate temperature (^oC); Pressure: working pressure (Pa); bias: bias voltage (V).

Sample	B	C	T	$CH_4/N_2/Ar$	Pressure	Bias	Composition
#1	130	130	25	0/5/10	0.5	–	$B_{0.136}C_{0.653}N_{0.211}$
#2	130	130	25	0/5/10	1.0	–	$B_{0.102}C_{0.633}N_{0.265}$
#3	130	130	25	0/5/10	1.5	–	$B_{0.099}C_{0.629}N_{0.272}$
#4	130	130	400	0/1/10	1.0	–	$B_{0.262}C_{0.47}N_{0.268}$
#5	130	130	400	0/5/10	1.0	–	$B_{0.199}C_{0.544}N_{0.267}$
#6	130	130	400	0/10/10	1.0	–	$B_{0.181}C_{0.568}N_{0.251}$
#7	130	130	400	0/1/10	1.0	–	$B_{0.308}C_{0.437}N_{0.255}$
#8	130	200	400	0/1/10	1.0	–	$B_{0.172}C_{0.619}N_{0.209}$
#9	130	260	400	0/1/10	1.0	–	$B_{0.162}C_{0.643}N_{0.194}$
#10	80	80	400	0/1/10	1.0	–	$B_{0.232}C_{0.515}N_{0.253}$
#11	100	100	400	0/1/10	1.0	–	$B_{0.262}C_{0.478}N_{0.26}$
#12	140	140	400	0/1/10	1.0	–	$B_{0.292}C_{0.433}N_{0.275}$
#13	200	200	400	0/1/10	1.0	–	$B_{0.306}C_{0.419}N_{0.275}$
#14	130	130	25	0/1/10	1.0	–	$B_{0.19}C_{0.571}N_{0.239}$
#15	130	130	200	0/1/10	1.0	–	$B_{0.274}C_{0.488}N_{0.238}$
#16	130	130	400	0/1/10	1.0	–	$B_{0.308}C_{0.437}N_{0.255}$
#17	130	–	25	2/10/20	1.0	– 150	$B_{0.134}C_{0.668}N_{0.198}$
#18	130	–	25	6/10/20	1.0	– 150	$B_{0.076}C_{0.802}N_{0.122}$
#19	130	–	25	10/10/20	1.0	– 150	$B_{0.042}C_{0.875}N_{0.082}$
#20	130	130	25	0/5/10	1.0	– 75	$B_{0.176}C_{0.551}N_{0.253}$
#21	130	130	25	0/5/10	1.0	– 150	$B_{0.187}C_{0.551}N_{0.253}$
#22	130	130	25	0/5/10	1.0	– 200	$B_{0.183}C_{0.557}N_{0.243}$
#23	130	130	400	0/5/10	1.0	0	$B_{0.194}C_{0.532}N_{0.251}$
#24	130	130	400	0/5/10	1.0	– 75	$B_{0.212}C_{0.51}N_{0.253}$
#25	130	130	400	0/5/10	1.0	– 150	$B_{0.215}C_{0.503}N_{0.259}$
#26	130	130	400	0/5/10	1.0	– 200	$B_{0.219}C_{0.499}N_{0.257}$

5.1.4 Chemical Compositions vs. Experimental Conditions*

Previously experimental revealed that the physical properties of B–C–N films exhibit strong dependence on their chemical compositions. For example, the wear rate of BC_xN ($0.2 < x < 5.5$) films degraded from $1E^{-13}$ $m^3/N{\cdot}m$ to $1E^{-16}$ $m^3/N{\cdot}m$ as the carbon content increases from 20% to 80%. The electrical properties are also closely related to the compositions. As the carbon content in B–C–N films varied from 6% to 30%, the electrical resistivity decreases

* Reference [10] in the list of publications

remarkably from 1×10^{12} Ω·cm to 3.4×10^{9} Ω·cm. In addition, chemical compositions of B–C–N films also show obvious effect on their optical properties. The optical band gaps of B–C–N films were blue–shifted from 1.5 eV to 2.0 eV as the boron content increases from 10% to 25%.

Based on the fact that chemical compositions play an important role in determining the physical properties of B–C–N films, the first essential step toward tailoring the physical properties of the B–C–N films is to achieve controllable chemical compositions. Previous studies revealed that the chemical compositions were affected by various experimental parameters during the deposition of B–C–N films. However, no systematic investigation has been performed to understand the relation between experimental conditions and film compositions. Here we explored a series of experimental parameters including working pressure, substrate temperature, sputtering power, and CH_4/N_2/Ar flow ratio to discuss the dependence of the chemical compositions of B–C–N films on various experimental conditions. We found that the chemical compositions of amorphous B–C–N films can be roughly controlled by the combination of several key experimental parameters. The detailed effects of working pressure, substrate temperature, sputtering power, and flow ratio on the B–C–N compositions are individually discussed in the following subsections.

5.1.4.1 Working Pressure

The role of working pressure is shown in Figure 5.1.2. In general, the working pressure has only a little effect on the compositions of B–C–N films. In the cases of low working pressures (0.5 ~ 1.0 Pa), the compositions show slight fluctuation, i.e., 63 ~ 65% for C at.%, 10 ~ 14% for B at.%, and 21 ~ 26% for N at.%. As the working pressure is higher than 1.0 Pa, the variation of the B–C–N compositions is even less (62.9 ~ 63.3% for C at.%, 9.9 ~ 10.2% for B at.%, and 26.5 ~ 27.2% for N at.%). Therefore, changing the working pressure is not an efficient way to control B–C–N composition. Based on this finding, the following experiments were carried out with a constant working pressure of 1.0 Pa.

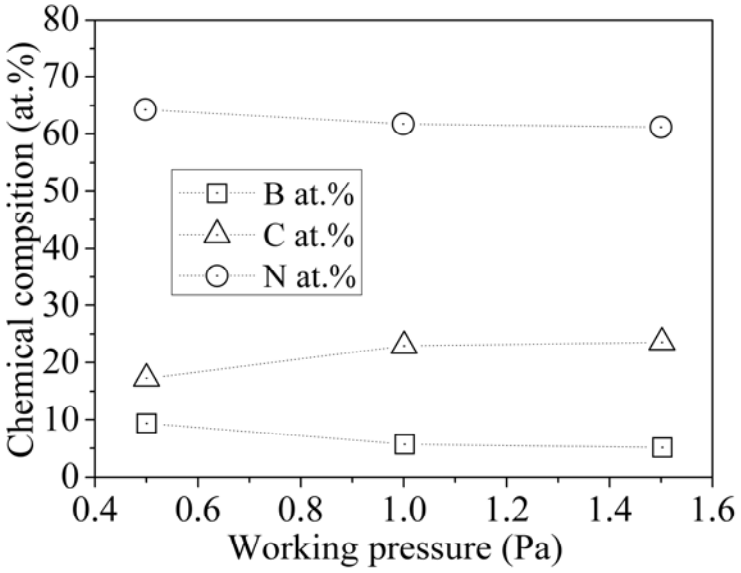

Figure 5.1.2: *B, C, and N atomic concentration as a function of working pressure.*

5.1.4.2 Substrate Temperature

With regard to the working pressure, the substrate temperature shows more pronounced effect on the compositions of B–C–N films. As shown in Figure 5.1.3, carbon concentration in B–C–N films decreases from 57 at.% to 43 at.% as the substrate temperature rises from 25 ^{o}C to 400 ^{o}C. The reduction of carbon fraction may be attributed to the formation of volatile $(CN)_2$ molecules at higher temperatures, as stated in Ref. [172]. In contrast, elevated substrate temperature benefits the inclusion of B content, which increases from 19 at.% to 27 at.%. The N concentration keeps around 24.5 at.%, nearly regardless of the substrate temperature. The oxygen impurity, which mainly originates from the water molecules on the vacuum chamber, is also affected greatly by the substrate temperature. When the substrate temperature rises up to 400 ^{o}C, the O fraction reduces to less than 3 at.%. Thus, elevating the substrate temperature is an efficient way to eliminate the oxygen impurity.

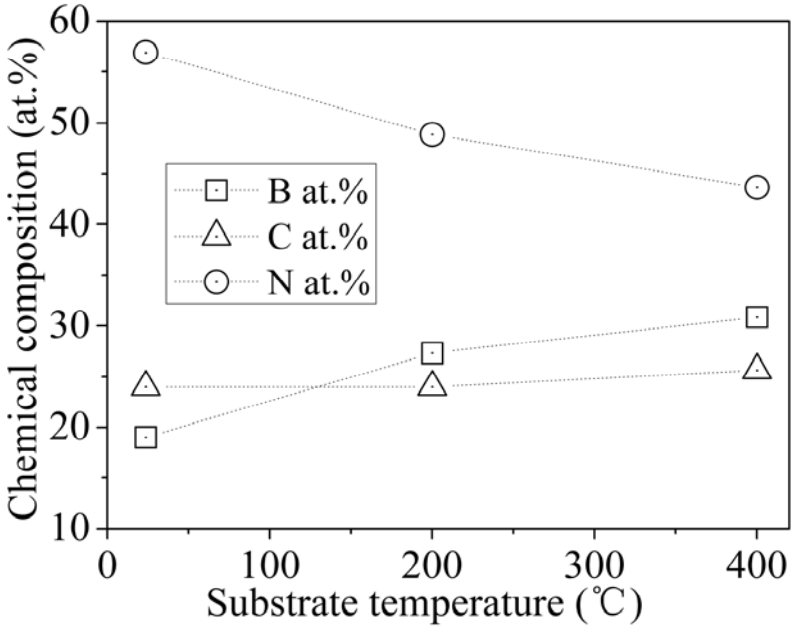

Figure 5.1.3: *B, C, and N atomic concentration as a function of substrate temperature.*

5.1.4.3 Sputtering Power

To study the effect of sputtering power applied to targets, two sets of power parameters were used: (I) changing only the power of graphite target with the values of 130 W, 200 W, and 260 W; (II) changing the powers of boron and graphite targets simultaneously corresponding to 80 W, 100 W, 140 W, and 200 W. The aim of these comparative experiments is to explore the possibility of tuning B–C–N compositions via sputtering power.

The relationship between sputtering power and film compositions is displayed in Figure 5.1.4. As the power applied to graphite target increases, the carbon, boron and nitrogen concentrations vary in the range of 44 ~ 64 at.%, 16 ~ 31 at.%, and 20 ~ 26 at.%, respectively. By contrast, simultaneous variations of the powers of boron and graphite targets show less effect on the compositions. The obtained B–C–N compositions vary in a narrower range, i.e., 42 ~ 51 at.% for carbon, 23 ~ 31 at.% for boron, 25 ~ 28 at.% for nitrogen. In addition, these two series of comparative experiments show opposite trends on the B–C–N compositions. In the cases of changing only the power of graphite target, the carbon content increases with target power while boron and nitrogen concentrations decrease. On the contrary, simultaneous increment of the powers of the two targets results in decrement of carbon content and

increment of boron and nitrogen fractions.

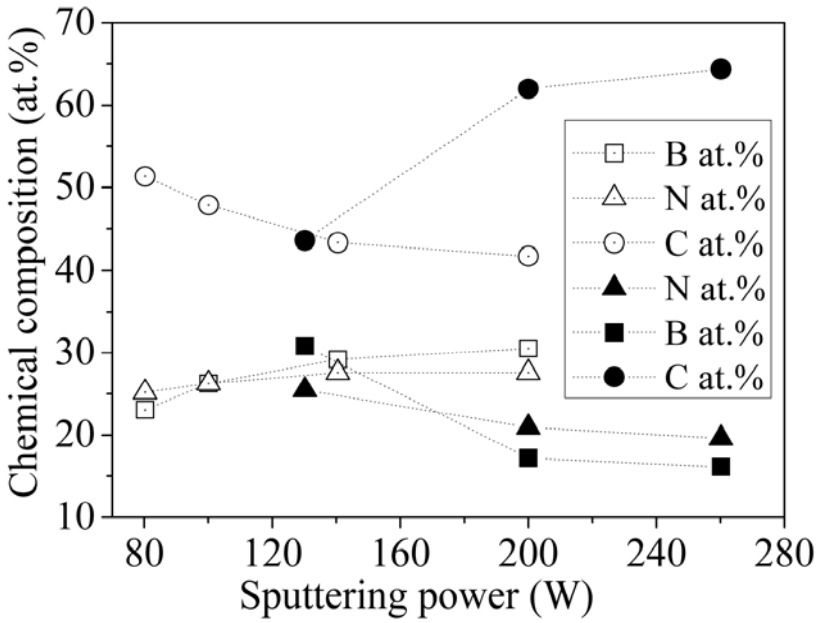

Figure 5.1.4: *Dependence of B, C, and N atomic concentration on the sputtering power. The compositions marked by solid symbols are obtained by changing the power of graphite target. The compositions marked by empty symbols are obtained by changing the powers of boron and graphite targets simultaneously.*

5.1.4.4 N_2/Ar Flow Ratio

Diverse kinds of reactive gases show different effects on the compositions of B–C–N films. We have shown that the chemical compositions are sensitive to the N_2/Ar flow ratio only in the lower range of N_2/Ar flow ratios [173]. Here, we introduced the CH_4 gas into the mixture of N_2/Ar. Interestingly, the carbon concentration in the synthesized B–C–N films can be evidently improved. As the CH_4/N_2/Ar flow ratio increases from 2/10/20 to 10/10/20, the carbon content becomes higher than 65 at.% (Figure 5.1.5). Within the range investigated, a maximum carbon content of ~ 87 at.% can be achieved as the CH_4/N_2/Ar flow ratio increases up to 10/10/20. After carefully analyzing the FTIR and XPS data of these compositions, we find that most of the carbon atoms in such B–C–N films exist as C = C bonds. In other words, the introduced carbon source from the CH_4 reactive gas prefer to forming the C = C bonds.

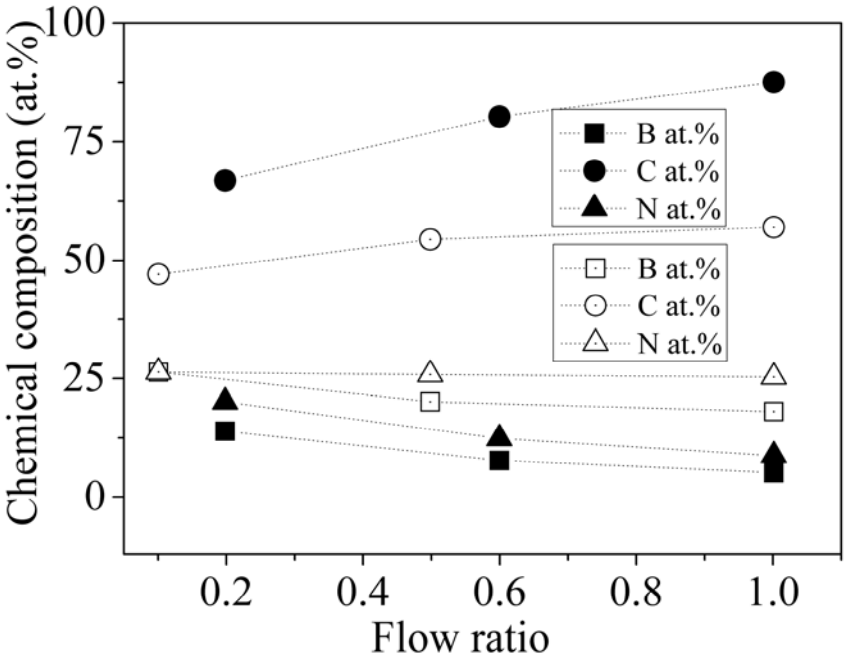

Figure 5.1.5: *Dependence of B, C, and N atomic concentration on gas flow ratios. The compositions marked by empty symbols are obtained by raising the flow ratio of N_2/Ar from 1/10 to 10/10. The compositions marked by black symbols are obtained by changing the flow ratio of CH_4/N_2/Ar from 2/10/20 to 10/10/20.*

5.1.5 Comparison with Theoretical Results

These obtained chemical compositions were collected and shown in the ternary B–C–N phase diagram. As shown in Figure 5.1.6, within the variation range of our experimental parameters, all samples are located in the upper rhombus, which correspond to our theoretical calculations as demonstrated in the last chapter.

Overall speaking, almost all the compositions distribute along the C–BN isoelectronic line and the C compositions span in a broad range (from 28 at.% to 87 at.%). It is of great interests that the trend of forming amorphous B–C–N materials is almost the same compared with the easier forming area (B: 15 ~ 35 at.%; C: 30 ~ 53 at.%; N: 15 ~ 35 at.%). That is, most of these compositions are located in the lower part of the rhombus. According to our theoretical results, this area is related to amorphous B–C–N samples with low formation energies. In other words, compositions in this area are easier to be obtained comparing with

other area of the upper rhombus. These results are consistent with our theoretical calculations, showing directly the reasonability of our theoretical calculations.

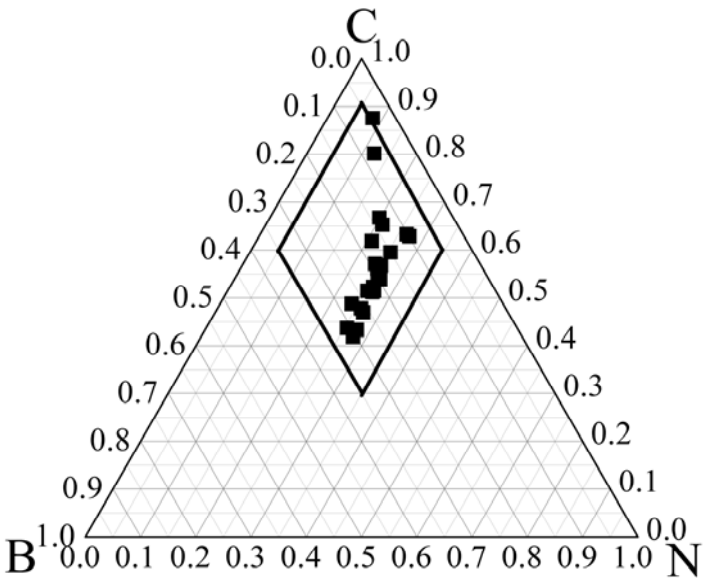

Figure 5.1.6: *Amorphous B–C–N samples with obtained chemical compositions are shown in the ternary B–C–N phase diagram. All samples that were successfully synthesized within the varied range of experimental parameters are located the area that has been studied by our theoretical calculations and they are mainly located at the area with low formation energies as indicated in the last chapter, directly verifying the reasonability of our theoretical results.*

5.1.6 Structural Characterization*

5.1.6.1 XRD

For all synthesized B–C–N films, X–ray diffraction (XRD) (D8 DISCOVER) with a Cuk$_\alpha$ radiation (40 kV, 40 mA) was employed to characterize the structures of synthesized B–C–N films. Figure 5.1.7 shows one representative XRD pattern of our obtained amorphous B–C–N samples. The XRD pattern of pure silicon substrate is also shown for comparison.

As shown in Figure 5.1.7, The XRD pattern of the B–C–N sample shows no distinct peak within the selected Bragg angle 2θ (20° ~ 80°) beyond the very sharp peak located at ~ 69^o,

* References [9, 10] in the list of publications

which corresponds to 400 peak of silicon substrate. The peak at ~ 69^{o} is so strong that it may cover other weak peaks from B–C–N samples. Therefore, the XRD pattern of the B–C–N film with the sharp peak masked is shown again as the inlet in the Figure 5.1.7. As well, no distinct peak can be observed clearly. This reveals that the B–C–N sample has the amorphous structure. Besides this one, we also checked a handful of other B–C–N films and all of them show the similar feature. Therefore, under the experimental conditions that we employed, our obtained B–C–N samples are mainly amorphous.

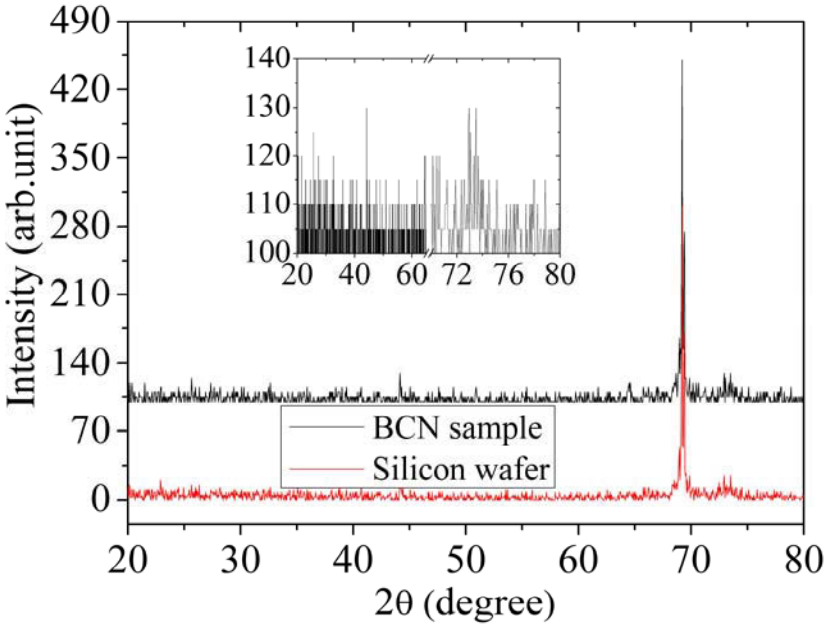

Figure 5.1.7: *A representative XRD pattern of our B–C–N samples (#2). The XRD pattern of the silicon substrate is also shown for comparison.*

5.1.6.2 Infrared Spectra

Bonding states in amorphous B–C–N samples are characterized by FTIR (NEXUS). Previous works have shown that film thicknesses have great influence on IR and XPS spectra. Therefore, before the IR analysis, the thicknesses of our B–C–N films are firstly measured by 3D Surface Profiler (Zygo NewView 5022). After measurements, we find that all our films have an approximate thickness of 700 nm.

Here IR spectra of the series of B–C–N films obtained under different gas flow ratios (samples #4–6) are chosen for analysis and displayed in Figure 5.1.8. IR spectra of the silicon

substrate and graphite target are also shown for comparison. IR spectrum of the pure boron not included in Figure 5.1.8 shows no noticeable absorption peak between 650 cm^{-1} and 2500 cm^{-1}, consistent with the previous results by Linss et al.[161].

Broad absorption peaks between 1100 cm^{-1} and 1700 cm^{-1} for the IR spectra of B–C–N films can be clearly seen from Figure 5.1.8. After subtracting the background IR intensities from the substrate and graphite target, the broad peaks in the range of 1100–1700 cm^{-1} remain remarkable, indicating that various chemical bonds are truly formed. Considering the effect of internal stress in the synthesized films, the broad absorption peaks should be contributed from the B–C, C–N, B–N, C–C (sp^2) bonds centered at 1100 cm^{-1} [174, 175], 1270 cm^{-1} [176], 1400 cm^{-1} [177, 178], and 1600 cm^{-1} [71], respectively. The abroad peaks around 2200 cm^{-1} and 600 cm^{-1} are attributed to the C ≡ N bonds [161] and Si–Si bonds [179], respectively. Most of these bonds do not exist in the boron and graphite targets except for the C–C (sp^2) bonds from the graphite target. Therefore, the IR peaks associated with the B–C, C–N, B–N bonds clearly demonstrate microscopic mixing of the three component elements (B, C, and N) in these B–C–N samples. In other words, B–C–N films deposited from boron and graphite targets can form atomic hybridization.

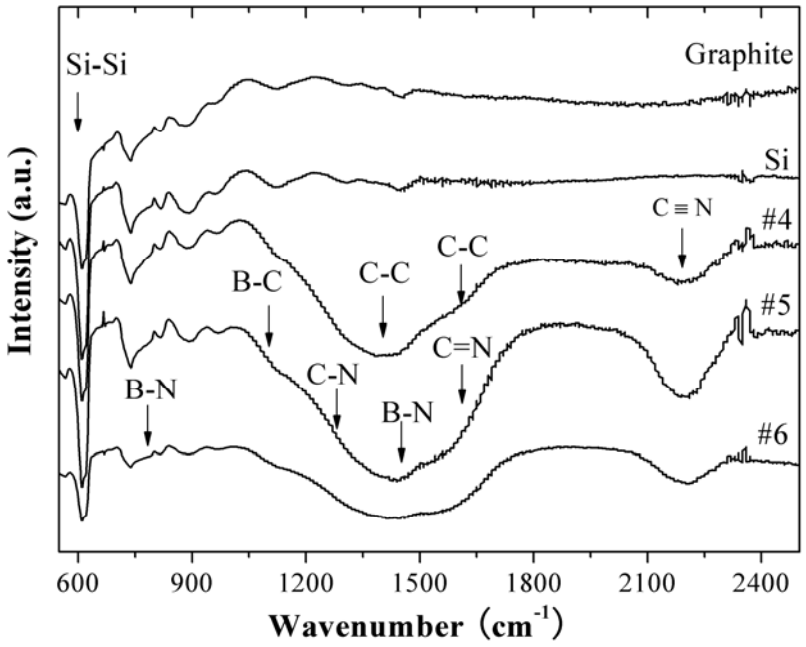

Figure 5.1.8: *IR spectra of B–C–N films (samples #4–6) deposited with different N_2/Ar flow ratios. The samples are obtained from boron and graphite targets with the N_2/Ar flow ratio of*

1/10, 5/10, and 10/10, respectively. The IR spectra of silicon substrate and graphite targets are also shown for comparison.

Figure 5.1.9 shows the IR spectra of B–C–N samples (#10–13) obtained under different sputtering powers of boron and graphite targets. All these IR spectra exhibit a broad absorption band in the range of 1100 ~ 1700 cm^{-1}. Two distinct absorption regions around 2200 cm^{-1} and 1400 cm^{-1} are observed. In general, the peak around 2200 cm^{-1} is assigned to C ≡ N bonds [180, 181] and the broad peak around 1400 cm^{-1} may be originated from the B–C, C–N, B–N, and C = C bonds centered at 1100 cm^{-1} [61, 69], 1300 cm^{-1} [182], 1400 cm^{-1} [158, 183], and 1600 cm^{-1} [184], respectively. As the sputtering power increases from 80 W to 140 W, the intensity of the absorption region around 1400 cm^{-1} is enhanced, indicating that the corresponding chemical bonds at this region are strengthened. Further increasing the sputtering power reduces the intensity of the absorption region, revealing that high sputtering power is detrimental to the formation of chemical bonds in B–C–N films.

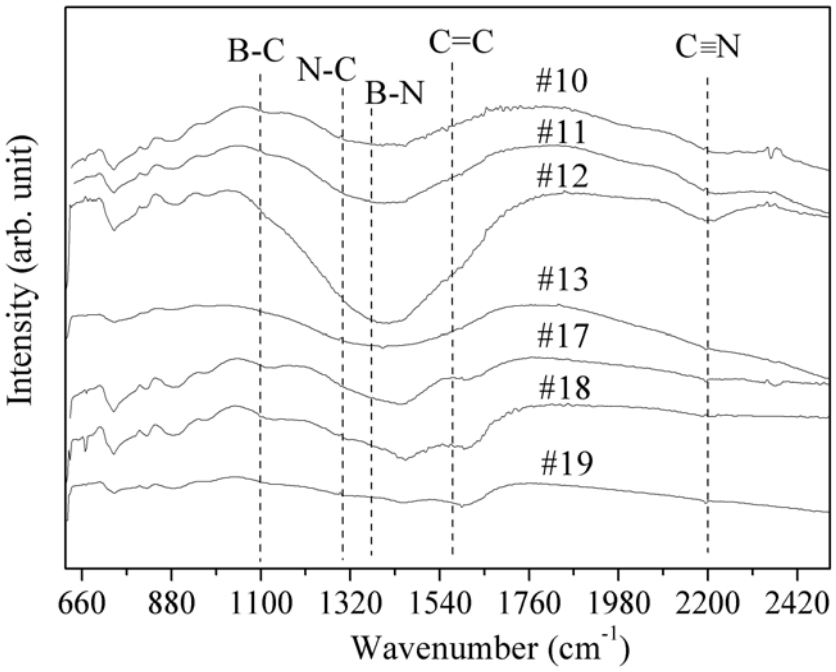

Figure 5.1.9: *IR spectra of B–C–N films obtained by changing the sputtering powers of boron and graphite targets (Samples #10–13) and by changing the $CH_4/N_2/Ar$ flow ratio (Samples #17–19). The applied sputtering power for samples #10–13 is 80 W, 100 W, 140 W, and 200 W, respectively. The $CH_4/N_2/Ar$ flow ratio is 2/10/20, 6/10/20, and 10/10/20, respectively.*

Figure 5.1.9 also presents the IR spectra of B–C–N films prepared by introducing methane into the reactive gases (#17–19). These spectra show apparent difference from those of samples (#10–13). When the CH_4 gas is introduced into the mixture of N_2/Ar, the absorption peak at 2200 cm^{-1} almost disappears while the IR peak at 1600 cm^{-1} emerges. Since these two peaks are usually assigned to C ≡ N (2200 cm^{-1}) and C = C (1600 cm^{-1}) bonds, the changes of IR spectra suggest that the C active groups in the plasma introduced by the CH_4 gas are beneficial for the formation of C = C bonds. As the CH_4/N_2/Ar flow ratio increases from 2/10/20 to 10/10/20, the intensity of the absorption peak at 1600 cm^{-1} increases, implying that more C = C bonds may be formed. Since the B–C, C–N, C = C, B–N, and C ≡ N bonds do not come directly from the boron and graphite targets, we infer that most of these bonds were formed during the deposition of B–C–N films. Therefore, the synthesized B–C–N films were not the products of separated phases of h–BN and graphite.

5.1.6.3 X–ray Phonon Spectra

XPS (ESCALAB250) is also used to examine the detail bonding states in amorphous B–C–N films. For the XPS measurement, a monochromatized Alk_α radiation (photon energy 1486.6 eV) was used as the excitation source. Before the measurement, B–C–N films were pre–sputtered for 60 s to clean the surface contamination. Figure 5.1.10 shows the variations of the atomic concentration of B, C, N, and O as a function of etching time from sample #6. It can be seen clearly that the atomic concentrations of B, C, N, and O are not changed after etching 30 s. Therefore, all the XPS information is taken after the pre–sputtering surface contamination. The full spectrum is shown in Figure 5.1.10b, showing that our samples mainly contain B, C, N, and O elements.

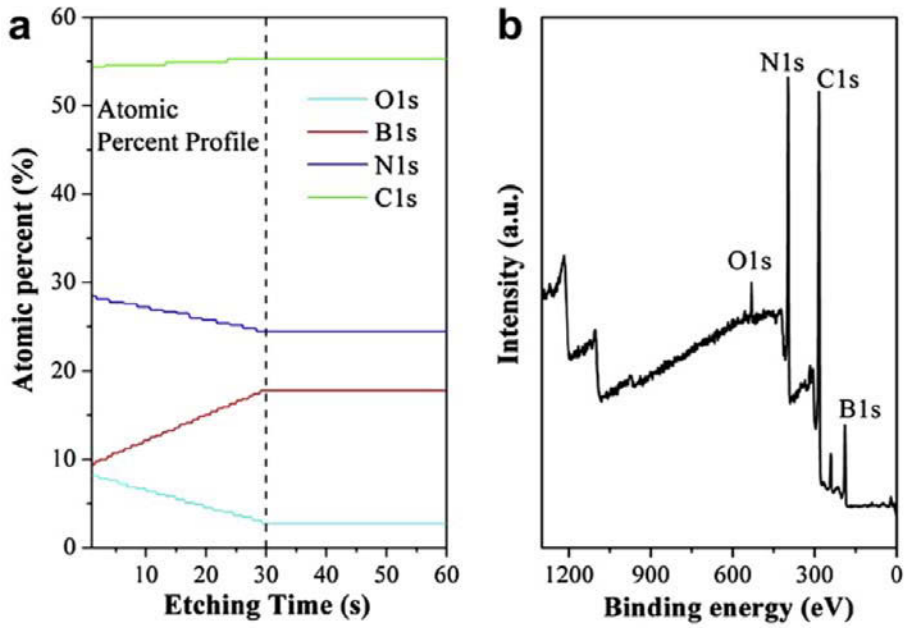

Figure 5.1.10: *Representative XPS characterization of sample #6. (a) Atomic concentration of B, C, N, and O as a function of etching time. (b) Full spectrum of B–C–N film from sample #6.*

Figure 5.1.11 shows the XPS spectra of the B1s, C1s, and N1s components for sample #6, which was obtained under the N_2/Ar gas flow ratio of 10/10 with the substrate temperature at 400 ^{o}C. The FWHM of the B1s main peak is about 2.8 eV, larger than that of BN film (~ 0.92 eV) [185], implying that the B atoms in the B–C–N film may be chemically bonded to C, N or O atoms in different ways from those in BN films.

The peak fitting of B1s spectrum reveals that it is composed of B–N (sp^3), B–N (sp^2), B–C ($BC_{3.4}$) and B–C (B_4C) located at 191 eV [186], 190.5 eV [61, 187], 189.4 eV [61, 187], and 188.4 eV [61], respectively. The FWHM of the main peaks of C1s and N1s spectra is about 3 eV, also wider than those of graphite (~ 0.35 eV) and BN (~ 0.92 eV) [185]. Similarly, decomposition of the C1s spectrum yields the components of C ≡ N (286.4 eV) [188], C–N(sp^2) (285.9 eV) [189], C–C(sp^2) (284.5 eV) [61] and B–C (283.5 eV) bonds [62], respectively; and the N1s spectrum can be decomposed into B–N(sp^2) (398.0 eV) [183], C ≡ N (398.4 eV) [190], C–N(sp^2) (399.3 eV) [59], and N–O (402.5 eV) bonds [191], respectively. The peak positions and corresponding FWHW values after decomposition are summarized in Table 5.1.2.

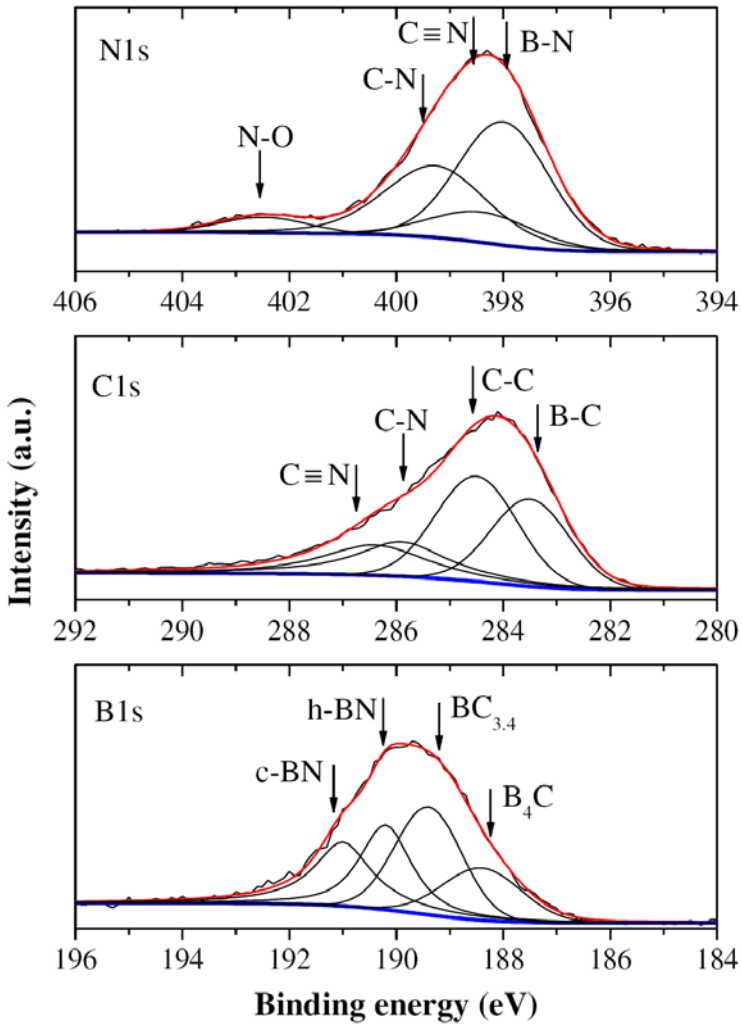

Figure 5.1.11: *Representative XPS spectra of B1s, C1s, and N1s from sample #6. These spectra are fitted by different small peaks corresponding to different bonding states. The red and blue curves represent the fitting curve of the main peaks and the background shapes.*

Figure 5.1.12 shows another XPS spectra of sample #13 obtained under different experimental parameters from that of sample #6. The sample #6 was obtained under the sputtering power of 200 W and the N_2/Ar flow ratio of 1/10. The full width at half maximum (FWHM) of B1s main peak (~ 2.5 eV) is wider than that of BN film (~ 0.92 eV) [185], suggesting that more than one chemical bonding states are involved. Fitting the B1s main peak yields three different peaks at 192.0 eV, 190.6 eV, and 189.4 eV, which can be attributed to B–O [61], B–N [192], and B–C bonds [158], respectively.

Table 5.1.2. *Peak position, possible bonding state, and FWHM of B1s, C1s, and N1s spectra of sample #6 corresponding to the decomposition peaks in Figure 5.1.11. The FWHM values*

from previous works are also shown for comparison. References a–e corresponds to Ref.[192], Ref.[189], Ref.[193], Ref.[188], and Ref.[179], respectively.

Sample #6	Peak Position (eV)	Possible Bond	FWHM (eV)	References FWHM (eV)
B1s	188.4	B–C (B_4C)	1.7	1.8[a]
	189.4	B–C ($BC_{3.4}$)	1.5	1.9[e]
	190.2	sp^2–BN	1.1	1.2[a]
	191	sp^3–BN	1.3	–
C1s	283.5	B–C (B_4C)	1.7	2.0[c]
	284.5	sp^2–CC	1.8	2.3[b]
	285.9	sp^2–CN	2.0	2.5[b]
	286.4	C ≡ N	2.3	2.1[c]
N1s	398.0	sp^2–BN	2.0	2.0[b]
	398.4	C ≡ N	2.3	2.0~2.7[d]
	399.3	C–N	2.3	2.1[b]
	402.5	N–O	1.9	–

The FWHM of C1s and N1s main peaks are ~ 3.2 eV and ~ 2.5 eV, which are broader than those of graphite (~ 0.35 eV) and BN film (~ 0.92 eV), indicating the existence of various bonding states. Similar analysis gives C ≡ N (286.7 eV) [188], C–N (285.9 eV) [60], C = C (284.5 eV) [183], and B–C (284.2 eV) bonds [194] for C1s, C–N (400.3 eV), B–N (398.8 eV), C ≡ N (398.4 eV) bonds for N1s, respectively. The XPS results reveal the existence of B–C, B–N and C–N bonds in the films, which further confirms that the synthesized B–C–N films are microscopic compound of C, B, and N, not the macroscopic mixture of carbon and BN.

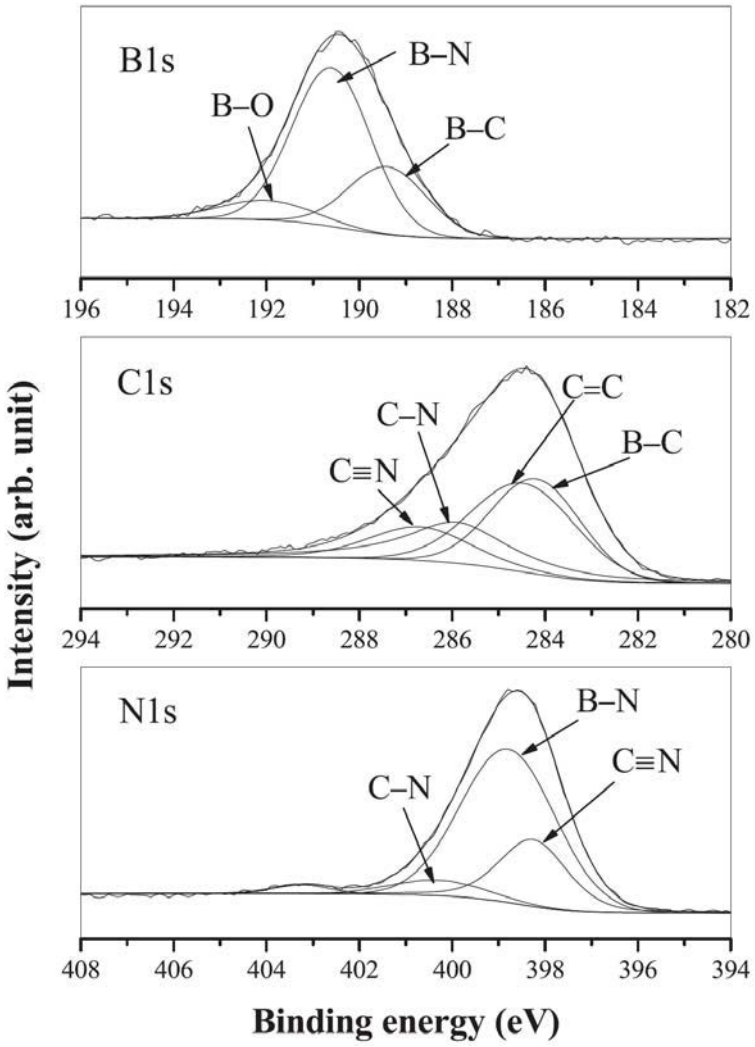

Figure 5.1.12: *Representative XPS spectra of B1s, C1s, and N1s from sample #13. These spectra are fitted by different small peaks corresponding to different bonding states.*

5.1.6.4 Shifts of XPS Peaks

During XPS analysis, we found that the positions of the main peaks of B1s, C1s, and N1s are also affected by the variations of experimental parameters. Here we show representatively the results of the series of B–C–N films (samples #4–6) obtained under different N_2/Ar flow ratios. Table 5.1.3 summarizes the position of the main B1s, C1s, and N1s peaks, all of which shift toward higher binding energies as the N_2/Ar flow ratio increases. For example, the main B1s peak shifts from 189.5 eV to 189.7 eV and then to 189.8 eV as the flow ratio of N_2/Ar increases from 1/10 to 5/10 and to 10/10. Same effect is observed for the C1s and N1s peaks, i.e., from 283.8 eV to 284.4 eV and to 284.5 eV for C1s; from 397.8 eV to 398.3 eV and to

398.5 eV for N1s as the N_2/Ar flow ratio rises.

The shifts of the main peaks of B1s, C1s, and N1s spectra can be related to the changes of bond environment in amorphous B–C–N films. Shift of the main C1s peaks toward higher binding energies indicates that more C atoms are bonded to N atoms due to the electronegative differences of B and N atom. Therefore, the corresponding C–N bond fractions increase while B–C bond fractions decrease as the N_2/Ar flow ratio increases. The respective increments and decrements of C–N and B–C bond contents in the deconvoluted peaks result in the shift of C1s main peak toward higher binding energies.

Here we also summarized the corresponding bond fractions for different bonding states in our B–C–N films, and showed them together in Table 5.1.3. As shown in Table 5.1.3, the C–N bond contents increase from 4.4% to 17.5% and then to 20.7% while the B–C bond contents decrease from 25.1% to 23.4% and then to 15.5% as the flow ratios of N_2/Ar increase. On the other hand, shifts of the main B1s and N1s peaks toward higher binding energies are related to the combined influence of different bond contents tuned by the N_2/Ar flow ratio, i.e., B–C, B–N, and B–O bond contents for B1s; N–B, N–C, and N–O bond contents for N1s.

Table 5.1.3. *Main peak shifts of B1s, C1s, and N1s spectra and relevant bond fractions from XPS analysis for the series of B–C–N films (samples #4–6) with relative to different gas flow ratios. The X–N represents the summation of C–N and O–N bond fractions.*

Sample	N_2/Ar	B1s			C1s			N1s		
		Peak	Bond (%)		Peak	Bond (%)		Peak	Bond (%)	
		(eV)	N–B	B–C	(eV)	N–C	C–B	(eV)	X–N	N–B
#4	1/10	189.5	7.8	14.7	283.8	4.4	25.1	397.8	11.6	7.7
#5	5/10	189.7	6.7	10.2	284.4	17.5	23.4	398.3	10.4	16.9
#6	10/10	189.8	8.1	8.0	284.5	20.7	15.5	398.5	13.7	12.1

5.1.7 Mechanical Properties

To examine the mechanical properties of these films, nanoindentation experiments were also carried out using the MTS XP system with a Berkovich diamond indenter. Here the series

of B–C–N films obtained by changing the N_2/Ar flow ratio are chosen for analysis. As shown in Table 5.1.4, the samples #4–6, synthesized at elevated substrate temperature, possess comparable mechanical properties. That is, the values of Vickers hardness for these samples are all around 10 GPa. In other words, as the flow ratio of N_2/Ar increases from 1/10 to 10/10, the hardness of the BCN films hardly changes.

In a previous study, Linss et al. [165] also reported that the hardness of B–C–N films fluctuated within a small range (7 ~ 10 GPa) when the N_2/Ar was higher than 10%. From the bond content analysis, we find that the B–C–N films synthesized under the current experimental conditions contain a large portion of sp^2 bonding states, which weakens the hardness of B–C–N films. To achieve hard B–C–N films, it would be crucial to reduce the sp^2 bonding states. Our further efforts on this direction are still under way.

Table 5.1.4. *Bond fractions of B–C, B–N, and C–N in samples #4–6. They were calculated from the corresponding decomposed peaks of B1s, C1s, and N1s spectra. The values of hardness of these samples are also listed.*

Sample	N_2/Ar	Bond content (%)			Hardness
		B–C	B–N	C–N	(GPa)
#4	1/10	39.8	15.5	15.4	10.6
#5	5/10	45.3	23	20	10.5
#6	10/10	23.5	20.2	32.9	10.2

5.1.8 Summary

Amorphous B–C–N films were synthesized on the silicon (100) substrate using radio frequency magnetron sputtering technique from boron and graphite targets by adjusting a series of experimental parameters. The bonding characteristics and chemical compositions of B–C–N films were characterized by FTIR and XPS. They were employed to examine whether the obtained B–C–N films are simply the products of phase separation or really atomic hybridization among B, C, and N atoms. The results from FTIR and XPS analysis confirm that our B–C–N films obtained from boron and graphite targets, not h–BN and graphite targets, can achieve atomic hybridization according to various bonding states in the spectra of

FTIR and XPS.

Within the current experimental conditions, the preferred B–C–N compositions mainly distribute along the C–BN isoelectronic line on the ternary phase diagram. Almost all the compositions that are obtained are located at the area corresponding to the area chosen for theoretical calculations. And furthermore, most of these compositions are distributed in the lower parts of the upper rhombus (low C content). In this area, B–C–N compositions are easier to be obtained according to the formation energy revealed by theoretical results that are presented in the last chapter. In other words, our experimental results are consistent with our theoretical prediction.

According to our experimental results, B–C–N compositions with low C contents can be obtained by decreasing the N_2/Ar flow ratio, increasing the power of boron and graphite targets simultaneously, or raising the substrate temperature; those carbon–rich compositions can be prepared by introducing the CH_4 gas into the mixture of N_2/Ar. In short, the compositions in the area with low carbon content can be roughly controlled by changing experimental parameters. Therefore, it is possible to control the compositions of B–C–N films by adjusting a set of experimental parameters. The present results are important for fabricating B–C–N films with destination compositions and consequently desirable physical properties.

The positions of the main peaks of B1s, C1s, and N1s spectra from XPS analysis are also affected during the variations of experimental parameters. For example, with increasing N_2 /Ar flows ratio, main peaks of B1s, C1s, and N1s spectra shift toward higher binding energies. The underlying mechanism behind this phenomenon can be attributed to the changes of the bonding environments under different experimental conditions, which can be described by the corresponding variations of different bond contents. Since the properties of materials are directly related to micro–structures at micro scale, the bond fractions and the peak shifts can give a deep understanding of the behaviors of materials such as mechanical, electrical, and optical properties.

5.2 Amorphous Si–C–N Materials*

For amorphous B–C–N materials, one of the most serious problems is the poor adhesion to the surface of silicon substrates. After a few methods were tried to improve the adhesive problem, we found that the addition of silicon element can greatly improve the adhesion between film and silicon substrate. This is probably because that silicon element can play a crucial role in connecting deposited films strongly with silicon substrates. In this section, we attempt to replace boron by silicon element to prepare ternary Si–C–N materials. Before preparation, a short introduction of Si–C–N materials is firstly given.

Binary compounds composed of silicon (Si), carbon (C) and nitrogen (N) have attracted significant attention during the last three decades [195-201]. For example, covalent bonded β–C_3N_4 has been predicted to have a high bulk modulus of 437 GPa [197]. This can be comparable to that of diamond (442 GPa) [195]. Silicon nitride has high hardness [196], good fracture toughness [198] and excellent wear resistance [199]. Its oxidation resistance can even reach up to ~ 1600 K [200]. Silicon carbides have superior stability at high temperature. They have been exploited for fusion and nuclear devices [201]. Therefore, the hybridization of the three elements to form ternary Si–C–N materials is expected to combine the excellent properties of carbon nitride, silicon nitride and silicon carbide. So far, this kind of materials has been extensively investigated for potential industrial applications [202-210].

At present, frequently used methods to prepare ternary Si–C–N materials are sputtering [202, 205, 207, 209] and chemical vapor deposition (CVD) techniques [203, 204, 206, 208, 210]. For sputtering method, the obtained Si–C–N materials can keep majority bonding states from SiC targets without breaking chemical bonds. In other words, phase separation can be commonly observed in such hard coatings [211]. For CVD method, substrate heating is commonly used to synthesize Si–C–N materials [203, 204, 208, 210]. Preparation of such materials at evaluated temperature may limit their broad applications. Here we attempt to prepare a series of ternary Si–C–N films without substrate heating by electron cyclotron resonance chemical vapor deposition technique (ECR–CVD). This subsection is organized

* Reference [6] in the list of publications

first to give the general preparation and characterization of amorphous Si–C–N materials. With regards to hardness of thin films, mechanism behind hardness and substrate effect are two important aspects that are worth to be further investigated. The remaining subsections are devoted to the exploration of the underlying mechanism behind hardness, and the substrate effect on the mechanical properties of such kind of materials.

5.2.1 Experimental Preparation and Characterization

5.2.1.1 Preparation Details

Si–C–N films were deposited on silicon (100) substrates from the gas mixture of helium (He), nitrogen (N_2) and trimethylsilane (TMS) by changing the N_2 and TMS flow ratios using ECR–CVD technique. For such a technique, the plasma was generated by 2.45 GHz microwave and guided into reactive chamber through quartz window. In the reactive chamber, the plasma was coupled with an 875 Gauss magnetic field, generated by magnetic coils at ECR resonance points, to obtain density plasma zones. Prior to deposition, silicon substrates were degreased by acetone, cleaned by ethanol and deionized water, and dried by nitrogen gas in sequence. The chamber was evacuated to a base pressure of 1.0×10^{-5} Pa through turbo molecular pump. No intentional heating was applied to substrates during the deposition processes. Reactant gases with various flow ratios were introduced into chamber through MKS mass flow meters. Samples #1–4 were prepared under the working pressure of 0.7 Pa and the microwave power of 250 W by changing the N_2 gas flows. That is, 40/23/15 for sample #1; 40/30/15 for sample #2; 40/40/15 for sample #3; 40/50/15 for sample #4. Samples #5–10 were prepared under the working pressure of 0.3 Pa and the microwave power of 200 W by changing the TMS gas flows. They are 40/13/10 for sample #5; 40/13/13 for sample #6; 40/13/15 for sample #7; 40/13/17 for sample #8; 40/13/20 for sample #9; 40/13/13 for sample #10. Among them, samples #6 and #10 were prepared under the same experimental parameters but with different film thickness by controlling deposition time. All these experimental parameters were collected in Table 5.2.1.

Table 5.2.1. *Samples #1–10 were prepared under different experimental conditions. The unit*

of Gas flow rate is sccm. The base pressure is 1.0 × 10^{-5} Pa. No heating was applied to substrates during the deposition processes. Samples #6 and #10 were produced under the same gas flow ratio, microwave power, and working pressure but with different deposition time.

Sample	He/N_2/TMS	Microwave Power (W)	Working Pressure (Pa)
#1	40/23/15	250	0.7
#2	40/30/15	250	0.7
#3	40/40/15	250	0.7
#4	40/50/15	250	0.7
#5	40/13/10	200	0.3
#6	40/13/13	200	0.3
#7	40/13/15	200	0.3
#8	40/13/17	200	0.3
#9	40/13/20	200	0.3
#10	40/13/13	200	0.3

5.2.1.2 Characterization Methods

The film thickness was characterized by FE–SEM (FESEM, Ultra 55, Zeiss). The surface morphology was examined by AFM (XE–100, Park Systems) in a non–contact mode, from which the surface roughness can be determined. The microstructures of our samples were investigated by TEM (Tecnai G2 F20). X–ray photoelectron spectroscopy (XPS) (ESCALAB250) with Al Kα radiation source (1486.6 eV) was employed to describe bonding states and chemical compositions in Si–C–N films. Infrared reflection (IR) was used to characterize possibly chemical bonds in Si–C–N films. Nanoindentation measurements, namely hardness and elastic modulus, were carried out by Nano Indenter XP with Berkovich diamond indenter (Nano Instruments Inc.) based on shape function calibrations on fused silica. For nanoindentation measurement, twenty five indentations were performed on each sample in a 5 × 5 array with a separation of 20 μm between indents. Load–controlled indentation testing followed a trapezoidal loading profile with the hold time of 10 s at peak load. Peak loads were ranged from 40 to 10000 μN with the loading rate of 400 μN/sec. Hardness and elastic modulus were determined from load–displacement curves over the region of the initial unloading segment of 20 ~ 95% using Oliver and Pharr method.

5.2.1.3 Morphologies and Microstructures

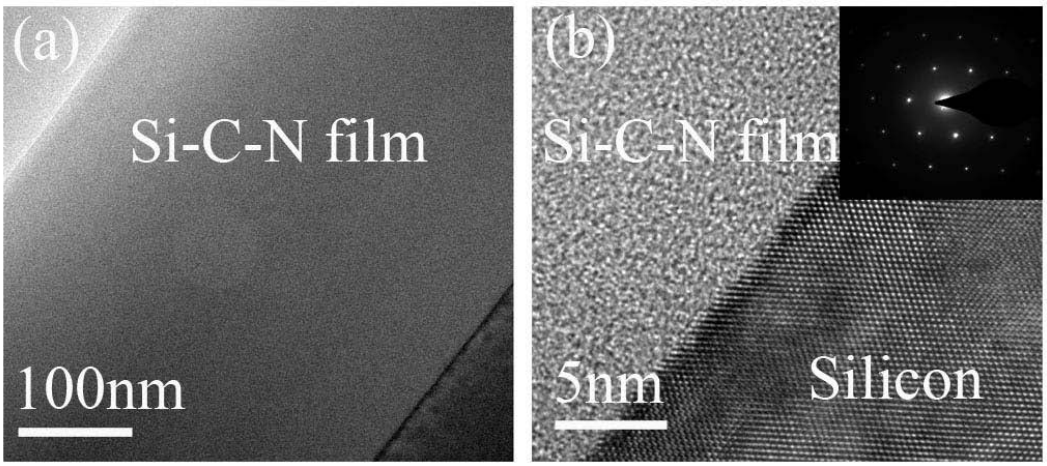

Figure 5.2.1: *A representative morphology of Si–C–N film (sample #1) characterized by TEM. (a) Cross section with low magnification. (b) Cross section with high magnification. The insert is selected area electron diffraction (SAED), in which only the diffraction spots of the silicon wafer were observed. No crystalline information from Si–C–N films can be detected.*

The thickness of thin film is firstly characterized by FE–SEM because it is an important parameter for the measurements of mechanical properties [212-215]. The thickness is 200 nm for sample #1 and 280 nm for samples #2–4. Figure 5.2.1 shows one representative morphology image of sample #1. Figure 5.2.1a describes the cross–section micrograph as characterized by TEM. It appears to be homogeneous throughout the cross section. Figure 5.2.1b shows the cross sections of the Si–C–N film and the silicon wafer with higher magnification. No crystalline particle can be observed. This is further confirmed by the selected area electron diffraction (SAED) as indicated by the insert in Figure 5.2.1b, where the silicon lattice from the substrate side can be seen clearly with periodic arrangements. However, no long–range ordered feature can be observed from the film side. Especially the selective area electron diffraction (SAED) inserted shows only the crystalline feature of the silicon substrate, suggesting that the film structure is amorphous without any crystalline particle imbedded in the matrix of the amorphous films. The amorphous structure is probably due to the fact that the silicon substrate was not heated during the film preparation because high temperature for substrates is in favor of the formation of nanocrystals in amorphous

matrix [209]. Anyhow, films with completely amorphous structure can be provided as preferred materials to explore the hardness mechanism. If nanocrystalline particles are mixed in films, the effects of the crystalline size on hardness have to be considered [216]. This can complicate the extraction of the derivation of hardness mechanism. Completely amorphous Si–C–N films can avoid such effects of nanocrystalline particles. In addition, the isotropic amorphous materials are exactly required to have a better understanding of the mechanical properties without the effects of nanocrystals for such kind of films. Furthermore, completely amorphous films are also isotropic with uniform mechanical properties. They can be served as good candidates of surface coatings for potential industrial applications.

5.2.1.4 Hardness and Reduced Modulus

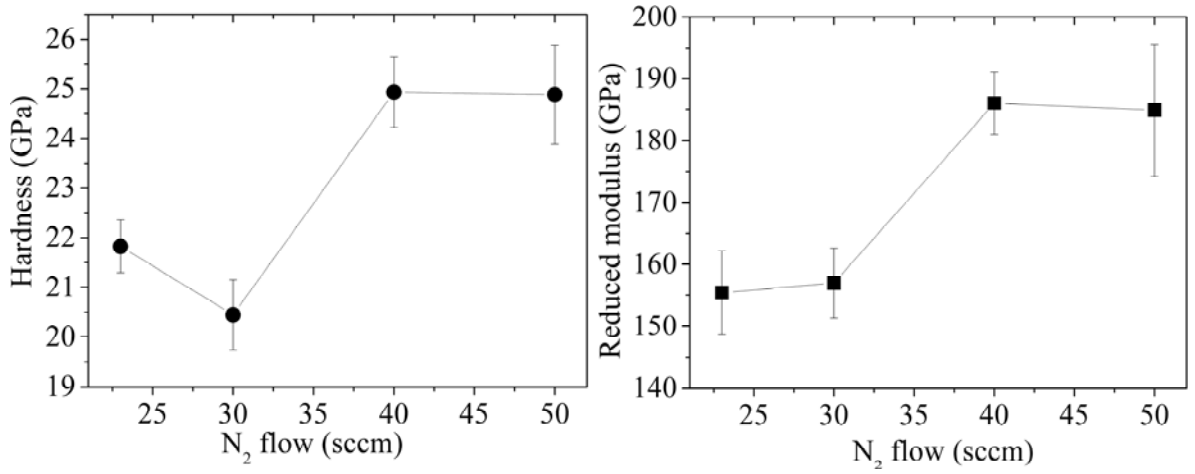

Figure 5.2.2: *Hardness and reduced modulus of samples #1–4 as a function of the N_2 flow ratio.*

From loading–unloading curve, hardness was determined at the maximum load and reduced modulus was obtained from the unloading segment at the initial stage using the Oliver and Pharr method [215, 217]. It is known that Oliver and Pharr method is mainly developed for monolithic materials [213, 217]. When it is used for thin films, film and substrate are commonly treated as homogeneous materials. However, if films have quite different elastic properties from substrates, then the measurements of the mechanical properties can by greatly affected by substrates.

Based on this consideration, the rule of thumb [213, 217], hardness values taken from those with film thickness < 10%, was used to determine the average values of hardness. Figure 5.2.2 shows the hardness and reduced modulus as functions of the N_2 flow ratio. No clear trend for the variations of hardness and reduced modulus can be observed as the N_2 flow ratio increases, but rather that the great deviation of hardness and reduced modulus can be noticeably seen from the error bar. For example, the average value of hardness for sample #1 is ~ 28 GPa. The deviation reaches up to ~ 4 GPa. Greater deviation of ~ 17 GPa can be seen from reduced modulus. In the following section, the possible reason for the obvious deviation is examined.

Although Figure 5.2.2 shows great deviations of the measurements for hardness and reduced modulus, we can still find that the average values of hardness are higher than that of silicon substrate (~ 12 GPa), revealing that the films have very different elastic properties from the silicon substrate. Therefore, the substrate effect may be responsible for the deviations.

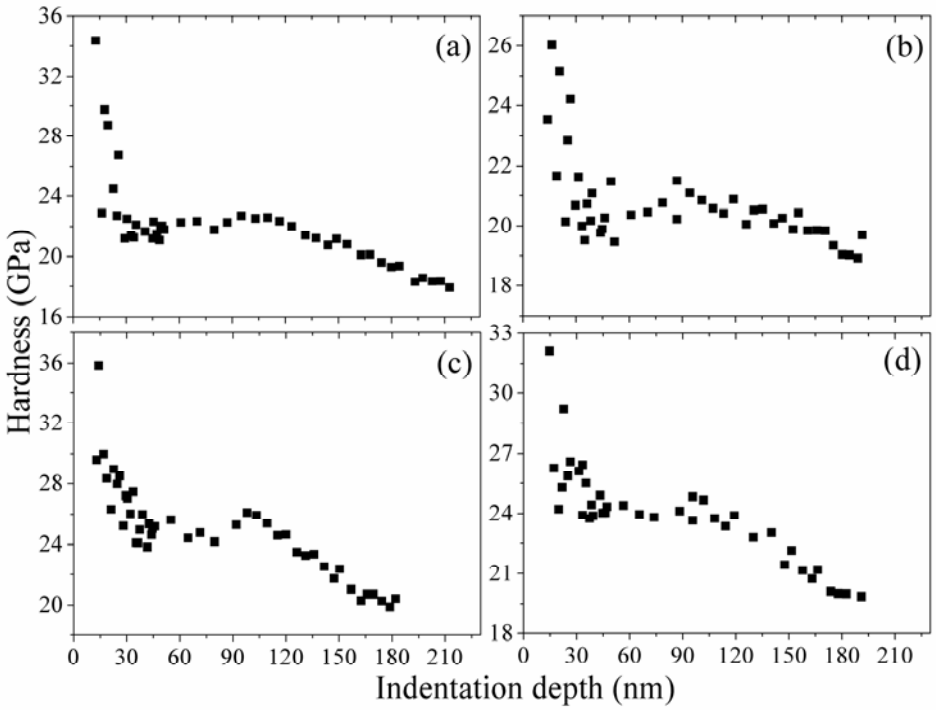

Figure 5.2.3: *Hardness as a function of the indentation depth for samples 1–4 as marked by (a) –(d) in sequence.*

Figure 5.2.3 shows the hardness of all the samples as functions of the indentation depth. All samples show a similar feature that the hardness values fluctuate greatly at shallow indentation depth (< 20 nm), less than 10% film thickness. Since the hardness value shown in Figure 5.2.2 is averaged over this indentation depth, the obvious deviations are mainly derived from the greater variations of the hardness value at this depth. It is important to note that the substrate effect over this indentation depth has still not been presented. This can be seen clearly from the relationship between stiffness and indentation depth. In general, the stiffness shows linear relations with the indentation depth for homogeneous materials, but the stiffness for elastic mismatched materials will deviate from linearity as the indentation depth increases [213]. Seen from Figure 5.2.4, the deviation of stiffness from linearity for all samples begins at the indentation depth of 30 ~ 40 nm, which is higher than 10% film thickness, not the range over which the hardness value is averaged. Therefore, substrate effect can be excluded.

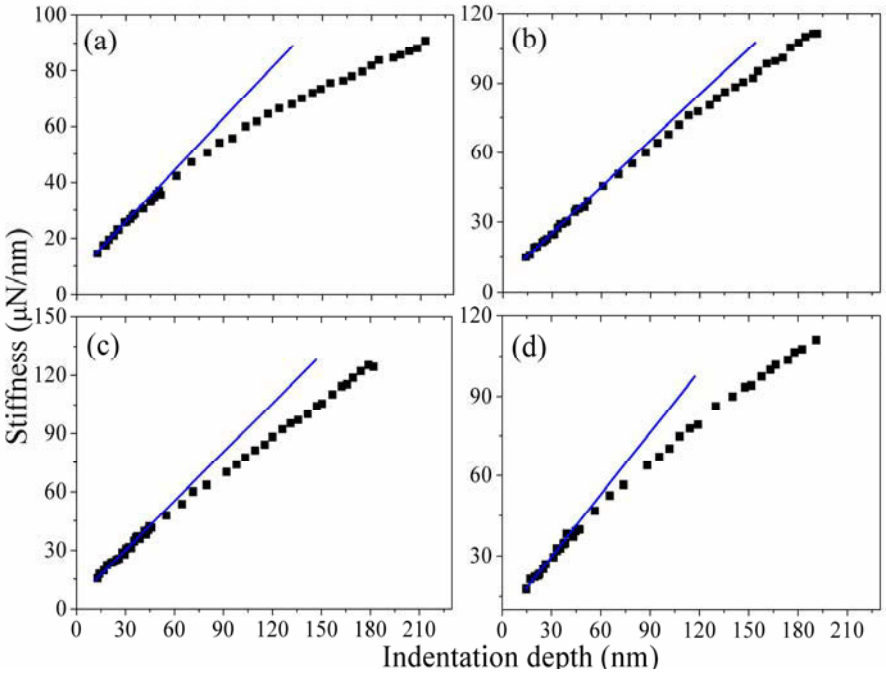

Figure 5.2.4: *Stiffness as a function of the indentation depth for samples #1–4 as marked by (a)–(d) in sequence.*

Since the great deviation takes places at shallow indentation depth, the surface roughness may be an important factor, especially for thin films. Figure 5.2.5 shows a representative

image of AFM to reveal the surface morphology and roughness. Surprisingly, the root–mean–square surface roughness is lower than 1nm. The average value over the measured area is ~ 0.8 nm. The roughness for sample #2–4 is 0.3 nm, 0.4 nm and 1.3 nm, respectively. This means that our films have very smooth surfaces. The roughness should not be the key factor for the great deviations of hardness and reduced modulus.

At present, the deviations are still not clear and they can also be commonly seen in previous works [218, 219]. Nevertheless, the hardness for each sample shows a "plateau" at the indentation depth between 30 nm and 60 nm. Thus values of hardness and reduced modulus at these plateaus are taken to evaluate the "true" properties of our films [213, 220]. After refinements from the plateaus, the hardness values for samples #1–4 are 21.8 ± 0.5 GPa, 20.5 ± 0.7 GPa, 24.9 ± 0.7 GPa and 24.9 ± 1 GPa, respectively. The corresponding reduced moduli are 155.4 ± 6.7 GPa, 156.9 ± 5.6 GPa, 186.1 ± 5 GPa and 184.9 ± 10.7 GPa, respectively.

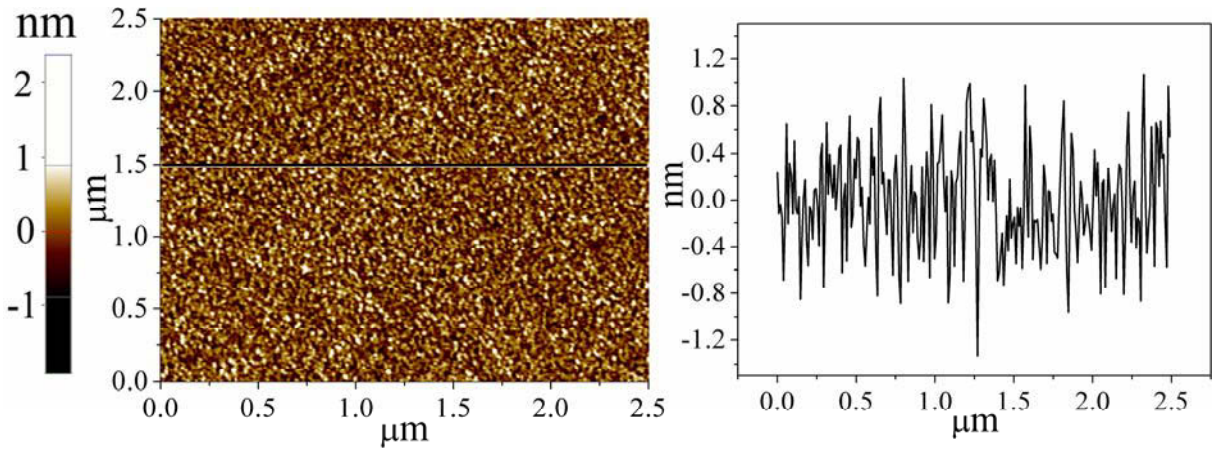

Figure 5.2.5: *AFM image of the representative Si–C–N film (sample #1) on silicon substrate. (left) 2D surface morphology; (right) line profile marked in the left panel.*

5.2.1.5 Hardness vs. Elastic Modulus

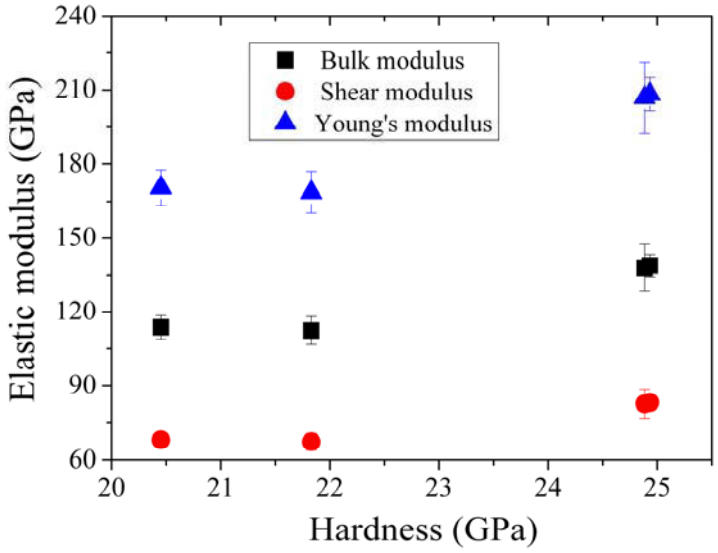

Figure 5.2.6: *Bulk modulus, shear modulus, and Young's modulus as a function of the hardness for samples #1–4.*

For isotropic materials, the bulk modulus (B) and the shear modulus (G) can be determined from Young's modulus (E) and Poisson's ratio (ν) by:

$$B = \frac{E}{3(1-2\nu)}, \tag{5.2.1}$$

$$G = \frac{E}{2(1+\nu)}. \tag{5.2.2}$$

The relations between hardness and elastic modulus are shown in Figure 5.2.6. No clear trend can be observed among bulk modulus, shear modulus, Young's modulus, and hardness. In addition, Si–C–N thin films with higher Young's modulus do not mean that they have higher hardness. For example, the Young's modulus is 168.6 GPa for sample #1 and 170.6 GPa for sample #2. The hardness is 21.8 GPa for sample #1 and 20.4 GPa for sample #2. This is different from crystalline materials with covalent bonds, where clear relations between Young's modulus and hardness can be observed.

5.2.1.6 Summary

Large area Si–C–N thin films with smooth surfaces can be obtained by ECR–CVD at low

microwave power without heating silicon substrates. Such Si–C–N thin films have very good adhension to the surface of silicon substrates after the replacement of boron element by silicon, thus demonstrating that silicon can be used as an additional elment to improve the adhension of amorphous B–C–N films onto silicon wafers. Reduced modulus of Si–C–N thin films shows an exponential decay relation with stiffness. Si–C–N thin films with similar elastic modulus have different hardness values, revealing that no clear relation can be found between hardness and elastic modulus for such kinds of thin films.

5.2.2 Underlying Mechanism behind Hardness

Hardness, the important parameter in the characterization of mechanical properties of engineering materials, is defined as the intrinsic resistance to deformation under pressure [221, 222]. It plays a central role in tailoring the chemical compositions of materials to achieve improved mechanical properties in experiments. It is also essential for designing novel materials with ultrahigh hardness in theoretical calculations [98, 216, 222-225]. However, extraction of the mechanism behind hardness is still challenging since hardness is linked to complex elastic–plastic deformation, cracks, and diverse defects (such as vacancies, dislocations) of materials [221, 226]. In addition, it is also dependent on the type of indenter, the applied loading, and the crystal orientation [227].

The complexity of the mechanism characterization of hardness has inspired scientists to explore the derivation of hardness at microscopic level using theoretical methods. For example, based on the nanoindentation measurements, Gao et al. [98] assumed that the hardness of covalent crystals is determined by the sum of the resistance of each bond per unit area to indenter. The hardness is related to energy gap and valence electron density. They proposed an empirical model to correlate hardness with bond length, charge density, and ionicity of chemical bonds. Good agreement between calculated values and experimental ones can be seen for various covalent crystals using the empirical model.

Simunek et al. [224] introduced the parameters, the bond strength and the reference energy, to describe the hardness of covalent and ionic crystals. The hardness expression proposed is also related to covalent electron numbers, covalent electron density, and number of bonds. Good agreement can also be observed between experiments and their empirical model. Li et al. [226] correlated bond electronegativity to electron–holding energy, bond hardness to the density of bond electronegativity. They took the electron–holding energy of bonds as the origin of material's hardness.

All these empirical models have essentially the common feature. That is, hardness is associated with covalent electron density and number of bonds based on covalent or ionic

crystals. For covalent crystals, covalent electrons are highly localized in hybridized orbital and mainly distributed between constituent atoms. As known, covalent bonds are directional. Constituent elements are orderly arranged in periodic and repeated unit cells. Therefore, the covalent electron density can also show periodic distributions on the repeated lattices of covalent crystalline materials.

The variations of covalent electron density with external loads applied can reveal some essential feature that is related to the hardness. However, neither the periodically atomic arrangement nor the ordered atomic coordinate can be detected for covalent amorphous compounds. Therefore, it is even more difficult to extract the relation between the microstructure and the derivation of hardness. The frequently used method to characterize covalent amorphous materials is the radial distribution function (RDF), which describes the variations of neighbor atomic density as a function of distance from a reference atom.

The common feature for the exploration of the derivation of hardness is that hardness is connected to the arrangements of neighbor atoms, namely the bond types, for both covalent crystalline and amorphous compounds. Crystalline compounds can be treated as the extreme case of the amorphous compounds with the condition of ordered and periodic atomic arrangements. Therefore, the characterization of hardness in materials can probably be illustrated from bonding states among different atoms, which has been unveiled from previous works based on the investigation of covalent cubic B–C–N crystalline materials [147, 228].

Here various bonding states and bond fractions in covalent amorphous Si–C–N materials are explored. Close relations between hardness and various bonding states in amorphous Si–C–N materials can be observed. These results can give a fundamental comprehension of the derivations of hardness in amorphous covalent compounds at the microscopic level.

5.2.2.1 Bonding Types

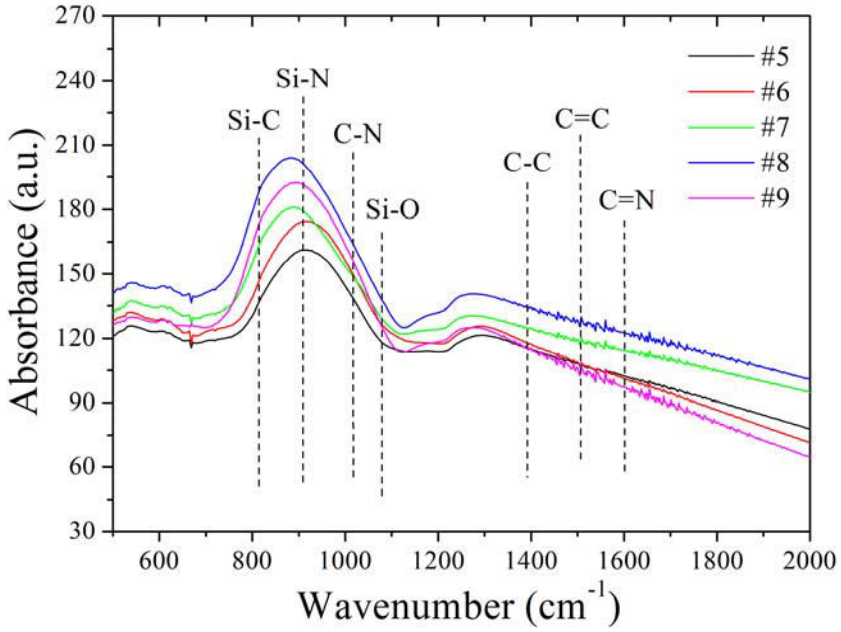

Figure 5.2.7: *Infrared reflection (IR) absorption spectra as a function of the wavenumber for all the five Si–C–N samples obtained by different TMS flow ratios.*

Figure 5.2.7 shows the infrared reflection (IR) spectra of the obtained Si–C–N films as a function of TMS flow ratio. In general, a broad absorption band (700 ~ 1100 cm^{-1}) can be observed for all five samples, together with a weak absorption band between ~ 1220 cm^{-1} and ~ 1400 cm^{-1}. As the TMS flow ratio increases, the main peak of the broad band (700 ~ 1100 cm^{-1}) shows not clear variation, only shifting slightly towards lower wavenumber. Since the IR values measured under different experimental conditions are not always identical, therefore, the IR data from previous works were collected and listed in Table 5.2.2 as reference.

In the broad absorption band (700 ~ 1100 cm^{-1}), several peaks may be presented. For example, Si–C bond centered ~ 810 cm^{-1}; Si–N bond at ~ 900 cm^{-1}; C–N bond or Si–O bond at ~ 1050 cm^{-1}. In the weak band (1220 ~ 1400 cm^{-1}), C–C bond (~ 1400 cm^{-1}) may also be presented. The C = C (~ 1500 cm^{-1}) and C = N (~ 1600 cm^{-1}) bonding information is hard to be detected. From the IR analysis, the bonding states in Si–C–N films may include Si–C, Si–N, C–N, C–C, and Si–O bonds.

Table 5.2.2. *IR data for different bonding types were collected from previous publications.*

Bonds	Wavenumber (cm^{-1}) from previous works					
Si–N	975–990[229]	917–973[208, 230]	850–910[231-233]	920–950[234]	960[235]	949[205, 236]
C–N	2190–2200[234]	1154–1176[204]	1137[208]	1086 [235]	1200[237]	
Si–C	800–820	780–820 [204]	780[208, 232, 235, 237]	800	772[236]	
Si–O	1087–1022[204]	1030–1050[233]	1040–1050[234]	1098[208]		
Si–H	2000–2200[231]	2150–2120[234]	2050[237]	870[229]		
C=C	1580[235]	1500[237]	1470[205]			
C=N	1200–1700[236]	1600	1470[205]			
C≡N	2200[232, 235-237]	2150[205]	2195[238]			
C–C	1500–1850[237]	1400[235]	1456[238]			
N–H	3400[229, 231]	3340[235]	3335[236]			
C–H	2812–2965	2900[229, 231]				

The chemical bonding state of Si–C–N films was further characterized by XPS. Figure 5.2.8 shows representative core–electron spectra of Si2p, C1s and N1s from sample #5. The intensity of the core–electron spectra was presented as a function of the binding energies. Similar to IR, the main peak of the core electron spectra in Si–C–N films, i.e., Si2p, C1s and N1s, can also show diverse values for specific experimental conditions. Therefore, the possible positions of the binding energies for different bonding states in the core electron spectra were also collected and listed in Table 5.2.3 as reference.

The full–width at half maximum (FWHM) of Si2p, C1s and N1s spectra is 2.4 eV, 2.2 eV, and 1.8 eV, respectively, which is larger than that of amorphous SiC (~ 1.84 eV), graphite (~ 0.35 eV), and BN (~ 0.92 eV). This indicates that the main peaks of Si2p, C1s and N1s spectra are not single chemical bonding state. In this work, all the main peaks of these spectra were decomposed by Gaussian curve fit with background subtraction.

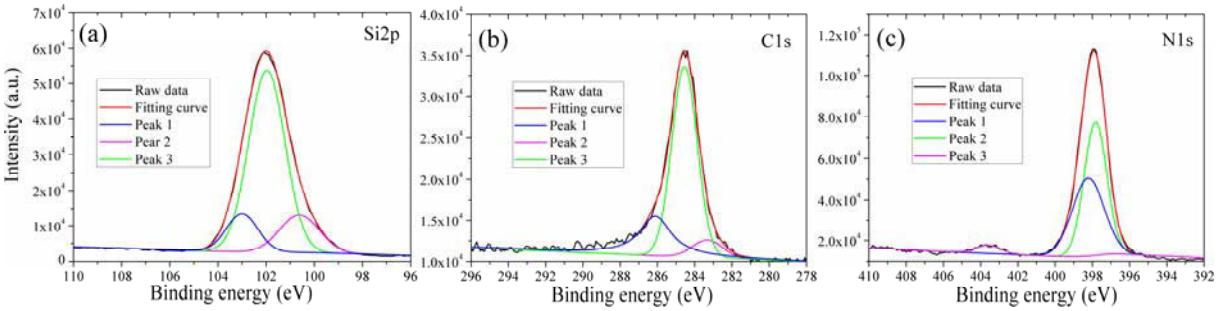

Figure 5.2.8: *Representative Si2p, C1s, and N1s spectra of Si–C–N films (sample #5) as a function of the binding energies.*

Table 5.2.3. *Binding energies for different bonds were collected from previous publications.*

Bonds	Bonding energies (eV) from previous works					
Si–N	102[239]	101.6[240]	101.8[241, 242]	102.7[243]	102.2–103.7[244]	
Si–C	100.4[240]	100.5[242]	100.3[243]	101.1[245]		
Si–Si	99.7[244]	99.5[242]	99.9[245]			
Si–O	103.6[241]	103[239]	104.6[243]	103.1[245]		
C–N	286[240, 241]	287.5[240, 241]	286.1[242]	287.7[242]	286.5[246]	284.5[242]
C–C	284.5[244]	284.6[239]	285.3[242]	285[240]	284.4[245]	285.1[245]
C–Si	282.7[242]	283.3 [245]	283.4[241]			
C–O	286.2[241]	286.4[245]	289.2 [247]			
N–C	398.8[241]	400.3[241]	399.2[239]	400[248]	398.3[248]	399.6[247]
N–Si	398.3[239]	397.7[241]	397.4[242]	398[249]		
N=C	400.4[239]	401.3[247]	404[250]	398.2–399.9[244]		
N≡C	398.4[191]	398.1[251]	400.3–400.4[244]			
N–O	402.5[242]	402.1[247]	402.3[252]			

In Figure 5.2.8a, the decomposition of the Si2p spectrum shows three main contributions from Si–C (~ 100.6 eV), Si–N (~ 101.9 eV), and Si–O (~ 103 eV) bonds, consistent with the broad absorption band (700 ~ 1100 cm^{-1}) in the IR spectra. According to the collected data of the binding energies listed in Table 5.2.3 from previous publications, the decomposition of the C1s main peak shown in Figure 5.2.8b is located at 283.3 eV, 284.6 eV, and 286.1 eV, which corresponds to C–Si, C–C, and C–N bonds, respectively.

In the N1s spectrum shown in Figure 5.2.8c, there are three main contributions from N–Si, N–C, and N–O bonds, which are centered at 397.8 eV, 398.2 eV, and 403.6 eV, respectively. No N = C or N ≡ C bond was detected. We attempted to fit the main peaks with N = C and N ≡ C bonds, but after Gaussian fitting, these decomposed peaks are nearly close to the

background. These XPS results also agree with the IR analysis, where nearly no C = N or N ≡ C or C = C bond were detected. For other samples, the main peaks of Si2p, C1s, and N1s spectra show slightly shift with the variation of TMS flow ratios. To sum up, the main chemical bonding states in the Si–C–N films are Si–N, Si–C, C–N and C–C bonds together with Si–O bonds.

5.2.2.2 Bond Content vs. Mechanical Properties

Table 5.2.4. *TMS flow ratios (sccm), hardness (H), reduced modulus (E_r), Young's modulus (E), shear modulus (G), bulk modulus (B), elastic constants (C_{11}, C_{12}, and C_{44}) (GPa) for all the five samples. Bulk modulus by* $B = \frac{E}{3(1-2\nu)}$; *shear modulus by* $G = \frac{E}{2(1+\nu)}$. *Elastic constants for our isotropic materials were calculated by:* $C_{44} = G$; $C_{11} - C_{12} = 2C_{44}$; $B = (C_{11} + 2C_{12})/3$. *The Poisson's ratio is taken as 0.25.*

Samples	TMS	H (GPa)	E_r (GPa)	E (GPa)	G (GPa)	B (GPa)	C_{11}	C_{12}	C_{44}
#5	10	17.6±0.9	151.5±2.9	163.7±3.7	65.5±1.5	109.1±7.1	196.4	65.4	65.5
#6	13	19.6±0.7	155.6±2.8	168.8±3.5	67.5±1.4	112.5±2.3	202.5	67.5	67.5
#7	15	23.3±1.2	170.3±7.1	187.5±9.1	75.1±3.6	125.1±6.1	225.2	75.1	75.1
#8	17	27.6±0.9	202.2±5.6	230.2±7.7	92.1±3.1	153.5±5.1	276.3	92.1	92.1
#9	20	25.9±0.7	200.2±5.7	227.4±7.7	91.1±3.1	151.6±5.2	273.1	90.9	91.1

The variations of mechanical parameters were listed in Table 5.2.4 and shown in Figure 5.2.9. Generally, the hardness, elastic moduli, and elastic constants increase as the TMS flow ratio increases up to 17 sccm. As the TMS flow further increases up to 30 sccm, the hardness, the elastic moduli, and the elastic constants show slightly decrement. This indicates that higher TMS flow ratio does not always mean better mechanical properties of such kinds of films. The hardness values change from ~ 18 GPa to ~ 28 GPa, comparable with other works as shown in Table 5.2.5 which are collected from previous publications.

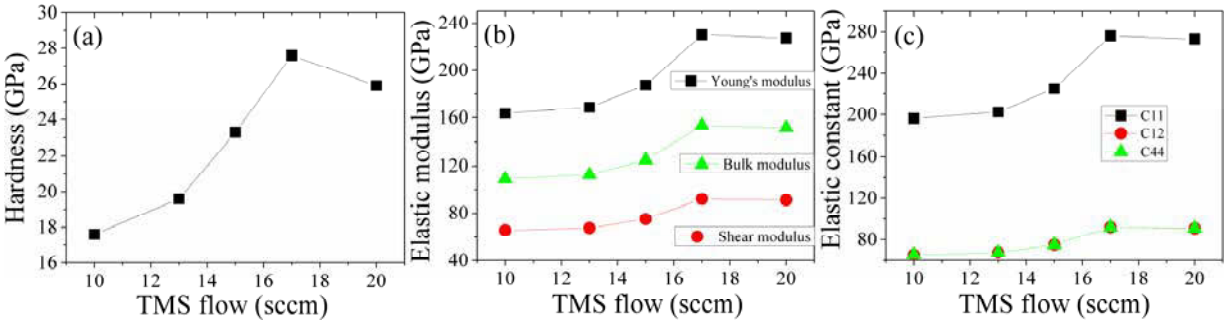

Figure 5.2.9: *Hardness, elastic modulus, and elastic constants of Si–C–N films as a function of TMS flow ratio.*

Table 5.2.5. *Hardness values and elastic moduli taken from previous works.*

Hardness (GPa)	Elastic modulus (GPa)	References
13 ~ 17	136 ~ 160	[231]
26.8 ~ 38	224 ~ 362	[253]
13 ~ 25	130 ~ 220	[254]
27 ~ 42	206 ~ 305	[255]
18 ~ 33	120 ~ 220	[240]
22 ~ 41	–	[241]
1 ~ 13	–	[256]
12 ~ 24	–	[209]

Now we come to the key issue in this work, that is, the correlation of bond fraction and hardness. The bond fraction was obtained by calculating the area of the fitted peaks relative to different bonds, and then divided the area by the total area of the Si2p, C1s, N1s and O1s spectra. Bond fractions for possible bonding states in Si–C–N films were listed in Table 5.2.6 and shown in Figure 5.2.10 as a function of the hardness.

As the hardness value varies from ~ 18 GPa to ~ 23 GPa, the N–O bond fraction shows slightly variation with a nearly constant value of ~ 1.2%. This means that the hardness is not sensitive to N–O bond. In other words, N–O bond does not play a key role in fluctuating the hardness of Si–C–N films. The Si–O, C–N, and C–C bond fractions decrease from ~ 3.4% to ~ 1.2%, ~ 18.5% to ~ 12.1%, and ~ 7.6% to ~ 1.2%, respectively. The Si–C and Si–N bonds increase from ~ 4.9% to ~ 11.8%, ~ 37.7% to ~ 65.8%, respectively. This indicates that as the silicon concentration increases, the C–C and C–N bonds are broken by high–energy plasma,

and new bonding states of Si–C and Si–N bonds are formed.

Table 5.2.6. *Hardness and various bond fractions in Si–C–N films.*

Samples	H	Si–C	Si–N	C–C	C–N	Si–O	N–O
#5	17.6	4.94	37.65	7.57	18.49	3.37	1.23
#6	19.6	9.58	51.33	1.77	13.97	2.18	1.21
#7	23.3	11.81	65.84	1.23	12.09	1.21	1.22
#8	27.6	14.67	60.95	1.49	13.88	1.23	1.83
#9	25.9	10.83	56.49	0.98	23.06	1.39	1.79

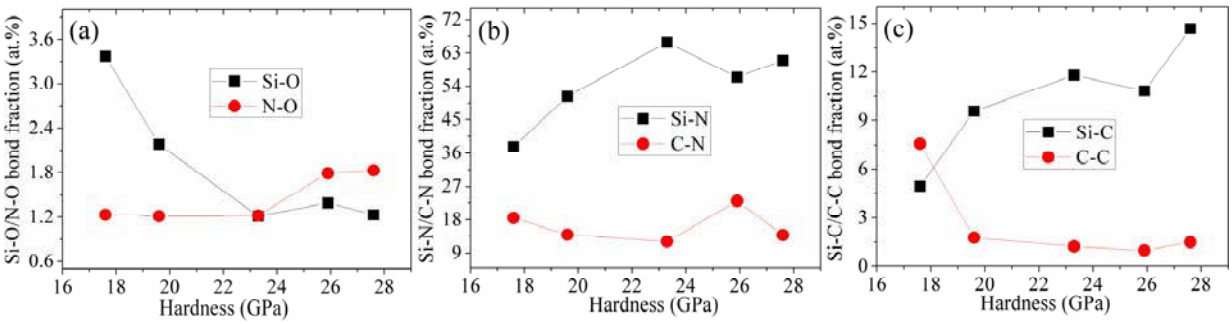

Figure 5.2.10: *Relations between bond fractions and hardness of Si–C–N films.*

As the hardness value further increases up to ~ 28 GPa, the Si–O and C–C bonds show small variations, revealing that Si–O and C–C bonds give not obvious contributions to hardness with higher values. The N–O bond fraction increases slightly. The Si–N and Si–C bonds show some fluctuations. Clearly, the Si–N bonds have the largest fraction in Si–C–N films comparing with other bonds. The variations of Si–N bond fraction together with Si–C play a key role in fluctuating the hardness values of Si–C–N films, especially the Si–N bonds with the largest bond fraction.

Therefore, to some extent, the variation of the hardness of Si–C–N films mainly depends on the Si–N bond fraction. Higher Si–N bond fraction indicates the Si–C–N films are closer to the amorphous compounds of silicon nitride, well known materials with high hardness. More Si–C bond fraction means our Si–C–N films are closer to amorphous silicon carbides, which are also hard materials. Therefore, it is not difficult to understand why these bond fractions are closely related to the hardness of our Si–C–N films. Surely, more C–C (sp^3) and C–N bonds can also be comparable to ta–C and carbon nitrides, which are also hard materials.

However, under present specific experimental conditions, these two kinds of bonds appear to not be the key issue to determine the hardness of Si–C–N films.

5.2.2.3 Summary

Bonding information in Si–C–N films was verified by IR spectra and Gaussian fitting of XPS curves. Bond fractions were calculated by the area of the corresponding fitted peaks divided by the total area of the Si2p, C1s, N1s, and O1s spectra. Bond fractions show clearly variations as hardness values are changed, in which the Si–N bond plays a leading role in determining the hardness fluctuations of Si–C–N films. Macroscopic hardness is correlated to microscopic various bonding information. This can give a deep understanding the origin of the hardness at the microscopic level.

5.2.3 Substrate Effect vs. Mechanical Properties

Determination of hardness and elastic modulus of thin films on substrates by nanoindentation is always intractable because of the unavoidable substrate effects [213, 214, 217, 220, 257-261]. So far, the most frequently used technique is based on Oliver and Pharr method [217, 262]. In this model, hardness is expressed by:

$$H = \frac{\mathrm{P_{max}}}{\mathrm{A}}, \tag{5.2.3}$$

where P is the load and A is the contact area at the maximum contact depth. Elastic modulus is determined from the combination of the following two expressions:

$$S = 2\beta E_r \sqrt{A/\pi}\,, \tag{5.2.4}$$

$$\frac{1}{E_r} = \frac{1-\nu_i^2}{E_i} + \frac{1-\nu_f^2}{E_f}, \tag{5.2.5}$$

where S is the contact stiffness, β is a constant that is related to indenter shape, E_r is the reduced modulus, E and ν are the Young's modulus and Poisson's ratio of indenter (*i*) and thin film (*f*). This method is primarily deduced from monolithic materials and mainly developed for homogeneous materials [262]. When implemented to thin films, it essentially treats the film and the substrate as unity and neglects substrate effects. This can be seen clearly from

equation (5.2.5), where only the factors of indenter and film are considered. But the application of the method will be limited if thin film and substrate have clearly different elastic properties [213, 263, 264].

To extend the capability of Oliver and Pharr method, great efforts have been made to consider substrate effects when nanoindentation is performed to measure mechanical properties of thin films [213, 258, 264, 265]. The representative work was carried out by Doerner [265]. In his work, weighting factors were introduced to distribute the contributions of silicon substrates and sputtered tungsten thin films. Unfortunately, the weighting factors in their modified equations are empirically constants. They are only feasible for some special materials that they considered. King extended Doerner's work using numerical method for flat–ended cylindrical, quadrilateral, and triangular punches [258]. They defined the reduced modulus as:

$$\frac{1}{E_r} = \frac{1-\nu_i^2}{E_i} + \frac{1-\nu_f^2}{E_f}(1-e^{-\alpha t/a}) + \frac{1-\nu_s^2}{E_s}e^{-\alpha t/a}, \tag{5.2.6}$$

where E and ν are the Young's modulus and Poisson's ratio of indenter (*i*), film (*f*), and substrate (*s*), a is the square root of the contact area, t is the film thickness under punch, and α is a scaling parameter that is related to a/t. Since the commonly used punch has Berkovich geometry, Saha made an assumption that the tip of the Berkovich indenter is taken as a flat punch [213], and modified the King's model as:

$$\frac{1}{E_r} = \frac{1-\nu_i^2}{E_i} + \frac{1-\nu_f^2}{E_f}(1-e^{-\alpha (t-h)/a}) + \frac{1-\nu_s^2}{E_s}e^{-\alpha (t-h)/a}, \tag{5.2.7}$$

where the effect film thickness under the tip is equal to t–h. After the modification, the equation can now be conveniently used for Berkovich indenter to evaluate substrate effects. However, this modified equation still overestimates the contribution of substrate, especially at deep indentation depth. Because there are still considerably contacts in the lateral facets of Berkovich indenter with film even when the indenter tip reaches the interface of film and substrate.

Most of the works that investigate the effect of substrate on mechanical behavior are based on metallic films [213, 214, 220, 261], for example, sputtered aluminum on glass

(Al/glass) [261], Al/glass and tungsten on sapphire (W/sapphire) [264], sputtered Al and W thin films on different substrates [220], Au/fused quartz substrates [214]. For metallic films, nano/micro–crystalline grain sizes in these films can complicate the analysis of substrate effects because of complex grain boundaries and dislocations [266-268]. Amorphous thin films are a good choice to avoid the effect of grain boundaries and dislocations.

Here completely amorphous Si–C–N and boron carbide thin films on silicon (100) substrates, frequently used in surface coatings with broad industrial applications [202, 206, 269], are employed to study the effect of substrate on their hardness and elastic modulus. These two kinds of thin films represent two different systems: hard films on "soft" substrates (Si–C–N films on Si (100)) and "soft" films on stiffer substrates (BC_x films on Si (100)). They (BC_x #1 and BC_x #2) were fabricated from B_4C target in Ar atmosphere by RF–magnetron sputtering technique. In addition, surface roughness is also crucial for determining the hardness and the elastic modulus of thin films [270, 271], especially for films with thickness less than 100nm and low indentation depth. In our work, Si–C–N and boron carbide films with surface roughness less than 3 nm were obtained and used to minimize the effect of the surface roughness on nanoindentation measurements.

5.2.3.1 Mechanical Parameters vs. Indentation Depth

Surface roughness is an important parameter for the measurements of mechanical properties of thin films. Large surface roughness can complicate the true contact area, which in turns can give an inaccurate evaluation of the contact area and further affect the measurements of mechanical properties of thin films. While small values of surface roughness can minimize the uncertainty. Here AFM (XE–100, Park Systems) was used to characterize the surface roughness of deposited films. The RMS roughness for samples #5–9, is 0.21 nm, 0.16 nm, 2.5 nm, 0.4 nm and 0.48 nm, respectively. These values can be comparable to fine polished silicon wafer, revealing that these samples have very smooth surfaces.

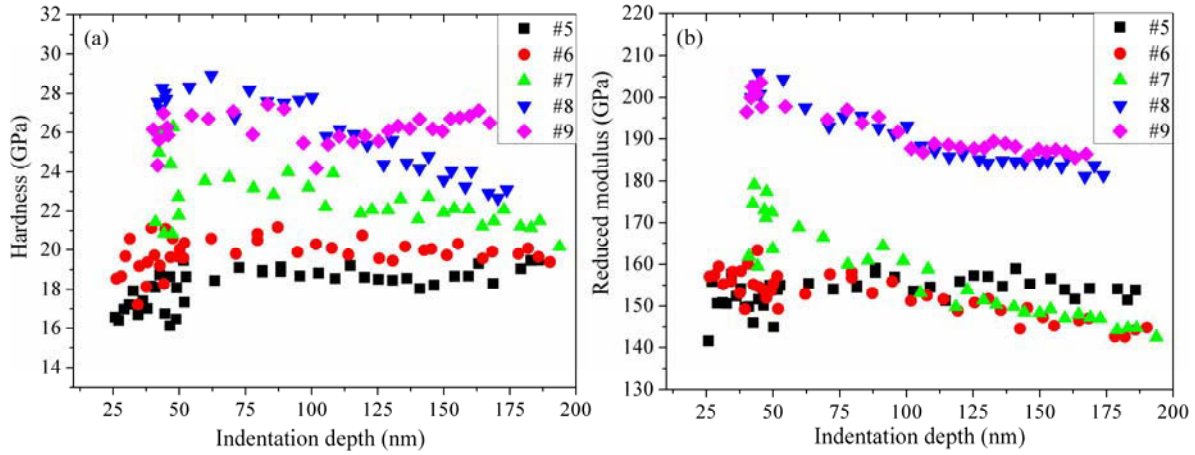

Figure 5.2.11: *Hardness and reduced modulus as a function of indentation depth for samples #5–9.*

For monolithic materials, hardness and elastic modulus should be independent of indentation depth or rather show small variations as indenter is pressed into such kinds of materials, this can be seen clearly from Saha's work [213]. However, for film systems, film and substrate have commonly different elastic properties. Therefore, as the indenter goes deeply into films, substrate effects can lead to the deviations of the measurements of mechanical properties from constant values. This can be seen from our measurements of samples #5–9.

As shown in Figure 5.2.11a, obvious fluctuations of hardness can be observed at shallow depth for samples #5–9 and at deep depth for samples #7 and #8. But for samples #5 and #6, the hardness is nearly constant for indentation depth between 50 ~ 120 nm. If we take the empirical rule of thumb [213, 262], hardness value extracted with film thickness less than 10%, to calculate the hardness of samples #5 and #6, the hardness values of samples #5 and #6 evaluated by Oliver and Pharr method are 17.6 GPa and 19.6 GPa, which are greater than that of silicon substrate (~ 12 GPa) [213]. For samples #7 and #9 with higher hardness than silicon substrate, the hardness decreases as the indentation depth increases.

In comparison with hardness, elastic modulus shows more dependence of indentation depth except for sample #5 as displayed in Figure 5.2.11b. As the indentation depth increases from 30 nm to 130 nm, the elastic moduli for samples #8 and #9 vary from ~ 205 GPa to ~ 185 GPa. Larger variations of elastic modulus can be seen in sample #7, from ~ 180 GPa to ~

140 GPa. Even for sample #6, although its hardness shows less dependence of indentation depth, its elastic modulus also begins to decrease as the indentation depth is higher than 60 nm.

Here we need to keep in mind that the hardness and reduced modulus are deduced from Oliver and Pharr method [262]. In this method, the substrate effect is not included or rather the substrate and the film are taken as homogeneous unity. Nevertheless, the substrate effects should be included, especially for thin films. Here the modified King's model is employed to incorporate the influence of substrates [213]. We assume that at shallow depth the reduced modulus can be taken as the "correct" value of thin films without substrate effects. From equation (5.2.5), the elastic modulus E_f can be obtained, which is put into equation (5.2.7) to get reduced modulus as a function of indentation depth. From equation (5.2.7), we can get:

$$\frac{1}{E_r} = \left(\frac{1-\nu_i^2}{E_i} + \frac{1-\nu_f^2}{E_f}\right) + \left(\frac{1-\nu_s^2}{E_s} - \frac{1-\nu_f^2}{E_f}\right)e^{-\alpha(t-h)/a}. \tag{5.2.8}$$

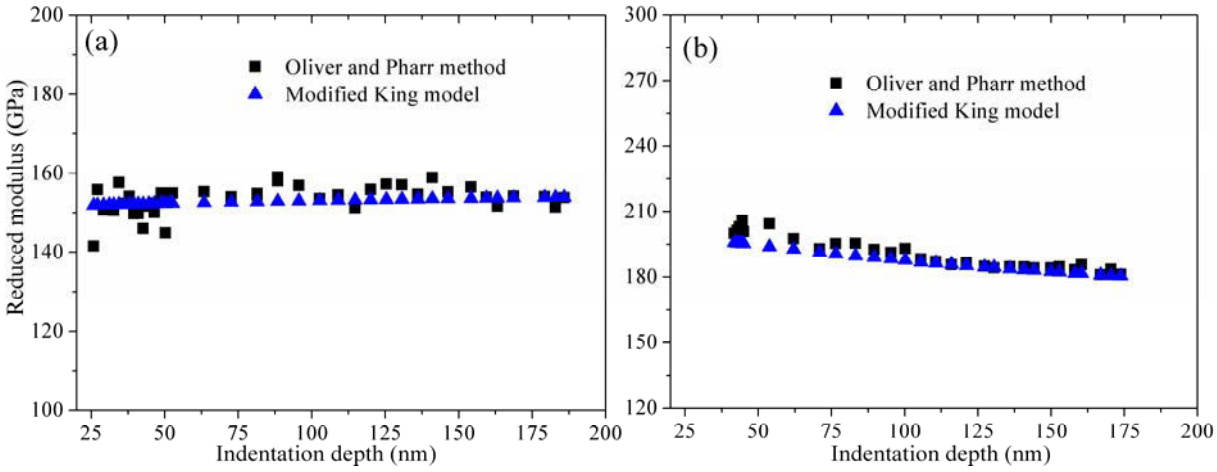

Figure 5.2.12: *Reduced moduli calculated by modified King model as a function of indentation depth for (a) sample #5 and (b) sample #9. The values from Oliver and Pharr method are also shown for comparison.*

The fraction from substrate effects is put together into the second term of equation (5.2.8). The exponential term $e^{-\alpha(t-h)/a}$ is greater than 0. If film and substrate have the same Poisson's

ratio, then only the coefficient $(1-\nu_s^2)/E_s - (1-\nu_f^2)/E_f$ is valuable to check the contribution of substrate effects. If thin films are stiffer than substrates ($E_f > E_s$), the positive coefficient means that substrate will weaken modulus as the indentation depth increases, otherwise the substrate works in an opposite way. If the substrate has the similar elastic properties ($E_f \approx E_s$), equation (5.2.8) falls back to equation (5.2.5), which is exactly the classical model of Oliver and Pharr.

Two representative samples were chosen for the reduced modulus calculation by modified King's model. Figure 5.2.12 shows the calculated modulus as a function of indentation depth. The values from Oliver and Pharr method are also shown for comparison. Surprisingly, the reduced moduli calculated by modified King's model compare well with those from Oliver and Pharr method for sample #5 (softer than substrate) and #9 (stiffer than substrate). Within the load range, reasonable consistency can be seen all our samples.

5.2.3.2 P/S^2 and H/E_r^2 vs. Indentation Depth

Combination of equation (5.2.3) and (5.2.4) gives:

$$\frac{P}{S^2} = \frac{\pi}{4\beta^2}\frac{H}{E_r^2}. \tag{5.2.9}$$

For monolithic materials, hardness and elastic modulus can be treated as constants without dependence of indentation depth [213]. Therefore, P/S^2 should also be constant regardless of the variations of indentation depth [213, 217]. This expectation can be seen clearly from the results of fused quartz [213]. But for thin films on substrates, variations of hardness and elastic modulus with indentation depth will change the P/S^2 values. Therefore, the variation of the parameter P/S^2 as a function of indentation depth can be used to evaluate the effect of substrate on mechanical behavior of thin film systems.

Equation (5.2.9) is firstly examined before the relation between P/S^2 and indentation depth is given. The left–hand side of equation (5.2.9) is composed of load P and stiffness S, in which the load can be directly measured during the indentation test and the stiffness can be determined from the unloading segment of the load–displacement curve. The right–hand side

of equation (5.2.9) contains hardness H and reduced modulus (E_r). Both of the two parameters are deduced from Oliver and Pharr method [262].

The significant problem for Oliver and Pharr method is that it does not account for pile–up effects around indenter impression [217]. Therefore, we need to check whether our materials are sink–in or pile–up. Figure 5.2.13 gives a representative indenter impression of sample #6 with the maximum load of 10mN. Unexpectedly, pile–up effects are observed in our films although sink–in phenomenon is commonly observed for stiffer films on soft substrates. We also examined the indenter impression with the normal load of 9 mN, 8 mN, 7 mN, 6 mN, and 5 mN under nanoindentation. All of them show pile–up behavior in AFM observations. Our results show that it is not a golden rule that stiffer film on softer substrate shows sink–in effects. Nevertheless, the pile–up effect is small (~ 5 nm). Here, each sample is treated with both P/S^2 (regardless of sink–in or pile–up effects) and $\frac{\pi}{4\beta^2}\frac{H}{E_r^2}$ (with area function calibration) as a function of indentation depth.

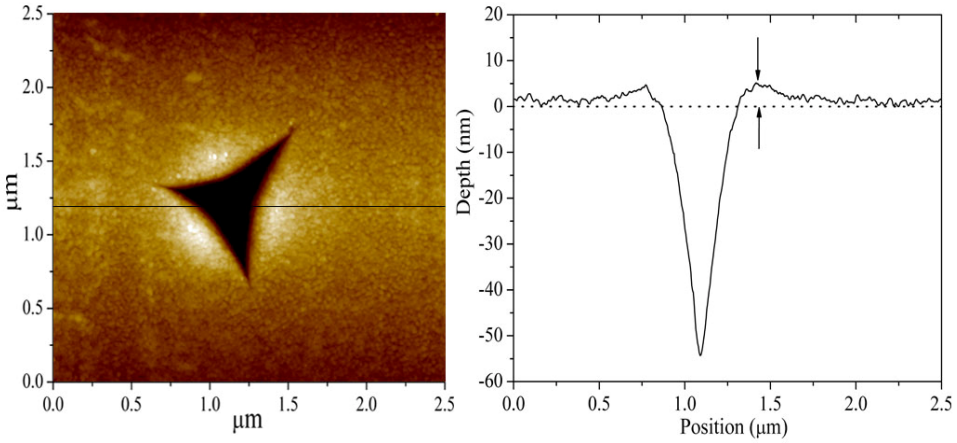

Figure 5.2.13: *A representative AFM image of nanoindenation profile (Sample #6) and the variation in height along the marked line in AFM image.*

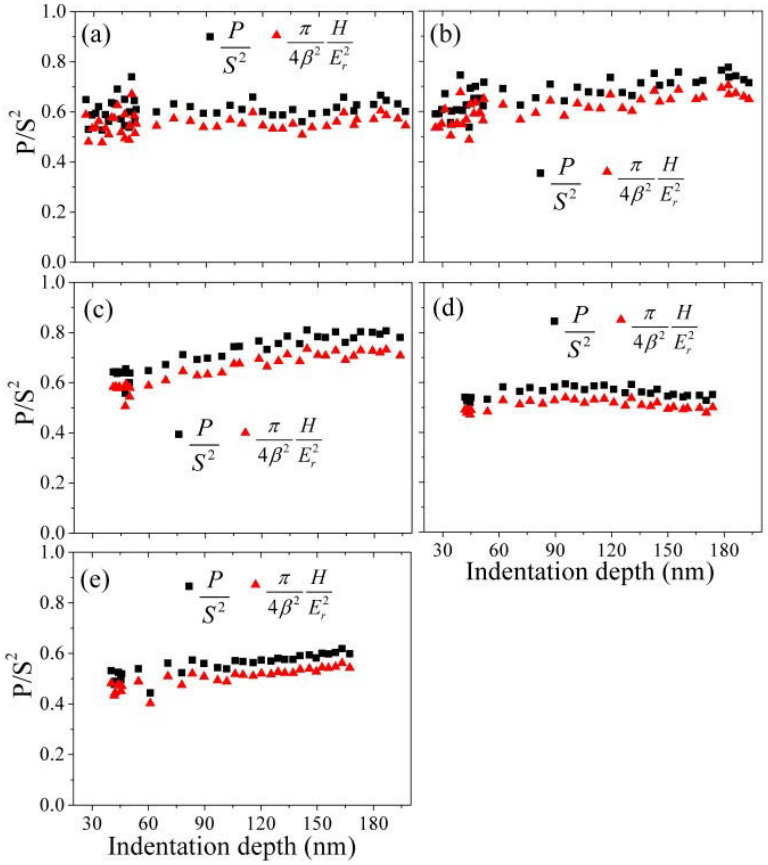

Figure 5.2.14: *Parameters P/S^2 as a function of indentation depth for samples #5–9. Two methods were used. One is calculated from the load P and the stiffness S, the other is calculated from the hardness and reduced modulus from Oliver and Pharr method.*

In Figure 5.2.14, the parameters P/S^2 and $\frac{\pi}{4\beta^2}\frac{H}{E_r^2}$ are plotted as a function of indentation depth for samples #5–9. For each sample, parameters P/S^2 and $\frac{\pi}{4\beta^2}\frac{H}{E_r^2}$ show nearly the same trend with increasing indentation depth. For all samples, P/S^2 shows small variations at shallow indentation depth (lower than 30 nm). This is probably because substrate effect has not been involved in the range of indentation depth. P/S^2 reveals the characterizations of "pure" films. Therefore, P/S^2 can be approximately treated as constants. As the indentation depth increases, the P/S^2 of the five samples shows different features.

For samples #5 and #9, P/S^2 shows small fluctuations as the indentation depth increases although they are two different kinds of films. If the average reduced modulus calculated from

Oliver and Pharr method is taken at indentation depth lower than 30 nm, the reduced modulus for sample #5 is ~ 151 GPa. It is lower than that of the silicon substrate (170 GPa) [213, 260]. Therefore, sample #5 is similar to the case of "soft" film on stiffer substrate. While the sample #9 behaviors in an opposite way, i.e., stiffer film (202 GPa) on soft substrate.

Here the results reveal that whether soft film on stiffer substrate or rather stiffer film on soft substrate can still display constant P/S^2 values in spite of the variations of indentation depth. For samples #6, #7 and #9, P/S^2 increases as indenter goes deeper into films. Sample #6 (~ 156 GPa) is "soft" film on stiffer substrate. Sample #7 (170.3 GPa) has the similar elastic properties as silicon substrate. Sample #9 is stiffer film on soft substrate. Although they are three different cases, their P/S^2 values still show the same increasing trend as a function of indentation depth.

5.2.3.3 Stiffness vs. Indentation Depth

As shown in equation (5.2.4), stiffness is related to the reduced modulus and the contact area according to Oliver and Pharr method. If the measured materials are homogeneous, the reduced modulus can be treated as constant [213, 260]. By considering the connection of contact radius and indentation depth [213], the stiffness in equation (5.2.4) is expected to have a linear relation with indentation depth for homogeneous materials [272]. But for film/substrate system with different elastic properties, the stiffness will deviate from linearity as the indentation depth increases [213, 272]. This "deviation" feature for film/substrate system can be used to monitor at which indentation depth the silicon substrate starts to affect the nanoindentation measurements of hardness and modulus in our thin film systems.

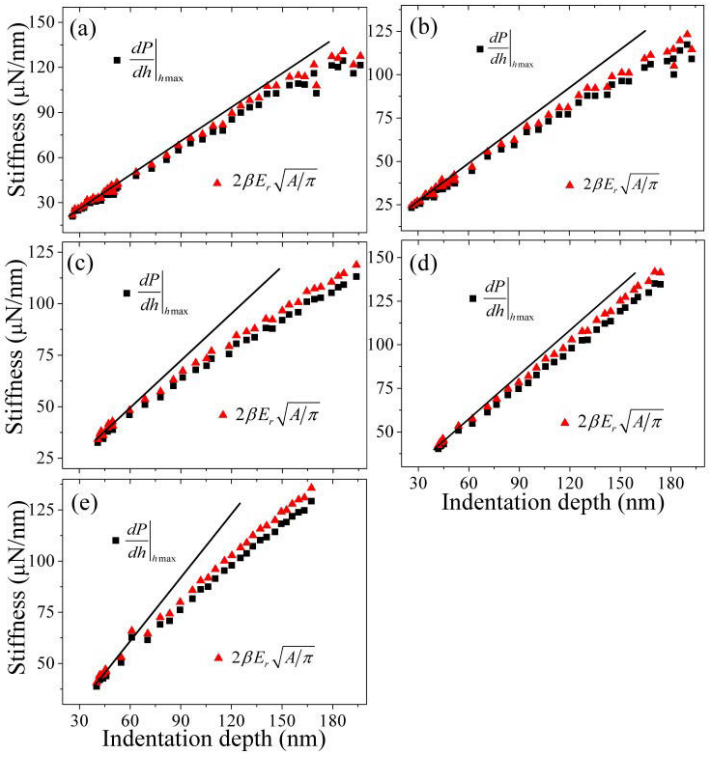

Figure 5.2.15: *Stiffness as a function of indentation depth for samples #5–9. Two methods were used to evaluate the stiffness. One is calculated from slope of the load P and indentation depth at maximum load, the other is calculated from Oliver and Pharr method. The straight line inside is to show the deviations of our data from linearity.*

Figure 5.2.15 gives the stiffness as a function of indentation depth for samples #5–9. The results calculated by the two methods have similar trends but show some divergences, probably due to the fitting procedure of the unloading segment. The stiffness for samples #5 and #6 shows obvious deviations as the indentation depth reaches up to 120 nm. For samples #7, #8 and #9, the deviations are not easy to be observed. However, the stiffness still shows detectable deviations when the indentation depth is higher than 40 nm. But we cannot be sure whether it is because substrate starts to show an increased effect. In the following section we will verify that it is not because of the substrate effects but because of the plastic deformation of thin films.

In the load–displacement curve, the loading and unloading parts can be approximated by power exponent relation [217, 262] as:

$$P = \alpha_1 h^{m_1}, \tag{5.2.10}$$

$$P = \alpha_2 (h - h_f)^{m_2}, \tag{5.2.11}$$

where P is load, h is indentation depth, h_f is final depth, and α_1, α_2, m_1, m_2 are fitting parameters. The total work [217, 273] done by indenter during loading is,

$$W_t = \int_0^{h_m} (\alpha_1 h^{m_1}) dh = \frac{P_m h_m}{m_1 + 1}, \tag{5.2.12}$$

and the elastic recovery work during unloading is,

$$W_e = \int_{h_f}^{h_m} (\alpha_2 (h - h_f)^{m_2}) dh = \frac{P_m (h_m - h_f)}{m_2 + 1}. \tag{5.2.13}$$

The total work done by indenter is divided into two parts [273]. One part is used for energy dissipation because of plastic deformation. The other part is used to resist the elastic recovery. Therefore, the energy dissipation for plastic deformation is:

$$\Delta W = W_t - W_e. \tag{5.2.14}$$

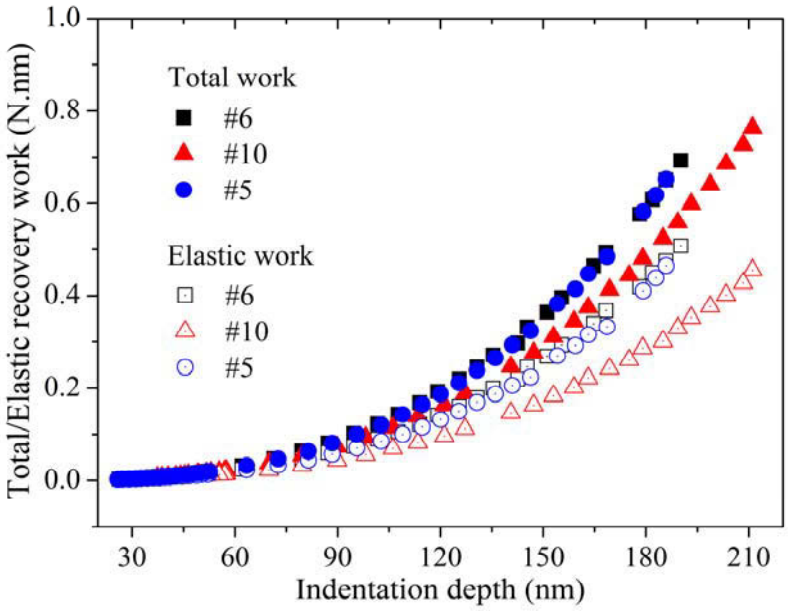

Figure 5.2.16: *Total work and elastic recovery work as a function of indentation depth for samples #5, #6 and #10. The total work is calculated by the area under loading curve, and the elastic recovery work is calculated by the area under unloading curve. The thickness of samples #5 and #6 is 570 nm and 510 nm, respectively. Sample #10 was deposited with the*

same experimental parameters as that of sample #6 but has a thickness of ~ 80 nm.

Figure 5.2.16 gives the total work W_t and the elastic recovery work W_e as a function of indentation depth for samples #5, #6 and #10. From Figure 5.2.16 we can see that at shallow indentation depth, the total work is nearly equal to the elastic recovery work. This means that the energy dissipation is nearly zero. In other words, there is no obvious plastic deformation. The total work is mainly used to restrain the elastic recovery. But the deviation between total work and elastic recovery work is gradually amplified when the indentation depth is deeper than 40 nm. This indicates that the plastic deformation is formed when the indentation depth is higher than 40nm. This indentation depth is nearly close to the depth that the stiffness begins to deviate from linearity. Furthermore, for samples #6 and #10 deposited with the same experimental parameters but different film thickness (#6: 510 nm; #10: 80 nm), the deviation between total work and elastic work is also nearly at 40 nm. This evidence clearly shows that the deviation of stiffness from linearity at ~ 40 nm is not because of the substrate effects but because of the effects of plastic deformation.

The effects of plastic deformation on the deviation of stiffness at shallow indentation depth reveal the differences of hardness measurements between traditional method and nanoindentation. For traditional measurements, the hardness is evaluated by examining the residual impression on material surface after unloading. Therefore, the traditional method shows the ability of plastic deformation. For nanoindentation measurements, the hardness is taken from the maximum load during loading and exhibits the combination of complex elastic and plastic deformation. Hardness values taken from the average over indentation depth less than 10% film thickness is still located in the range of elastic deformation. Therefore, nanoindentation measurements display the ability of elastic deformation for our samples.

5.2.3.4 Penetration of Si–C–N and BC_x Thin Film

According to Oliver and Pharr method [217, 262], the hardness for the five samples #5–10 used for analysis is 17.6 GPa, 19.6 GPa, 23.3 GPa, 27.8 GPa and 25.9 GPa. All of them are higher than that of silicon substrate (~ 12 GPa) [213]. This corresponds to the condition of

hard film on soft substrate. As known, when the indenter is pressed into films, the harder film can disperse the force applied by indenter. The substrate effects may not be clearly revealed. To clearly see the substrate effects on such engineering films, thinner Si–C–N films (80 nm) were deposited. In addition, "soft" boron carbide films were also obtained to check the effect of soft films on hard substrates.

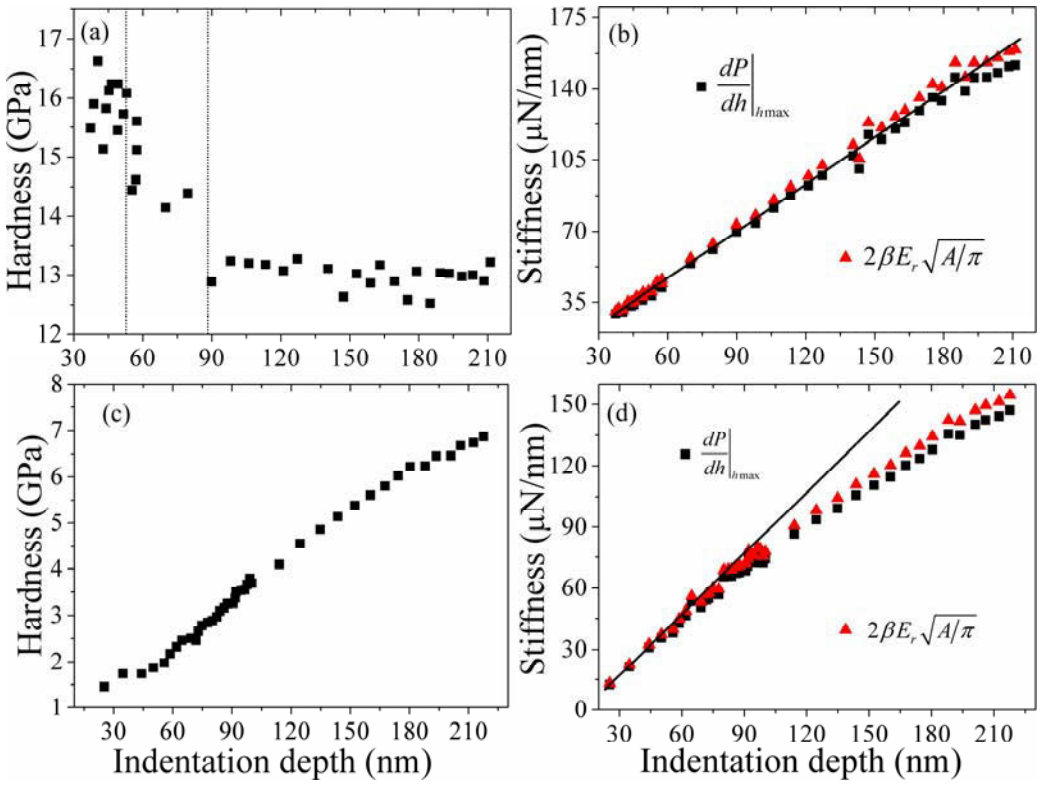

Figure 5.2.17: *Hardness and stiffness as a function of indentation depth. (a) and (b) Si–C–N films (sample #10) with the film thickness of 80 nm, (c) and (d) boron carbide films with film thickness of 100 nm.*

Figure 5.2.17 shows the hardness and stiffness of Si–C–N and boron carbide films with the thickness of 80 nm (sample #10) and 100 nm as a function of indentation depth. Clear evidence of substrate effects can be evidently seen from the hardness distribution of the Si–C–N thin film. For indentation depth lower than 40nm, the hardness varies between 15 GPa and 16 GPa. As the indentation depth increases from 40nm up to ~ 70 nm, the hardness decreases quickly down to a value close to that of the silicon substrate.

After the indenter penetrates the film into substrate (> 70 nm), the hardness value no

longer shows obvious variations. For soft boron carbide film, it is as expected that the hardness increases as a function of indentation depth. For such kind of soft film, even at shallow depth, a platform for hardness value can still not be found. This reveals that the hard substrates show greater effects on the measurements of mechanical properties for soft boron carbide films. In the range of film thickness (80 nm and 100 nm), stiffness is not sensitive to indentation depth. It shows no detectable deviation as the indentation depth increases. Besides, the hardness has also some fluctuations for samples #6 and #10 with different film thickness although they are deposited with the same experimental parameters. The variations of film thickness maybe results in the insensitivity of stiffness.

5.2.3.5 Energy Dissipation vs. H/E_r

Oliver and Pharr method is based on the calibrated area function without considering pile–up effects. It is mainly developed for homogeneous materials [217, 262]. In fact, pile–up effects are commonly seen in soft films on stiffer substrates [261, 274-276]. Therefore, errors are unavoidable in the determination of hardness and elastic modulus. If the calibration of area function can be avoided, the accuracy will be greatly improved.

Equation (5.2.9) gives the relationship between H/E_r^2 and P/S^2, which means that H/E_r^2 can be determined from P/S^2. In other words, H/E_r^2 can be obtained through P/S^2 without calibrating area function. If another relationship relating H and E with other measurable parameters can be found, then the hardness and elastic modulus can be deduced without considering any calibration for the contact area. Cheng's work by numerical method [277, 278] gives a clue that H/E is related to dissipated energy and total work evaluated from the loading and unloading curves. Here the relationship between the ratio of dissipated energy and total work and the ratio of H/E_r is examined.

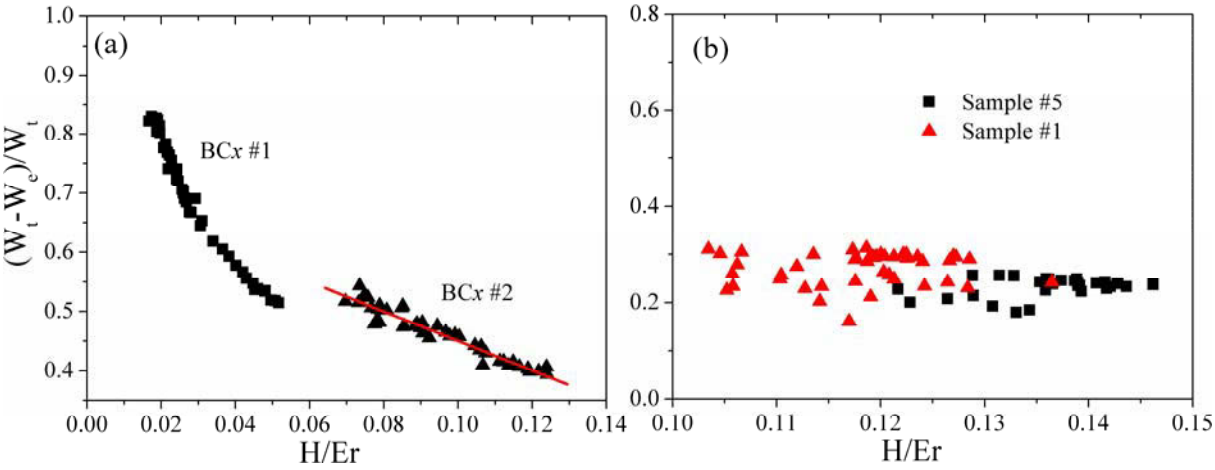

Figure 5.2.18: *Energy dissipation as a function of the ratio of hardness and reduced modulus (H/E_r) for boron carbide films and Si–C–N films (samples #5 and #9); the film thickness for BC_x #1 and BC_x #2 is 70 nm and 100 nm, respectively.*

Figure 5.2.18 shows the relationship between energy dissipation and H/E_r. Indeed, linear relation can be found in boron carbide films with 70 nm thickness. However, for the film with 100 nm thickness, the relation is obviously deviated from linearity. This means that even for the same kind of films, there is still no universal relation between energy dissipation and H/E_r that can be extracted. For Si–C–N film, the energy dissipation shows nearly constant in spite of the variations of H/E_r. Therefore, for such kinds of engineering films, the relations of energy dissipation and H/E_r is closely correlated to specifically experimental conditions.

5.2.3.6 Hardness vs. Elastic Modulus

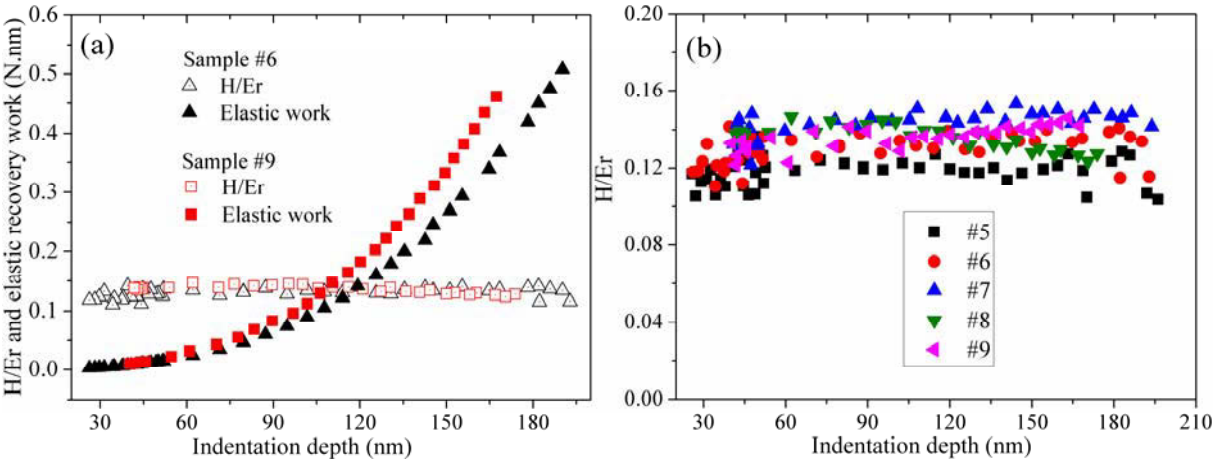

Figure 5.2.19: *(a) Elastic recovery work for samples #6 and #9 and (b) Ratio of the hardness*

and reduced modulus (H/E_r) for samples #5–9 as a function of indentation depth.

One of the most important observations in Musil's work [279] is that if the ratio H/E is constant, hard nano-composite coatings can exhibit the same elastic recovery work even if they have very different hardness. Following his idea, our samples are also examined. Figure 5.2.19a shows H/E_r and elastic recovery work of samples #6 and #9 as a function of indentation depth. The assumption that the ratio H/E_r is approximately constant is satisfied. That is, samples #6 and #9 have nearly the same ratio H/E_r. Furthermore, samples #6 and #9 also have different hardness values, i.e., 19.6 GPa for sample #6 and 25.9 GPa for sample #9 measured by Oliver and Pharr method. However, the elastic recovery work for the two samples follows not the same trend as a function of indentation depth.

At shallow indentation depth (< 30 nm), the elastic recovery work for the two samples matches well, but it begins to diverge as the indentation depth increases from 30 nm. As mentioned before, the indentation depth between 30 ~ 40 nm is the exact position that the samples have the tendency to plastic deformation. Therefore, we can refine Musil's work and conclude that for samples with similar ratio H/E_r, even if they have very different hardness, they can still have the same elastic recovery work providing that the indentation depth is located in the range of elastic deformation. Besides samples #6 and #9, the ratio H/E_r for samples #5, #7 and #8 is also shown in Figure 5.2.19b. In general, the ratio H/E_r shows less dependence of indentation depth, but the ratio H/E_r for different samples is not the same and shows some fluctuations.

In the last part, relations between elastic modulus and hardness are presented. At present experiments, it is quite difficult to synthesize arbitrary material with desired composition and properties independently. Therefore, it is not easy to extract more universal rule for composition design or property characterization. Empirical relations obtained are normally limited to specifically experimental conditions.

In the theoretical side, arbitrary composition design can be achieved, but no robust model is developed to model the hardness of amorphous films although other mechanical parameters like Young's modulus, bulk modulus and shear modulus are easily determined by

first–principles calculations at the atomic level [7, 9]. If the universal rule can be found between elastic modulus and hardness, theoretical calculation can be used to explore materials with undetected compositions and extreme properties, especially for attractive engineering materials. Figure 5.2.20 shows the relations between elastic modulus and hardness. Data from other publications [231, 280-282] are also collected for comparison. Clearly, the relations are closely correlated to specifically experimental conditions. Si–C–N films by different experiments show diversely approximate linear relations. Therefore, no universal rule can be extracted for such kind of coatings. Nevertheless, a weak trend can be seen that parts of the data follow the linear relation as marked by direct line in Figure 5.2.20.

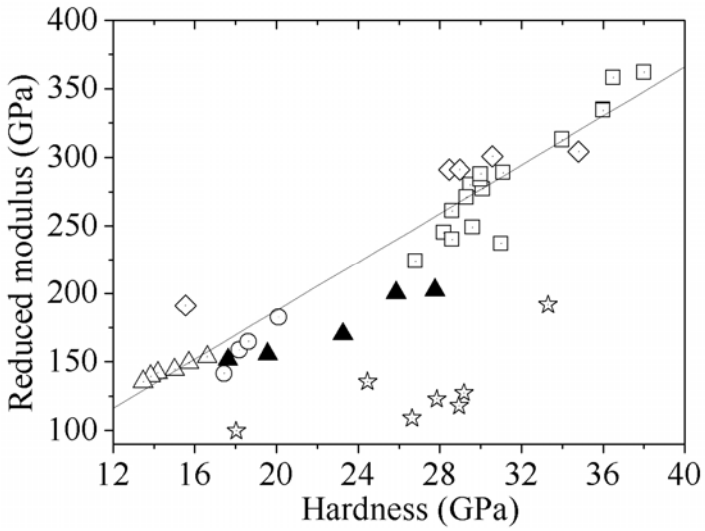

Figure 5.2.20: *Relationship between hardness and reduced modulus. Data from other publications [231, 280-282] are also shown for comparison. Data shown with solid triangle are the values from our experiments.*

5.2.3.7 Summary

The effect of substrate on attractive engineering film materials, Si–C–N and BC_x thin films, are examined. Unexpectedly, hard Si–C–N films on "soft" silicon substrates also show pile–up effects. This contrasts traditional observation of sink–in effects for hard films on soft substrates. For hard films on soft substrates, the parameter P/S^2 is not sensitive to the depth at shallow indentation depth. The deviation of stiffness at shallow indentation depth is not due to the substrate effects but rather a result of the effects of plastic deformation as revealed by the

total work and the elastic recovery work. No universal rule can be extracted to correlate energy dissipation with the ratio of hardness and elastic modulus. Revealed by the deviations between total work and elastic recovery work, hardness values from nanoindentation measurements exhibit the features of elastic deformation, inherently different from the traditional measurements of hardness, which are taken from the residual impression after unloading and display the characterization of plastic deformation.

6 Summary and Outlook

6.1 Summary

First–principles calculations, as a powerful tool to predict diverse properties of materials, are employed to investigate the novel superhard crystalline BC_2N phase with diamond–like structure. Almost all previous predictions on the structure of crystalline BC_2N phase are based on the general principle of searching for structural models with the lowest energy regardless of observations in experiments. Therefore, the structural models proposed in previous works mainly have high symmetry with orderly atomic arrangements over crystal lattices. On the contrary, it is the experimental observations that enlighten us to propose our random solid solution models. That is, B, C, and N atoms are randomly distributed over crystal lattices. These are two completely different approaches for predicting the structure of the cubic BC_2N phase: one is simply conforming to the basic concept in theoretical calculations of finding the optimized lowest energy structures. Our approach is based on starting from more reasonable structural models that were suggested by the experimental observations.

A parameter, the degree of mixture χ, is introduced to classify the produced structural models of cubic BC_2N phases. After classification, we find that our random solid solution models can explain the contradictions that existed in experiments and in theoretical calculations. With regards to the experiments, the inconsistency of both lattice parameters and mechanical properties can be understood from the different ways of mixing among B, C, and N atoms over crystal lattices, i.e., different degrees of mixture. Higher values of degree of mixture correspond to more random distributions of B, C, and N atoms, resulting in the expansion of lattice parameters and the weakness of mechanical properties. This is possible because the extreme synthesis conditions, such as high pressure high temperature (HPHT), can provide

enough energy to allow atomic relaxation towards maximum entropy according to statistical thermodynamics, corresponding to more random distributions of B, C, and N atoms. Even for the cubic BC_2N phase, different experimental conditions for atomic relaxation can result at different degrees of mixture, therefore yielding different lattice parameters and mechanical properties. With regards to the theoretical calculations, the proposed models in previous works correspond to low degree of mixture with orderly atomic arrangements over the crystal lattices. Our random solid solution models can unify the divergences shown in experiments and also in theoretical calculations.

Besides the BC_2N composition, we extended the random solid solution model to other compositions that lie along the C–BN iso–electronic line and in the upper rhombus of the ternary B–C–N phase diagram to further explore potential superhard phases and superhard areas. We found that there indeed exist some attractive compositions of carbon–rich BC_xN crystals with better structural stability and mechanical properties in comparison to the intensively investigated c–BC_2N. Since BC_2N has been successfully synthesized in experiments, we expect that these compositions can be synthesized in the near future, too. In addition, we also found that the area within B: 25 ~ 35 at.%; C: 45 ~ 55 at.%; N: 5 ~ 20 at.% in the ternary B–C–N phase diagram has relatively low formation energies, good ductility, and intermediate hardness (~ 66 GPa), which might be synthesized and have some technological applications. These findings indicate that some other compositions with even more stable and better properties in the ternary B–C–N phase diagram beyond the popular BC_2N composition are more attractive to promote further experimental works. We also extended our random solid solution model to the crystalline B–C system, particularly the cubic BC_5 phase, a crystalline phase intensively investigated in the last few years. The excellent agreement with the structural information (XRD) strongly demonstrates the portability of our models to such kinds of diamond–like structures, further verifying the commonality of our models in dealing with diamond–like crystalline phases formed by light elements like B, C, N, O etc.

For the calculations of amorphous B–C–N materials, to the best of our knowledge

it is the first time to perform real first–principle calculations on amorphous B–C–N materials at the atomic scale, and it is also the first report of a relation between chemical composition and mechanical properties on such plenty of different compositions. Therefore, we can achieve a general comprehension of the mechanical behavior on such a large area on the ternary B–C–N phase diagram. The theoretical results can generally guide future experimental works to intentionally prepare those amorphous B–C–N materials with good mechanical properties.

We also performed experimental works on amorphous B–C–N materials to validate our theoretical results. Our successfully obtained B–C–N compositions are almost exactly located in the area that has low formation energy according to the theoretical results, demonstrating the reasonability of our theoretical calculations on amorphous B–C–N materials. However, amorphous B–C–N materials have usually bad adhesive abilities to silicon substrates. They can be easily peeled off from the silicon substrate, resulting in the difficulty of measuring their mechanical properties. That is why most of the previous works about amorphous B–C–N films only focused on the structural characterization. We attempted to improve the adhesion ability by introducing a silicon source in the film to form quaternary Si–B–C–N materials. We found that the addition of silicon can greatly improve the adhesion ability of films to silicon substrates. Then we attempt to replace boron by silicon to prepare ternary Si–C–N materials, and we found that Si–C–N materials also have good adhesion and mechanical properties that can be comparable to amorphous B–C–N and Si–B–C–N materials.

In addition, no perfect theory or model of hardness for amorphous materials has been proposed yet. It is quite difficult to extract the essence behind the hardness of amorphous materials because the disordered atomic arrangements in amorphous materials exacerbate the complexity of hardness characterization. Nevertheless, the hardness theory for covalent crystalline materials enlightens us to explore the derivation of hardness in amorphous materials from the point of bonding types and bond fractions in amorphous materials. Based on the investigation of amorphous

Si–C–N materials, we found that the bonding types and bond fractions play a crucial role in determining the mechanical properties of amorphous Si–C–N materials.

6.2 Outlook

At present, it is still not easy to synthesize amorphous Si–C–N materials with a broad range of chemical compositions in experiments. The actual case is that the obtained compositions are still located in a very narrow range even when we change diverse experimental parameters. Theoretical calculations are very powerful tools to overcome the difficulty shown up in the experiments. The compositions can be designed and their mechanical properties can also be calculated. Therefore, our future work will be focused on the theoretical calculation of amorphous Si–C–N materials together with the quaternary Si–B–C–N materials to give positive guidance for experimental synthesis of such amorphous materials.

References

[1] A. A. Voevodin, M. S. Donley, J. S. Zabinski, Surf. Coat. Technol. 92 (1997) 42.

[2] S. PalDey, S. C. Deevi, Mater. Sci. Eng. A 342 (2003) 58.

[3] J. E. Sundgren, H. T. G. Hentzell, J. Vac. Sci. Technol. A 4 (1986) 2259.

[4] T. Irifune, A. Kurio, S. Sakamoto, T. Inoue, H. Sumiya, Nature 421 (2003) 599.

[5] F. X. Lu, J. M. Liu, G. C. Chen, W. Z. Tang, C. M. Li, J. H. Song, Y. M. Tong, Diamond Relat. Mater. 13 (2004) 533.

[6] L. Vel, G. Demazeau, J. Etourneau, Mater. Sci. Eng. B 10 (1991) 149.

[7] C. Zhuang, J. Zhao, X. Jiang, X. Jiang, J. Phys.: Condens. Matter 21 (2009) 405401.

[8] S. K. Estreicher, C. H. Chu, D. S. Marynick, Phys. Rev. B 40 (1989) 5739.

[9] J. Zhao, C. Zhuang, X. Jiang, Diamond Relat. Mater. 19 (2010) 1419.

[10] A.R. Badzian, Mater. Res. Bull. 16 (1981) 1385.

[11] T. Sasaki, M. Akaishi, S. Yamaoka, Y. Fujiki, T. Oikawa, Chem. Mater. 5 (1993) 695.

[12] S. Nakano, M. Akaishi, T. Sasaki, S. Yamaoka, Chem. Mater. 6 (1994) 2246.

[13] T. Komatsu, M. Nomura, Y. Kakudate, S. Fujiwara, J. Mater. Chem. 6 (1996) 1799.

[14] T. Komatsu, J. Mater. Chem. 14 (2004) 221.

[15] T. Komatsu, M. Samedima, T. Awano, Y. Kakadate, S. Fujiwara, J. Mater. Process. Technol. 85 (1999) 69.

[16] T. Komatsu, M. Nomura, Y. Kakudate, S. Fujiwara, J. Chem. Soc. Faraday Trans. 94 (1998) 1649.

[17] T. Komatsu, A. Goto, J. Mater. Chem. 12 (2002) 1288.

[18] V. L. Solozhenko, D. Andrault, G. Fiquet, M. Mezouar, D. C. Rubie, Appl. Phys. Lett. 78 (2001) 1385.

[19] H. W. Hubble, I. Kudryashov, V. L. Solozhenko, P. V. Zinin, S. K. Sharma, L. C.

Ming, J. Raman Spectrosc. 35 (2004) 822.

[20] Y. Zhao, D. W. He, L. L. Daemen, T. D. Shen, R. B. Schwarz, Y. Zhu, D. L. Bish, J. Huang, J. Zhang, G. Shen, J. Qian, T. W. Zerda, J. Mater. Res. 17 (2002) 3139.

[21] J. L. He, Y. J. Tian, D. L. Yu, T. S. Wang, S. M. Liu, L. C. Guo, D. C. Li, X. P. Jia, L. X. Chen, G. T. Zou, O. Yanagisawa, Chem. Phys. Lett. 340 (2001) 431.

[22] J. L. He, Y. J. Tian, D. L. Yu, T. S. Wang, F. R. Xiao, A. D. Li, C. Li, Y. G. Peng, L. Li, J. Mater. Sci. Lett. 19 (2000) 2061.

[23] G. Sun, Z. Liu, Z. Zhou, J. He, D. Yu, Y. Tian, Diamond Relat. Mater. 15 (2006) 1659.

[24] E. Knittle, R. B. Kaner, R. Jeanloz, M. L. Cohen, Phys. Rev. B 51 (1995) 12149.

[25] S. N. Tkachev, V. L. Solozhenko, P. V. Zinin, M. H. Manghnani, L. C. Ming, Phys. Rev. B 68 (2003) 052104.

[26] Y. Tateyama, T. Ogitsu, K. Kusakabe, S. Tsuneyuki, S. Itoh, Phys. Rev. B 55 (1997) R10161.

[27] R. Q. Zhang, K. S. Chan, H. F. Cheung, S. T. Lee, Appl. Phys. Lett. 75 (1999) 2259.

[28] H. Sun, S. H. Jhi, D. Roundy, M. L. Cohen, S. G. Louie, Phys. Rev. B 64 (2001) 094108.

[29] Y. Zhang, H. Sun, C. Chen, Phys. Rev. Lett. 93 (2004) 195504.

[30] Z. Pan, H. Sun, C. Chen, Phys. Rev. B 70 (2004) 174115.

[31] X. Luo, X. Guo, B. Xu, Q. Wu, Q. Hu, Z. Liu, J. He, D. Yu, Y. Tian, Phys. Rev. B 76 (2007) 094103.

[32] X. Zhou, J. Sun, Y. Fan, J. Chen, H. Wang, X. Guo, J. He, Y. Tian, Phys. Rev. B 76 (2007) R100101.

[33] X. Luo, X. Guo, Z. Liu, J. He, D. Yu, B. Xu, Y. Tian, H. Wang, Phys. Rev. B 76 (2007) 092107.

[34] X. Luo, Z. Liu, J. He, B. Xu, D. Yu, H. Wang, Y. Tian, J. Appl. Phys. 105 (2009) 043509.

[35] X. Luo, X. Zhou, Z. Liu, J. He, B. Xu, D. Yu, H. Wang, Y. Tian, J. Phys. Chem. C 112 (2008) 9516.

[36] X. Luo, L. Li, W. Wang, Y. Tian, J. Appl. Phys. 109 (2011) 023516.

[37] L. Hou, F. Gao, H. Gou, Z. Wang, M. Tian, Crys. Growth Design 8 (2008) 1972.

[38] S. Chen, X. G. Gong, S. H. Wei, Phys. Rev. Lett. 98 (2007) 015502.

[39] S. Chen, X. Gong, S. Wei, Phys. Rev. B 77 (2008) 014113.

[40] W. R. L. Lambrecht, B. Segall, Phys. Rev. B 40 (1989) 9909.

[41] J. Widany, W. S. Verwoerd, T. Frauenheim, Diamond Relat. Mater. 7 (1998) 1633.

[42] J. C. Zheng, H. Q. Wang, A. T. S. Wee, C. H. A. Huan, Phys. Rev. B 66 (2002) 092104.

[43] M. Mattesini, S. F. Matar, Comput. Mater. Sci. 20 (2001) 107.

[44] A. Zaoui, F. E. H. Hassan, Superlattice Microst. 32 (2002) 91.

[45] E. Kim, T. Pang, W. Utsumi, V. L. Solozhenko, Y. Zhao, Phy. Rev. B 75 (2007) 184115.

[46] J. Yue, W. Cheng, X. Zhang, D. He, G. Chen, Thin Solid Films 375 (2000) 247.

[47] A. Lousa, J. Esteve, S. Muhl, E. Martinez, Diamond Relat. Mater. 9 (2000) 502.

[48] D. He, W. Cheng, J. Qin, J. Yue, E. Xie, G. Chen, Appl. Surf. Sci. 191 (2002) 338.

[49] Y. Wada, Y. K. Yap, M. Yoshimura, Y. Mori, T. Sasaki, Diamond Relat. Mater. 9 (2000) 620.

[50] Y. K. Yap, Y. Wada, M. Yanmaoka, M. Yoshimura, Y. Mori, T. Sasaki, Diamond Relat. Mater. 10 (2001) 1137.

[51] I. Caretti, I. Jimenez, J. M. Albella, Diamond Relat. Mater. 12 (2003) 1079.

[52] F. Zhou, K. Adachi, K. Kato, Thin Solid Films 497 (2006) 210.

[53] D. Hegemann, R. Riedel, C. Oehr, Thin Solid Films 339 (1999) 154.

[54] H. Ahn, L. Alberts, J. Wohle, K. T. Rie, Surf. Coat. Technol. 142-144 (2001) 894.

[55] H. Sota, C. Kimura, K. Aoki, T. Sugino, Diamond Relat. Mater. 19 (2011) 1441.

[56] S. Stoeckel, K. Weise, D. Dietrich, T. Thamm, M. Braun, R. Cremer, D. Neuschuetz, G. Marx, Thin Solid Films 420-421 (2002) 465.

[57] E.R. Engbrecht, Y.M. Sun, K.H. Junker, J.M. White, J.G. Ekerdt, J. Vac. Sci. Technol. A 22 (2004) 2152.

[58] J. Lv, H. Li, P. Zhu, X. Lv, Y. Li, Appl. Surf. Sci. 257 (2011) 4963.

[59] P. C. Tsai, Surf. Coat. Technol. 201 (2007) 5108.

[60] Y. K. Yap, Y. Wada, M. Yamaoka, M. Yoshimura, Y. Mori, T. Sasaki, Diamond Relat. Mater. 10 (2001) 1137.

[61] Z. F. Zhou, I. Bello, M. K. Lei, K. Y. Li, C. S. Lee, S. T. Lee, Surf. Coat. Technol. 128-129 (2000) 334.

[62] M. K. Lei, Q. Li, Z. F. Zhou, I. Bello, C. S. Lee, S. T. Lee, Thin Solid Films 389 (2001) 194.

[63] S. C. Chien, S. Chattopadhyay, L. C. Chen, S. T. Lin, K. H. Chen, Diamond Relat. Mater. 12 (2003) 1463.

[64] X. M. Yang, X. M. Wu, L. J. Zhuge, F. Zhou, Appl. Surf. Sci. 255 (2009) 4279.

[65] S. Ulrich, A. Kratzsch, H. Leiste, M. Stueber, P. Schossmacher, H. Holleck, J. Binder, D. Schild, S. Westermeyer, P. Becker, H. Oechsner, Surf. Coat. Technol. 116-119 (1999) 742.

[66] T. Hasegawa, K. Yamamoto, Y. Kakudate, M. Ban, Surf. Coat. Technol. 169-170 (2003) 270.

[67] T. Hasegawa, K. Yamamoto, Y. Kakudate, Diamond Relat. Mater. 11 (2002) 1290.

[68] Y. Chen, S. Yang, J. Zhang, Appl. Surf. Sci. 255 (2009) 8575.

[69] I. Caretti, I. Jimenez, R. Gago, D. Caceres, B. Abendroth, J.M. Albella, Diamond Relat. Mater. 13 (2004) 1532.

[70] Q. Yang, C. B. Wang, S. Zhang, D. M. Zhang, Q. Shen, L. M. Zhang, Surf. Coat. Technol. 204 (2010) 1863.

[71] V. Linss, I. Hermann, N. Schwarzer, U. Kreissig, F. Richter, Surf. Coat. Technol. 163-164 (2003) 220.

[72] X. Chen, Z. Wang, S. Ma, V. Ji, P. K. Chu, Diamond Relat. Mater. 19 (2010) 1225.

[73] V. O. Todi, B. P. Shantheyanda, R. M. Todi, K. B. Sundaram, K. Coffey, Mater. Sci. Eng. B 176 (2011) 878.

[74] M. Born, J. R. Oppenheimer, Ann. Phys. 84 (1927) 457.

[75] D. R. Hartree, Proc. R. Soc. London A113 (1928) 621.

[76] J. C. Slater, Phys. Rev. 35 (1930) 210.

[77] V. Fock, Z. Phys. 61 (1930) 126.

[78] D. R. Hartree, W. Hartree, Proc. Roy. Soc. A150 (1935) 9.

[79] L. H. Thomas, Proc. Cambridge Philos. Soc. 23 (1927) 542.

[80] E. Fermi, Z. Phys. 48 (1928) 73.

[81] P. Hohenberg, W. Kohn, Phys. Rev. 136 (1964) B864.

[82] W. Kohn, L. J. Sham, Phys. Rev. 140 (1965) A1133.

[83] J. P. Perdew, K. Burke, M. .Ernzerhof, Phys. Rev. Lett. 77 (1996) 3865.

[84] B. Hammer, L. B. Hansen, J. K. Norskov, Phys. Rev. B 59 (1999) 7413.

[85] J. P. Perdew, J. A. Chevary, S. H. Vosko, K. A. Jackson, M. R. Pederson, D. J. Singh, C. Fiolhais, Phys. Rev. B 46 (1992) 6671.

[86] Z. Wu, R. E. Cohen, Phys. Rev. B 73 (2006) 235116.

[87] J. P. Perdew, A. Ruzsinszky, G. I. Csonka, O. A. Vydrov, G. E. Scuseria, L. A. Constantin, X. Zhou, K. Burke, Phys. Rev. Lett. 100 (2008) 136406.

[88] N. Troullier, J. L. Martins, Phys. Rev. B 43 (1991) 1993.

[89] D. Vanderbilt, Phys. Rev. B 41 (1990) 7895.

[90] G. Kresse, J. Furthmuller, Comput. Mater. Sci. 6 (1996) 50.

[91] V. L. Solozhenko, E. Gregoryanz, Mater. Today 8 (2005) 44.

[92] W. R. L. Lambrecht, B. Segall, Phy. Rev. B 40 (1898) 9909.

[93] W. R. L. Lambrecht, B. Segall, Phy. Rev. B 47 (1993) 9289.

[94] M. D. Segall, P. J. D. Lindan, M. J. Probert, C. J. Pickard, P. J. Hasnip, S. J. Clark, M. C. Payne, J. Phys.: Condens. Matter 14 (2002) 2717.

[95] J. P. Perdew, J. A. Chevary, S. H. Vosko, K. A. Jackson, M. R. Pederson, D. J. Singh, C. Fiolhais, Phys. Rev. B 46 (1992) 6671.

[96] R. Hill, Proc. Phys. Soc. 64 (1952) 349.

[97] V. L. Solozhenko, S. N. Dub, N. V. Novikov, Diamond Relat. Mater. 10 (2001) 2228.

[98] F. Gao, J. He, E. Wu, S. Liu, D. Yu, D. Li, S. Zhang, Y. Tian, Phys. Rev. Lett. 91 (2003) 015502.

[99] X. J. Guo, Z. Y. Liu, X. G. Luo, D. L. Yu, J. L. He, Y. J. Tian, J. Sun, H. T. Wang, Diamond Relat. Mater. (2007) 526.

[100] R. H. Telling, C. J. Pickard, M. C. Payne, J. E. Field, Phys. Rev. Lett. 84 (2000)

5160.

[101]D. Roundy, C. R. Krenn, M. L. Cohen, J. W. Morris, Phys. Rev. Lett. 82 (1999) 2713.

[102]D. Roundy, C. R. Krenn, M. L. Cohenab, J. W. M. Jr., Phil. Mag. A 81 (2001) 1725.

[103]M. Grimsditch, E. S. Zouboulis, A. Polian, J. Appl. Phys. 76 (1994) 832.

[104]C. B. Samantaray, R. N. Singh, Inter. Mater. Rev. 50 (2005) 313.

[105]X. W. Zhang, H. G. Boyen, P. Ziemann, F. Banhart, Appl. Phys. A 80 (2005) 735.

[106]X. Jiang, C.P. Klages, R. Zachai, M. Hartweg, H.J. Füsser, Appl. Phys. Lett. 62 (1993) 3438.

[107]M. W. Geis, J. C. Twichell, N. N. Efremow, K. Krohn, T. M. Lyszczarz, Appl. Phys. Lett. 68 (1996) 2294.

[108]L. Vegard, Z. Phys. 5 (1921) 17.

[109]X. G. Luo, X. J. Guo, Z. Y. Liu, J. L. He, D. L. Yu, Y. J. Tian, H. T. Wang, J. Appl. Phys. 101 (2007) 083505.

[110]J. C. Zheng, C. H. A. Huan, A. T. S. Wee, R. Z. Wang, Y. M. Zheng, J. Phys.: Condens. Matter 11 (1999) 927.

[111]M. C. Payne, M. T. Teter, D. C. Allen, T. A. Arias, J. D. Joannopoulos, Rev. Mod. Phys. 64 (1992) 1045.

[112]D. R. Hamann, M. Schluter, C. Chiang, Phys. Rev. Lett. 43 (1979) 1494.

[113]J. P. Perdew, Y. Wang, Phys. Rev. B 45 (1992) 13244.

[114]F. Langenhorst, V. L. Solozhenko, Phys. Chem. Chem. Phys. 4 (2002) 5183.

[115]R. D. Paiva, S. Azevedo, J. Phys.: Condens. Matter 18 (2006) 3509.

[116]J. L. Reno, E. D. Jones, Phys. Rev. B 45 (1992) 1440.

[117]N. Bouarissa, Phys. B 399 (2007) 126.

[118]G. Ciatto, F. Boscherini, A. A. Bonapasta, F. Filippone, A. Polimeni, M. Capizzi, M. Berti, G. Bisognin, Phys. Rev. B 79 (2009) 165205.

[119]P. S. Branicio, J. P. Rino, F. Shimojo, R. K. Kalia, A. Nakano, P. Vashishta, J. Appl. Phys. 94 (2003) 3840.

[120]E. Bengu, M. Genisel, O. Gulseren, R. Ovali, Thin Solid Films 518 (2009) 1459.

[121]J. He, L. Guo, E. Wu, X. Luo, Y. Tian, J. Phys.: Condens. Matter 16 (2004) 8131.

[122]X. Jiang, C. Zhuang, X. Li, L. Sai, J. Zhao, Diamond Relat. Mater. 20 (2011) 891.

[123]X. Jiang, J. Zhao, Comput. Mater. Sci. 50 (2011) 2287.

[124]R. Weihrich, S. Matar, E. Betranhandy, J. Phys. Chem. Solids 64 (2003) 1539.

[125]S. Kamran, K. Chen, L. Chen, Phys. Rev. B 79 (2009) 024106.

[126]C. Zhuang, X. Li, J. Zhao, L. Liu, X. Jiang, J. Phys.: Condens. Matter 22 (2010) 215401.

[127]L. Vitos, P. Korzhavyi, B. Jöhansson, Phys. Rev. Lett. 88 (2002) 155501.

[128]S. Pugh, Philos. Mag. 45 (1954) 823.

[129]V. L. Solozhenko, O. O. Kurakevych, D. Aandrault, Y. L. Godec, M. Mezouar, Phys. Rev. Lett. 102 (2009) 015506.

[130]M. Calandra, F. Mauri, Phys. Rev. Lett. 101 (2008) 016401.

[131]Y. Liang, W. Zhang, J. Zhao, L. Chen, Phys. Rev. B 80 (2009) 113401.

[132]L. E. Jones, P. A. Thrower, Carbon 29 (1991) 251.

[133]T. Yokoya, T. Nakamura, T. Matsushita, T. Muro, Y. Takano, M. Nagao, T. Takenouchi, H. Kararada, T. Oguchi, Nature 438 (2005) 647.

[134]X. Blase, C. Adessi, D. Connetable, Phys. Rev. Lett. 93 (2004) 237004.

[135]J. E. Moussa, M. L. Cohen, Phys. Rev. B 77 (2008) 064518.

[136]H. J. Xiang, Z. Li, J. Yang, J. G. Hou, Q. Zhu, Phys. Rev. B 70 (2004) 212504.

[137]V. A. Sidorov, E. A. Ekimov, S. M. Stishov, E. D. Bauer, J. D. Thompson, Phys. Rev. B 71 (2005) 060502.

[138]E. Bustarret, J. Kacmarcik, C. Marcenat, E. Gheeraert, C. Cytermann, J. Marcus, T. Klein, Phys. Rev. Lett. 93 (2004) 237005.

[139]C. Jiang, Z. Lin, Y. Zhao, Phys. Rev. B 80 (2009) 184101.

[140]P. Lazar, R. Podloucky, Appl. Phys. Lett. 94 (2009) 251904.

[141]Y. Yao, J.S. Tse, D.D. Klug, Phys. Rev. B 80 (2009) 094106.

[142]Y. J. Wang, C. Y. Wang, J. Appl. Phys. 106 (2009) 043513.

[143]X. Shao, Chin. Phys. Lett. 27 (2010) 016101.

[144]R. F. Zhang, S. Veprek, A. S. Argon, Phys. Rev. B 80 (2009) 233401.

[145]E. A. Ekimov, V. A. Sidorow, E. D. Bauer, N. N. Melnik, N. J. Curro, J. D. Thompson, S. M. Stishov, Nature 428 (2004) 542.

[146]P. V. Zinin, L. C. Ming, S. K. Sharma, S. M. Hong, Y. Xie, T. Irifune, T. Shinmei, J. Phys.: Conf. Ser. 121 (2008) 062002.

[147]C. Zhuang, J. Zhao, X. Jiang, X. Jiang, J. Phys.: Condens. Matter 21 (2009) 405401.

[148]N. Dubrovinskaia, G. Eska, G. A. Sheshin, H. Braun, J. Appl. Phys. 99 (2006) 033903.

[149]F. Pruvost, E. Bustarret, A. Deneuville, Diamond Relat. Mater. 9 (2000) 295.

[150]L. L. G. Silva, M. K. Franco, F. Yokaichiya, N. G. Gerreira, E. J. Corat, Diamond Relat. Mater. 11 (2002) 153.

[151]T. Shirasaki, A. Derre, M. Menetrier, A. Tressaud, S. Flandrois, Carbon 38 (2000) 1461.

[152]V. L. Solozhenko, N. A. Dubrovinskaia, L. S. Dbrovinsky, Appl. Phys. Lett. 85 (2004) 1508.

[153]P. V. Zinin, L. C. Ming, I. Kudryashov, N. Konishi, M. H. Manghnani, S. K. Sharma, J. Appl. Phys. 100 (2006) 013516.

[154]E. Martinez, J. L. Andujar, M. C. Polo, J. Esteve, J. Robertson, W. I. Milne, Diamond Relat. Mater. 10 (2001) 145.

[155]J. Tersoff, Phys. Rev. B 39 (1989) 5568.

[156]T. Thamm, K. U. Korner, W. Bohne, E. Strub, J. Rohrich, S. Stockel, G. Marx, Appl. Surf. Sci. 252 (2005) 223.

[157]T. Hasegawa, K. Yamamoto, Y. Kakudate, M. Ban, Surf. Coat. Technol. 169-170 (2003) 270.

[158]D. H. Kim, E. Byon, S. Lee, J. K. Kim, H. Ruh, Thin Solid Films 447-448 (2004) 192.

[159]I. Caretti, I. Jimenez, J. M. Albella, Diamond Relat. Mater. 12 (2003) 1079.

[160]S. Stockel, K. Weise, T. Thamm, K.U. Korner, D. Dietrich, G. Marx, Anal. Bioanal. Chem. 375 (2003) 884.

[161]V. Linss, S. E. Rodil, P. Reinke, M. G. Garnier, P. Oelhafen, U. Kreissig, F. Richter, Thin Solid Films 467 (2004) 76.

[162]E. Martinez, A. Lousa, J. Esteve, Diamond Relat. Mater. 10 (2001) 1892.

[163]Y. Chen, Y. W. Chung, S. Y. Li, Surf. Coat. Technol. 200 (2006) 4072.

[164]S. Ulrich, T. Theel, J. Schwan, H. Ehrhardt, Surf. Coat. Technol. 97 (1997) 45.

[165]V. Linss, N. Schwarzer, T. Chudoba, M. Karniychuk, F. Richter, Surf. Coat. Technol. 195 (2005) 287.

[166]K. Yamamoto, H. Ito, S. Kujime, Surf. Coat. Technol. 201 (2007) 5244.

[167]D. Kurapov, J. M. Schneider, Plasma Chem. Plasma Proc. 25 (2005) 613.

[168]I. Caretti, J. M. Albella, I. Jimenez, Diamond Relat. Mater. 16 (2007) 63.

[169]I. Caretti, I. Jimenez, R. Gago, D. Caceres, B. Abendroth, J.M. Albella, Diamond Relat. Mater. 13 (2004) 1532.

[170]K. Chen, L. Zhao, J. Rodgers, J. Tse, J. Phys. D: Appl. Phys. 36 (2003) 2725.

[171]H. Zhang, B. Johansson, L. Vitos, Phys. Rev. B 79 (2009) 224201.

[172]S. Ulrich, A. Kratzsch, H. Leiste, M. Stüber, P. Schloßmacher, H. Holleck, J. Binder, D. Schild, S. Westermeyer, P. Becker, H. Oechsner, Surf. Coat. Technol. 116-119 (1999) 742.

[173]F. C. Jia, C. Q. Zhuang, C. Y. Guan, J. J. Zhao, Y. Z. Bai, X. Jiang, Vacuum 85 (2011) 887.

[174]K. Shirai, S. Emura, S. I. Gonda, J. Appl. Phys. 78 (1995) 3392.

[175]S. I. Aoqui, H. Miyata, T. Ohshima, T. Ikegami, K. Ebihara, Thin Solid Films 407 (2002) 126.

[176]D. Y. He, W. J. Cheng, J. Qin, J. S. Yue, E. Q. Xie, G. H. Chen, Appl. Surf. Sci. 191 (2002) 338.

[177]T. Sugino, Y. Etou, T. Tai, H. Mori, Appl. Phys. Lett. 80 (2001) 649.

[178]T. Sugino, H. Hieda, Diamond Relat. Mater. 9 (2000) 1233.

[179]S. Xu, X. Ma, M. Su, IEEE. Trans. Plasma Sci. 34 (2006) 1199.

[180]A. Essafti, E. Ech-Chamikh, J. L.G. Fierro, Diamond Relat. Mater. 14 (2005) 1663.

[181]S. Chattopadhyay, S. C. Chien, L. C. Chen, K. H. Chen, H. Y. Lee, Diamond

Relat. Mater. 11 (2002) 708.

[182]Y. M. Chen, Z. X. Zeng, S. R. Yang, J. Y. Zhang, Diamond Relat. Mater. 18 (2009) 20.

[183]T. Hasegawa, K. Yamamoto, Y. Kakudate, Diamond Relat. Mater. 12 (2003) 1045.

[184]H. S. Kim, I. H. Choi, Y. J. Baik, Surf. Coat. Technol. 133-134 (2000) 473.

[185]M. O. Watanabe, S. Itoh, K. Mizushima, T. Sasaki, Appl. Phys. Lett. 68 (1996) 2962.

[186]E. Byon, M. Son, K. H. Lee, K. S. Nam, N. Hara, K. Sugimoto, Electrochim. Acta 51 (2006) 2660.

[187]M. O. Watanabe, T. Sasaki, S. Itoh, K. Mizushima, Thin Solid Films 281-282 (1996) 334.

[188]J. M. Ripalda, I. Montero, L. Galan, Diamond Relat. Mater. 7 (1998) 402.

[189]F. Zhou, K. Adachi, K. Kato, Wear 261 (2006) 301.

[190]L. Galan, I. Montero, F. Rueda, Surf. Coat. Technol. 83 (1996) 103.

[191]C. Q. Zhuang, J. J. Zhao, F. C. Jia, C. Y. Guan, Z. L. Wu, Y. Z. Bai, X. Jiang, Surf. Coat. Technol. 204 (2009) 713.

[192]M. N. Oliveira, A. M. B. D. Rego, O. Conde, Surf. Coat. Technol. 100-101 (1998) 398.

[193]T. Tai, T. Sugiyama, T. Sugino, Diamond Relat. Mater. 12 (2003) 1117.

[194]H. Kiinzli, P. Gantenbein, R. Steiner, P. Oelhafen, J. Anal. Chem. 346 (1993) 41.

[195]M. L. Cohen, Phys. Rev. B 32 (1985) 7988.

[196]A. Zerr, M. Kempf, M. Schwarz, E. Kroke, M. Goken, R. Riedel, J. Am. Ceram. Soc. 85 (2002) 86.

[197]A.Y. Liu, R. M. Wentzcovitch, Phys. Rev. B 50 (1994) 10362.

[198]Y. Maniette, M. Inagaki, M. Sakai, J. Eur. Ceram. Soc. 7 (1991) 255.

[199]D. Scott, J. Blackwell, Wear 24 (1973) 61.

[200]A. Badzian, T. Badzian, W. D. Drawl, R. Roy, Diamond Relat. Mater. 7 (1998) 1519.

[201]T. Nozawa, T. Hinoki, A. Hasegawa, A. Kohyama, Y. Katoh, L. L. Snead, C. H.

H. Jr., J. B. J. Hegeman, J. Nucl. Mater. 386-388 (2009) 622.

[202]A. S. Bhattacharyya, S. K. Mishra, J. Micromech. Microeng. 21 (2011) 015011.

[203]I. Blaszczyk-Lezak, A. M. Wrobel, D. M. Bielinski, Diamond Relat. Mater. 15 (2006) 1650.

[204]I. Blaszczyk-Lezak, A. M. Wrobel, M. P. M. Kivitorma, I. J. Vayrynen, Chem. Vap. Deposition 11 (2005) 44.

[205]G. Lehmann, P. Hess, J.-J. Wu, C. T. Wu, T. S. Wong, K. H. Chen, L. C. Chen, H.-Y. Lee, Phys. Rev. B 64 (2001) 165305.

[206]Y. Awad, M. A. Khakani, C. Aktik, J. Mouine, N. Camire, M. Lessard, M. Scarlete, H. A. Al-Abadleh, R. Smirani, Surf. Coat. Technol. 204 (2009) 539.

[207]J. Vicek, M. Kormunda, J. Cizek, V. Perina, J. Zemek, Diamond Relat. Mater. 12 (2003) 1287.

[208]A. M. Wrobel, I. Blaszczyk-Lezak, P. Uznanski, B. Glebocki, Chem. Vap. Deposition 16 (2010) 211.

[209]T. Berlind, N. Hellgren, M. P. Johansson, L. Hultman, Surf. Coat. Technol. 141 (2001) 145.

[210]D. H. Kuo, D. G. Yang, Thin Solid Films 374 (2000) 92.

[211]J. Haug, P. Lamparter, M. Weinmann, F. Aldinger, Chem. Mater. 16 (2004) 72.

[212]J. Musil, F. Kunc, H. Zeman, H. Polakova, Surf. Coat. Technol. 154 (2002) 304.

[213]R. Saha, W.D. Nix, Acta Mater. 50 (2002) 23.

[214]N. Tayebi, A. A. Polycarpou, T. F. Conry, J. Mater. Res. 19 (2004) 1791.

[215]W. C. Oliver, G. M. Pharr, J. Mater. Res. 7 (1992) 1564.

[216]J. S. Tse, J. Superhard. Mater. 32 (2010) 46.

[217]W. C. Oliver, G. M. Pharr, J. Mater. Res. 19 (2004) 3.

[218]D. S. Gospodinova, Z. Burghard, T. Dufaux, M. Burghard, J. Bill, Compos. Sci. Technol. 71 (2011) 931.

[219]G. M. Pharr, D. L. Callahan, S. D. McAdams, T. Y. Tsui, C. S. Bhatia, S. R. P. Silva, J. Robertson, Appl. Phys. Lett. 68 (1996) 779.

[220]S. M. Han, R. Saha, W. D. Nix, Acta Mater. 54 (2006) 1571.

[221]J. Haines, J. Leger, G. Bocquillon, Annu. Rev. Mater. Res. 31 (2001) 1.

[222]M. M. Smedskjaer, J. C. Mauro, Y. Yue, Phys. Rev. Lett. 105 (2010) 115503.

[223]S. H. Jhi, S. G. Louie, M. L. Cohen, J. Ihm, Phys. Rev. Lett. 86 (2001) 3348.

[224]A. Simunek, J. Vackar, Phys. Rev. Lett. 96 (2006) 085501.

[225]J. J. Gilman, Mater. Sci. Eng. A A209 (1996) 74.

[226]K. Li, X. Wang, F. Zhang, D. Xue, Phys. Rev. Lett. 100 (2008) 235504.

[227]X. Chen, H. Niu, D. Li, Y. Li, Intermetallics 19 (2011) 1275.

[228]J. Zhao, C. Zhuang, X. Jiang, Diamond Relat. Mater. 19 (2010) 1419.

[229]P. Jedrzejowski, J. Cizek, A. Amassian, J. E. Klemberg-Sapieha, L. M. J. Vlcekb, Thin Solid Films 447-448 (2004) 201.

[230]I. B. Lezak, A. M. Wroble, M. P. M. Kivitorma, I. J. Vayrynen, Chem. Vap. Deposition 11 (2005) 44.

[231]Y. Awad, M. A. E. Khakani, C. Aktik, J. Mouine, N. Camiré, M. Lessard, M. Scarlete, H. A. Al-Abadleh, R. Smirani, Surf. Coat. Technol. 204 (2009) 539.

[232]F. J. Gómez, P. Prieto, E. Elizalde, J. Piqueras, Appl. Phys. Lett. 69 (1996) 773.

[233]N. M. Park, S. H. Kim, G. Y. Sung, J. Appl. Phys. 94 (2003) 2725.

[234]A. M. Wrobel, I. Błaszczyk, A. Walkiewicz-Pietrzykowsk, A. Tracz, J.E. Klemberg-Sapieh, T. Aoki, Y. Hatanaka, J. Mater. Chem. 13 (2003) 731.

[235]Y. Gao, J. Wei, D. H. Zhang, Z. Q. Mo, P. Hing, X. Shi, Thin Solid Films 377-378 (2000) 562.

[236]X. C. Xiao, Y. W. Li, L. X. Song, X. F. Peng, X. F. Hu, Appl. Surf. Sci. 156 (2000) 155.

[237]Y. Awad, M. A. E. Khakani, M. Scarlete, C. Aktik, R. Smirani, N. Camiré, M. Lessard, J. Mouine, J. Appl. Phys. 107 (2010) 033517.

[238]K. B. Sundaram, J. Alizadeh, Thin Solid Films 370 (2000) 151.

[239]D. H. Zhang, Y. Gao, J. Wei, Z. Q. Mo, Thin Solid Films 377-378 (2000) 607.

[240]P. Jedrzejowski, J. Cizek, A. Amassian, J. E. Klemberg-Sapieha, J. Vlcek, L. Martinu, Thin Solid Films 447-448 (2004) 201.

[241]J. Vlcek, M. Kormunda, J. Cizek, V. Perina, J. Zemek, Surf. Coat. Technol. 160 (2002) 74.

[242]K. Yamamoto, Y. Koga, S. Fujiwara, Diamond Relat. Mater. 10 (2001) 1921.

[243]C. W. Chen, C. C. Huang, Y. Y. Lin, L. C. Chen, K. H. Chen, Diamond Relat. Mater. 14 (2005) 1126.

[244]H. L. Chang, C. T. Kuo, Mater. Chem. Phys. 72 (2001) 236.

[245]S. Trusso, F. Barreca, F. Neri, J. Appl. Phys. 92 (2002) 2485.

[246]Y. C. Chou, S. Chattopadhyay, L. C. Chen, Y. F. Chen, K. H. Chen, Diamond Relat. Mater. 12 (2003) 1213.

[247]E. Riedo, F. Comin, J. Chevrier, F. Schmithusen, S. Decossas, M. Sancrotti, Surf. Coat. Technol. 125 (2000) 124.

[248]D. Marton, K. J. Boyd, A. H. Al-Bayati, S. S. Todorov, J. W. Rabalais, Phys. Rev. Lett. 73 (1994) 118.

[249]Q. Cheng, S. Xu, K. Ostrikov, J. Mater. Chem. 20 (2010) 5853.

[250]D. Yang, A. Velamakanni, G. Bozoklu, S. Park, M. Stoller, R. Piner, S. Stankovich, I. Jung, D. A. Field, C. A. V. Jr, R. S. Ruoff, Carbon 47 (2009) 145.

[251]A. Majumdar, S. C. Das, T. Shripathi, R. Hippler, Chem. Phys. Lett. 524 (2012) 62.

[252]B. Zhang, Y. Yu, Z. Wang, J. Zhang, Appl. Surf. Sci. 256 (2010) 6506.

[253]A. Bendeddouche, R. Berjoan, E. Beche, R. Hillel, Surf. Coat. Technol. 111 (1999) 184.

[254]X. He, T. N. Taylor, R. S. Lillard, K. C. Walter, M. Nastasi, J. Phys.: Condens. Mater 12 (2000) L591.

[255]S. Boughaba, G. I. Sproule, J. P. McCaffrey, M. Islam, M. J. Graham, Thin Solid Films 402 (2002) 99.

[256]I. V. Afanasyev-Charkin, M. Nastasi, J. Vac. Sci. Technol. A 21 (2003) 1909.

[257]Y. Jung, B. R. Lawn, M. Martyniuk, H. Huang, X. Z. Hu, J. Mater. Res. 19 (2004) 3076.

[258]R. B. King, Int. J. Solids Struc. 23 (1987) 1657.

[259]G. M. Pharr, A. Bolshakov, J. Mater. Res. 17 (2002) 2660.

[260]R. Saha, W. D. Nix, Mater. Sci. Eng.: A 319-321 (2001) 898.

[261]T. Y. Tsui, G. M. Pharr, J. Mater. Res. 14 (1999) 292.

[262]W. C. Oliver, G. M. Pharr, J. Mater. Res. 7 (1992) 1564.

[263]S. M. Han, R. Saha, W. D. Nix, Acta Mater. 54 (2006) 1571.

[264]H. Xu, G. M. Pharr, Scripta Mater. 55 (2006) 315.

[265]M. F. Doerner, W. D. Nix, J. Mater. Res. 1 (1986) 601.

[266]R. C. Cammarata, T. E. Schlesinger, C. Kim, S. B. Qadri, A. S. Edelstein, Appl. Phys. Lett. 56 (1990) 1862.

[267]W. D. Nix, Mater. Sci. Eng.: A 234-236 (1997) 37.

[268]A. Gouldstone, H. J. Koh, K. Y. Zeng, A. E. Giannakopoulos, S. Suresh, Acta Mater. 48 (2000) 2277.

[269]X. Dua, Y. Fu, J. Sun, P. Yao, J. Appl. Phys. 99 (2006) 093503.

[270]C. Walter, T. Antretter, R. Daniel, C. Mitterer, Surf. Coat. Technol. 202 (2007) 1103.

[271]W. G. Jiang, J. J. Su, X. Q. Feng, Eng. Fract. Mech. 75 (2008) 4965.

[272]X. Li, B. Bhushan, Mater. Character. 48 (2002) 11.

[273]Y. W. Bao, W. Wang, Y. C. Zhou, Acta Mater. 52 (2004) 5397.

[274]Y. Cao, S. Allameh, D. Nankivil, S. Sethiaraj, T. Otiti, W. Soboyejo, Mater. Sci. Eng.: A 427 (2006) 232.

[275]S. M. Han, R. Shah, R. Banerjee, G. B. Viswanathan, S. M. Clemens, W. D. Nix, Acta Mater. 53 (2005) 2059.

[276]D. Beegan, S. Chowdhury, M. T. Laugier, Thin Solid Films 466 (2004) 167.

[277]Y. T. Cheng, C. M. Cheng, Appl. Phys. Lett. 73 (1998) 614.

[278]Y. T. Cheng, C. M. Cheng, J. Appl. Phys. 84 (1998) 1284.

[279]J. Musil, F. Kunc, H. Zeman, H. Polakova, Surf. Coat. Technol. 154 (2002) 304.

[280]Y. Awad, M. A. E. Khakani, C. Aktik, J. Mouine, N. Camiré, M. Lessard, M. Scarlete, H. A. Al-Abadleh, R. Smirani, Surf. Coat. Technol. 204 (2009) 539.

[281]I. Blaszczyk-Lezak, A. M. Wrobel, D. M. Bielinski, Diamond Relat. Mater. 15 (2006) 1650.

[282]A. Bendeddouche, R. Berjoan, E. Beche, R. Hillel, Surf. Coat. Technol. 111 (1999) 184.